

Department of Physics and Astronomy
Heidelberg University

Master Thesis in Physics
submitted by

Rafet Kavak

born in Akşehir (Türkiye)

2024

Investigating the properties of quark-gluon plasma through Bayesian inference

This Master Thesis has been carried out by Rafet Kavak at the
Physikalisches Institut Heidelberg
under the supervision of
Prof. Dr. Silvia Masciocchi

ABSTRACT

Heavy ion collisions conducted at facilities such as the Large Hadron Collider (LHC) and the Relativistic Heavy Ion Collider (RHIC) create an extremely hot and dense state of matter known as the quark-gluon plasma (QGP). This plasma exists for only about 10^{-23} seconds before transitioning into discrete particles. Although the QGP cannot be observed directly, its properties can be inferred by comparing the results of computational collision models with experimental data. In this thesis, Bayesian parameter estimation is employed to systematically compare model results to data in order to investigate the properties of the QGP. The model includes the `TRENTO` package for initial conditions, `FLUIDUM` for simulating relativistic viscous hydrodynamics, and `FASTRESO` for incorporating resonance decays. The first part of the analysis focuses on quantifying the pion excess in the low transverse momentum regime in heavy-ion collisions. This analysis is conducted across different centrality classes and collision systems at both the LHC and the top RHIC energy. The second part presents a phenomenological analysis of experimental measurements on transverse momentum spectra and flow observables of identified charged hadrons in Pb-Pb and Xe-Xe collisions at the LHC. The Bayesian framework is utilized to constrain model parameters and transport coefficients of the QGP, including shear and bulk viscosities, initialization time, and the kinetic freezeout temperature.

ZUSAMMENFASSUNG

Schwerionenkollisionen, die an Einrichtungen wie dem Large Hadron Collider (LHC) und dem Relativistic Heavy Ion Collider (RHIC) durchgeführt werden, erzeugen einen extrem heißen und dichten Materiezustand, der als Quark-Gluon-Plasma (QGP) bekannt ist. Dieses Plasma existiert nur etwa 10^{-23} Sekunden, bevor es in diskrete Teilchen übergeht. Obwohl das QGP nicht direkt beobachtet werden kann, lassen sich seine Eigenschaften durch den Vergleich der Ergebnisse von rechnerischen Kollisionsmodellen mit experimentellen Daten ableiten. In dieser Arbeit wird die Bayessche Parameterschätzung angewendet, um systematisch Modellergebnisse mit Daten zu vergleichen und so die Eigenschaften des QGP zu untersuchen. Das Modell umfasst das `TRENTO` Paket für die Anfangsbedingungen, `FLUIDUM` für die Simulation relativistischer viskoser Hydrodynamik und `FASTRESO` zur Einbeziehung von Resonanzzerfällen. Der erste Teil der Analyse konzentriert sich auf die Quantifizierung des Pionenüberschusses im Niedrigtransversalimpulsbereich bei Schwerionenkollisionen. Diese Analyse wird über verschiedene Zentralitätsklassen und Kollisionssysteme sowohl am LHC als auch bei der höchsten RHIC-Energie durchgeführt. Der zweite Teil präsentiert eine phänomenologische Analyse experimenteller Messungen der Transversalimpuls-Spektren und Flussobservablen identifizierter geladener Hadronen in Pb-Pb- und Xe-Xe-Kollisionen am LHC. Der Bayesianische Rahmen wird verwendet, um die Modellparameter und Transportkoeffizienten des QGP zu beschränken, einschließlich Scher- und Bulkviskositäten, Initialisierungszeit und kinetischer Freezeout Temperatur, zu beschränken.

ACKNOWLEDGEMENTS

I owe my deepest gratitude to my supervisor, Prof. Dr. Silvia Masciocchi. She gave me the chance to be a part of the ALICE Heidelberg and ALICE@GSI groups, as well as the ISOQUANT Collaboration. These opportunities not only made this work possible but also led to many lasting friendships, none of which would have happened without her support. From her, I learned the value of dedication and hard work, which are qualities you expect from a great advisor. However, what I found most remarkable was how she always managed to react with genuine enthusiasm, even when hearing something from a new learner that she had probably heard hundreds of times before. This is something that will always inspire me. I know that in the future when I come across things I am very familiar with, I will try to share the same excitement and encouragement with those who are just learning. She also taught me how to juggle many things at once. Whether it was preparing for a conference or getting work done on a train, she showed me that with focus, you can accomplish a lot, no matter what external distractions there might be. Lastly, she showed me the importance of taking action at the right time and being honest but kind in supporting students. These lessons will stay with me as I continue my journey beyond graduate school.

Second, I want to express my heartfelt thanks to Dr. Andrea Dubla. During my thesis period, he was the person I interacted with the most and learned from the most. He was more than just a mentor to me; he was a guide and a friend. For me, physics becomes truly enjoyable when you can share your thoughts and outcomes with colleagues, and Andrea was the one I could always turn to. No matter how uncertain or unpolished my ideas were, he listened patiently, questioning everything I did—sometimes critiquing, sometimes encouraging—but always guiding me to find my own path. I genuinely enjoyed the time we spent together, and he helped me see that the world is not a fairy tale; it is complex, but that is what makes it interesting. Andrea went above and beyond, dedicating his personal time to help me, whether it was during weekends or even while on vacation. He played a crucial role in structuring my thesis and provided incredibly detailed feedback after proofreading it. If I were to list everything I learned from Andrea, this acknowledgments section would never end. But to summarize, he taught me that relationships develop over time and that it is important not to judge someone at first glance. We had our ups and downs, but we always found a way to be constructive. Over time, we formed a strong bond—or at least, that is how I feel. I will miss him a lot.

I also want to extend my thanks to Andreas Kirchner and Federica Capellino. I consider myself incredibly lucky to have worked with such outstanding individuals, both academically and personally. When learning something new, we often have those simple questions that could easily be answered with a quick search. Andreas and Federica were the ones I could always go to with those questions. They never made me feel silly—instead, we would usually end up laughing about their simplicity and then diving into deeper discussions. From them, I learned the importance of being welcoming and how a warm advisor-student rela-

tionship can significantly boost one's performance. They were there for me throughout my thesis period, offering feedback and sometimes just providing the emotional support I needed. It was a true honor to work with them, and I am grateful for the impact they have had on both my academic journey and my personal growth.

I also want to express my gratitude to my phenomenology colleague, Rossana Facen, for her unwavering support and friendship. I will miss our shared frustrations over code bugs and the joy we felt when we finally solved them. Your smile and positive energy will always stay with me.

I want to sincerely thank Prof. Dr. Klaus Reygiers for his kindness in agreeing to be the second evaluator for my thesis. His lectures on quark-gluon plasma and statistical methods in particle physics provided me with a deep understanding of these complex topics. The insights and knowledge I acquired from his lectures were highly beneficial in shaping my thesis. I am truly grateful for this.

I would also like to extend my gratitude to the Duke QCD group for providing the `TRENTo` package, to Stefan Floerchinger, Eduardo Grossi, and Jorrit Lion for their work on the `FLUIDUM` package, and to Aleksas Mazeliauskas for the `FASTRESO` package. My thanks also go to Lukas Kreis, Christian Sonnabend, Yannis Seemann, and Luuk Vermunt for their contributions to the development of our Bayesian framework. I am grateful to Ilya Selyuzhenkov and Pengzhong Lu for our collaborative studies on the quantification of the low- p_T pion excess in heavy-ion collisions. I want to thank Izaak Neutelings for his skillful illustrations using TikZ, and I appreciate Bastian Rieck for providing the LaTeX template used in this thesis.

Lastly, I am incredibly thankful to my dear friends Alica Marie Enderich, Anouk Kaiser, Bent Buttwill, Effrosyni (Frosso) Zachou, Fabian Koenigstein, Johannes Hensler, Mika Holzem, Phil Stahlhut, Rossana Facen (once more), Simon Groß-Bölting, and Tim Weinreich for their sincere friendship. The past year and a half we spent together has been truly special. I will forever cherish our conversations, our trips, our dinners—especially at Flammkuchenhof—our parties, our games, our shared jokes, our complaints, our moments of joy and sadness, and most of all, the support we offered each other. I will miss you all deeply, and I sincerely hope that our paths will cross again in the future.

CONTENTS

1	INTRODUCTION	1
1.1	Quantum chromodynamics	1
1.2	Quark-gluon plasma	3
1.3	Heavy-ion collisions	4
1.4	Experimental observables	7
1.4.1	Transverse momentum spectra	7
1.4.2	Anisotropic flow coefficients	9
2	MODELLING HEAVY-ION COLLISIONS	11
2.1	Initial conditions	11
2.1.1	T _R ENTo	11
2.2	Hydrodynamic evolution of QGP	13
2.2.1	Non-relativistic fluid dynamics	14
2.2.2	Relativistic ideal fluid dynamics	14
2.2.3	Relativistic viscous fluid dynamics	15
2.2.4	FLUIDUM	17
2.3	Equation of state and transport properties	21
2.3.1	Equation of state	21
2.3.2	Transport coefficients	23
2.4	Hadronization and final state observables	25
2.4.1	Cooper-Frye freeze-out and thermal spectra	25
2.4.2	Particle spectra including resonance decays	27
2.4.3	Construction of flow coefficients	28
3	BAYESIAN INFERENCE	33
3.1	Parameter space	36
3.1.1	Parameter ranges	36
3.1.2	Sampling of the parameter space	36
3.2	Neural network emulation	38
3.2.1	Neural networks	39
3.2.2	Neural network uncertainty quantification via ensemble method	43

3.3	Bayesian parameter estimation	45
3.3.1	Prior choice	45
3.3.2	Likelihood formulation	45
3.3.3	Markov chain Monte Carlo sampling	46
4	QUANTIFICATION OF THE PION EXCESS IN THE LOW TRANSVERSE MOMENTUM REGIME IN HEAVY-ION COLLISIONS	49
4.1	Determination of the optimal transverse momentum fitting range	53
4.2	Pion excess in the low transverse momentum regime	57
5	MAPPING PROPERTIES OF THE QGP	63
5.1	Analysis of individual collision systems	63
5.1.1	Experimental data	63
5.1.2	Parameter intervals, initial conditions, and partial chemical equilibrium	64
5.1.3	All results in a tabular form	66
5.1.4	Results for Pb-Pb collisions at $\sqrt{s_{NN}} = 2.76$ TeV	67
5.1.5	Results for Pb-Pb collisions at $\sqrt{s_{NN}} = 5.02$ TeV	82
5.1.6	Results for Xe-Xe collisions at $\sqrt{s_{NN}} = 5.44$ TeV	85
5.2	Combined analysis of multiple collision systems	88
6	CONCLUSION AND OUTLOOK	97
A	ADDITIONAL PRIORS AND POSTERiors	99
B	QUANTITATIVE COMPARISONS OF MODEL CALCULATIONS TO EXPERIMENTAL DATA	105
C	ANALYSIS OF MARGINAL POSTERIOR DISTRIBUTIONS FOR MODEL PARAMETERS ACROSS CENTRALITY CLASSES IN Pb-Pb COLLISIONS AT $\sqrt{s_{NN}} = 2.76$ TeV	111
	BIBLIOGRAPHY	115

1 INTRODUCTION

1.1 QUANTUM CHROMODYNAMICS

Quantum chromodynamics (QCD) is the gauge field theory that describes the strong interaction, one of the four fundamental forces in nature [1]. QCD governs the behavior of quarks, the elementary constituents of matter, which interact through the exchange of massless vector gauge bosons known as gluons. Although QCD shares conceptual similarities with quantum electrodynamics (QED), the theory of electromagnetic interactions, it is built on a more complex gauge structure, $SU(3)_{\text{color}}$, compared to the simpler $U(1)$ symmetry of QED. This $SU(3)_{\text{color}}$ symmetry introduces a variety of novel features and complexities, most notably the self-interaction of gluons, which carry a quantum property known as color charge, analogous to electric charge in QED.

The self-coupling of gluons in QCD leads to a unique behavior of the strong coupling constant, α_s , which serves as the QCD analogue of the fine-structure constant α in QED. α_s exhibits a strong dependence on the distance scale or momentum transfer involved in a process. At large distances or low momentum transfers—corresponding to momentum scales $Q < 1 \text{ GeV}/c$ or distances greater than 1 fm—the coupling constant α_s becomes large. This increase in coupling strength at low energies provides a qualitative explanation for the phenomenon known as confinement: quarks and gluons cannot exist freely but are perpetually bound together to form color-neutral composite particles known as hadrons, such as protons, neutrons, and pions.

Hadrons are composed of quarks that carry one of three possible color charges—red, green, or blue. These quarks combine in such a way that the resulting hadron is colorless, a requirement dictated by the $SU(3)_{\text{color}}$ symmetry. Baryons, for instance, are formed by three quarks (or three antiquarks), while mesons consist of a quark-antiquark pair. In contrast to the electrically neutral photon of QED, gluons in QCD are not color-neutral; instead, they carry a combination of color and anti-color charges, allowing them to interact with one another.

While QCD does not provide an explicit value for the strong coupling constant α_s at any given momentum transfer Q , it does predict the functional form of its variation with Q . This variation is encapsulated in the concept of asymptotic freedom, a fundamental property of QCD discovered in the 1970s [2, 3]. Asymptotic freedom refers to the phenomenon where α_s decreases as the momentum transfer increases, leading to weaker interactions between quarks and gluons at short distances or high Q . Mathematically, as Q becomes very large ($Q \rightarrow \infty$), the strong coupling constant α_s approaches zero, effectively rendering quarks and gluons nearly free at such scales. This behavior contrasts sharply with the confinement at low momen-

tum transfers, and it is this dual nature of QCD that underpins much of our understanding of high-energy particle physics.

To understand the variation of α_s with Q , we rely on the renormalization group equation [4], which governs the Q dependence of α_s :

$$Q^2 \frac{\partial \alpha_s(Q^2)}{\partial Q^2} = \beta(\alpha_s(Q^2)), \quad (1.1)$$

where $\beta(\alpha_s)$ is the β function, which accounts for quantum corrections to the running of α_s . While the β function is typically expanded and calculated to the 4-loop approximation [4, 5], for simplicity, we consider the expansion up to the 2-loop:

$$\beta(\alpha_s(Q^2)) = -\beta_0 \alpha_s^2(Q^2) - \beta_1 \alpha_s^3(Q^2) + \mathcal{O}(\alpha_s^4), \quad (1.2)$$

where $\beta_0 = \frac{33-2N_f}{12\pi}$ and $\beta_1 = \frac{153-19N_f}{24\pi^2}$, with N_f representing the number of active quark flavors at the energy scale Q . These coefficients, β_0 and β_1 , are derived from the group constants $C_A = N$ and $C_F = \frac{N^2-1}{2N}$, which are specific to theories with $SU(N)$ symmetry. In the case of QCD, where $SU(3)$ symmetry applies, $C_A = 3$ and $C_F = \frac{4}{3}$.

The renormalization group equation, in its one-loop approximation—where higher-order terms in β_1 and beyond are neglected—yields the following solution:

$$\alpha_s(Q^2) = \frac{\alpha_s(\mu^2)}{1 + \alpha_s(\mu^2)\beta_0 \ln\left(\frac{Q^2}{\mu^2}\right)}, \quad (1.3)$$

where μ^2 acts as an integration constant. This expression not only relates the values of α_s at two different momentum transfers— μ^2 and Q^2 —but also illustrates the property of asymptotic freedom. As Q^2 approaches infinity, the strong coupling constant α_s diminishes toward zero, provided that the number of active quark flavors N_f remains below 17, affirming that quarks and gluons behave as free particles at high energies.

The determination of α_s at a particular Q is an essential task, akin to measuring fundamental constants such as the electromagnetic coupling α , the elementary electric charge, or the gravitational constant. However, testing the predictions of QCD requires more than just a single measurement of α_s . It necessitates precise measurements across a wide range of energy scales to compare experimental results with theoretical calculations and validate the theory's predictions, particularly regarding confinement at low energies and asymptotic freedom at high energies.

Relating the underlying concepts of QCD to observable phenomena is challenging, as exact analytical solutions to the QCD equations are often impractical. For high-energy interactions, where the momentum transfer Q^2 exceeds $1 \text{ GeV}^2/c^2$, perturbative QCD (pQCD) becomes a reliable tool. In pQCD, the strong coupling constant α_s is small enough to allow the expansion of the equations in terms of α_s , enabling accurate calculations of scattering matrix elements and other quantities of interest. These theoretical predictions can then be directly compared with experimental data, as illustrated in [Figure 1.1](#).

At low energies, however, the strong coupling constant α_s becomes too large for perturbative methods to be effective. In this regime, non-perturbative approaches such as lattice QCD (LQCD) [7] are employed.

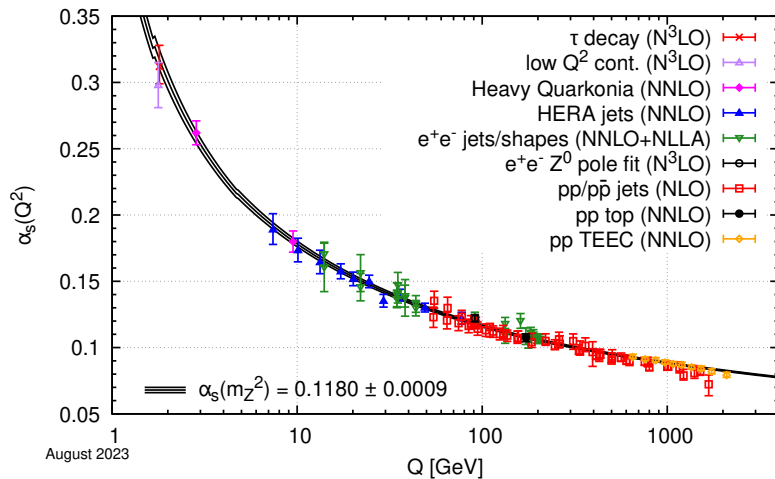


Figure 1.1: Measurements of the strong coupling constant α_s as a function of the momentum transfer Q [6]. The pQCD method used to determine each value is indicated in parentheses, allowing for comparison with experimental data.

LQCD involves discretizing space-time into a finite grid, enabling the numerical computation of QCD interactions. Despite its computational intensity, requiring supercomputing resources, LQCD has been successful in accurately predicting various hadronic properties, including masses and decay rates [8, 9].

1.2 QUARK-GLUON PLASMA

The variation of the strong coupling constant α_s with Q leads to the prediction of distinct phases of nuclear matter within QCD, each characterized by different dominant degrees of freedom. In ordinary nuclear matter, where the temperature T is close to zero and the baryon chemical potential μ_B is approximately 1 GeV—indicating a slight excess of matter over antimatter—quarks and gluons are confined within color-neutral hadrons due to the strong coupling at low energies. This confinement ensures that quarks and gluons cannot move freely over large distances. However, at extremely high temperatures, on the order of 150–160 MeV (equivalent to temperatures exceeding 10^{12} K), and/or at high baryon densities, QCD predicts that quarks and gluons can escape this confinement. In such conditions, they can move freely over distances larger than the size of a nucleon, forming a deconfined state of matter known as quark-gluon plasma (QGP) [10, 11].

The different phases of strongly interacting matter can be illustrated using a QCD phase diagram, where temperature and baryon chemical potential serve as the primary thermodynamic variables. A schematic version of this phase diagram is shown in Figure 1.2. At low temperatures and small baryon chemical potential, quarks and gluons remain confined within hadronic states, maintaining the color-neutral property of nuclear matter. Ordinary nuclear matter, like that found in atomic nuclei, occupies this region of the phase diagram at $T \sim 0$ and $\mu_B \sim 1$ GeV.

As the temperature increases, the system may transition into the QGP phase. For conditions where the baryon chemical potential μ_B is nearly zero, LQCD calculations indicate that this transition is not a sharp phase change but rather a smooth crossover [13]. The critical temperature at which this crossover occurs has

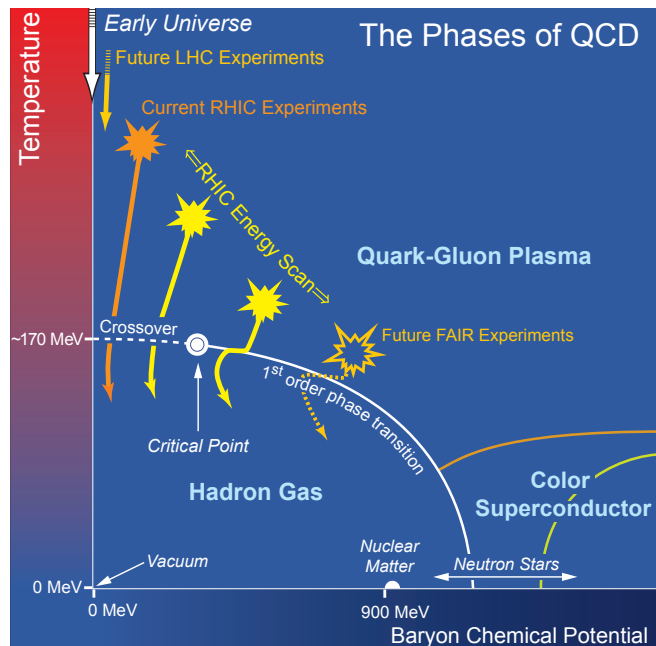


Figure 1.2: Schematic representation of the QCD phase diagram for nuclear matter, illustrating the phase boundaries between different states of matter. The solid lines indicate the boundaries separating the distinct phases, with the solid circle marking the critical point. The diagram also shows possible trajectories for systems created in the QGP phase at various accelerator facilities, which differ in center-of-mass collision energy and colliding species [12].

been estimated by LQCD to be $T_c = 154 \pm 9$ MeV [14]. This state of matter is believed to have existed in the early universe, microseconds after the Big Bang, before the universe cooled below the critical temperature T_c and quarks and gluons became confined within hadrons once again [15].

At finite temperatures close to zero and increasing baryon chemical potential, QCD predicts a first-order phase transition to a deconfined state, potentially exhibiting color-superconducting properties [16]. Such a phase might exist in the dense cores of neutron stars, where extreme conditions prevail.

1.3 HEAVY-ION COLLISIONS

Ultra-relativistic heavy-ion collisions serve as a powerful tool for probing the QGP because they generate the extreme temperatures and energy densities required to reach this deconfined state of matter. Currently, there are two major experimental facilities in the world capable of achieving such conditions: the Large Hadron Collider (LHC) at the European Organization for Nuclear Research (CERN) in Geneva, Switzerland, and the Relativistic Heavy Ion Collider (RHIC) at Brookhaven National Laboratory (BNL) in New York, USA.

RHIC is a circular accelerator primarily dedicated to colliding heavy ions, although it also conducts experiments with protons and light ions. It operates at center-of-mass energies per nucleon pair ranging from $\sqrt{s_{NN}} = 7.7$ to 200 GeV [17–20]. While RHIC’s maximum energy is lower than that of the LHC, it offers several unique advantages, such as longer operational periods for heavy-ion collisions and highly configurable beam settings. This versatility enables detailed studies of various collision systems and energies, making RHIC an invaluable facility for QGP research.

The LHC, like RHIC, is a large circular collider, but it is distinguished by its unprecedented beam energies. The LHC has achieved proton-proton collision energies up to $\sqrt{s_{NN}} = 13$ TeV [21] and heavy-ion collision energies up to $\sqrt{s_{NN}} = 5.44$ TeV [22], which is more than an order of magnitude higher than the maximum energies reached at RHIC. Although heavy-ion collisions constitute a smaller fraction of the LHC's overall physics program compared to RHIC, the LHC's higher energies provide a complementary perspective, allowing the study of QGP under extreme conditions.

When two ultra-relativistic heavy ions collide, the system undergoes a complex evolution that can be visualized as a space-time diagram, as depicted in Figure 1.3.

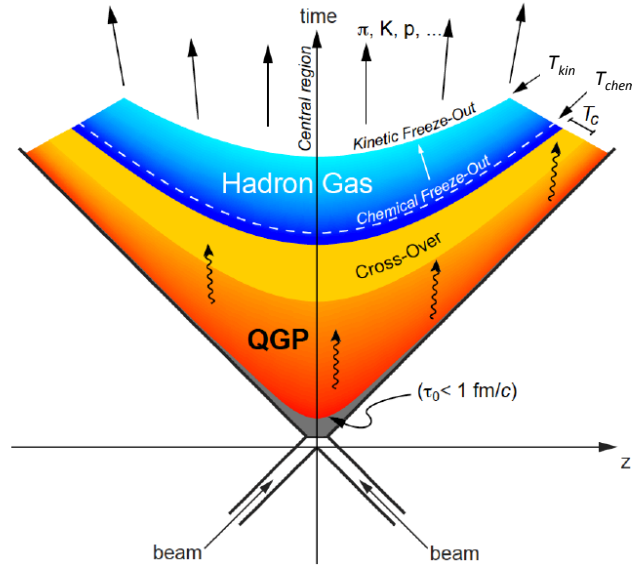


Figure 1.3: Illustration of the space-time evolution of a heavy-ion collision in the laboratory frame. The hyperbolic curves represent regions of constant proper-time τ . The figure is taken from [23].

The basic concept of the space-time evolution during a heavy-ion collision was first introduced by Bjorken in 1982 [24]. In the Bjorken coordinate system, the horizontal axis represents the longitudinal direction, parallel to the initial beam, while the vertical axis represents time. The QGP forms near the origin and expands hydrodynamically in both the transverse plane (x - y) and the longitudinal direction z . At any given z position, the fluid's longitudinal velocity is approximately z/t . As the colliding nuclei continue to separate, the fluid forms at later times away from $z = 0$, approximately along a spacetime hyperbola defined by the constant proper time $\tau \equiv \sqrt{t^2 - z^2} \sim 1$ fm/ c [25].

Since the QGP phase exists for only about $\tau \sim 10$ fm/ c , corresponding to 10^{-23} s, its properties must be inferred indirectly through the analysis of the entire evolution of the heavy-ion collision. Understanding the various stages of this evolution is therefore crucial and can be described as follows:

- **Before the collision ($\tau < 0$ fm/ c):** The initial stage of a heavy-ion collision involves two heavy nuclei approaching each other at velocities near the speed of light. Due to relativistic effects, the colliding nuclei are significantly Lorentz-contracted along the longitudinal (z) direction, resembling thin pancakes as they move toward the point of collision.

- **Initial state** ($\tau = 0 \text{ fm}/c$): At the moment of collision, the nuclei overlap, and the energy density reaches its peak, primarily due to the extreme Lorentz contraction. The transverse structure of the nuclei at this instant is characterized by the spatial distribution of the nucleons. The majority of quarks and gluons involved in the collision undergo low-momentum transfer interactions, predominantly soft collisions between gluons, which carry only a small fraction of the total momentum of the nuclei [26]. A small fraction of partons, however, engage in hard collisions, involving significant momentum transfer and resulting in the production of particles with large transverse momentum. The majority of the entropy produced in the collision occurs during this initial moment [27].
- **Pre-equilibrium phase** ($0 < \tau \lesssim 1 \text{ fm}/c$): During this phase, the system is far from thermal equilibrium, and the interaction rate between partons is extremely high. Hard scattering processes may occur, leading to the production of high-energy particles known as hard probes. These probes are of particular interest as they carry information about the early stages of the collision. The system rapidly approaches local thermal equilibrium, with the thermalization time expected to be $\tau_0 \lesssim 1 \text{ fm}/c$ [28].
- **Hydrodynamic phase** ($1 \lesssim \tau \lesssim 10 \text{ fm}/c$): Once local thermal equilibrium is achieved, the system can be described as a QGP. In this phase, the QGP exhibits significant transverse and longitudinal pressure gradients, which drive its expansion. These pressure gradients arise from the differences in matter density compared to the vacuum and from the inhomogeneities present in the initial state. The evolution of the QGP during this phase is well-described by the equations of relativistic fluid dynamics. As the QGP continues to expand, its energy density and temperature gradually decrease.
- **Hadronization and freeze-out** ($\tau \sim 10 \text{ fm}/c$): As the system cools down and the energy density drops below a critical threshold, the QGP undergoes a phase transition into a hadron gas. During this transition, the strong interactions between particles weaken, causing the fluid dynamic description to become less applicable. Chemical freeze-out occurs when inelastic collisions cease, fixing the composition of the hadrons. LQCD calculations and experimental measurements have shown that the chemical freeze-out temperature aligns closely with the QGP crossover temperature at high collision energies [29]. Following chemical freeze-out, particles continue to scatter elastically until the system becomes sparse enough that the momentum distribution of the particles no longer changes. This final stage is known as kinetic freeze-out.
- **Final detected particles** ($\tau \gg 10 \text{ fm}/c$): After kinetic freeze-out, particles stream freely toward the detectors. As they travel, long-lived unstable particles decay, contributing to the mix of primary and decay products that are eventually detected. The primary particles detected are predominantly pions, kaons, and protons. By analyzing these final-state particles, we can infer the entire timeline and dynamics of the collision.

1.4 EXPERIMENTAL OBSERVABLES

An experimental observable refers to any measurable quantity or parameter that can be derived from experimental data obtained during heavy-ion collisions. The experimental observables related to the QGP can broadly be categorized into two classes: particle yield measurements and particle correlation measurements.

Particle yields are often measured in relation to various kinematic variables such as the rapidity y , pseudorapidity η , or the transverse momentum p_T of identified particles. These measurements can also be examined with respect to event characteristics, like the charged hadron multiplicity N_{ch} , which represents the number of particles produced in the collision. The relevant kinematic quantities are defined as follows:

$$y = \frac{1}{2} \ln \frac{E + p_z}{E - p_z}, \quad (1.4)$$

$$\eta = -\ln \tan(\theta/2), \quad (1.5)$$

$$p_T = \sqrt{p_x^2 + p_y^2}, \quad (1.6)$$

where θ is the polar angle and E is the energy. It is important to note that while pseudorapidity η approximates rapidity y when $p_T \gg m$, where m is the particle's mass, they should not be confused with spacetime rapidity η_s . The former operates on the energy-momentum vector, while the latter pertains to spacetime position.

Basic yield measurements provide insight into the cross sections of the underlying production processes [30], where yield ratios between different hadron species can provide information about the hadronization process [31]. In addition to yield measurements, particle correlations represent another essential class of observables. Correlations are typically calculated between the kinematic variables of particular identified particles or between all particles produced in a collision event. For example, correlations in the azimuthal angle provide information about anisotropic flow coefficients [32], whereas momentum correlations are more sensitive to the spatial evolution of the system [33]. In this section, we will focus on two key experimental observables that are central to the analyses throughout this thesis: transverse momentum spectra and anisotropic flow coefficients.

1.4.1 TRANSVERSE MOMENTUM SPECTRA

The transverse momentum (p_T) spectra represent the distribution of particle yields as a function of transverse momentum. Mathematically, the differential p_T spectra can be expressed as:

$$E \frac{d^3 N}{d^3 \mathbf{p}} = \frac{1}{2\pi p_T} \frac{d^2 N}{dp_T dy}, \quad (1.7)$$

where $E \frac{d^3 N}{d^3 \mathbf{p}}$ represents the invariant yield as a function of momentum and $\frac{d^2 N}{dp_T dy}$ is the differential yield per unit transverse momentum and rapidity. The factor $\frac{1}{2\pi p_T}$ accounts for the phase space density, where p_T is treated as a polar or cylindrical radius in momentum space.

By integrating Equation 1.7 over the transverse momentum and rapidity, one can obtain the multiplicity of particles. The multiplicity is a key observable that depends strongly on the impact parameter b in the transverse plane, which is defined as the distance between the centers of mass of the two colliding nuclei at the point of closest approach. Since the impact parameter cannot be directly measured, collision events are categorized into centrality classes based on the total charged-particle multiplicity. Centrality classes provide a way to classify collision events according to the degree of overlap between the colliding nuclei. These classes are typically expressed as percentiles. For instance, the 0–5% centrality class corresponds to the 5% of events with the highest multiplicity, indicating the most central, head-on collisions. Conversely, higher centrality percentiles correspond to more peripheral collisions, where the overlap between the nuclei is smaller.

As previously discussed, the chemical freeze-out marks the point at which the abundances of different hadronic species become fixed. However, the shapes of their momentum spectra can still be altered during the subsequent hadronic phase due to elastic scatterings. It is only after the kinematic freeze-out—when the system has expanded and cooled sufficiently that it becomes too dilute for further interactions—that the momentum spectra of particles become fixed and unchanging.

To analyze the spectral shapes of hadronic species, particularly in the low p_T region, it is useful to transform to the transverse mass variable $m_T = \sqrt{p_T^2 + m^2}$, where m is the rest mass of the particle. The m_T distributions are often considered because they exhibit a universal pattern, known as " m_T scaling," at low m_T [34]. This transformation is expressed as:

$$\frac{1}{2\pi} \frac{d^2N}{p_T dp_T dy} = \frac{1}{2\pi} \frac{d^2N}{m_T dm_T dy}, \quad (1.8)$$

where the transverse mass distribution can be described by an exponential function:

$$\frac{1}{2\pi} \frac{d^2N}{m_T dm_T dy} = \exp\left(-\frac{m_T}{T_{\text{slope}}}\right). \quad (1.9)$$

Here, T_{slope} represents the universal inverse slope parameter. This parameter characterizes the m_T spectra and represents the slope of the p_T distribution.

For an expanding system, the parameter T_{slope} is influenced by both the kinetic freeze-out temperature T_{kin} and the collective expansion velocity of the system, denoted as $\langle v_{\perp} \rangle$. This expansion is referred to as radial flow [30]. In the low p_T regime ($p_T \leq 2 \text{ GeV}/c$), T_{slope} can be expressed as:

$$T_{\text{slope}} = T_{\text{kin}} + \frac{1}{2} m_i \langle v_{\perp} \rangle^2, \quad (1.10)$$

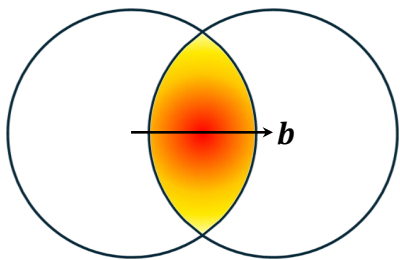
where m_i is the mass of the particle species. This relationship demonstrates how the observed inverse slope parameter T_{slope} encapsulates both the thermal motion of particles at kinetic freeze-out and the additional momentum boost from the system's collective expansion. Thus, by analyzing the p_T spectra, we can attempt to constrain the freeze-out temperatures.

1.4.2 ANISOTROPIC FLOW COEFFICIENTS

One of the most pivotal discoveries associated with the formation of the QGP is the evidence of collective flow within the system. Before the first ultra-relativistic heavy-ion collisions were conducted at RHIC, it was widely anticipated that the QGP would behave as a weakly-coupled gas [35]. This assumption, based on the idea that particle production occurs independently at various points within the heavy-ion collision, implied that the final hadron yields would exhibit weak correlations with respect to the azimuthal angle ϕ . Under this scenario, significant azimuthal correlations were expected to arise primarily from jets and other hard scatterings, which generate back-to-back particle showers near midrapidity.

However, the initial measurements at RHIC presented a strikingly different scenario. The data revealed that particles produced in each collision exhibited strong correlations with respect to the azimuthal angle ϕ , and these correlations extended far from midrapidity [36], contradicting the weakly-coupled predictions [37]. The observed pattern was more consistent with a strongly-coupled system, where the QGP behaves like a nearly perfect, low-viscosity liquid.

Initial state spatial anisotropy



Final state momentum anisotropy

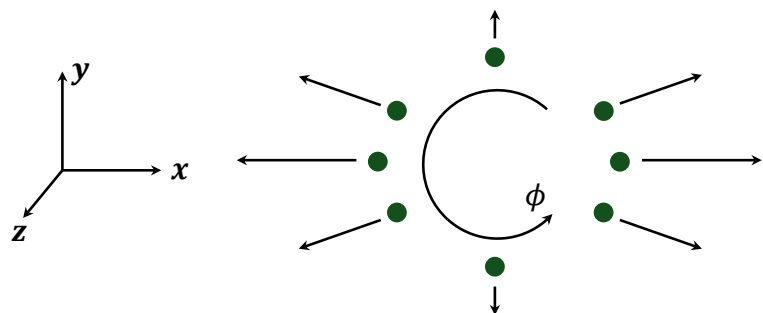


Figure 1.4: Left: The asymmetric overlap region formed by two colliding nuclei (represented by circles) with a non-zero impact parameter b . Right: The resulting anisotropic emission of particles in the transverse plane. The figure is inspired from [25].

The development of azimuthal correlations in the context of heavy-ion collisions can be understood through the lens of hydrodynamic flow. In a typical collision between two ultra-relativistic nuclei, as depicted on the left side of Figure 1.4, the nuclei collide with a non-zero impact parameter b , resulting in an asymmetric overlap region that resembles an almond shape. This region, where the hot and dense QGP forms, exhibits a steeper pressure gradient. The pressure difference from the central region to the surrounding vacuum is more significant along the x -axis than the y -axis due to the shorter distance over which this change occurs. These anisotropic pressure gradients drive the fluid-like expansion of the QGP more strongly in the x -direction. As the QGP cools and hadronizes, this directional momentum is transferred to the outgoing particles, leading to a transverse momentum distribution that is anisotropic as illustrated on the right side of Figure 1.4. As a result, there is an enhanced particle yield near azimuthal angles $\phi = 0$ and $\phi = \pi$, reflecting the initial spatial asymmetry in the collision.

Experimentally, this anisotropy in particle yield is quantified by expanding the azimuthal particle distribution into a Fourier series [38, 39]:

$$\frac{dN}{d\phi} \propto 1 + 2 \sum_{n=1}^{\infty} v_n \cos[n(\phi - \Psi_n)], \quad (1.11)$$

where Ψ_n represents the event plane angle, which corresponds to the direction of maximum final-state particle density. The integer n denotes the harmonic order, with the first harmonic v_1 known as directed flow, the second harmonic v_2 as elliptic flow, the third harmonic v_3 as triangular flow, and so forth.

These flow coefficients, or harmonics, are calculated by:

$$v_n = \langle \langle \cos[n(\phi - \Psi_n)] \rangle \rangle. \quad (1.12)$$

The notation $\langle \langle \dots \rangle \rangle$ represents an average taken first over all particles within a single event, and then averaged over all events within a defined event class. These classes are typically categorized based on parameters such as centrality, rapidity, and transverse momentum. When the flow is analyzed as a function of p_T within narrow p_T bins, it is referred to as differential flow and denoted as $v_n(p_T)$. In contrast, integrated flow refers to the flow coefficients v_n that are averaged over the entire transverse momentum range, quantifying the overall azimuthal anisotropy within a given centrality class.

Flow coefficients are sensitive indicators of the viscous properties of the QGP. The shear and bulk viscosities of the QGP influence the evolution of its flow patterns by altering the system's response to initial spatial anisotropies. Shear viscosity, which induces anisotropic deviations from local equilibrium, acts to smooth out differences in expansion rates across various directions, thereby reducing the anisotropic flow generated by the initial geometric anisotropies of the collision zone. Consequently, higher shear viscosity leads to smaller flow coefficients, reflecting a diminished ability of the medium's collectivity to convert initial state spatial anisotropies into final state momentum anisotropies [35]. In contrast, bulk viscosity introduces isotropic pressure corrections that counteract the expansion, primarily affecting the radial flow and resulting in steeper p_T spectra. By precisely measuring flow coefficients and comparing them with theoretical models, we can extract valuable constraints on the shear and bulk viscosities of the QGP.

2 MODELLING HEAVY-ION COLLISIONS

2.1 INITIAL CONDITIONS

Initial condition models play an essential role in defining the entropy or energy density at the thermalization time τ_0 , the point at which the QGP is formed and fluid-dynamic descriptions become applicable. There are two primary approaches to modeling the initial state. The first approach explicitly models the pre-equilibrium stage, as in the IP-Glasma model [40], which incorporates the interactions and dynamics of the constituent particles to provide a more realistic description of the early-time evolution. However, since this approach is not utilized in our framework, further details are not included here.

The other approach treats the initial state of the collisions as a superposition of binary nucleon-nucleon collisions, commonly referred to as the Glauber model [41]. This method is based on several key assumptions. Firstly, due to their large longitudinal momentum, nucleons travel along straight-line trajectories, and their positions within the nuclei remain effectively unchanged. Upon collision, nucleons undergo binary nucleon-nucleon scattering, with the likelihood of such an interaction determined by the experimentally measured inelastic nucleon-nucleon cross section. The transverse momentum gained in these interactions is relatively small compared to the original longitudinal momentum, allowing for the assumption that the nucleons continue on straight-line trajectories after collision. In these events, the deposition of entropy occurs, and in the absence of a first-principles description, its distribution remains dependent on the specific model employed. These models provide the energy or entropy density at τ_0 and serve as the initial conditions for the subsequent fluid dynamics of the QGP without addressing the thermalization process itself. The focus is predominantly on the transverse dynamics within the participant region, with no modeling of the longitudinal dynamics or the behavior of spectators (nucleons that do not participate in scattering). Since a majority of the entropy in heavy-ion collisions is generated during the initial state, the particle yield in the final state is proportional to the initial entropy, which is used to categorize collisions into centrality classes. In our analysis, the TRENTo model¹ is employed to generate the initial conditions for hydrodynamic evolution, thereby omitting a specific description of the pre-equilibrium stage.

2.1.1 TRENTo

This section is primarily based on the works of Moreland et al. [43, 44]. For a comprehensive understanding, readers are encouraged to refer to these sources.

¹A 3D version of TRENTo also exists [42], which computes a fully three-dimensional energy density profile including longitudinal fluctuations. However, we use the 2D version in our framework.

TRENTo is an effective model designed to generate realistic Monte Carlo initial entropy profiles without assuming specific physical mechanisms for entropy generation, pre-equilibrium dynamics, or thermalization [44]. The model employs the Monte Carlo Glauber formalism [45] as its foundation and parametrizes entropy deposition as a function of local participant nuclear density. The key operational principles of TRENTo are summarized as follows:

1. The nucleon positions for nuclei A and B are sampled from a standard uncorrelated Woods-Saxon distribution and shifted by $\pm b/2$, where b is the impact parameter (assumed to be along the x direction), such that $\rho_{A,B} = \rho(x \pm b/2, y, z)$. Additionally, a minimum distance criterion $|x_i - x_j| > d_{min}$ can be introduced to emulate the repulsive interactions between individual pairs of nucleons.
2. Inelastic nucleon-nucleon collisions, i.e., participants, are sampled using an impact parameter-dependent nucleon-nucleon collision profile adapted from the analytic Glauber model:

$$P_{\text{coll}}(b) = 1 - \exp[-\sigma_{gg} T_{nn}(\mathbf{b})], \quad (2.1)$$

where σ_{gg} denotes the effective parton-parton cross section, ensuring that the total nucleon-nucleon cross section matches the experimentally observed inelastic nucleon-nucleon cross section. The nucleon density is modeled as a three-dimensional Gaussian distribution with width w . The nucleon thickness function is then given by:

$$T_n(\mathbf{x}_\perp) = \frac{1}{2\pi w^2} \exp\left(-\frac{|\mathbf{x}_\perp|^2}{2w^2}\right), \quad (2.2)$$

and the nucleon-nucleon overlap function $T_{nn}(b)$ is defined as:

$$T_{nn}(b) = \int d^2x T_n(\mathbf{x}_\perp) T_n(\mathbf{x}_\perp - \mathbf{b}) = \frac{1}{4\pi w^2} \exp\left(-\frac{b^2}{4w^2}\right). \quad (2.3)$$

3. The density of each nucleon, ρ_n , is summed over $N_{A,B}$, the total number of participants in each nucleus, to produce a three-dimensional participant density field:

$$\tilde{\rho}_{A,B}^{\text{part}}(\mathbf{x}) = \frac{1}{N_{A,B}} \sum_{i=1}^{N_{A,B}} \gamma_i \rho_n(\mathbf{x} - \mathbf{x}_i \pm \mathbf{b}/2), \quad (2.4)$$

where γ_i are the nucleon weights sampled from a gamma distribution with a unit mean and variance $1/k$. Each constituent density ρ_n is described by a Gaussian distribution of width v :

$$\rho_n(\mathbf{x}) = \frac{1}{(2\pi v^2)^{3/2}} \exp\left(-\frac{\mathbf{x}^2}{2v^2}\right), \quad (2.5)$$

and each constituent's position \mathbf{x}_i in Equation 2.4 is sampled from a Gaussian radial distribution. The participant density $\tilde{\rho}_{A,B}^{\text{part}}(\mathbf{x})$ is then projected onto the transverse plane, \mathbf{x}_\perp , by integrating over z to construct two participant thickness functions:

$$\tilde{T}_{A,B}(\mathbf{x}_\perp) = \int dz \tilde{\rho}_{A,B}^{\text{part}}(\mathbf{x}_\perp, z). \quad (2.6)$$

These participant thickness functions describe the fluctuating density of participant matter in each nucleus as observed by a probe moving parallel to the beam axis and intersecting the transverse coordinate \mathbf{x}_\perp .

4. The entropy density s at midrapidity and at thermalization time is set proportional to the reduced thickness function, defined as the generalized mean of the participant thickness functions:

$$s(\tau_0, \mathbf{x}_\perp)|_{\eta_s=0} \propto T_R(p; \tilde{T}_A, \tilde{T}_B) \equiv \left(\frac{\tilde{T}_A + \tilde{T}_B}{2} \right)^{1/p}, \quad (2.7)$$

where τ_0 is the thermalization time and η_s is the spacetime rapidity. This parametrization introduces a continuous entropy deposition parameter p , which effectively interpolates among different entropy deposition schemes. For $p = (1, 0, -1)$, the generalized mean reduces to the arithmetic, geometric, and harmonic means, respectively, while for $p \rightarrow \pm\infty$, it asymptotically approaches the minimum and maximum functions.

2.2 HYDRODYNAMIC EVOLUTION OF QGP

Hydrodynamics, also referred to as fluid dynamics, is the theoretical framework that governs the motion of fluids. Originally developed to describe the behavior of water, this theory is applicable to a wide range of materials. Hydrodynamics serves as an effective theory for the long-wavelength behavior of systems where there is a sufficient separation of scales. In such systems, macroscopic motions vary so slowly in space and time that they are largely insensitive to the underlying microscopic dynamics. For instance, in the case of water, when macroscopic quantities such as pressure and temperature vary slowly in space relative to the average molecular distance and slowly in time relative to the molecular scattering rate, the fluid's behavior can be accurately described by the equations of hydrodynamics.

The bulk dynamics of the quark-gluon plasma can be effectively described using the framework of viscous relativistic hydrodynamics [46, 47], grounded in the fundamental principles of energy and momentum conservation. The core equations governing these dynamics are derived from these conservation laws. To gain a deeper understanding, it is useful to first review the conventional non-relativistic formulation of hydrodynamics, which provides the foundation upon which relativistic theories are built.

2.2.1 NON-RELATIVISTIC FLUID DYNAMICS

The conventional non-relativistic formulation of hydrodynamic equations describes the evolution of fluid properties such as velocity $\mathbf{v}(t, \mathbf{x})$, pressure $p(t, \mathbf{x})$, and mass density $\rho(t, \mathbf{x})$ at each point in space and time. These properties are governed by the following equations [48, 49]:

$$\frac{\partial \rho}{\partial t} + \nabla \cdot (\rho \mathbf{v}) = 0, \quad (2.8)$$

$$\frac{\partial \mathbf{v}}{\partial t} + (\mathbf{v} \cdot \nabla) \mathbf{v} = -\frac{1}{\rho} \nabla p. \quad (2.9)$$

These equations, known as the continuity equation (Equation 2.8) and Euler equation (Equation 2.9), respectively, express the conservation of mass and momentum for an ideal fluid, which is a fluid without dissipation. To complete the system of equations, an additional relation, typically an equation of state $p = p(\rho)$, is required.

For non-ideal fluids where dissipative effects are significant, the Euler equation is extended to the Navier-Stokes equations [50, 51]:

$$\frac{\partial v^i}{\partial t} + v^k \frac{\partial v^i}{\partial x^k} = -\frac{1}{\rho} \frac{\partial p}{\partial x^i} - \frac{1}{\rho} \frac{\partial \Pi^{ki}}{\partial x^k}, \quad (2.10)$$

$$\Pi^{ki} = -\eta \left(\frac{\partial v^i}{\partial x^k} + \frac{\partial v^k}{\partial x^i} - \frac{2}{3} \delta^{ki} \frac{\partial v^l}{\partial x^l} \right) - \zeta \delta^{ik} \frac{\partial v^l}{\partial x^l}. \quad (2.11)$$

The viscous stress tensor Π^{ki} incorporates the shear viscosity (η) and bulk viscosity (ζ). The coefficients, similar to the equation of state, depend on the specific fluid in question and reflect information about its microscopic dynamics.

2.2.2 RELATIVISTIC IDEAL FLUID DYNAMICS

To extend the discussion to a relativistic framework, we introduce the energy-momentum tensor $T^{\mu\nu}(x)$. This symmetric tensor encapsulates the distribution of energy and momentum within a system. In any chosen reference frame, the component T^{00} represents the energy density, $T^{0i} = T^{i0}$ indicates the i -th component of the momentum density, and T^{ik} represents the flux of the i -th component across the x^k surface.

The conservation of energy and momentum in relativistic terms is expressed as:

$$\partial_\mu T^{\mu\nu} = 0. \quad (2.12)$$

At each point in space-time, we define the local rest frame of the fluid, where the momentum density is zero, $T^{0i}(x) = 0$. The velocity of this local rest frame relative to a fixed laboratory frame defines a fluid 4-velocity $u^\mu(x)$. In the local rest frame, this 4-velocity is $u_{rest}^\mu = (1, 0, 0, 0)$, and it satisfies $u^2 = u^\mu u_\mu = 1$. Thus, we have $u_\mu T^{\mu\nu} = \epsilon u^\nu$, where $\epsilon(x)$ is the energy density in the fluid's rest frame.

The equations of relativistic ideal hydrodynamics arise from the conservation equation [Equation 2.12](#) when the energy-momentum tensor is isotropic (rotationally invariant) in the local rest frame:

$$T_{ideal,rest}^{\mu\nu} = \begin{pmatrix} \epsilon & 0 & 0 & 0 \\ 0 & p & 0 & 0 \\ 0 & 0 & p & 0 \\ 0 & 0 & 0 & p \end{pmatrix}. \quad (2.13)$$

In a general reference frame, the covariant form is given by:

$$T_{ideal}^{\mu\nu} = (\epsilon + p)u^\mu u^\nu - pg^{\mu\nu} = \epsilon u^\mu u^\nu - p\Delta^{\mu\nu}, \quad (2.14)$$

where $p(x)$ is the isotropic pressure in the rest frame, $g^{\mu\nu} = \text{diag}(1, -1, -1, -1)$ is the metric tensor, and $\Delta^{\mu\nu} \equiv g^{\mu\nu} - u^\mu u^\nu$ is the projection operator orthogonal to the fluid velocity. This operator satisfies the properties $\Delta^{\mu\nu}u_\mu = \Delta^{\mu\nu}u_\nu = 0$ and $\Delta^{\mu\nu}\Delta_\nu^\alpha = \Delta^{\mu\alpha}$.

The hydrodynamic equations can be expressed using this projection operator to separate components parallel ($u_\nu \partial_\mu T^{\mu\nu}$) and perpendicular ($\Delta_\nu^\alpha \partial_\mu T^{\mu\nu}$) to the fluid velocity. These components are explicitly given by:

$$u_\nu \partial_\mu T_{ideal}^{\mu\nu} = (\epsilon + p)\partial_\mu u^\mu + u^\mu \partial_\mu \epsilon = (\epsilon + p)\partial_\mu u^\mu + D\epsilon = 0, \quad (2.15)$$

$$\Delta_\nu^\alpha \partial_\mu T_{ideal}^{\mu\nu} = (\epsilon + p)u^\mu \partial_\mu u^\alpha - \Delta^{\mu\alpha} \partial_\mu p = (\epsilon + p)Du^\alpha - \nabla^\alpha p = 0, \quad (2.16)$$

where the shorthand notation for derivatives stands for projected parallel ($D \equiv u^\mu \partial_\mu$) and perpendicular ($\nabla^\alpha = \Delta^{\mu\alpha} \partial_\mu$) to the fluid velocity.

As illustrated in [Equation 2.15](#) and [Equation 2.16](#), the description of a perfect fluid requires three key fields: ϵ , p , and u^μ . Together, these fields represent five degrees of freedom. However, since the conservation laws yield only four independent equations, an additional relationship is needed to fully determine the system. This is provided by the equation of state, $p = p(\epsilon)$, which closes the system of equations. With the inclusion of the equation of state and given initial conditions for ϵ , p , and u^μ , the fluid's dynamics can be fully resolved.

2.2.3 RELATIVISTIC VISCOUS FLUID DYNAMICS

To account for dissipative, or viscous, effects, the hydrodynamic equations can be extended by considering a more comprehensive form of the energy-momentum tensor:

$$T^{\mu\nu} = T_{ideal}^{\mu\nu} + \Pi^{\mu\nu} = \epsilon u^\mu u^\nu + (-p + \pi_{\text{bulk}})\Delta^{\mu\nu} + \pi^{\mu\nu}, \quad (2.17)$$

where $\Pi^{\mu\nu}$ represents the viscous stress tensor, which includes contributions from dissipative processes to the overall energy-momentum tensor $T^{\mu\nu}$.

From energy-momentum conservation, one obtains evolution equations for energy density and fluid velocity,

$$u^\mu \partial_\mu \epsilon + (\epsilon + p + \pi_{\text{bulk}}) \nabla_\mu u^\mu + \pi^{\mu\nu} \nabla_\mu u_\nu = 0, \quad (2.18)$$

$$(\epsilon + p + \pi_{\text{bulk}}) u^\nu \nabla_\nu u^\mu + \Delta^{\mu\nu} \partial_\nu (p + \pi_{\text{bulk}}) + \Delta^\mu_\nu \nabla_\rho \pi^{\rho\nu} = 0. \quad (2.19)$$

In this form, the system of evolution equations is not closed but needs to be supplemented by additional constitutive relations for the stress tensor $\pi^{\mu\nu}$ and the bulk viscous pressure π_{bulk} . In the first order of derivatives with respect to the fluid velocity, the shear stress tensor and the bulk viscous pressure can be approximated by

$$\pi^{\mu\nu} = -2\eta \left(\frac{1}{2} \Delta^{\mu\alpha} \Delta^{\nu\beta} + \frac{1}{2} \Delta^{\mu\beta} \Delta^{\nu\alpha} - \frac{1}{3} \Delta^{\mu\nu} \Delta^{\alpha\beta} \right) \nabla_\alpha u_\beta = -2\eta \sigma^{\mu\nu}, \quad (2.20)$$

$$\pi_{\text{bulk}} = -\zeta \nabla_\mu u^\mu, \quad (2.21)$$

where the shear viscosity η and the bulk viscosity ζ are introduced as in the non-relativistic fluid dynamics case. This formulation represents a relativistic generalization of the Navier-Stokes theory. While this procedure represents a direct extension of the non-relativistic case, it has been demonstrated that the relativistic formulation of Navier-Stokes theory violates the principle of relativistic causality and exhibits linear instability [52]. As a viable solution to the causality issues inherent in first-order theories, the second-order hydrodynamics developed by Israel, Stewart, and Müller [53, 54] introduces dynamical equations for the shear stress tensor $\pi^{\mu\nu}$ and the bulk viscous pressure π_{bulk} , ensuring their evolution adheres to equations of motion [55],

$$P^\mu_{\nu\rho\sigma} [\tau_{\text{shear}} (u^\lambda \nabla_\lambda \pi^\sigma_\rho - 2\pi^{\sigma\lambda} \omega_{\rho\lambda}) + 2\eta \nabla_\rho u^\sigma - \varphi_7 \pi^\lambda_\rho \pi^\sigma_\lambda + \tau_{\pi\pi} \pi^\sigma_\lambda \sigma^\lambda_\rho - \lambda_{\pi\Pi} \pi_{\text{bulk}} \nabla_\rho u^\sigma] + \pi^\mu_\nu [1 + \delta_{\pi\pi} \nabla_\rho u^\rho - \varphi_6 \pi_{\text{bulk}}] = 0, \quad (2.22)$$

$$\tau_{\text{bulk}} u^\mu \partial_\mu \pi_{\text{bulk}} + \pi_{\text{bulk}} + \zeta \nabla_\mu u^\mu + \delta_{\Pi\Pi} \pi_{\text{bulk}} \nabla_\mu u^\mu - \varphi_1 \pi_{\text{bulk}}^2 - \lambda_{\Pi\pi} \pi^{\mu\nu} \nabla_\mu u_\nu - \varphi_3 \pi^\mu_\nu \pi^\nu_\mu = 0. \quad (2.23)$$

where Equation 2.22 is evolution equation for shear stress and Equation 2.23 is the evolution equation for π_{bulk} .

The projector $P^\mu_{\nu\rho\sigma}$ onto the symmetric, transverse, and traceless part of a tensor is defined as follows:

$$P^\mu_{\nu\rho\sigma} = \frac{1}{2} \Delta^\mu_\rho \Delta^\nu_\sigma + \frac{1}{2} \Delta^\mu_\sigma \Delta^\nu_\rho - \frac{1}{3} \Delta^{\mu\nu} \Delta_{\rho\sigma}. \quad (2.24)$$

Additionally, we define the symmetric $\sigma_{\mu\nu}$ and antisymmetric $\omega_{\mu\nu}$ combinations of fluid velocity gradients. These expressions are given by:

$$\sigma_{\mu\nu} = P_{\mu\nu}^{\rho\sigma} \nabla_\rho u_\sigma, \quad (2.25)$$

$$\omega_{\mu\nu} = \frac{1}{2} (\nabla_\mu u_\nu - \nabla_\nu u_\mu) = \frac{1}{2} (\partial_\mu u_\nu - \partial_\nu u_\mu). \quad (2.26)$$

Among the various transport coefficients introduced in Equation 2.22 and Equation 2.23, the most critical are the shear viscosity η and bulk viscosity ζ , both of which also appear in the Navier-Stokes approximation. The parametrization of these viscosities will be discussed in detail in Subsection 2.3.2. Additionally, the relaxation times τ_{shear} and τ_{bulk} play a crucial role in determining the rate at which the shear stress tensor and bulk viscous pressure relax towards their asymptotic forms, $\pi^{\mu\nu} = -2\eta\sigma^{\mu\nu}$ and $\pi_{\text{bulk}} = -\zeta\nabla_{\mu}u^{\mu}$, respectively. Beyond these, there are several second-order transport coefficients, including $\tau_{\pi\pi}$, $\delta_{\pi\pi}$, $\lambda_{\pi\Pi}$, $\delta_{\Pi\Pi}$, and $\lambda_{\Pi\pi}$, which are of the order $\mathcal{O}(\text{Kn Re}^{-1})$ (where Kn is the Knudsen number—the ratio of a microscopic scale, such as the mean free path, to a macroscopic scale over which the macroscopic fields change effectively—and Re^{-1} is the inverse Reynolds number, where the Reynolds number is the ratio of a macroscopic length scale to the scale at which perturbations are damped by viscosity [56]), as well as φ_7 , φ_6 , φ_1 , and φ_3 , which are of the order $\mathcal{O}(\text{Re}^{-2})$. These coefficients can be interpreted as nonlinear modifications to the relaxation-type equations, as discussed in [57].

The Israel-Stewart-Müller equations of motion constitute a closed system of partial differential equations governing the energy density ϵ , the independent components of fluid velocity, the shear stress tensor components, and the bulk viscous pressure. While these equations are generally complex and non-linear, making them difficult to solve analytically in most realistic scenarios, analytical solutions can be obtained under certain simplifying assumptions or symmetries [55]. For more general cases, however, numerical methods must be developed to accurately describe the dynamics of the QGP.

2.2.4 FLUIDUM

This subsection is mostly based on [55] and in parts inspired by [58].

Accurately modeling the evolution of the QGP requires solving the equations of motion derived from relativistic viscous fluid dynamics. Given the complexity of these partial differential equations, analytical solutions are unattainable, thus necessitating the use of numerical methods. One such method is implemented in the specialized software package Fluid dynamics of heavy-ion collisions with Mode expansion (FLUIDUM [55]). FLUIDUM numerically evolves fluid fields based on Equation 2.22, Equation 2.23, and initial conditions. In this subsection, we will elaborate on the main principles and methodologies of FLUIDUM as detailed in [55], emphasizing its relevance and application in the context of heavy-ion collisions.

To effectively describe the dynamics of heavy-ion collisions, selecting an appropriate coordinate system is crucial. While Cartesian coordinates (t, x, y, z) can be used with the origin placed at the collision center, they are not well-suited for capturing the underlying symmetries and kinematic features of the collisions, particularly the longitudinal boost invariance observed in the early stages of the system's evolution.

By introducing the proper time, or Bjorken time, τ and space-time rapidity η , defined as

$$\tau = \sqrt{t^2 - z^2}, \quad (2.27)$$

$$\eta = \text{arctanh}(z/t), \quad (2.28)$$

one can describe the dynamics in a way that naturally reflects the boost-invariant expansion along the longitudinal (beam) direction. This transformation simplifies the equations of motion and makes it easier to impose boundary conditions and initial states that are consistent with the symmetries of the collision, with t and z expressed as $t = \tau \cosh(\eta)$ and $z = \tau \sinh(\eta)$. In the transverse plane, cylindrical coordinates are convenient, with the radial coordinate r and azimuthal angle ϕ defined by

$$r = \sqrt{x^2 + y^2}, \quad (2.29)$$

$$\phi = \arctan(y/x). \quad (2.30)$$

This coordinate system is particularly advantageous for describing the approximate azimuthal rotation symmetry $\phi \rightarrow \phi + \Delta\phi$, and the approximate longitudinal rapidity boost symmetry $\eta \rightarrow \eta + \Delta\eta$ observed in heavy-ion collisions. Consequently, every space-time point can be described using (τ, η, r, ϕ) , facilitating the numerical solution of the equations of motion in FLUIDUM.

After establishing the coordinate system, one can describe the scheme for solving the equations of motion. This involves considering a general set of hyperbolic, quasi-linear partial differential equations, which can be expressed as

$$\begin{aligned} \mathbf{A}(\Phi, \tau, r) \cdot \partial_\tau \Phi + \mathbf{B}(\Phi, \tau, r) \cdot \partial_r \Phi + \mathbf{C}(\Phi, \tau, r) \cdot \partial_\phi \Phi \\ + \mathbf{D}(\Phi, \tau, r) \cdot \partial_\eta \Phi - \mathbf{S}(\Phi, \tau, r) = 0. \end{aligned} \quad (2.31)$$

In this equation, $\Phi(\tau, r, \phi, \eta)$, referred to as the "Nambu spinor", represents a vector characterized by N independent components such as the fluid temperature T , the four-velocity u^μ , the shear stress tensor, the bulk viscous pressure, and any other field necessary for a local description of the fluid. The matrices \mathbf{A} , \mathbf{B} , \mathbf{C} , and \mathbf{D} are $N \times N$ coefficient matrices, while \mathbf{S} , the source term, is an N -component vector. These components are functions of Φ , τ , and r , with the explicit dependence on τ and r arising from the chosen coordinate system. By comparing this general form to the specific equations of motion for a relativistic dissipative fluid, the appropriate coefficients can be identified, thereby tailoring the general framework to the specific physical scenario.

BACKGROUND-FLUCTUATION SPLITTING

The core concept behind FLUIDUM involves decomposing the field Φ into a symmetric background component and a symmetry-breaking perturbation. Specifically, we write:

$$\Phi(\tau, r, \phi, \eta) = \Phi_0(\tau, r) + \epsilon \Phi_1(\tau, r, \phi, \eta), \quad (2.32)$$

where $\Phi_0(\tau, r)$ represents the background field, which is symmetric under azimuthal rotations and Lorentz boosts in the longitudinal (η) direction. The term $\Phi_1(\tau, r, \phi, \eta)$ represents the perturbation or fluctuation field, capturing deviations from this symmetric background. The ϵ is taken as a formal expansion parameter (i.e., the equations of motion are expanded in orders of ϵ) but will be set $\epsilon \rightarrow 1$ at the end.

In FLUIDUM, $\Phi_0(\tau, r)$ is defined as a boost-invariant statistical expectation value, averaged over a large number of collision events where the event average only cancels out ϕ dependence. Conversely, $\Phi_1(\tau, r, \phi, \eta)$ represents the fluctuations specific to each individual event. This decomposition offers a significant advantage over traditional event-by-event simulations of the QGP evolution. In standard methods, each collision is simulated individually, generating an initial entropy density that evolves hydrodynamically according to the equations of motion. The mean behavior is then extracted by averaging over all simulated events. This approach is computationally intensive due to the necessity of simulating thousands of events. In contrast, FLUIDUM involves averaging before solving the equations of motion. This allows the mean evolution behavior to be inferred from a single evolution calculation, making it computationally more efficient.

To solve the partial differential equations within this framework, Equation 2.32 can be substituted into Equation 2.31. This results in the following expression:

$$\begin{aligned} & \mathbf{A}(\Phi_0 + \epsilon\Phi_1, \tau, r) \cdot \partial_\tau(\Phi_0 + \epsilon\Phi_1) + \mathbf{B}(\Phi_0 + \epsilon\Phi_1, \tau, r) \cdot \partial_r(\Phi_0 + \epsilon\Phi_1) \\ & + \mathbf{C}(\Phi_0 + \epsilon\Phi_1, \tau, r) \cdot \partial_\phi(\Phi_0 + \epsilon\Phi_1) + \mathbf{D}(\Phi_0 + \epsilon\Phi_1, \tau, r) \cdot \partial_\eta(\Phi_0 + \epsilon\Phi_1) \\ & - \mathbf{S}(\Phi_0 + \epsilon\Phi_1, \tau, r) = 0. \end{aligned} \quad (2.33)$$

From Equation 2.33, one can derive the equations of motion for the background field Φ_0 by retaining only the terms of zeroth order in ϵ . To obtain the linearized equations for the perturbations Φ_1 , one must isolate the terms linear in ϵ . Higher-order terms, which include quadratic and beyond, account for interactions among perturbation modes. The equations of motion for the background fields are reduced to a set of partial differential equations in $1 + 1$ dimensions

$$\mathbf{A}_0(\Phi_0, \tau, r) \cdot \partial_\tau \Phi_0(\tau, r) + \mathbf{B}_0(\Phi_0, \tau, r) \cdot \partial_r \Phi_0(\tau, r) - \mathbf{S}_0(\Phi_0, \tau, r) = 0. \quad (2.34)$$

Due to symmetry constraints, the background fields Φ_0 generally possess fewer independent components compared to Φ . For instance, in the context of Israel-Stewart-type fluid dynamics employed here, one can express Φ_0 as $(T, v, \pi_\phi^\phi, \pi_\eta^\eta, \pi_{\text{bulk}})$. The matrices \mathbf{A}_0 and \mathbf{B}_0 represent the projections of the matrices \mathbf{A} and \mathbf{B} onto this reduced space of independent components, evaluated for the background configuration Φ_0 .

For the perturbations, at linear order in ϵ , we obtain:

$$\begin{aligned} & \mathbf{A}_1(\Phi_0, \tau, r) \cdot \partial_\tau \Phi_1 + \mathbf{B}_1(\Phi_0, \tau, r) \cdot \partial_r \Phi_1 + \mathbf{C}_1(\Phi_0, \tau, r) \cdot \partial_\phi \Phi_1 \\ & + \mathbf{D}_1(\Phi_0, \tau, r) \cdot \partial_\eta \Phi_1 - \mathbf{S}_1(\Phi_0, \tau, r) \cdot \Phi_1 = 0. \end{aligned} \quad (2.35)$$

The matrices \mathbf{A}_1 , \mathbf{B}_1 , \mathbf{C}_1 , and \mathbf{D}_1 are obtained by evaluating \mathbf{A} , \mathbf{B} , \mathbf{C} , and \mathbf{D} at the background configuration Φ_0 . In contrast, the source term matrix \mathbf{S}_1 includes additional contributions arising from the linearization of \mathbf{A} and \mathbf{B} around Φ_0 :

$$\mathbf{S}_1(\Phi_0, \tau, r) = \frac{\partial}{\partial \Phi} [\mathbf{S}(\Phi, \tau, r) - \mathbf{A}(\Phi, \tau, r) \cdot \partial_\tau \Phi_0 - \mathbf{B}(\Phi, \tau, r) \cdot \partial_r \Phi_0]_{\Phi=\Phi_0}. \quad (2.36)$$

MODE EXPANSION

To efficiently solve the equations governing the dynamics of perturbations in a system, it is often advantageous to employ certain simplifications. One effective approach is the introduction of a background-fluctuation splitting ansatz, as discussed earlier. This method allows for the reduction of the dimensionality of the background field equations from 3+1 dimensions to 1+1 dimensions. This reduction is particularly beneficial for numerical algorithms, as it significantly simplifies the computational process required to solve the system of equations.

However, while the background field equations benefit from this dimensional reduction, the perturbation fields themselves are still governed by equations that span the full 3+1 dimensions. To address this challenge and optimize the numerical treatment of these perturbations, we introduce a mode expansion in Fourier space. The perturbation field $\Phi_1(\tau, r, \phi, \eta)$ can be expanded as a sum over Fourier modes:

$$\Phi_1(\tau, r, \phi, \eta) = \sum_{m=-\infty}^{\infty} \int \frac{dk}{2\pi} e^{im\phi + ik\eta} \Phi_1^{(m,k)}(\tau, r), \quad (2.37)$$

where m represents discrete mode numbers due to the periodic symmetry in the angular coordinate ϕ ($\phi = \phi + 2\pi$), and k is the wave number associated with the longitudinal coordinate η . The use of this Fourier expansion is particularly advantageous because, in Fourier space, differential operators simplify to algebraic multiplications, which greatly facilitates the computational process.

Applying this expansion to the perturbation equations transforms the original 3+1 dimensional problem into a set of 1+1 dimensional equations for each mode. The evolution of each perturbation mode $\Phi_1^{(m,k)}(\tau, r)$ is then governed by the following set of partial differential equations:

$$\begin{aligned} \mathbf{A}_1(\Phi_0, \tau, r) \cdot \partial_\tau \Phi_1^{(m,k)}(\tau, r) + \mathbf{B}_1(\Phi_0, \tau, r) \cdot \partial_r \Phi_1^{(m,k)}(\tau, r) + im\mathbf{C}_1(\Phi_0, \tau, r) \cdot \Phi_1^{(m,k)}(\tau, r) \\ + ik\mathbf{D}_1(\Phi_0, \tau, r) \cdot \Phi_1^{(m,k)}(\tau, r) - \mathbf{S}_1(\Phi_0, \tau, r) \cdot \Phi_1^{(m,k)}(\tau, r) = 0. \end{aligned} \quad (2.38)$$

To reconstruct the full solution, it is necessary to perform the sum and integral in [Equation 2.37](#), yielding:

$$\Phi(\tau, r, \phi, \eta) = \Phi_0(\tau, r) + \epsilon \sum_{m=-\infty}^{\infty} \int \frac{dk}{2\pi} e^{im\phi + ik\eta} \Phi_1^{(m,k)}(\tau, r). \quad (2.39)$$

As previously discussed, the Bjorken boost symmetry allows us to neglect the η -dependence, which simplifies the problem by considering only the $k = 0$ mode. This reduction results in the following expression:

$$\Phi(\tau, r, \phi) = \Phi_0(\tau, r) + \epsilon \sum_{m=-\infty}^{\infty} e^{im\phi} \Phi_1^{(m)}(\tau, r). \quad (2.40)$$

The summation over the m modes must be truncated for practical purposes, but this approximation is well-justified in [\[59\]](#). The structure of [Equation 2.40](#) also plays a crucial role in the construction of flow

coefficients, as detailed in [Subsection 2.4.3](#). The perturbation modes introduced here will be later translated into response functions, which quantify their influence on the final particle distribution.

To proceed with the mode expansion, it is necessary to specify the initial field values for the perturbation modes $\Phi_1^{(m,k)}(\tau, r)$. At the initial time τ_0 , all fields are assumed to be zero, except for the energy-related field. The initial energy density $\epsilon(r, \phi)$ at time τ_0 can be decomposed into Fourier modes and is expressed as:

$$\epsilon(r, \phi) = \sum_{m=-\infty}^{\infty} e^{im\phi} \epsilon^{(m)}(r). \quad (2.41)$$

To factor out event-by-event fluctuations in the initial perturbation configuration, this energy density is further decomposed into a set of nonfluctuating radial basis functions $\psi_l^{(m)}(r)$, characterized by a radial wave number l and expansion coefficients $\epsilon_l^{(m)}(k)$. For the purposes of this analysis, we neglect the dependence of these coefficients on the longitudinal wave number k , focusing instead on the boost-invariant dynamics typical of heavy-ion collisions. To establish initial conditions, we choose a set of radial basis functions that span the r -coordinate space for each m mode at time $\tau = \tau_0$:

$$\epsilon^{(m)}(r) = \sum_{l=1}^{\infty} \epsilon_l^{(m)} \psi_l^{(m)}(r), \quad (2.42)$$

where $\epsilon_l^{(m)}$ are expansion coefficients and $\psi_l^{(m)}(r)$ are the radial basis functions. The choice of these basis functions is detailed in [\[60\]](#). While this decomposition is primarily discussed in the context of energy density, it is important to note that all other fields are similarly decomposed into l and m modes, though they are initially set to zero. To ensure consistency with our parameterization of the perturbation fields, the initial energy density for each perturbation mode is converted to enthalpy density using the equation of state. At the initial time, the full fields are given by:

$$\Phi(\tau_0, r, \phi) = \Phi_0(\tau_0, r) + \sum_{m=-\infty}^{\infty} \sum_{l=1}^{\infty} e^{im\phi} \epsilon_l^{(m)} \Phi_l^{(m)}(\tau_0, r), \quad (2.43)$$

where $\Phi_0(\tau_0, r)$ represents the initial field values of the background fields (which will be discussed in detail in [Chapter 4](#)), and $\Phi_l^{(m)}(\tau_0, r)$ denotes the initial field values for each mode. As before, all fields are set to zero initially, except for those corresponding to energy. The complete solution then requires evolving these initial background fields and each of the m and l modes over time.

2.3 EQUATION OF STATE AND TRANSPORT PROPERTIES

2.3.1 EQUATION OF STATE

The equation of state (EoS) is a fundamental relation that describes the state of a physical system by relating its state variables. For a given system, the equation of state links variables such as pressure (p), volume (V), temperature (T), and sometimes additional quantities such as density (ρ) or energy density (ϵ). From the

standpoint of fluid dynamics, an EoS $p = p(\epsilon)$ is necessary to complete the set of conservation equations given in Equation 2.12. The EoS is typically derived from the partition function of the system Z ,

$$p = \frac{T}{V} \left(\frac{\partial \ln Z}{\partial V} \right)_T. \quad (2.44)$$

For QGP, assuming that the net baryon chemical potential is approximately zero at sufficiently high collision energies, the equation of state can be computed using lattice QCD techniques [61]. Furthermore, the evolution of the fireball must be considered since the quarks and gluons combine into hadrons at lower temperatures. During this hadronic phase, the EoS shifts to reflect the properties of the hadron resonance gas (HRG) model [62].

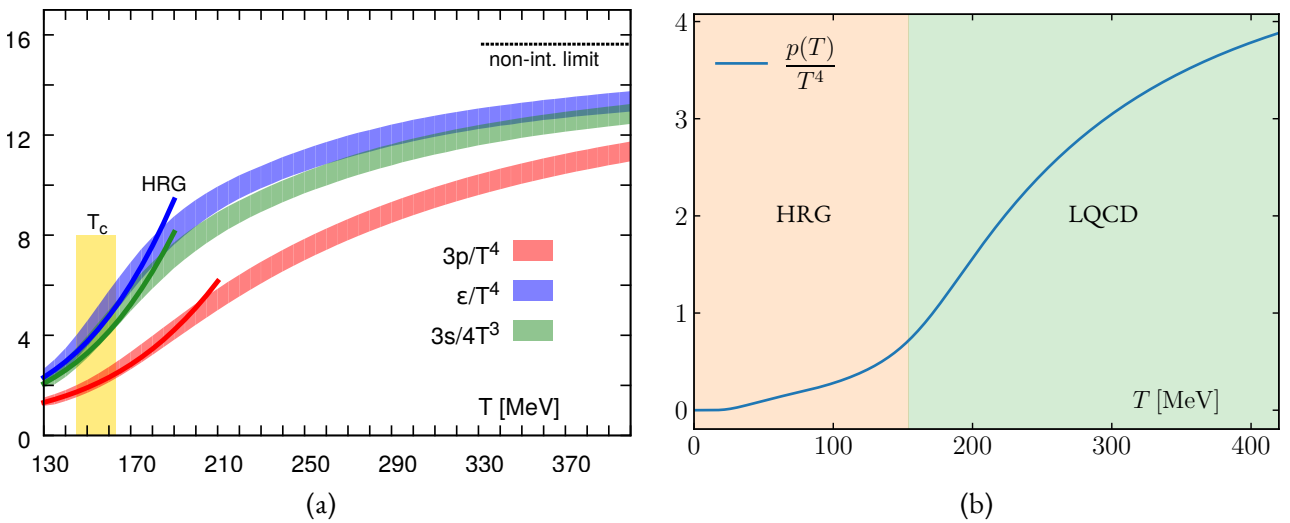


Figure 2.1: (a) The QCD equation of state (EoS) provided by the HotQCD Collaboration [63] is illustrated with colored bands representing the normalized pressure, energy density, and entropy density, all plotted as functions of temperature as predicted by lattice QCD (LQCD). The widths of these bands denote the associated uncertainties. In contrast, the solid lines depicts the corresponding predictions from the Hadron Resonance Gas (HRG) model. The vertical yellow band marks the crossover region at $T_c = 154 \pm 9$ MeV. (b) Thermodynamic pressure $p(T)$ as a function of temperature, derived from the equation of state used in FLUIDUM across the temperature range. In the green-shaded region, the data from LQCD was used for the fit, while the orange-shaded region represents the HRG model. The two regions are connected smoothly across the transition area, ensuring a continuous equation of state.

Figure 2.1a depicts the variation of pressure, energy density, and entropy density as functions of temperature, derived from the HotQCD Collaboration's latest lattice calculations of the EoS for (2+1)-flavor QCD at zero net baryon density [63]. These results indicate a crossover deconfinement transition occurring at $T_c = 154 \pm 9$ MeV. At low temperatures, the predictions of the two models converge, allowing the use of the HRG model as the EoS. However, at higher temperatures, where quarks and gluons become the relevant degrees of freedom, the HRG approximation becomes invalid, necessitating the use of lattice QCD (LQCD) to determine the EoS of the system.

For the background-fluctuation splitting ansatz and the numerical implementation of FLUIDUM using spectral methods, it is essential to have a continuous and differentiable equation of state. The numerical

solution must also account for regions of the system that have already frozen out, which requires the EoS to be valid in both the quark-gluon plasma and hadronic phases. To achieve a continuous EoS $p(T)$ that meets these criteria, a parametrization of the pressure is fitted to LQCD data above the critical temperature $T_c = 154$ MeV and to the HRG model below T_c . The parametrization is given by:

$$\frac{p(T)}{T^4} = \exp\left[-c^2\hat{T} - d^2\hat{T}^2\right] \left[\frac{\frac{(16+21/2N_f)\pi^2}{90} + a_1\tilde{T} + a_2\tilde{T}^2 + a_3\tilde{T}^3 + a_4\tilde{T}^4}{1 + b_1\tilde{T} + b_2\tilde{T}^2 + b_3\tilde{T}^3 + b_4\tilde{T}^4} \right], \quad (2.45)$$

where $\tilde{T} = T_c/T$, $T_c = 154$ MeV, $N_f = 3$ is the number of quark flavors, and $\hat{T} = 100/T$ MeV. The best-fit parameters for this parametrization are provided in [Table 2.1](#).

Table 2.1: Best-fit parameters for the thermodynamic equation of state as parametrized in [Equation 2.45](#). These parameters were obtained from the table presented in [\[58\]](#).

a_1	-15.53	a_2	18.62	a_3	-10.73	a_4	2.74	c	-1.05
b_1	-3.31	b_2	5.31	b_3	-4.65	b_4	1.86	d	0.10

[Figure 2.1b](#) shows the resulting pressure across the temperature range. In the green-shaded region, the data from lattice QCD was used for the fit, while the orange-shaded region represents the hadron resonance gas model. The two regions are connected smoothly across the transition area, ensuring a continuous equation of state.

2.3.2 TRANSPORT COEFFICIENTS

Understanding the behavior of the QGP requires a detailed examination of its transport properties, which govern the transfer of momentum, energy, and other quantities within the medium. These transport coefficients, including shear and bulk viscosity, encapsulate the fluid's response to various perturbations and external forces and are particularly sensitive to temperature and the baryon chemical potential.

Shear viscosity, η , quantifies a fluid's resistance to shear deformation. A fluid with low shear viscosity is typically strongly interacting, meaning it efficiently transmits shear stress throughout its volume, and its constituents have short mean free paths. In contrast, a nearly ideal (weakly interacting) gas exhibits high shear viscosity because its particles do not scatter frequently enough to effectively transmit shear stress, resulting in a less efficient response to applied strain. Bulk viscosity, ζ , on the other hand, is associated with the fluid's resistance to uniform compression or expansion. In the context of QGP, bulk viscosity plays a crucial role by modulating the plasma's expansion rate. Specifically, it tends to suppress radial expansion, leading to a reduction in the average transverse momentum of particles emitted during the collision.

The transport coefficients are often normalized by the entropy density s to provide dimensionless ratios, such as η/s and ζ/s , which offer deeper insights into the fluid's behavior. The ratio η/s , known as the specific shear viscosity or shear viscosity to entropy density ratio, is of particular interest because it provides a measure of the fluid's "quality." In natural units where $\hbar = k_B = 1$, η/s is dimensionless and serves as an intensive property of the fluid.

While the calculation of these transport properties from first principles is still challenging, we employ parametrizations to describe their temperature dependence. To model the temperature dependence of η/s , we apply a parametrization based on calculations from Yang-Mills theory, as detailed in Ref. [64] with updated parameters provided in [65]. The analytic fit formula used to describe η/s in SU(3) Landau gauge Yang-Mills theory is given by:

$$\frac{\eta}{s}(T)_{\text{YM}} = a \left(\frac{T}{T_c} - d \right)^2 + \frac{b}{(T/T_c)^\delta}. \quad (2.46)$$

For simplicity, the first term in this expression has been slightly modified from its original form in Ref. [64], as these changes do not significantly impact hydrodynamic applications [65]. The best fit to the Yang-Mills results yields the parameters: $a = 0.0613$, $b = 0.00588$, $d = -0.709$, and $\delta = 40.3$. In the low-temperature regime, where the system is dominated by glueball dynamics rather than a hadron resonance gas, the parameters b and δ are adjusted to 0.02 and 6.0, respectively, to better capture the behavior of the system. A global correction factor of $4/3$ is applied to account for differences in scales and running couplings between Yang-Mills theory and QCD [64]. To further refine this model for QCD, a global scaling parameter $(\eta/s)_{\text{scale}}$ is introduced, which will be estimated through Bayesian analysis:

$$\frac{\eta}{s}(T)_{\text{QCD}} = (\eta/s)_{\text{scale}} \cdot \frac{4}{3} \cdot \left[a \left(\frac{T}{T_c} - d \right)^2 + \frac{0.02}{(T/T_c)^6} \right]. \quad (2.47)$$

In addition to shear viscosity, the bulk viscosity to entropy density ratio ζ/s is also considered temperature dependent. We assume it to take the Lorentzian form [66]:

$$\frac{\zeta}{s}(T) = \frac{(\zeta/s)_{\text{max}}}{1 + \left(\frac{T - T_{\text{peak}}}{T_{\text{width}}} \right)^2}. \quad (2.48)$$

In this parametrization, the peak temperature T_{peak} is set to 175 MeV, and the width T_{width} is fixed at 24 MeV, as informed by the findings in Ref. [66]. The maximum value $(\zeta/s)_{\text{max}}$ serves as a free parameter that will be determined through Bayesian analysis.

The corresponding relaxation times are defined as follows:

$$\frac{\tau_{\text{bulk}}}{\zeta/(\epsilon + p)} = \frac{1}{15 \left(\frac{1}{3} - c_s^2 \right)^2} + \frac{0.1 \text{ fm}/c}{\zeta/(\epsilon + p)}, \quad (2.49)$$

$$\frac{\tau_{\text{shear}}}{\eta/(\epsilon + p)} = \begin{cases} 5 & \text{for } T \geq T_{\text{chem}}, \\ 5 + (T - T_{\text{chem}})3 \text{ MeV} & \text{for } T < T_{\text{chem}}. \end{cases} \quad (2.50)$$

The adjustment of the shear relaxation time below the chemical freeze-out temperature ensures that this time scale remains significantly larger than the characteristic scale of the hadron resonance gas, where scattering processes become increasingly infrequent. Regarding the other coefficients that appear in Equation 2.23, the parameter $\delta_{\pi\pi}$ is set to $4\tau_{\text{shear}}/3$, while all other second-order transport coefficients are neglected [58].

2.4 HADRONIZATION AND FINAL STATE OBSERVABLES

2.4.1 COOPER-FRYE FREEZE-OUT AND THERMAL SPECTRA

At a certain stage in the evolution of the QGP, the system cools down and undergoes a transition where quarks and gluons become confined within hadrons, a process referred to as hadronization. This transition occurs as the system passes through the crossover temperature, T_c . The modeling of this phase requires translating the continuous fluid fields, described by hydrodynamics, into discrete particles while conserving energy and momentum. This is typically achieved through the Cooper-Frye procedure [67], which defines a freeze-out hypersurface, Σ_μ . The hypersurface is characterized by a constant freeze-out temperature, T_{fo} , typically around 150 MeV, at which the hadronization is assumed to occur rapidly enough for the system to be describable by a thermal distribution of particles.

On the freeze-out surface, the fluid fields are converted into particles using the Cooper-Frye formula, which involves integrating the single-particle distribution function over the freeze-out hypersurface. The spectrum of hadron species a on the freeze-out hypersurface Σ_μ can be expressed by

$$E_{\mathbf{p}} \frac{dN_a}{d^3\mathbf{p}} = -\frac{\nu_a}{(2\pi)^3} \int_{\Sigma} f_a p^\mu d\Sigma_\mu, \quad (2.51)$$

where $\frac{dN_a}{d^3\mathbf{p}}$ is the number of particles per phase space volume, $f_a = f_a(p^\mu, T(x), u^\mu(x), \pi^{\mu\nu}(x), \pi_{\text{bulk}}(x))$ is the particle distribution function, and ν_a is the degeneracy factor accounting for spin or polarization states. The Cooper-Frye formula ensures that the transition from the fluid phase to the particle phase is consistent with the principles of relativistic hydrodynamics and conserves the overall energy and momentum of the system.

On the freeze-out surface, the distribution function f_a is assumed to be close to equilibrium and is expressed as

$$f_a = f_{a,\text{eq}} + \delta f_a^{\text{bulk}} + \delta f_a^{\text{shear}}, \quad (2.52)$$

where $f_{a,\text{eq}}$ represents the equilibrium distribution, which is given by either the Bose-Einstein or Fermi-Dirac distribution depending on the particle species,

$$f_{a,\text{eq}} = \frac{1}{e^{-\frac{p_\nu u^\nu + \mu_a}{T}} \pm 1}. \quad (2.53)$$

The corrections δf_a^{bulk} and $\delta f_a^{\text{shear}}$ account for bulk viscosity and shear viscosity effects, respectively, and can be parameterized as [68, 69]:

$$\delta f_a^{\text{bulk}} = f_{a,\text{eq}}(1 \pm f_{a,\text{eq}}) \left[\frac{\bar{E}_{\mathbf{p}}}{T} \left(\frac{1}{3} - c_s^2 \right) - \frac{m^2}{3T\bar{E}_{\mathbf{p}}} \right] \frac{\pi_{\text{bulk}}}{\zeta/\tau_{\text{bulk}}}, \quad (2.54)$$

$$\delta f_a^{\text{shear}} = f_{a,\text{eq}}(1 \pm f_{a,\text{eq}}) \frac{\pi_{\rho\nu} p^\rho p^\nu}{2(\epsilon + p)T^2}. \quad (2.55)$$

where \bar{E}_p is the energy of the particle in the reference frame, c_s^2 is the speed of sound squared in the medium at the freeze-out temperature, m is the mass of the primary resonance, ζ is the bulk viscosity, and τ_{bulk} is the bulk relaxation time. Similarly, $\pi_{\rho\nu}$ represents the shear stress tensor, and $(\epsilon + p)$ is the enthalpy density.

By substituting the distribution function from Equation 2.52 into Equation 2.51, one can compute the thermal spectra on the freeze-out hypersurface. However, these spectra do not directly correspond to what is observed in the detector. Although the particles cease to interact with each other after freeze-out, the spectra are still influenced by the decays of unstable particles, such as resonances, as they travel to the detector. These resonances decay into lighter, stable particles, and their contributions must be included to accurately predict the final particle spectra observed in experiments.

To fully understand the intricacies of particle production in heavy-ion collisions, it is crucial to distinguish between the different stages of freeze-out. In the previous discussion, we introduced the assumption of a single freeze-out temperature, $T_{\text{fo}} = T_{\text{ch}} = T_{\text{kin}}$, where chemical freeze-out, which determines the relative abundances of various particle species, and kinetic freeze-out, which sets the momentum distributions of these particles, are assumed to occur at the same time. While this simplification can be useful, it overlooks the more complex reality where these freeze-out processes actually occur at different stages as the system evolves. As the system expands and cools, the interactions among hadrons become less frequent, leading to a departure from chemical equilibrium, though kinetic equilibrium can persist for a while longer. To address this complexity, our model utilizes the concept of partial chemical equilibrium (PCE) [70]. After the initial freeze-out, the hadron density remains high enough to allow for elastic scatterings, which preserve kinetic equilibrium even as chemical equilibrium is lost. This requires us to distinguish between the chemical freeze-out temperature, T_{ch} , where inelastic collisions stop, and particle yields are fixed, and the kinetic freeze-out temperature, T_{kin} , where elastic scatterings cease, finalizing the momentum distributions. By incorporating these two distinct freeze-out temperatures, our model represents the gradual decoupling of hadrons as they transition from an interacting medium to free-streaming particles. The detailed implementation of PCE in our model can be found in [60].

Finally, in the context of mode expansion, when the fluid fields are translated into particle yields on the freeze-out surface, the complete final particle distribution for a given particle species "a"—depending on its mass m_a , transverse momentum p_T , and azimuthal angle φ —can be expressed as [59]:

$$\frac{dN_a}{p_T dp_T d\varphi} = S_a(m_a, p_T, \varphi) = S_{0;a}(m_a, p_T) + \sum_{n=-\infty}^{\infty} \sum_{l=1}^{\infty} \epsilon_l^{(n)} e^{in\varphi} S_{l;a}^{(n)}(m_a, p_T). \quad (2.56)$$

In this expression, $S_{0;a}(m_a, p_T)$ represents the contribution from the azimuthally symmetric, or background, part of the initial fields, while $S_{l;a}^{(n)}(m_a, p_T)$ captures the response to azimuthally dependent perturbations in the initial fields. It is important to note that the dependence on rapidity is omitted, as we focus exclusively on the midrapidity region, $|\eta_P| < 0.5$, where the rapidity dependence is negligible. The final expressions for the thermal background spectrum $S_{0;a}(m_a, p_T)$ and the thermal perturbation spectrum $S_{l;a}^{(n)}(m_a, p_T)$, as implemented in FLUIDUM, are detailed in [60].

2.4.2 PARTICLE SPECTRA INCLUDING RESONANCE DECAYS

After hadronization, many of the particles produced are unstable and undergo decays before reaching the detector. These decays, particularly those of short-lived resonances, significantly influence the final particle spectra observed in heavy-ion collision experiments. To accurately account for these effects, it is necessary to simulate the decay processes of these resonances, which can result in cascades of decays, leading to the formation of lighter, stable particles.

Mathematically, the final particle spectrum, including contributions from decaying resonances, can be expressed as:

$$E_{\mathbf{p}} \frac{dN_b}{d^3\mathbf{p}} = \sum_a \int \frac{d^3\mathbf{q}}{(2\pi)^3 2E_{\mathbf{q}}} D_b^a(\mathbf{p}, \mathbf{q}) E_{\mathbf{q}} \frac{dN_a}{d^3\mathbf{q}}, \quad (2.57)$$

where $D_b^a(\mathbf{p}, \mathbf{q})$ is the decay map, which encapsulates the Lorentz-invariant probability of a resonance a with momentum \mathbf{q} decaying into a particle b with momentum \mathbf{p} (Typically, a decays into two particles, $a \rightarrow b + c$, but for simplicity, c is omitted here). The decay maps are computed considering phase-space integrals, four-momentum conservation, and the relevant branching ratio for each decay channel.

A conventional approach for incorporating resonance decays relies on Monte-Carlo generators [71, 72], which are computationally intensive due to the need to simulate all intermediate states within the decay chains. In our framework, a more computationally efficient method called FASTRESO [73] is utilized to handle resonance decays.

FASTRESO computes the final decay spectra of direct resonance decays by directly utilizing the hydrodynamic fields on the freeze-out surface. It applies the decay map, Equation 2.57, to the distribution function of primary particles prior to the Cooper–Frye integration, thereby determining the distribution function for the decay products. Subsequently, the final particle spectrum is obtained through a Cooper–Frye freeze-out integral. A key advantage of FASTRESO is that it eliminates the need for repeated calculations of intermediate particle decays, which are typically computed event-by-event. The essential components of the decay particle distribution function are computed only once, enabling the calculation of the spectrum for a few significant hadron species, including the feed-down from all direct decays, for any arbitrary freeze-out surface. This method not only significantly reduces the computational load associated with direct resonance decays but also ensures that the effects of these decays on the final particle spectra are accurately captured.

While FASTRESO provides a comprehensive framework for calculating the final decay spectra, the detailed exploration of thermal particle spectra that include resonance decays extends beyond the primary focus of this thesis. For readers interested in the most up-to-date versions of these spectra, along with their associated kernels, detailed information can be found in [58]. Instead, this thesis focuses on comparing the spectra of pions, kaons, and protons, including the effects of resonance decays, with experimentally measured p_T -differential spectra of identified hadrons.

2.4.3 CONSTRUCTION OF FLOW COEFFICIENTS

This subsection is mainly inspired by [59, 74].

The collective behavior of the fluid in a heavy-ion collision is commonly referred to as the flow of the system. To quantify this flow, one can construct flow coefficients from the final particle distribution. A starting point is to consider the so-called fully integrated flow coefficients. The flow coefficient v_n can be expressed in terms of the one-particle momentum distribution $f(\mathbf{p})$, which represents the number of particles expected in a given momentum region [74]:

$$v_n(\mathcal{D}) \equiv \langle e^{in\varphi} \rangle = \frac{\int_{\mathcal{D}} e^{in\varphi} f(\mathbf{p}) d^3\mathbf{p}}{\int_{\mathcal{D}} f(\mathbf{p}) d^3\mathbf{p}}, \quad (2.58)$$

where the angle brackets denote an average over many events, φ is the azimuthal angle of the particle's momentum in the plane perpendicular to the beam axis, measured relative to the reaction plane of the collision, and \mathcal{D} represents a phase space region in the (p_T, y) plane where the flow is measured, typically corresponding to the detection region of an experimental apparatus.

Direct evaluation of Equation 2.58 requires the reconstruction of the reaction plane for each event. However, this can be challenging in practice, so correlation functions are often employed to infer the flow coefficients. Since the exact orientation of the reaction plane is not directly accessible in experiments, measurements are typically limited to relative azimuthal angles between outgoing particles. The standard approach in flow analysis involves two-particle azimuthal correlations, which utilize the two-particle distribution function $f(\mathbf{p}_1, \mathbf{p}_2) = dN/d^3\mathbf{p}_1 d^3\mathbf{p}_2$:

$$\langle 2_n \rangle = \langle e^{in(\varphi_1 - \varphi_2)} \rangle_{\mathcal{D}_1 \times \mathcal{D}_2} = \frac{\int_{\mathcal{D}_1 \times \mathcal{D}_2} e^{in(\varphi_1 - \varphi_2)} f(\mathbf{p}_1, \mathbf{p}_2) d^3\mathbf{p}_1 d^3\mathbf{p}_2}{\int_{\mathcal{D}_1 \times \mathcal{D}_2} f(\mathbf{p}_1, \mathbf{p}_2) d^3\mathbf{p}_1 d^3\mathbf{p}_2}, \quad (2.59)$$

where φ_1 and φ_2 are the azimuthal angles of two different particles measured in the laboratory frame, and the integration is performed over the phase space window $\mathcal{D}_1 \times \mathcal{D}_2$.

In standard analysis, it is often assumed that nonflow correlations—those not related to the reaction plane—are negligible. Under this assumption, the two-particle momentum distribution factorizes:

$$f(\mathbf{p}_1, \mathbf{p}_2) = f(\mathbf{p}_1)f(\mathbf{p}_2), \quad (2.60)$$

which leads to the relation:

$$\langle e^{in(\varphi_1 - \varphi_2)} \rangle_{\mathcal{D}_1 \times \mathcal{D}_2} = v_n(\mathcal{D}_1)v_n(\mathcal{D}_2). \quad (2.61)$$

This equation indicates that the azimuthal correlation between two particles arises solely from their mutual correlation with the reaction plane. However, it is important to recognize that reconstructing flow coefficients from two-particle correlators is inherently an approximation. To reduce the influence of nonflow

effects and few-particle correlations in these estimates, higher-order cumulants, constructed from multi-particle correlators, can be employed.

In the discussion above, all particles were used to calculate the so-called integrated flow coefficients. By narrowing down the phase space under consideration, one can define differential flow coefficients. To achieve this, the measured particles are divided into particles of interest (POIs) and reference flow particles (RFPs). Typically, POIs are selected within a specific range of transverse momentum, while RFPs encompass all other particles. By restricting the phase space window of one particle to a particular p_T value, we can define the p_T -dependent two-particle correlator:

$$\langle 2'_n \rangle(p_T) = \frac{\sum_{i=1}^{m_p} \sum_{j=1}^M e^{in(\varphi_i - \varphi_j)}}{\sum_{i=1}^{m_p} \sum_{j=1}^M 1}, \quad (2.62)$$

where m_p is the number of POIs, M is the total number of particles, and the primed sum indicates that all indices are distinct. Here, φ_i represents the azimuthal angles of the particles as measured in the laboratory frame. For simplicity, we have assigned all particle weights to unity. The correlator $\langle 2'_n \rangle(p_T)$ now depends on the p_T region from which the POIs are selected. It is assumed that POIs are chosen based solely on their transverse momentum, regardless of particle species. The differential two-particle correlators are defined using continuous distribution functions as:

$$\langle 2'_n \rangle(p_T) = \frac{\int_{\mathcal{D}_1} \int_{\mathcal{D}_2(p_T)} e^{in(\varphi_1 - \varphi_2)} f(\mathbf{p}_1, \mathbf{p}_2) d\mathbf{p}_1 d\varphi_2 d\eta_2}{\int_{\mathcal{D}_1} \int_{\mathcal{D}_2} f(\mathbf{p}_1, \mathbf{p}_2) d\mathbf{p}_1 d\varphi_2 d\eta_2}, \quad (2.63)$$

where the p_T dependence arises because, within one phase space window, only the azimuthal angle and rapidity are integrated over. With the differential two-particle correlators established, one can also define the differential flow estimates from two-particle correlations. According to [75], these estimates are given by:

$$v'_n \{2\}(p_T) = \frac{\langle \langle 2'_n \rangle(p_T) \rangle}{\sqrt{c_n \{2\}}}, \quad (2.64)$$

where $c_n \{2\}$ is the cumulant defined as $c_n \{2\} = \langle \langle 2_n \rangle \rangle$, and the second averaging bracket represents an average over all events within the centrality class under consideration. The differential flow estimates naturally inherit their momentum dependence from the differential two-particle correlator. Furthermore, higher-order correlators can be employed for differential flow estimates, as described in [75].

In principle, POIs can be selected not only within a specific momentum region but also based on particle species, leading to particle-species-dependent flow estimates. In this context, the two-particle correlator is denoted as $d_{n;a} \{2\}(m_a, p_T)$, where the dependence on the particle species "a" is explicitly included.

Finally, we aim to construct flow coefficients using the mode expansion technique. For simplicity, we will begin by focusing on the flow coefficients of charged particles. As discussed in Equation 2.59, flow coefficients can be derived from two-particle correlation functions. We will now apply a similar approach, starting with the calculation of the two-particle correlator for charged particles. Since our current model does not explicitly incorporate two-particle correlations, the two-particle distribution function can be approximated as

a product of one-particle distribution functions. In the general case, the two-particle distribution function for particles of species "a" and "b", with masses m_a and m_b respectively, is given by:

$$f_{a,b}(m_a, m_b, \mathbf{p}_1, \mathbf{p}_2) = \frac{d^6 N_{a,b}}{p_{T_1} p_{T_2} d\varphi_1 d\varphi_2 dp_{T_1} dp_{T_2} dy_1 dy_2} = S_a(m_a, p_{T_1}, \varphi_1) S_b(m_b, p_{T_2}, \varphi_2). \quad (2.65)$$

Since we are initially calculating flow estimates for charged particles without distinguishing between species, all charged particles must be correlated with each other. Consequently, we can work with the two-particle distribution function for charged particles, which is obtained by summing over the different species:

$$\begin{aligned} f(\mathbf{p}_1, \mathbf{p}_2) &= \sum_a S_a(m_a, p_{T_1}, \varphi_1) \sum_b S_b(m_b, p_{T_2}, \varphi_2), \\ &= S(p_{T_1}, \varphi_1) S(p_{T_2}, \varphi_2), \end{aligned} \quad (2.66)$$

where the summation includes all charged particles—pions, kaons, and protons in this case. We introduced the shorthand notation $S(p_T, \varphi) = \sum m_a S_a(m_a, p_T, \varphi)$. Substituting Equation 2.56 into Equation 2.66 and applying Equation 2.59, while neglecting terms of higher than second order in the expansion coefficients $\epsilon_{l_1}^m$, we obtain the following expression for $n \neq 0$:

$$\langle 2_n \rangle = \frac{\sum_{l_1, l_2=1}^{\infty} S_{l_1}^{(-n)} \epsilon_{l_1}^{(-n)} \epsilon_{l_2}^{(n)} S_{l_2}^{(n)}}{S_0^2}, \quad (2.67)$$

where $S_l^{(n)} = \int dp_T p_T \sum m_a S_{l;a}^{(n)}(m_a, p_T)$ and $S_0 = \int dp_T p_T \sum m_a S_{0;a}(m_a, p_T)$. This expression represents the two-particle correlator for a single event. To obtain the flow estimates, we must average over multiple events. Given that only the expansion coefficients depend on the specific event, the averaging process can be carried out within the summation. The integrated flow estimate for charged particles, derived from two-particle correlations, is then given by:

$$v_n^2\{2\} = \langle \langle 2_n \rangle \rangle = \frac{\sum_{l_1, l_2=1}^{\infty} S_{l_1}^{(-n)} \langle \epsilon_{l_1}^{(-n)} \epsilon_{l_2}^{(n)} \rangle S_{l_2}^{(n)}}{S_0^2}, \quad (2.68)$$

where $v_n\{2\} = \sqrt{c_n\{2\}}$. The averaging process in Equation 2.68 encompasses all events within a given centrality class. The detailed computation of the correlators $\langle \epsilon_{l_1}^{(-n)} \epsilon_{l_2}^{(n)} \rangle$, which represent the initial mode coefficients, is thoroughly discussed in [58, 76]. These correlators can be evaluated across different models, establishing a direct connection between the response functions and the resulting flow coefficients.

The calculation of charged particle differential flow estimates follows a similar approach to the one used for integrated flow coefficients. As previously mentioned, when dealing with differential flow coefficients, the particles of interest are selected within a narrow p_T interval. In the continuous framework, this corresponds to omitting the integration over one of the two transverse momenta, resulting in a continuous function of p_T . When comparing with experimental data, it is necessary to introduce transverse momentum bins, as these are used in the extraction of experimental measurements. By applying the same approxima-

tion—considering only terms up to second order in the expansion coefficients—we obtain the p_T -dependent two-particle correlator:

$$\langle 2'_n \rangle(p_T) = \frac{\sum_{l_1, l_2=1}^{\infty} S_{l_1}^{(-n)}(p_T) \epsilon_{l_1}^{(-n)} \epsilon_{l_2}^{(n)} S_{l_2}^{(n)}}{S_0 S_0(p_T)}, \quad (2.69)$$

where $S_l^{(m)}(p_T) = \sum_a S_{l;a}^{(m)}(m_a, p_T)$ and $S_0(p_T) = \sum_a S_0(m_a, p_T)$. Similar to the integrated flow coefficients, the event-averaging process can be straightforwardly performed by averaging the factor $\epsilon_{l_1}^{(-n)} \epsilon_{l_2}^{(n)}$. Using Equation 2.64, we can directly link the response functions and the correlation functions of the initial weights to the differential flow coefficients.

For single-particle flow coefficients, only one particle species is correlated with all others. Following similar calculations, the integrated single-particle species flow estimates derived from two-particle correlations are given by:

$$v_{n;a}^2 \{2\}(m_a) = \frac{\sum_{l_1, l_2=1}^{\infty} S_{l_1;a}^{(-n)}(m_a) \langle \epsilon_{l_1}^{(-n)} \epsilon_{l_2}^{(n)} \rangle \tilde{S}_{l_2;a}^{(n)}(m_a)}{\tilde{S}_{0;a}(m) S_{0;a}(m)}, \quad (2.70)$$

In this expression:

- $S_{l;a}^{(n)}(m_a)$ represents the integrated spectra modes, defined as:

$$S_{l;a}^{(n)}(m_a) = \int dp_T p_T S_{l;a}^{(n)}(m_a, p_T). \quad (2.71)$$

- $S_{0;a}(m_a)$ denotes the integrated spectra, which is calculated as:

$$S_{0;a}(m_a) = \int dp_T p_T S_{0;a}(m_a, p_T). \quad (2.72)$$

- $\tilde{S}_{l;a}^{(n)}(m_a)$ corresponds to the integrated spectra modes for charged particles, expressed as:

$$\tilde{S}_{l;a}^{(n)}(m_a) = \int dp_T p_T \sum_{b \neq a} S_{l;b}^{(n)}(m_b, p_T). \quad (2.73)$$

- $\tilde{S}_{0;a}(m_a)$ is the integrated spectra for charged particles, given by:

$$\tilde{S}_{0;a}(m_a) = \int dp_T p_T \sum_{b \neq a} S_{0;b}(m_b, p_T). \quad (2.74)$$

For the differential flow estimates, the expression is:

$$d_{n;a} \{2\}(m_a, p_T) = \frac{\sum_{l_1, l_2=1}^{\infty} S_{l_1;a}^{(-n)}(m_a, p_T) \langle \epsilon_{l_1}^{(-n)} \epsilon_{l_2}^{(n)} \rangle \tilde{S}_{l_2;a}^{(n)}(m_a)}{\tilde{S}_{0;a}(m_a) S_{0;a}(m_a, p_T)}, \quad (2.75)$$

and the differential flow coefficient is finally given by:

$$v_{n;a}\{2\}(m_a, p_T) = \frac{d_{n;a}\{2\}(m_a, p_T)}{v_{n;a}\{2\}(m_a)}. \quad (2.76)$$

In [Chapter 5](#), the results of [Equation 2.76](#) will be used to compare the differential flow coefficients obtained from the model with experimental data.

3 BAYESIAN INFERENCE

Understanding the behavior of matter under extreme conditions, as experienced in heavy-ion collisions, necessitates sophisticated computational models, as shown in the previous chapter. These models require a set of input parameters that represent the physical properties of interest. Ideally, they should simulate the entire evolution of the collision, producing outputs directly comparable to experimental measurements. By comparing these model calculations with experimental data, we can infer the true values of the physical properties involved.

This approach presents significant challenges. The sheer number of input parameter configurations requires an extensive exploration of the model's parameter space, which can be computationally demanding. Additionally, correlations exist between these model parameters, meaning a single parameter might influence multiple measurable quantities.

Bayesian statistics offers a systematic approach to estimating model parameters while accounting for uncertainties inherent in the data. Through Bayesian inference, the final outcome is represented as a posterior probability distribution, which reflects the probability of different parameter values being the true values given the observed data. The general methodology can be summarized as follows. Let $\theta = (\theta_1, \theta_2, \dots, \theta_n)$ denote the parameters of interest, and y represent the experimental data. Bayesian inference involves defining three key probability distributions:

- **Prior distribution** $P(\theta)$: This distribution encodes our initial beliefs or knowledge about the parameters before considering any data. It represents our assumptions about the parameter values prior to conducting the experiment.
- **Likelihood** $P(y|\theta)$: This conditional probability distribution reflects how well the model, with a specific set of parameters θ , fits the observed data y . It incorporates all sources of uncertainty in the measurement process and quantifies the probability of observing the data given the parameters.
- **Evidence** $P(y)$: Also known as the marginal likelihood, is the probability of the observed data under all possible parameter values. Since the evidence remains constant regardless of the parameter values, it does not impact the shape or range of the posterior distribution or the parameter estimates themselves. Therefore, it acts as a normalization constant and is typically omitted in parameter estimation. Mathematically, the evidence is computed as $P(y) = \int P(y|\theta)P(\theta)d\theta$.

Bayes' theorem is then used to update the prior distribution with the likelihood of the observed data, resulting in the posterior distribution:

$$P(\theta|y) = \frac{P(y|\theta)P(\theta)}{P(y)} \propto P(y|\theta)P(\theta). \quad (3.1)$$

The posterior distribution represents the updated understanding of the parameters after incorporating the experimental data. While the posterior provides a comprehensive picture of all parameter values, we are often interested in individual parameters and their uncertainties. To focus on a specific parameter, we integrate (marginalize) the posterior distribution over all other parameters. For example, to obtain the marginal distribution for parameter θ_1 , we integrate the posterior $P(\theta|y)$ over all other parameters ($\theta_2, \theta_3, \dots, \theta_n$) as shown in [Equation 3.2](#):

$$P(\theta_1|y) = \int d\theta_2, d\theta_3, \dots, d\theta_n P(y|\theta). \quad (3.2)$$

This marginal distribution, $P(\theta_1|y)$, represents the probability distribution of the parameter θ_1 after considering the data. From this marginalized distribution, we can extract key information such as the most likely value and the associated uncertainty of θ_1 .

For many realistic models in Bayesian parameter estimation, the posterior distribution of the parameters is analytically intractable. This intractability arises primarily due to two key reasons: the complexity of the likelihood function and the high dimensionality of the parameter space.

Firstly, even when the likelihood function is well-defined (such as a multivariate Gaussian in our case), the correlation between parameters and the shape of the posterior distribution can be highly complex. These complexities make it challenging to express the likelihood in a simple mathematical form. Moreover, when combined with prior distributions that are not conjugate to the likelihood, the resulting posterior distribution can lack a closed-form solution, making direct analytical integration impossible.

Secondly, the parameter space in many Bayesian models is high-dimensional. In our case, with six model parameters, the parameter space becomes substantially large. High-dimensional spaces pose significant challenges for analytical integration because the volume of the space increases exponentially with the number of dimensions. This exponential growth makes it computationally infeasible to perform the necessary integrals to normalize the posterior distribution or to marginalize over some parameters.

Given these challenges, Markov chain Monte Carlo (MCMC) sampling provides a practical solution. MCMC is a computational technique that allows us to efficiently generate a large number of samples from the posterior distribution. It works by constructing a Markov chain, a sequence of parameter vectors where each step depends only on the previous one but ultimately explores the entire parameter space according to the posterior distribution. This approach offers two main advantages:

- MCMC avoids the need for complex integrations required for marginalization. Instead, we can simply extract the values of the desired parameters from each parameter vector in the generated sample.
- The generated sample provides a wealth of information beyond just marginal distributions. We can directly analyze the entire set of parameter vectors to understand relationships between parameters (joint distributions), visualize the parameter space, and estimate various quantities of interest.

While MCMC offers a powerful solution for exploring the posterior distribution, a significant challenge arises when dealing with computationally expensive models, as is often the case for simulating heavy-ion collisions. Each sample in the MCMC chain requires a model evaluation, which can become a major bottleneck.

To address this obstacle, researchers have developed the concept of model emulators. These emulators act as fast, simplified substitutes for the full model. They achieve this by:

1. Targeted model evaluations: The full model is evaluated at a strategically chosen set of points within the parameter space.
2. Emulator training: This data, consisting of model inputs and corresponding outputs, is used to train the emulator.
3. Surrogate model: The trained emulator then serves as a surrogate for the full model during MCMC sampling. It can rapidly predict the model's output for any parameter set within the trained range.

By relying on the emulator for most evaluations, the overall computation time required for MCMC sampling is reduced by several orders of magnitude. This effectively overcomes the limitations imposed by the full model's computational cost and allows for efficient exploration of the posterior distribution.

In the following sections, the various components and techniques essential for implementing Bayesian inference in the context of heavy-ion collisions will be discussed. An overview of the inference process is presented in [Figure 3.1](#).

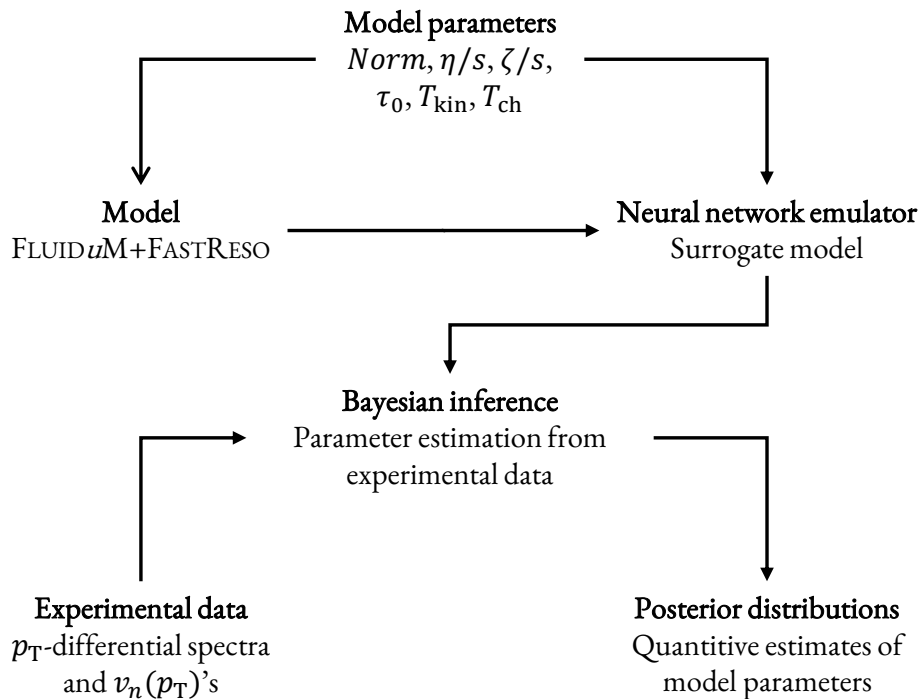


Figure 3.1: Overview of the Bayesian parameter estimation conducted in this analysis. The figure is inspired from [25].

3.1 PARAMETER SPACE

In any scientific model or simulation, the term "parameter space" refers to the multidimensional set of all possible values that the parameters of the model can take. Our phenomenological models in heavy-ion physics consist of several parameters, and the primary objective of this thesis is to estimate them along with their uncertainties. Given the complexity of our models and the limitations of computational resources, it is impractical to explore the entire parameter space exhaustively. Therefore, the first crucial step in our analysis is defining the range of model parameters. Once we establish these ranges, we need to develop efficient methods to sample the parameter space intelligently.

3.1.1 PARAMETER RANGES

The determination of the parameter ranges is a critical step, as it directly influences the model's ability to reproduce observed phenomena. Narrow ranges might limit the model's capacity to capture the experimental observables, while overly broad ranges can hinder the identification of optimal parameter values and the interpretation of model outputs. To address this challenge, let us first remind six parameters introduced in [Chapter 2](#):

1. Norm: Normalization factor for the initial entropy density profile.
2. τ_0 (fm/c): Initialization time of QGP phase.
3. $(\eta/s)_{\text{scale}}$: Scale value of the temperature dependent shear viscosity to entropy density parametrization given in [Equation 2.47](#). $(\eta/s)_{\text{scale}}$ can be converted to $(\eta/s)_{\text{min}}$, representing the minimum of the shear viscosity to entropy density, using [Equation 2.47](#).
4. $(\zeta/s)_{\text{max}}$: The maximum temperature of the bulk viscosity to entropy density ratio in [Equation 2.48](#).
5. T_{kin} (GeV): Kinetic freeze-out temperature.
6. T_{ch} (GeV): Chemical freeze-out temperature.

Among these six parameters, *Norm* and τ_0 exhibit system dependence, indicating their variation across distinct collision systems. The remaining parameters are hypothesized to converge toward the same values, independent of the specific collision system or energy. The primary objective of the Bayesian approach is the simultaneous determination of all six parameters. This involves allowing each parameter to explore all possibilities within predefined intervals, which will be outlined in [Chapter 5](#).

3.1.2 SAMPLING OF THE PARAMETER SPACE

There are several parameter sampling methods used in simulations [77]. In this thesis, only three of them will be discussed. The first sampling method could be the factorial design, where the points in the parameter space are placed on a uniform lattice. In low dimensions, this is the best approach to cover the parameter

space uniformly. However, in high dimensions, it becomes not feasible anymore. For a factorial design with k values for each n dimensions, the number of points increases exponentially with k^n .

Random sampling is another widely used method in simulations, particularly advantageous in high-dimensional spaces where factorial design becomes impractical. Unlike factorial design, random sampling distributes points randomly across the parameter space, offering better coverage and efficiency in higher dimensions. This approach mitigates the exponential increase in required points that factorial design suffers from, making it more scalable and computationally feasible. However, random sampling is not without its drawbacks. One significant limitation is the potential for clustering of points in certain regions of the parameter space and sparse coverage in others. This clustering can lead to biased results or inaccurate representations of the system under study.

To address these issues, we turn to alternative sampling methods such as Latin Hypercube Sampling (LHS) [78]. LHS is a systematic sampling technique designed to overcome the shortcomings of both factorial design and random sampling. It partitions the parameter space into equally probable intervals along each dimension and then randomly selects a single point from each interval, ensuring even coverage across the entire space. One of the key advantages of LHS is its ability to ensure a more uniform distribution of samples compared to random sampling, consequently minimizing the occurrence of clustering and sparse regions. LHS also ensures a thorough exploration of each dimension within the parameter space, making it well-suited for sensitivity analysis and uncertainty quantification tasks. This attribute holds particular significance for the performance of the neural network emulator, which will be introduced in the next section. Inadequate distribution of training data across the parameter space can worsen uncertainties within our model and the posterior probability densities of model parameters. The systematic approach of LHS facilitates the identification of relationships between input parameters and model outputs, enhancing the robustness and reliability of simulation results.

To visually illustrate the differences between sampling methods, Figure 3.2 presents 2D samplings generated by all methods. LHS aims to provide a more evenly distributed set of samples compared to random sampling, which can exhibit local clusterings within the parameter space.

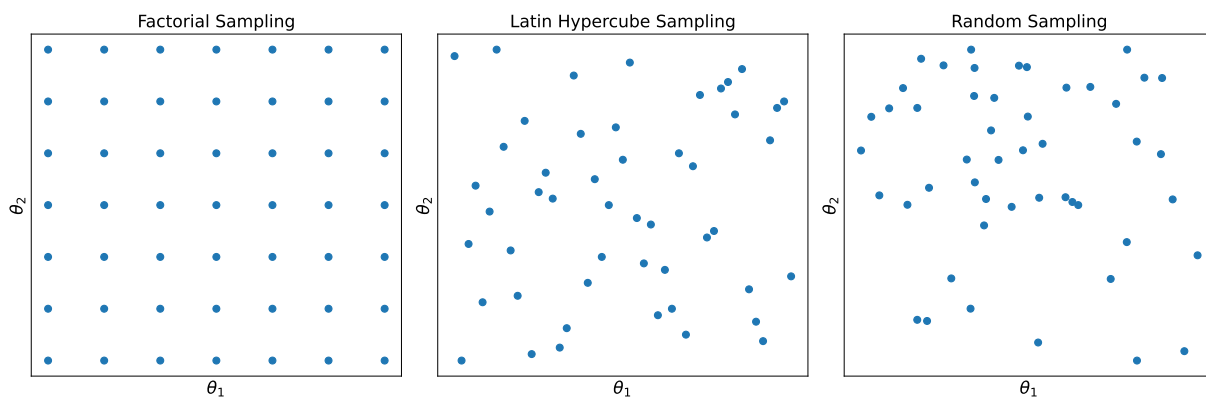


Figure 3.2: Comparison of parameter sampling methods: Factorial sampling, Latin Hypercube Sampling (LHS), and random sampling. While factorial sampling appears reasonable in 2D, it is imperative to acknowledge its limitations in higher dimensions. Specifically, factorial sampling exhibits sparsity as the dimensionality increases.

In the implementation of LHS within our framework, we use the `pyDOE3` Python Library [79]. In our analyses, we employ a sample size of 20000, strategically selected to balance parameter density with computational efficiency.

3.2 NEURAL NETWORK EMULATION

This section is mainly inspired by [80].

Following the selection of parameters, we execute our models and incorporate the resultant data in training the neural network emulator. Emulation is the process of constructing a surrogate model that replicates the behavior of a more intricate system or simulation. The primary objective of this surrogate, known as an emulator, is to develop a function that can evaluate the model for any set of parameters within the parameter range. The construction of the emulator relies on training it with input-output pairs $\{\theta_i, y_i\}$, where the θ_i represent the parameter samples obtained through LHS and y_i represent the model results, in our case, experimental observables.

Among the methodologies embraced within the Bayesian frameworks of heavy-ion physics, Gaussian process regression (GPR) [81] stands out as a frequently utilized emulation technique. It has been widely adopted by many research groups [82–87] for two primary reasons. Firstly, GPR offers a flexible nonparametric framework for emulation modeling. Secondly, it efficiently quantifies the predictive uncertainty associated with interpolating between training points in the n -dimensional parameter space. However, the computational cost of model simulations and the scaling of GPR with $\mathcal{O}(n^2)$ in memory and $\mathcal{O}(n^3)$ in computation pose significant challenges, making it infeasible to rely solely on GPR. Consequently, to mitigate these issues, an alternative approach is adopted in our framework: Neural network emulation.

Research has shown that sufficiently large neural networks are as flexible as GPR and can thus fit multi-dimensional functions comparably well. In fact, it has been demonstrated that infinitely wide neural networks can converge to GPR [88]. Unlike Gaussian process regression, neural networks offer favorable scaling properties with the number of training samples. The computation time for training scales linearly with $\mathcal{O}(n)$, while the model’s memory consumption remains unaffected by the number of samples. Additionally, neural networks can be tailored to accommodate varying numbers of inputs and outputs simply by adjusting the number of input and output nodes. It’s worth noting that alongside GPR and neural network emulation, alternative emulation methods such as transfer learning have also been explored in the literature [89]. Readers interested in more details on emulation in heavy-ion physics are encouraged to see [90] along with associated references therein.

3.2.1 NEURAL NETWORKS

A neural network can be defined by a sequence of definitions.

Definition 3.1. An *activation function* is a function $\sigma : \mathbb{R}^n \rightarrow \mathbb{R}^n$ which applies typically a non-linear transformation, $g : \mathbb{R} \rightarrow \mathbb{R}$, to the input vector x element-wise:

$$\sigma(x) = (g(x_1), g(x_2), \dots, g(x_n))^T. \quad (3.3)$$

Definition 3.2. An *artificial neuron* with weights $\{w_{j,i} \in \mathbb{R} : i = 1, \dots, n\}$, bias $b_j \in \mathbb{R}$ and activation function $\sigma : \mathbb{R} \rightarrow \mathbb{R}$ is defined as the function $a_j : \mathbb{R}^n \rightarrow \mathbb{R}$ given by

$$a_j(x_1, \dots, x_n) = \sigma \left(\sum_{i=1}^n w_{j,i} x_i + b_j \right). \quad (3.4)$$

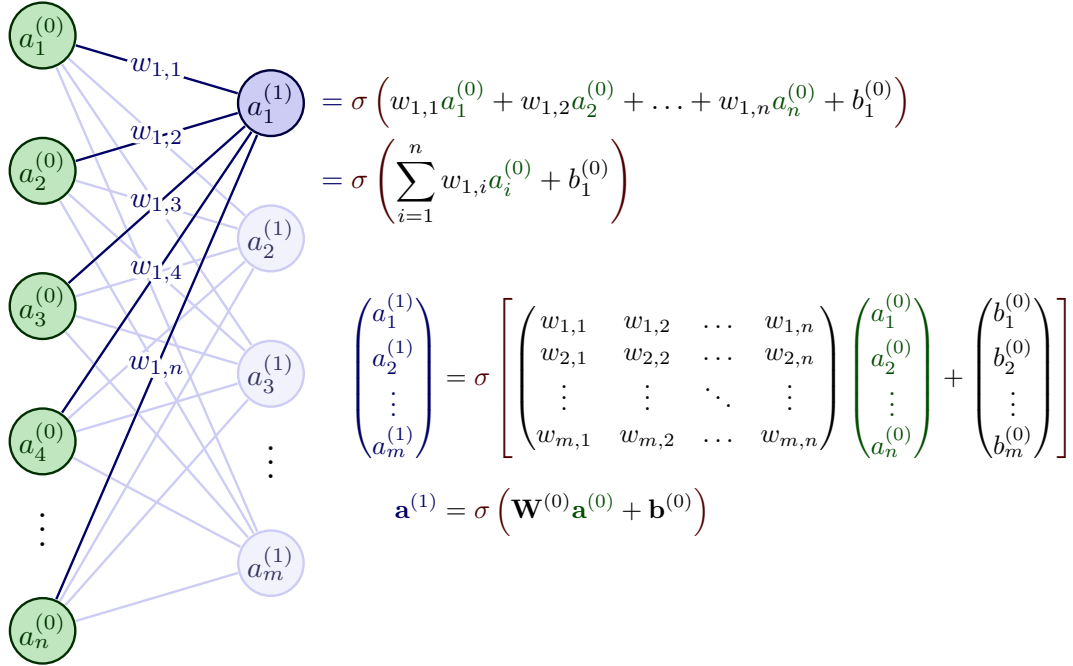


Figure 3.3: Activation function in one neuron and one layer in matrix notation [91].

Definition 3.3. A *dense layer* of size m is a set of m neurons. For the k 'th dense layer we have the collection of neurons $\{a_j^{(k)} : j = 1, \dots, m\}$ where each neuron in the set has the same domain. The activation of layer k , $A^{(k)} : \mathbb{R}^n \rightarrow \mathbb{R}^m$, is given by:

$$A^{(k)}(x) = (a_1^{(k)}(x), a_2^{(k)}(x), \dots, a_m^{(k)}(x))^T. \quad (3.5)$$

Activation functions in one neuron and one dense layer in matrix notation are illustrated in Figure 3.3. A neural network is then built by concatenating dense layers. This leads to the following definition.

Definition 3.4. A neural network of depth d is a composition of d dense layers, forming a map $f : \mathbb{R}^n \rightarrow \mathbb{R}^l$ defined by the function $f : x \mapsto f(x)$, where

$$f(x) = A^{(d)} \circ A^{(d-1)} \circ \dots \circ A^{(2)} \circ A^{(1)}(x), \quad (3.6)$$

with \circ denoting functional composition. Each layer $A^{(i)}$ is a function $A^{(i)} : \mathbb{R}^{n_{i-1}} \rightarrow \mathbb{R}^{n_i}$, where $n_0 = n$ and $n_d = l$. For the composition to be valid, the codomain of any layer $A^{(i)}$ must match the domain of the subsequent layer $A^{(i+1)}$. That is, if $A^{(i)} : \mathbb{R}^{n_{i-1}} \rightarrow \mathbb{R}^{n_i}$, then $A^{(i+1)} : \mathbb{R}^{n_i} \rightarrow \mathbb{R}^{n_{i+1}}$ for $i = 1, 2, \dots, d-1$.

Such neural networks can be illustrated using directed acyclic graphs, as shown in Figure 3.4. In our case, n is the number of model parameters, and k is the total number of p_T binning of experimental data.

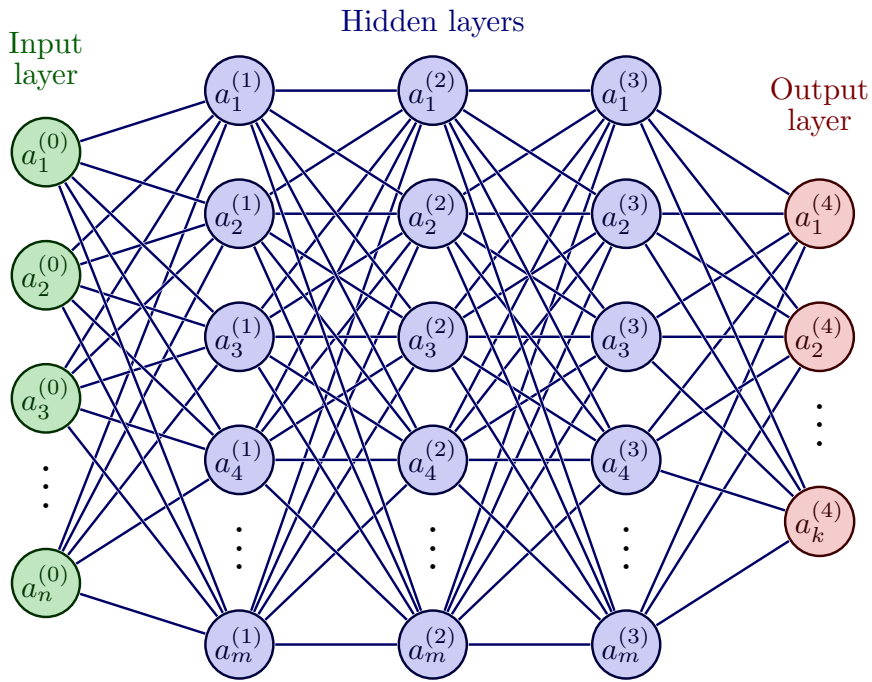


Figure 3.4: Architecture of a feed-forward, fully connected neural network with three hidden layers [91].

NEURAL NETWORK TRAINING AND HYPERPARAMETERS

The ultimate goal of neural network training is to find a set of parameters that results in the best possible performance on a given task, such as classification or regression. For regression tasks, a common loss function is the Mean Squared Error (MSE), defined as:

$$J(\mathbf{w}) = \frac{1}{n} \sum_{i=1}^n (y_i - \hat{y}_i(\mathbf{w}))^2, \quad (3.7)$$

where n is the number of samples, y_i is the true value, and \hat{y}_i is the predicted value.

To minimize MSE, the gradient descent algorithm is employed. This iterative optimization method aims to locate the local minimum of a differentiable function, a fundamental task in neural network training.

Central to this process is the computation of gradients for each parameter, which is crucial for effective network optimization. Backpropagation [92] plays a pivotal role in this regard, iteratively computing gradients throughout the neural network by leveraging the chain rule. By calculating partial derivatives of the loss concerning the model parameters, backpropagation enables the network to iteratively adjust and enhance its predictions over time.

The process initiates with the initialization of weights and biases using random values. Following this initialization, a forward pass is executed to compute the network's predictions. Subsequently, the chosen loss function is evaluated to quantify the deviation between predicted and actual values. At this juncture, the backpropagation mechanism is employed, enabling the computation of gradients with respect to the weights and biases. These gradients inform the subsequent adjustment of weights and biases, aligning them in the direction of the negative gradient. This adjustment process is governed by an update rule for each weight w , which is expressed as:

$$\mathbf{w}_{j+1} = \mathbf{w}_j - \eta \nabla J(\mathbf{w}_j) = \mathbf{w}_j - \frac{\eta}{n} \sum_{i=1}^n \nabla J(\mathbf{w}_j; \theta_i, y_i), \quad (3.8)$$

where η is the learning rate, a hyperparameter that controls the step size of each update. These steps are repeated for a predefined number of epochs or until the loss converges to a satisfactory value.

Following the optimization through gradient descent, our attention turns to hyperparameters, which are pivotal in shaping the network's architecture and training process. Unlike weights and biases, hyperparameters are predefined settings that remain fixed throughout training. These settings play a crucial role in determining the model's performance and convergence behavior. Important hyperparameters are listed below:

- **Number of layers:** The number of layers in the neural network. More layers allow the network to model more complex functions but can also increase the risk of overfitting and computational complexity.
- **Number of nodes per layer:** The number of neurons in each layer. More neurons can capture more features of the data, but like the number of layers, too many neurons can lead to overfitting and increased computational cost.
- **Activation function:** The function applied to each neuron's output. Common choices include ReLU (Rectified Linear Unit), sigmoid, and tanh. The activation function introduces non-linearity into the network, enabling it to learn more complex patterns.
- **Weight initialization:** The method used to initialize the network's weights before training. Proper initialization can help speed up convergence and avoid issues like vanishing or exploding gradients. Common methods include Xavier initialization [93] and He initialization [94].
- **Number of epochs:** The number of times the entire training dataset is passed through the network during training. More epochs can lead to better learning, but excessive epochs can cause overfitting.

- **Batch size:** The number of training examples used in one iteration to update the network parameters. Smaller batch sizes can make the training process noisier but provide more frequent updates, while larger batch sizes result in more stable updates but can be computationally more intensive.
- **Learning rate:** The learning rate is a crucial hyperparameter in gradient descent. If the learning rate is too large, the algorithm may overshoot the minimum, causing it to diverge. If the learning rate is too small, the algorithm may take too long to converge, getting stuck in a local minimum. Choosing an appropriate learning rate is essential for efficient and effective training.
- **Patience:** Used in early stopping and learning rate scheduling. Patience is the number of epochs to wait for an improvement in the loss before stopping training or reducing the learning rate. It helps prevent overfitting and reduces training time.
- **Factor:** In learning rate scheduling, the factor by which the learning rate is reduced when the performance metric has stopped improving. A common choice is to reduce the learning rate by a factor of 0.1.
- **Loss function:** The function that measures the difference between the predicted outputs and the actual target values. Common loss functions for regression include Mean Squared Error (MSE), and for classification, Cross-Entropy Loss.
- **Optimization algorithm:** The method used to minimize the loss function. While gradient descent is a basic method, more advanced optimizers like Adam [95], RMSprop, and Adagrad [96] often provide better performance and faster convergence.

In the training phase, it's essential to divide the dataset into distinct subsets for training, validation, and testing purposes. This division ensures that the model is trained on a subset of data while also being evaluated on data it hasn't seen before, thereby assessing its generalization capabilities. In our study, we partitioned the 20,000 FLUIDUM +FASTRESO results into 83.3% for training data and reserved 16.7% for validation and test data. During training, the neural network learns to map input data to desired outputs by adjusting its parameters based on the training data's features and corresponding labels. The performance of the model is monitored using the validation dataset, which acts as a proxy for unseen data. By periodically evaluating the model's performance on the validation set, we can make adjustments to hyperparameters or detect overfitting, where the model performs well on the training data but fails to generalize to new data.

The neural network was implemented in our framework using the PYTORCH [97] package, a widely-used open-source machine learning library that provides robust support for tensor computation and automatic differentiation, making it well-suited for deep learning applications. To optimize the hyperparameters of the neural network, we utilized the TUNE [98] package, a scalable hyperparameter tuning library. TUNE provides advanced features such as early stopping, distributed hyperparameter search, and integration with various search algorithms, which collectively enhance the efficiency and effectiveness of the hyperparameter tuning process.

Several hyperparameters crucial for the neural network’s architecture and training process have been previously determined, as detailed in [80]. These hyperparameters serve as foundational settings and have been outlined in Table 3.1.

Table 3.1: Previously determined hyperparameters.

Parameter	Value
Loss function	MSE
Activation function	ReLU
Batch size	100
Epochs	300
Weight initialization	Xavier
Optimizer	Adam

Additionally, certain hyperparameters have been fine-tuned specifically for this thesis through a grid search process. The search regions for hyperparameter tuning for different collision systems are outlined in Table 3.2.

Table 3.2: Hyperparameter tuning search regions for different collision systems.

Parameter	Search region
Learning rate	0.0005-0.5
Number of hidden layers	2-4
Number of nodes per hidden layer	128 - 1024
Patience	5-10
Factor	0.1-0.8
Trainable parameters	1-3M

3.2.2 NEURAL NETWORK UNCERTAINTY QUANTIFICATION VIA ENSEMBLE METHOD

While neural networks offer powerful predictions, they are often considered black-box models, providing little interpretability. In simpler terms, understanding why a neural network makes a specific decision is rarely feasible. Moreover, these models tend to be overly confident, attributing low uncertainty to their predictions even when uncertainty is actually large in reality. Studies have demonstrated that employing an ensemble of models, rather than using a single neural network, yields more reliable uncertainty estimates [99–101].

To address these challenges, within our framework, the ensemble model is constructed by averaging the outputs of multiple neural networks, which is illustrated in Figure 3.5. In practice, the ensemble prediction is often computed by averaging the individual predictions from each member of the ensemble as

$$y(\theta) := \frac{1}{M} \sum_{i=1}^M y_i(\theta), \quad (3.9)$$

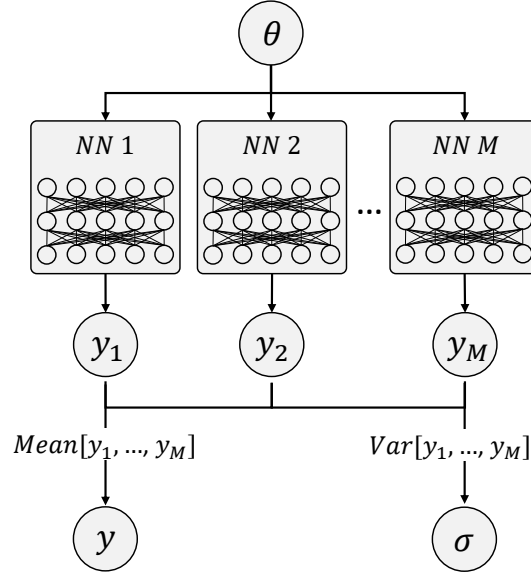


Figure 3.5: Representation of a neural network ensemble.

where $y(\theta)$ represents the ensemble prediction, $y_i(\theta)$ denotes the prediction of the i -th member of the ensemble, and M is the total number of ensemble members. Additionally, the spread of the different ensemble members can be quantified by the standard deviation of the member predictions, given by:

$$\hat{\sigma}_{\text{emu}}(\theta) = \sqrt{\frac{1}{M} \sum_{i=1}^M (y_i(\theta) - y(\theta))^2}, \quad (3.10)$$

where $\hat{\sigma}_{\text{emu}}(\theta)$ is the standard deviation. However, the $\hat{\sigma}_{\text{emu}}(\theta)$ itself may not adequately capture the full uncertainty in the ensemble predictions. It assumes that the predictions from different ensemble members are uncorrelated, which is not the case. To address this limitation and incorporate correlations among the ensemble members, we introduce an additional term into the uncertainty quantification process as in [Equation 3.11](#)

$$\sigma_{\text{emu}}(\theta) = \sqrt{\frac{\frac{1}{M} + \frac{M-1}{M}\rho}{1-\rho}} \cdot \sqrt{\frac{1}{M} \sum_{i=1}^M (y_i(\theta) - y(\theta))^2} = c \cdot \hat{\sigma}_{\text{emu}}(\theta). \quad (3.11)$$

In the new equation, $\hat{\sigma}_{\text{emu}}(\theta)$ is scaled by a factor that takes into consideration the correlation coefficient ρ among the ensemble predictions. A detailed derivation of [Equation 3.11](#) can be found in [80]. The introduced term, called as correction factor c , is determined by fitting a t-distribution to $(y_{\text{model}}(\theta) - y(\theta))/\hat{\sigma}_{\text{emu}}(\theta)$ (y_{model} represents the original FLUIDUM + FASTRESO output), which ideally follows a standard normal distribution if the prediction uncertainty accurately captures the prediction error.

Lastly, the model covariance matrix can be computed from the ensemble output as follows:

$$\Sigma_{\text{model}} = \Sigma_{\text{emu}}^{j,k}(\theta) = c^2 \cdot \frac{1}{M-1} \sum_{i=1}^M [(y_i^j(\theta) - y^j(\theta))(y_i^k(\theta) - y^k(\theta))], \quad (3.12)$$

where y_i^j is the j -th output value of y_i and y^j is the mean prediction for the j -th output. Here, Σ_{model} denotes the model covariance matrix, which plays a crucial role in quantifying the uncertainty associated with the predictions of an emulator in the MCMC phase. This matrix characterizes the variability and correlation among the predicted outputs of the emulator across different input parameter configurations. Each element $\Sigma_{emu}^{j,k}(\theta)$ of the model covariance matrix represents the covariance between the j -th and k -th output dimensions, normalized by a scaling factor c^2 and the number of samples M .

3.3 BAYESIAN PARAMETER ESTIMATION

3.3.1 PRIOR CHOICE

When we have minimal information about the parameters, it is appropriate to use a uniform prior, which means $\pi(\theta)$ is constant. In our current methodology, we define specific finite ranges for each parameter. Consequently, the neural network emulator is confined to making predictions within these predefined limits. Thus, we can select a prior that remains constant within the design region and drops to zero outside this region as

$$\pi(\theta) \propto \begin{cases} 1, & \text{if } \min(\theta_i) \leq \theta_i \leq \max(\theta_i) \text{ for all } i, \\ 0, & \text{otherwise.} \end{cases} \quad (3.13)$$

where θ_i are the input parameters.

Assuming the prior is zero beyond the design region imposes a significant constraint, as it suggests that we entirely rule out the possibility of any parameter value falling outside the specified range. To prevent inadvertently excluding any reasonable parameter values, we define our parameter ranges broadly, informed by the literature, as described in [Subsection 3.1.1](#).

3.3.2 LIKELIHOOD FORMULATION

This subsection is mainly inspired by [25].

The likelihood $\mathcal{L}(\mathcal{D}|\theta)$ represents the probability of observing the data given a set of parameters. It measures how well the model's predictions, at a specific point θ in the parameter space, align with the experimental data.

In our Bayesian inference framework, we employ a multivariate normal distribution for the likelihood function, as detailed in Ref. [25].

First, let \mathbf{y}_{exp} denote the vector of experimental data, which results from observing the hypothetical "true" values \mathbf{y}_{exp}^{true} with some measurement error $\boldsymbol{\epsilon}_{exp}$. This relationship can be expressed as:

$$\mathbf{y}_{exp} = \mathbf{y}_{exp}^{true} + \boldsymbol{\epsilon}_{exp}, \quad \boldsymbol{\epsilon}_{exp} \sim \mathcal{N}(\mathbf{0}, \Sigma_{exp}), \quad (3.14)$$

where the error follows a multivariate normal distribution with mean zero and covariance matrix Σ_{exp} . This covariance matrix accounts for all sources of experimental uncertainty, including statistical and systematic

errors. In our analyses, we assume that there is no correlation between the experimental uncertainties. Consequently, Σ_{exp} is a diagonal matrix given by:

$$\Sigma_{exp} = \text{diag}[\sigma_1^2, \sigma_2^2, \dots, \sigma_k^2], \quad (3.15)$$

where each σ_i^2 represents the total uncertainty for the i -th measurement, composed of the statistical uncertainty $(\sigma_i^{stat})^2$ and the systematic uncertainty $(\sigma_i^{sys})^2$, thus, $\sigma_i^2 = (\sigma_i^{stat})^2 + (\sigma_i^{sys})^2$.

Second, the model outputs \mathbf{y}_{model} for input parameters θ are given by:

$$\mathbf{y}_{model}(\theta) = \mathbf{y}_{model}^{ideal}(\theta) + \boldsymbol{\epsilon}_{model}, \quad \boldsymbol{\epsilon}_{model} \sim \mathcal{N}(\mathbf{0}, \Sigma_{model}), \quad (3.16)$$

where $\boldsymbol{\epsilon}_{model}$ follows a multivariate normal distribution with mean zero and covariance matrix Σ_{model} . In this context, the "ideal" model outputs refer to the hypothetical results generated by a perfect physical model with infinite precision. Since we are using a model emulator, $\mathbf{y}_{model}(\theta)$ represents the emulator's predictions. The model covariance matrix Σ_{model} accounts for the uncertainties derived from the emulator, as explained in [Equation 3.12](#).

Assuming there are true values for the parameters θ^* where the ideal model calculations align with the actual experimental data: $\mathbf{y}_{exp}^{true} = \mathbf{y}_{model}^{ideal}(\theta^*)$. Integrating this assumption with [Equation 3.14](#) and [Equation 3.16](#), we obtain:

$$\mathbf{y}_{model}(\theta^*) - \mathbf{y}_{exp} = \boldsymbol{\epsilon}, \quad \boldsymbol{\epsilon} \sim \mathcal{N}(\mathbf{0}, \Sigma), \quad \Sigma = \Sigma_{exp} + \Sigma_{model}. \quad (3.17)$$

This relationship between the model results and the experimental data indicates that the likelihood follows a multivariate normal distribution, with Σ representing the total covariance matrix that encompasses all sources of uncertainty

$$\mathcal{L}(\mathcal{D}|\theta) = \frac{1}{\sqrt{(2\pi)^n \det \Sigma}} \exp \left[-\frac{1}{2} (\mathbf{y}_{model}(\theta) - \mathbf{y}_{exp})^T \Sigma^{-1} (\mathbf{y}_{model}(\theta) - \mathbf{y}_{exp}) \right], \quad (3.18)$$

where n is the number of parameters.

3.3.3 MARKOV CHAIN MONTE CARLO SAMPLING

Markov chain Monte Carlo aims to construct a Markov chain on the state space \mathcal{S} whose stationary distribution is the target density $\mathcal{P}(\theta|\mathcal{D})$, the posteriors we are after. A Markov chain is a stochastic process that satisfies the Markov property, which can be formally defined as follows:

$$p(\Theta_{t+1} = \theta_{t+1} \mid \Theta_0 = \theta_0, \Theta_1 = \theta_1, \dots, \Theta_t = \theta_t) = p(\Theta_{t+1} = \theta_{t+1} \mid \Theta_t = \theta_t), \quad (3.19)$$

for all $t \geq 1$ and all $\theta_0, \theta_1, \dots, \theta_{t+1} \in \mathcal{S}$. This property essentially states that the probability of transitioning to the next state $\Theta_{t+1} = \theta_{t+1}$ depends solely on the current state $\Theta_t = \theta_t$, independent of the sequence of

past states. MCMC generates samples that are correlated in a way that allows for a more efficient exploration of the target distribution compared to independent samples from basic Monte Carlo methods.

The frequently encountered MCMC algorithms include Gibbs sampling [102], the Metropolis-Hastings (MH) algorithm [103, 104], and Slice sampling [105]. While these methods have demonstrated effectiveness, they have become somewhat dated. Given the advancements in sampling algorithms over the years, newer approaches often outperform these traditional methods. In our MCMC sampling, we utilize the `EMCEE` Python Library [106], which represents a significant advancement over traditional MCMC methods such as the MH algorithm. Unlike the MH algorithm, which relies on single-step proposals, `EMCEE` employs an ensemble of "walkers" that evolve simultaneously, utilizing sophisticated moves like "stretch moves" and "shrink moves" based on affine transformations [107]. This approach, known as affine-invariant ensemble sampling, adapts dynamically to the local structure of the parameter space. This adaptability allows `EMCEE` to explore the parameter space more efficiently and converge to the target distribution more rapidly.

Comprehending the fundamental concepts and terminology of MCMC aids in evaluating the efficiency and effectiveness of such algorithms. These key concepts are listed as:

- **Walkers:** Walkers are independent chains or trajectories in the parameter space. Each walker represents a potential sequence of parameter values generated by the Markov chain. The ensemble of walkers explores the parameter space collectively, providing a more comprehensive sampling compared to a single chain.
- **Autocorrelation:** Autocorrelation measures the correlation between consecutive samples in a Markov chain. Large autocorrelation indicates that successive samples are highly dependent on each other, suggesting inefficient exploration of the parameter space. Low autocorrelation indicates more effective sampling, as each sample contains more independent information. Autocorrelation is often used as a diagnostic tool to assess the mixing and convergence of MCMC chains. In MCMC simulations, the integrated autocorrelation time (τ_f) quantifies the rate at which successive samples become effectively independent. This parameter is crucial for determining the effective number of samples and controlling sampling error.
- **Burn-in:** Burn-in refers to the initial phase of an MCMC simulation where the Markov chain is allowed to reach its equilibrium distribution. During burn-in, samples are typically discarded because they may not be representative of the target distribution. The length of the burn-in period depends on the specific problem and the convergence properties of the algorithm.
- **Number of Steps:** The number of steps in an MCMC simulation refers to the total number of iterations or samples generated by the algorithm. This parameter determines the length of the Markov chain and affects the quality of the resulting samples. A larger number of steps generally leads to a more accurate estimation of posterior distributions but may also increase computational time.

To ensure adequate convergence of the Markov chain, it is essential to minimize the sampling error of the MCMC method to less than 1%. This error is diminished by the ratio of the integrated autocorrelation time

3 Bayesian inference

(τ_f) to the number of samples N . Consequently, the total exploration effort, determined by the product of the number of walkers (set to 400 in our study) and the length of the chains, must exceed $10000\tau_f$. Additionally, to prevent premature termination, we stipulate that the variation in τ_f (evaluated every 100 MCMC steps) remains below 1% [80].

4 QUANTIFICATION OF THE PION EXCESS IN THE LOW TRANSVERSE MOMENTUM REGIME IN HEAVY-ION COLLISIONS

This chapter is mainly based on the article: P. Lu, R. Kavak, A. Dubla, S. Masciocchi, and I. Selyuzhenkov. *Quantification of the low- p_T pion excess in heavy-ion collisions at the LHC and top RHIC energy*. 2024. ([arXiv:2407.09207](https://arxiv.org/abs/2407.09207)). My primary contribution to this work involved performing all the Bayesian analyses presented throughout this chapter. The quantification of the pion excess was primarily conducted by my colleague, Pengzhong Lu. The interpretation of the results was a collaborative effort within our research group, ensuring a comprehensive understanding of the phenomena under study.

In the previous chapters, we have explored the foundational aspects of viscous hydrodynamics and its role in describing the QGP formed in heavy-ion collisions. Over the years, extensive theoretical and phenomenological advancements have deepened our understanding of how relativistic hydrodynamics describes the complex dynamics of the QGP. These studies have broadened the applicability of hydrodynamic models, enabling more accurate descriptions of the QGP's behavior across different collision energies and system sizes. As a result, viscous hydrodynamics has emerged as the “standard model” for interpreting a wide range of experimental observables in heavy-ion collisions, effectively capturing key features such as anisotropic flow and particle spectra [108, 109]. While this framework provides a robust description of many aspects of the QGP and its evolution, certain phenomena, particularly at low transverse momentum (p_T), remain inadequately understood.

Among these phenomena, the enhancement observed in the low- p_T pion spectra stands out as a particularly intriguing feature that challenges the completeness of hydrodynamic models. This chapter is dedicated to exploring this low- p_T pion excess, which current hydrodynamic models fail to fully account for. Understanding the origins of this excess is crucial, as it likely points to physical processes beyond those captured by standard fluid dynamic descriptions.

The current understanding suggests that the low- p_T pion excess may arise from a combination of several physical effects, each contributing to the enhancement observed in the spectra. One possibility is Bose-Einstein condensation, where pions, being bosons, may accumulate in the lowest momentum states, leading to a macroscopic occupation of these states and an excess of low- p_T pions [110, 111]. Another contributing factor could be an enhanced resonance population, where the decay of a larger-than-expected number of resonances, such as ρ mesons, results in a greater yield of low- p_T pions [30]. Additionally, the ρ meson, having

a finite width in its mass distribution rather than a fixed mass, can decay into pions with a range of energies. This broader mass spectrum leads to an increased overall pion yield, particularly in the low- p_T region [112].

The investigation of low p_T pion production continues at the latest heavy-ion colliders. Significant efforts by the ALICE Collaboration [113–116] at the LHC and the PHENIX and STAR Collaborations [117–120] at RHIC have reported a low p_T pion excess across different collision systems and energy levels when experimental outcomes are contrasted with hydrodynamic models [121–128]. Typically, these pion p_T spectra measurements extend down to $p_T = 0.1$ GeV/ c at the LHC and $p_T = 0.2$ GeV/ c at RHIC. The exact amount of the pion excess and the kinematic regime at which it starts to dominate over thermally generated particles are still unknown.

This chapter is dedicated to systematically investigating the low- p_T pion excess at the LHC, specifically in Pb–Pb collisions at $\sqrt{s_{NN}} = 2.76$ TeV [113] and 5.02 TeV [114], as well as in Xe–Xe collisions at $\sqrt{s_{NN}} = 5.44$ TeV [115], and at the top RHIC energy, examining Au–Au collisions at $\sqrt{s_{NN}} = 200$ GeV [117, 120]. Through Bayesian inference analysis of the p_T spectra for pions, kaons, and protons, we identify the optimal p_T range where fluid dynamic simulations best match the observed pion spectra. The pion excess is extracted across various centrality intervals: 0-5%, 5-10%, 10-20%, 20-30%, and 30-40% for ALICE data, and 0-5%, 5-10%, 10-15%, 15-20%, 20-30%, and 30-40% for RHIC data. This extraction focuses on the low- p_T region where the fluid dynamic model fails to provide an adequate description.

PARAMETER INTERVALS AND INITIAL CONDITIONS

To perform a robust Bayesian analysis, it is essential to accurately define the parameter intervals of the adopted model. As described in Chapter 3, our Bayesian inference approach is centered around several key free parameters, including the overall normalization constant Norm, $(\eta/s)_{\text{scale}}$ and $(\zeta/s)_{\text{max}}$ in the shear and bulk viscosity to entropy density ratio, the starting time of the hydrodynamic phase τ_0 , and the two freeze-out temperatures T_{kin} and T_{ch} . In our Bayesian inference analyses, we try to constrain these six model parameters within predefined intervals.

The parameter intervals used in this study are summarized in Table 4.1. Their ranges are chosen based on previous works [29, 82–85, 113, 123, 129, 130]. A posteriori confirmation revealed that the optimal parameter values reside within the predefined intervals rather than at their edges. In instances where the analysis did not show definitive convergence, the parameter intervals were subsequently expanded to ensure a comprehensive exploration of the parameter space.

Table 4.1: Defined intervals for the six model parameters across the four collision systems. Norm and τ_0 are recognized as system-dependent parameters.

	$(\eta/s)_{\text{scale}}$	$(\zeta/s)_{\text{max}}$	T_{kin} (GeV)	T_{ch} (GeV)	Norm	τ_0 (fm/ c)
Pb–Pb, $\sqrt{s_{NN}} = 2.76$ TeV	0.08–0.78	10^{-4} –0.3	0.110–0.140	0.130–0.155	5–80	0.01–3.0
Pb–Pb, $\sqrt{s_{NN}} = 5.02$ TeV					80–140	2.0–7.0
Xe–Xe, $\sqrt{s_{NN}} = 5.44$ TeV					70–150	2.0–7.0
Au–Au, $\sqrt{s_{NN}} = 200$ GeV					3–80	0.05–3.0

In addition to these parameters, the initial condition parameters for the T_RENTo model, as outlined in [Subsection 2.1.1](#), are crucial for the analysis. The T_RENTo model parameters are not estimated through Bayesian analysis in this study. Instead, they are fixed and chosen based on the work by the Duke group, as detailed in Ref. [131], and are listed in [Table 4.2](#). While the number of constituents inside the nucleon does not exhibit a sharply peaked distribution, the remaining parameters are well-constrained. Furthermore, through comparative analysis, we found that these parameters yielded the most accurate model results in terms of describing the experimental data. Specifically, they outperformed several other initial condition parameter combinations that were tested [84, 124, 132], as evidenced by a superior data-to-model ratio and a lower resulting reduced χ^2 value.

Table 4.2: Input parameters for the T_RENTo model adopted from [131].

Parameter	Description	Value
w [fm]	Gaussian nucleon width	0.98
v [fm]	Gaussian constituent width	0.473
m	Number of constituents inside the nucleon	6
p	Reduced thickness parameter	0.013
k	Gamma distribution shape parameter for nucleon fluctuations	0.1835
d [fm]	Minimum nucleon-nucleon distance	1.13

The nucleon-nucleon cross section values used in this analysis are derived from measurements by the ALICE Collaboration [133] and the PHENIX Collaboration [134]. Specifically, the cross section values are 61.8 mb for Pb–Pb collisions at $\sqrt{s_{\text{NN}}} = 2.76$ TeV, 67.6 mb for Pb–Pb collisions at $\sqrt{s_{\text{NN}}} = 5.02$ TeV, 68.4 mb for Xe–Xe collisions at $\sqrt{s_{\text{NN}}} = 5.44$ TeV, and 42.3 mb for Au–Au collisions at $\sqrt{s_{\text{NN}}} = 200$ GeV.

All ions are sampled from the Woods-Saxon distribution. The Pb ion exhibits spherical symmetry, characterized by a radius of $R = 6.65$ fm and a surface thickness of $a = 0.54$ fm. The Xe ion features spheroidal deformation, with a radius of $R = 5.60$ fm, a surface thickness of $a = 0.49$ fm, and deformation parameters $\beta_2 = 0.21$ and $\beta_4 = 0.0$ [135]. Lastly, the Au ion is described by a radius of $R = 6.38$ fm and a surface thickness of $a = 0.535$ fm. Employing this parameter set, a dataset comprising 50 million minimum-bias events is generated. T_RENTo events are created with random impact parameters and incorporate multiplicity fluctuations of the generated profiles, leading to initial entropy density profiles across all centrality classes from 0% to 100%.

Classification of the T_RENTo events into centrality classes is achieved through the integrated transverse density $\int d^2x T_{\text{R}}(\mathbf{x})$, which demonstrates a linear monotonic relationship with multiplicity [136]. This approach enables the sorting of events into narrow one-percent multiplicity classes, mimicking the experimental procedure where events are categorized based on the number of produced particles. To improve statistical accuracy and reduce computational costs, the statistics of the event-averaged entropy density profiles are increased by integrating out the ϕ -dependence of the initial profiles. Typically, the T_RENTo model provides the transverse profile $T_{\text{R}}(r, \phi)$, which is a function of both the radial coordinate r and the azimuthal angle ϕ . In practice, we are primarily interested in the radially averaged profile $T_{\text{R}}(r)$. A conventional approach

would be to evaluate $T_R(r, \phi)$ along a single radial axis, but this method employs only a fraction of the available data, thereby underutilizing the statistical information from the entire profile. Instead, to fully leverage the independent directions, we evaluate $T_R(r, \phi)$ along 100 different directions and sum the results. Thus, integrating out the ϕ -dependence in this manner can reduce the computational effort by up to a factor of 100. Mathematically, this is expressed as:

$$\langle T_R(r) \rangle = \frac{1}{2\pi} \int_0^{2\pi} d\phi \langle T_R(r, \phi) \rangle. \quad (4.1)$$

The representation of $\langle T_R(r) \rangle$ for Pb–Pb collisions at $\sqrt{s_{NN}} = 2.76$ TeV is shown in Figure 4.1 (left panel). The resulting averaged entropy densities for larger experimental centrality classes are produced by combining the corresponding distributions from narrower classes. The right panel of Figure 4.1 compares the averaged entropy densities for centrality classes 0-5%, 5-10%, 10-20%, 20-30%, and 30-40% for Pb–Pb collisions at $\sqrt{s_{NN}} = 2.76$ TeV (solid lines) and Xe–Xe collisions at $\sqrt{s_{NN}} = 5.44$ TeV (dashed lines). Notably, the most central collisions in Xe–Xe correspond to the 10-20% centrality class in Pb–Pb at $\sqrt{s_{NN}} = 2.76$ TeV, while the 30-40% centrality class in Xe–Xe corresponds to the 40-50% centrality class in Pb–Pb at $\sqrt{s_{NN}} = 5.02$ TeV, considering particle multiplicity, as supported by experimental measurements [137].

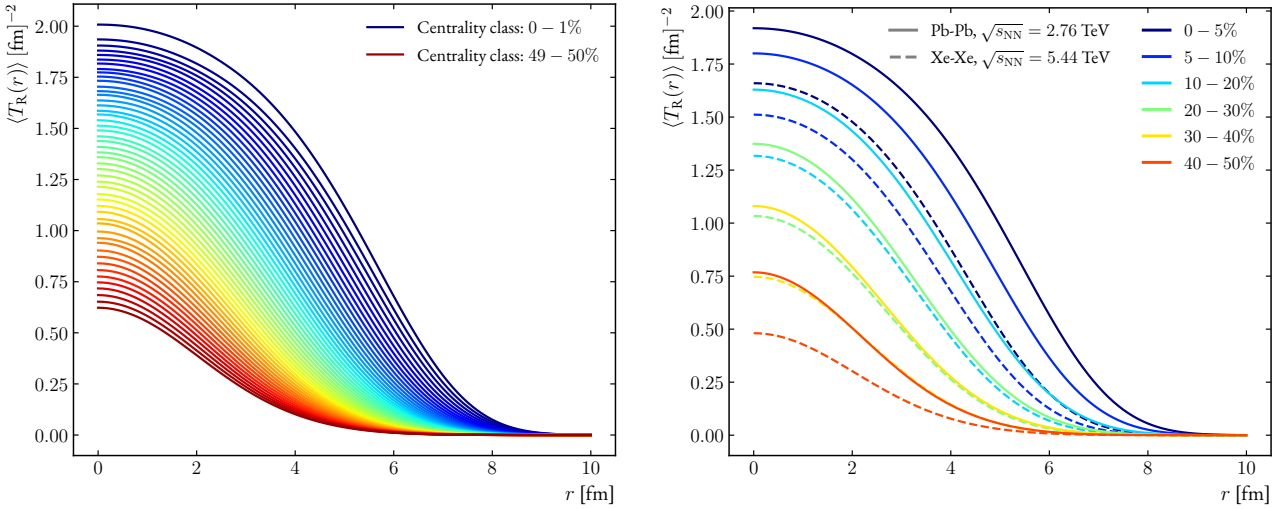


Figure 4.1: Average transverse entropy density profiles. (Left) The representation of $\langle T_R(r) \rangle$ for Pb–Pb collisions at $\sqrt{s_{NN}} = 2.76$ TeV across 50 narrow centrality classes. (Right) Comparison of the averaged entropy densities for centrality classes 0-5%, 5-10%, 10-20%, 20-30%, and 30-40% for Pb–Pb collisions at $\sqrt{s_{NN}} = 2.76$ TeV (solid lines) and Xe–Xe collisions at $\sqrt{s_{NN}} = 5.44$ TeV (dashed lines).

Then, for each centrality class, the averaged entropy density profile is determined as follows:

$$s(r) = \frac{\text{Norm}}{\tau_0} \langle T_R(r) \rangle, \quad (4.2)$$

where $\langle \dots \rangle$ denotes the average over all the events in the class with a random reaction plane angle. The normalization constant Norm is introduced to ensure the correct multiplicity scaling of the TRENTo events.

Additionally, the factor is scaled by the initialization time τ_0 to account for the longitudinal expansion effect at early times.

4.1 DETERMINATION OF THE OPTIMAL TRANSVERSE MOMENTUM FITTING RANGE

The objective of this section is to systematically investigate the pion excess in the low- p_T regime and examine its dependence on collision centrality and collision systems at both LHC and top RHIC energies. Several hydrodynamical fits to experimental data have consistently revealed a noticeable excess of pions at low- p_T [122, 124, 125]. However, the exact magnitude of this pion excess and the specific kinematic regime at which it begins to dominate over thermally generated particles have not been quantified. To achieve this, the Bayesian inference analysis is conducted separately for each centrality class and collision system rather than attempting a global fit using all available data. In contrast to Chapter 5, which focuses on constraining the physical parameters of the QGP, this section aims to determine the optimal p_T fitting range for pion data to be used in Bayesian inference.

The analysis utilizes the p_T -differential spectra of pions, kaons, and protons across various centrality classes measured by the ALICE Collaboration at the LHC and by the PHENIX Collaboration at RHIC. The selection of these specific experimental data is motivated by several key considerations that align with the objectives of this study. Firstly, the data spans a variety of collision systems (Pb–Pb, Xe–Xe, and Au–Au) and covers a broad range of center-of-mass energies, from 200 GeV at RHIC to 5.44 TeV at the LHC. This variety is crucial for investigating how different initial conditions, such as collision energy and system size, affect the properties of QGP and the subsequent particle production. Furthermore, the data is analyzed across multiple centrality classes, which is essential for understanding how the collision geometry influences the p_T spectra. The focus on identified particles—pions, kaons, and protons—rather than unidentified hadrons, is another important aspect of the data selection. Identified particle spectra provide more precise information about the hadronization process and the freeze-out conditions of different particle species, which is critical for studying phenomena such as the π excess. A detailed summary of the experimental data used is provided in Table 4.3.

Table 4.3: Experimental data used for Bayesian parameter estimation in low- p_T pion studies.

Collision system	Observables	Particles	Centrality classes	Ref.
Pb–Pb, $\sqrt{s_{NN}} = 2.76$ TeV	p_T -differential spectra	π^+ , K^+ , p	0-5, 5-10, 10-20, 20-30, 30-40	[113]
Pb–Pb, $\sqrt{s_{NN}} = 5.02$ TeV	p_T -differential spectra	π^+ , K^+ , p	0-5, 5-10, 10-20, 20-30, 30-40	[114]
Xe–Xe, $\sqrt{s_{NN}} = 5.44$ TeV	p_T -differential spectra	π^+ , K^+ , p	0-5, 5-10, 10-20, 20-30, 30-40	[115]
Au–Au, $\sqrt{s_{NN}} = 200$ GeV	p_T -differential spectra	π^- , K^- , \bar{p}	0-5, 5-10, 10-15, 15-20, 20-30, 30-40	[117]

This study focuses on the single π excess, utilizing π^+ p_T spectra in Pb–Pb at $\sqrt{s_{NN}} = 2.76$ TeV and averaging π^+ and π^- in Pb–Pb at $\sqrt{s_{NN}} = 5.02$ TeV and Xe–Xe at $\sqrt{s_{NN}} = 5.44$ TeV. For the Au–Au

system, the π^- p_T spectra are utilized to compute the pion excess instead of the π^+ spectra. This choice is driven by the phenomenon of baryon stopping, which refers to the process where baryons from the colliding nuclei lose a significant portion of their longitudinal momentum as they interact with the medium in the collision zone [138]. In heavy-ion collisions at lower energies, such as those at RHIC, baryon stopping is more pronounced, especially at midrapidity ($y = 0$), where the net baryon density—the difference between the number of baryons and antibaryons—is higher. This, in turn, affects the production of pions, particularly π^+ , due to the associated changes in the chemical environment. The presence of stopped baryons, which are predominantly protons, alters the chemical environment in the collision zone. This can influence the production of pions, particularly π^+ , due to the increased baryon density. As a result, the π^+ spectra may reflect these changes in the chemical environment, complicating the interpretation of the π^+ excess. Since the theoretical model employed in this study does not account for baryon transport or the stopping of baryons at midrapidity, using the π^+ spectra could introduce biases related to these unmodeled effects. In contrast, π^- production is less sensitive to the presence of stopped baryons, as it primarily originates from processes that do not involve baryon number conservation. Therefore, the π^- p_T spectra provide a more reliable measure of the pion excess in this context, ensuring that the analysis remains consistent with the assumptions and limitations of the model.

In this analysis, the uncertainties associated with the p_T -differential spectra include both statistical and systematic components. These uncertainties have been summed in quadrature and treated as fully uncorrelated among different particle species and transverse momentum intervals, as there is currently no clear guidance on the precise degree of correlation in the experimental systematic uncertainties. While this assumption simplifies the error propagation in the Bayesian inference process, it introduces a limitation: the assumption of uncorrelated uncertainties may not accurately reflect the true nature of the experimental errors. In reality, systematic uncertainties often contain correlated components, particularly across different p_T intervals or between various particle species. Neglecting these correlations could lead to an underestimation of the total uncertainty and potentially bias the resulting parameter estimates. Therefore, while the current treatment provides a practical framework for analysis, it is important for the reader to recognize this limitation. Future studies would benefit from experimental input on the degree of correlation among the uncertainties across p_T intervals and particle species, enabling a more comprehensive treatment of systematic uncertainties to enhance the robustness of the inferred QGP properties.

To determine the optimal p_T^π ranges for the experimental measurements to be used in the inference and to accurately compute the low- p_T pion excess, we systematically varied the p_T interval of the pion spectra. Throughout this process, the kaon and proton spectra were fixed at $p_T^{K,p} < 2.0 \text{ GeV}/c$. The joint inference of pion, kaon, and proton spectra is particularly important due to the mass differences among these particles. Pions, being the lightest hadrons, are most sensitive to the thermal motion at kinetic freeze-out, while kaons and protons provide additional constraints on the radial flow and the thermal freeze-out temperature. As described in Equation 1.10, the parameter T_{slope} depends on both the kinetic freeze-out temperature T_{kin} and the expansion velocity $\langle v_\perp \rangle$, with the mass of the particle species playing a critical role. By using different kinds of particles, we can obtain a more precise estimation of certain model parameters, such as the chemical and kinetic freeze-out temperatures.

We began by optimizing the starting p_T^π range within the interval $x_1 < p_T^\pi < 2.0$ GeV/ c , where x_1 was systematically varied from 0.1 to 1.0 GeV/ c . The choice of 0.1 GeV/ c as the lower bound was dictated by the experimental data, as it represents the lowest available data point. Subsequently, we optimized the upper bound of the p_T^π range by focusing on the interval $0.5 < p_T^\pi < x_2$ GeV/ c , with x_2 varied from 2.0 to 3.0 GeV/ c . The upper limit of 3.0 GeV/ c was chosen because, beyond this point, the p_T region transitions from soft (low- p_T) dynamics to hard scattering processes, where hydrodynamic models lose their applicability. By constraining the analysis to the soft region, we ensure that the extracted parameters, such as the freeze-out temperature, are derived from data where hydrodynamics remains valid and reliable. The purpose of this systematic variation and optimization of the p_T^π range was to identify the best fitting range that would provide the most accurate and meaningful constraints on the model parameters.

While the primary objective of this study is not to constrain the physical parameters of the QGP, it is nevertheless crucial to carefully analyze the performance and convergence of these parameters during the optimization of the p_T^π range. Ensuring that the selected p_T range in the Bayesian inference procedure leads to reliable convergence is vital for the validity and robustness of the results. In [Figure 4.2](#), the evolution of key parameters for the 0 – 5% centrality class in Pb–Pb collisions at $\sqrt{s_{NN}} = 2.76$ TeV is illustrated. These parameters are attempted to be constrained through a systematic Bayesian inference process, which involves fitting the p_T spectra of pions, kaons, and protons. The parameters Norm and τ_0 are presented in the form of a ratio (Norm/ τ_0) because, within our model, the expected entropy density profile is determined by their ratio, as described in [Equation 4.2](#). The top panel illustrates the optimization process for the starting p_T^π range, while the bottom panel addresses the optimization of the ending p_T^π . The plotted points represent the median values of the parameters obtained from the analysis, and the associated error bars denote the 68% confidence intervals derived from their respective marginalized posterior distributions.

The stability of the model parameters varies across different p_T fitting ranges. In the top panel, a convergence of parameter values is observed when x_1 surpasses a threshold of approximately 0.5 GeV/ c . This indicates that including the low p_T pion region ($x_1 < 0.5$ GeV/ c , depicted in red) in the Bayesian analysis would introduce instabilities in the estimation of physical parameters, suggesting that a fluid dynamic framework struggles to adequately describe the experimentally observed low- p_T pion spectra. In the bottom panel of [Figure 4.2](#), the parameters begin to diverge from their stable values when the analysis incorporates spectra values beyond $p_T^\pi > 2.0$ GeV/ c . This divergence aligns with the expectation that, at higher p_T , particle production becomes increasingly dominated by hard partonic scattering processes, with partonic energy loss mechanisms playing a more prominent role in shaping the spectral distributions, rather than the thermal production processes that are central to hydrodynamic models.

Beyond the issue of parameter instabilities, it is observed that FLUIDUM calculations could not reproduce the experimental data accurately when either the low- p_T or high- p_T spectra are included in the inference. This leads to significant discrepancies between the model predictions and the experimental observations at both extremes of the p_T spectrum. To ensure the consistency of these findings, the same analysis was performed for the 30 – 40% centrality interval in Pb–Pb collisions at $\sqrt{s_{NN}} = 2.76$ TeV, yielding comparable results across the different centrality classes. Consequently, the p_T range of $0.5 < p_T^\pi < 2.0$ GeV/ c was determined to be the optimal interval for Bayesian inference across all centrality classes and collision systems,

4 Quantification of the pion excess in the low transverse momentum regime in heavy-ion collisions

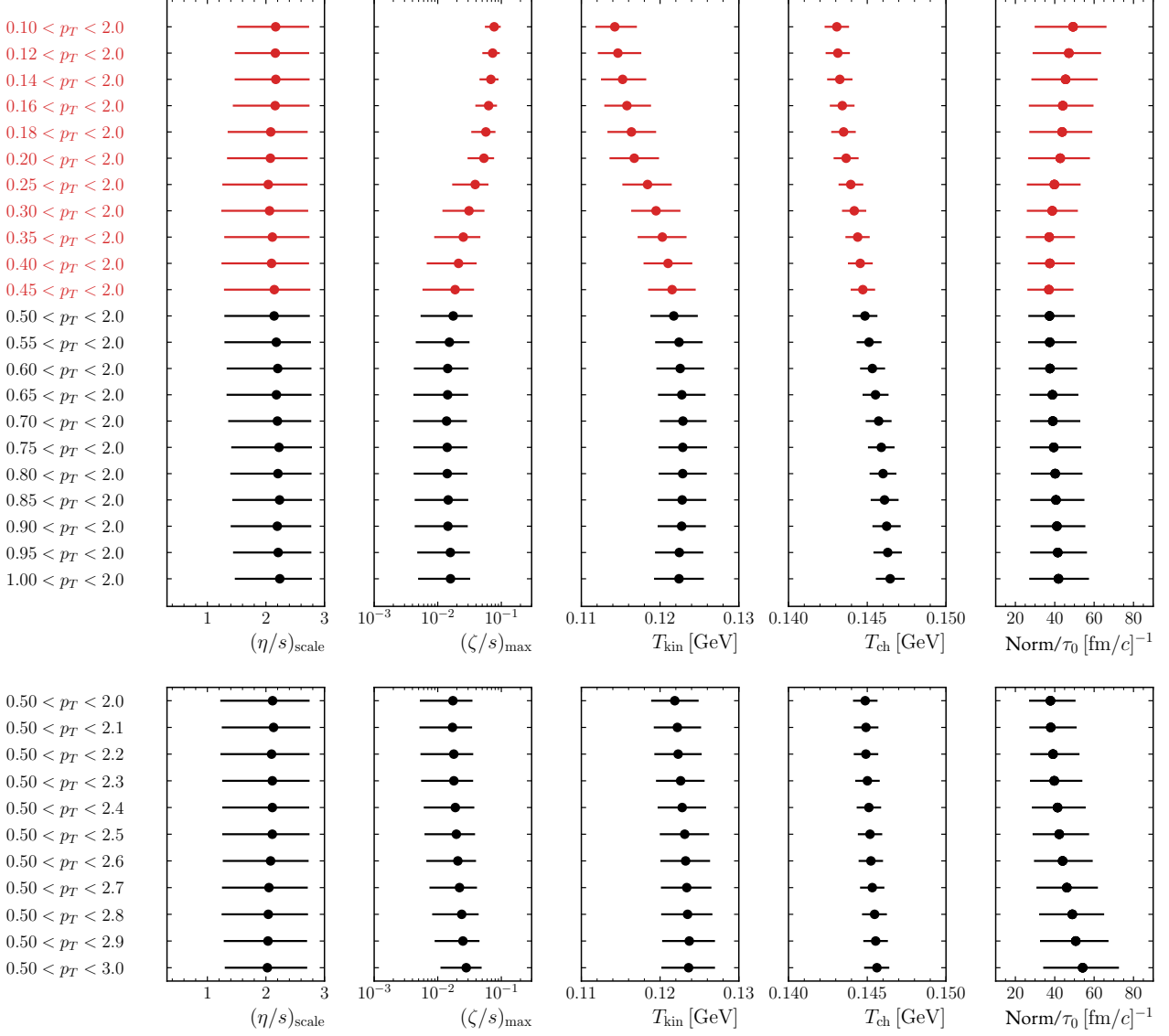


Figure 4.2: Parameter values within different p_T fitting ranges for the 0 – 5% centrality class in Pb–Pb collisions at $\sqrt{s_{\text{NN}}} = 2.76$ TeV. The top panel presents the variation of the starting p_T from 0.1 GeV/ c to 1.0 GeV/ c , while the bottom panel displays the variation of the ending p_T from 2.0 GeV/ c to 3.0 GeV/ c . The uncertainty bars denote 68% confidence intervals of the marginalized posterior distributions for each model parameter.

providing the most reliable and accurate results.

Figure 4.3 presents the posterior distributions of the model parameters across all centrality classes for Pb–Pb collisions at $\sqrt{s_{\text{NN}}} = 2.76$ TeV. These distributions are mostly well-contained within the prior intervals specified in Table 4.1, rather than clustering at the boundaries, suggesting that the chosen parameter space is appropriate. However, the $(\eta/s)_{\text{scale}}$ parameter is not well-constrained, as its distribution spans several orders of magnitude, indicating significant uncertainty in its value. This behavior is consistent with previous findings on the p_T spectra [122], which show that the p_T spectra alone are insufficient to tightly constrain the $(\eta/s)_{\text{scale}}$ parameter. Therefore, additional observables, such as anisotropic flow coefficients, are required

to impose further constraints and achieve a more precise determination of this parameter. Despite this, the plot demonstrates a high level of consistency in the other model parameters across different centrality classes, with variations generally staying within one standard deviation.

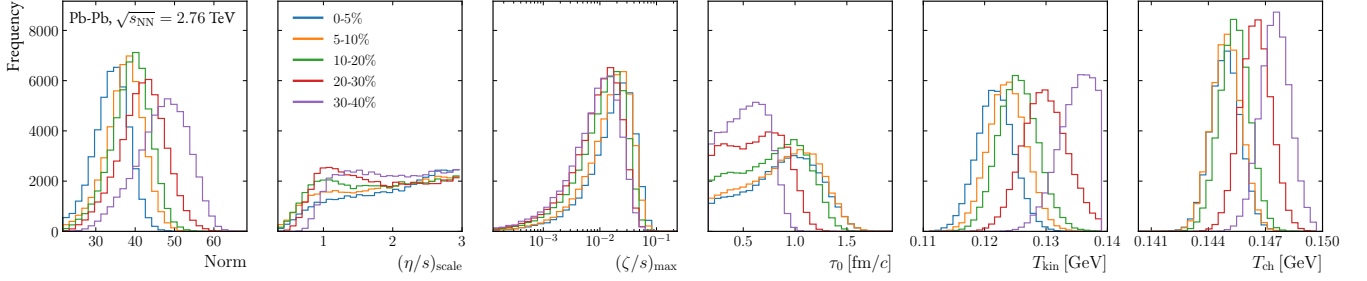


Figure 4.3: Marginal posterior distributions of the model input parameters for the five analyzed centrality classes in Pb-Pb collision at $\sqrt{s_{\text{NN}}} = 2.76$ TeV.

One particularly noteworthy feature is the systematic shift observed in the median value of the kinetic freeze-out temperature, T_{kin} , as centrality decreases. This shift indicates a trend toward more rapid expansion in central collisions, where the particle density is higher, leading to a longer-lived fireball with less pronounced radial pressure gradients. In contrast, more peripheral collisions, which have lower particle densities, are associated with a fireball that expands more quickly but has a shorter lifespan and stronger radial pressure gradients. This behavior aligns with findings from previous studies using blast-wave fits [139] and is consistent with theoretical expectations regarding the dynamics of the fireball in peripheral collisions [113].

This study determined that the optimal p_{T} range for the pion p_{T} spectra is $0.5 < p_{\text{T}}^{\pi} < 2.0$ GeV/ c . Consequently, the interval required to quantify the low- p_{T} pion excess is defined as $0.1 < p_{\text{T}}^{\pi} < 0.5$ GeV/ c for the LHC and $0.2 < p_{\text{T}}^{\pi} < 0.5$ GeV/ c for RHIC.

4.2 PION EXCESS IN THE LOW TRANSVERSE MOMENTUM REGIME

In this section, we will analyze the low- p_{T} pion excess by utilizing the maximum a posteriori (MAP) estimates. The MAP estimate refers to the set of model parameters that corresponds to the mode of the posterior distribution, representing the point in parameter space with the highest posterior probability. This approach is particularly useful in parameter estimation, as it provides the parameters that best fit the experimental data. Given that uniform priors are employed in our Bayesian inference framework, the MAP values are equivalent to the parameters that maximize the likelihood function.

To determine the MAP values, we used numerical optimization algorithms to minimize the negative logarithmic posterior distribution using the SciPy package [140]. This approach aligns with the methodology detailed in reference [82].

In Figure 4.4, the data-to-model ratios for pions, kaons, and protons are presented for MAP estimates. The figure is organized with rows corresponding to each particle type and columns to each collision system. The bands represent the combined statistical and systematic experimental uncertainties, summed in quadrature. The model calculations produce nearly flat data-to-model ratios, consistent with unity within

4 Quantification of the pion excess in the low transverse momentum regime in heavy-ion collisions

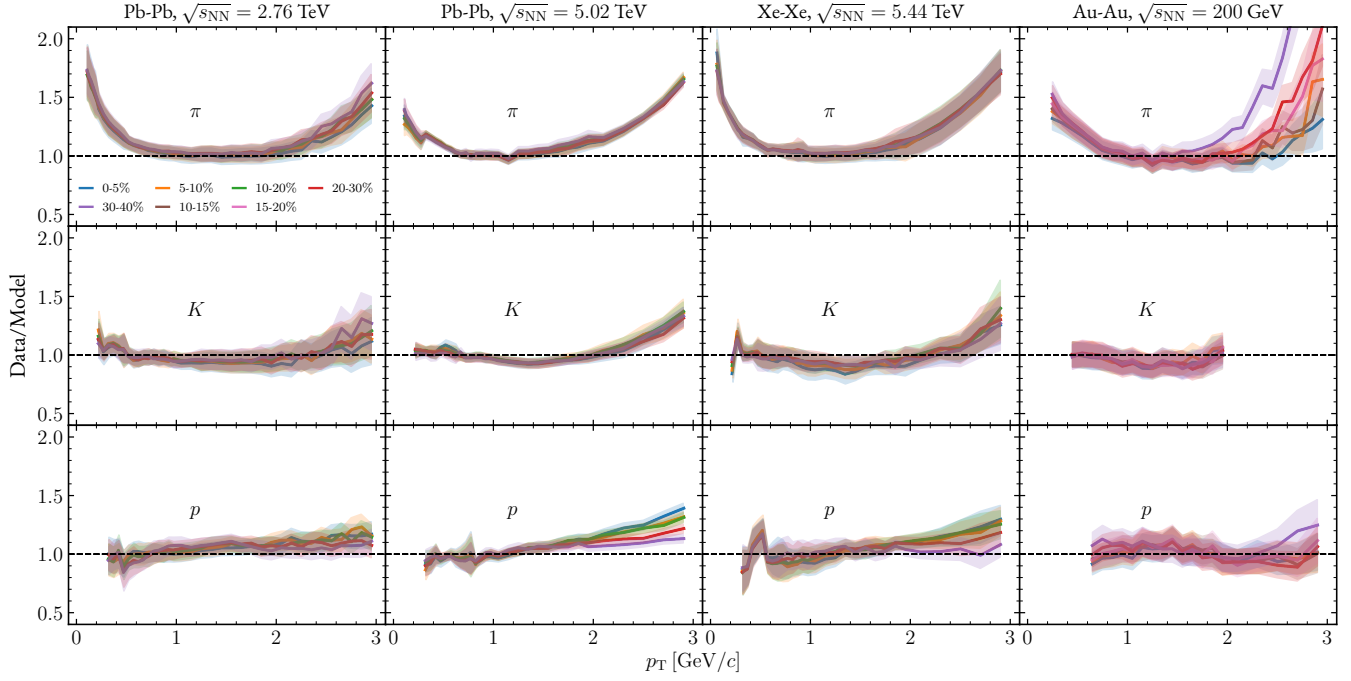


Figure 4.4: Comparison of differential yields for pions (π), kaons (K), and protons (p) with model spectra across 0 – 40% centrality classes in various collision systems: Pb–Pb at $\sqrt{s_{\text{NN}}} = 2.76$ TeV [113], Pb–Pb at $\sqrt{s_{\text{NN}}} = 5.02$ TeV [114], Xe–Xe at $\sqrt{s_{\text{NN}}} = 5.44$ TeV [115], and Au–Au at $\sqrt{s_{\text{NN}}} = 200$ GeV [117]. Each row corresponds to a different particle species, while each column represents one of the four collision systems under study. Within each panel, the ratios are divided by centrality classes ranging from 0 – 40%. The shaded bands indicate the statistical and systematic uncertainties of the experimental data combined in quadrature.

one standard deviation across the fitted p_{T} range for pions, kaons, and protons. This consistency is observed across all centrality intervals and collision systems within the ranges used in the Bayesian analysis. However, outside of the fitted p_{T} range, deviations in the data-to-model ratios are observed.

The model calculations for all hadrons begin to deviate from experimental measurements after $p_{\text{T}} > 2.0$ GeV/ c . This suggests that the higher p_{T} domain may not be predominantly governed by soft processes, which are typically described by fluid dynamic calculations. The observed deviations are more significant for pions compared to heavier particles, such as protons, supporting the idea that hadrons originate from a fluid with a unified velocity field. According to Equation 1.10, the transverse momentum distribution is influenced by both the thermal motion at freeze-out and the radial flow of the system, with T_{slope} incorporating the particle mass m_i . Since the radial flow velocity $\langle v_{\perp} \rangle$ is the same for all particles, heavier particles like protons receive a greater momentum boost compared to lighter particles like pions, pushing protons to higher p_{T} values. This effect causes the proton p_{T} spectrum to extend to higher values, whereas the pion spectrum, due to the pions' smaller mass, peaks at lower p_{T} . The early thermal freeze-out of pions, which have a smaller mass and are more susceptible to dissipative effects, further limits their contribution to higher p_{T} , while the thermal production of heavier hadrons like protons continues at higher p_{T} . This dynamic interplay between mass, radial flow, and thermal freeze-out explains the more pronounced deviation of pions

from the model calculations and supports the concept of a unified velocity field driving the hadronization process.

In the low- p_T range ($p_T < 0.5$ GeV/ c), the data-to-model ratios for pions exceed unity across all centrality classes and collision systems, in contrast to kaons and protons. This indicates a systematic excess of pion production in the experimental measurements compared to fluid dynamic production. Even when the low- p_T pion spectra are included in the Bayesian inference, the model fails to accurately describe the data in this interval as discussed in the previous section.

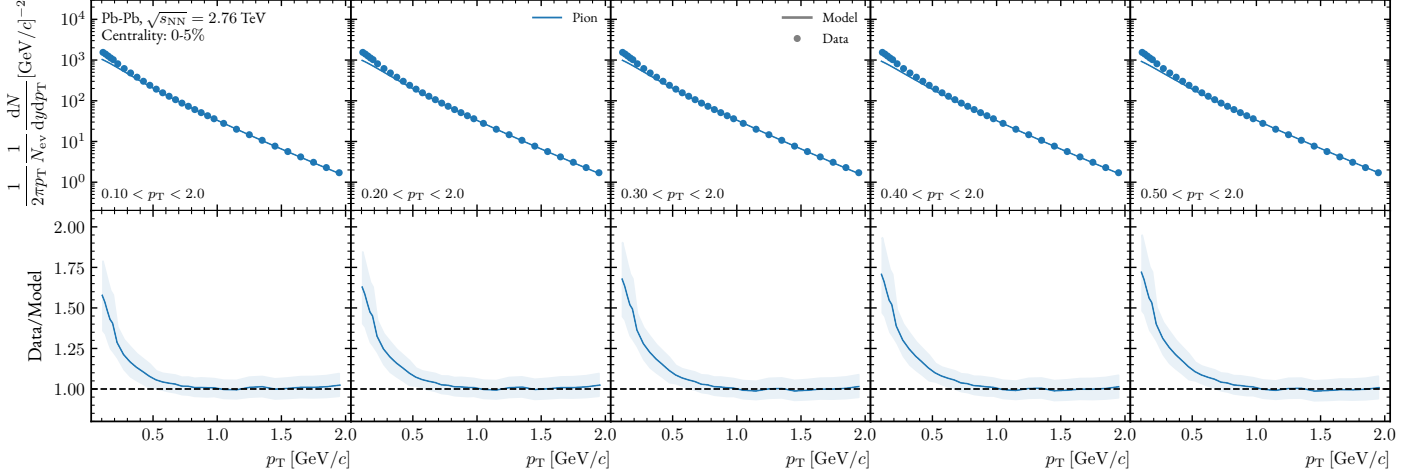


Figure 4.5: Comparison of p_T spectra for pions in Pb–Pb collisions at $\sqrt{s_{\text{NN}}} = 2.76$ TeV for the 0-5% centrality class across different p_T fitting intervals. The upper panel shows the model predictions versus experimental data, while the lower panel displays the data-to-model ratios with combined statistical and systematic uncertainties of the experimental data, summed in quadrature.

Figure 4.5 illustrates the pion excess in Pb–Pb collisions at $\sqrt{s_{\text{NN}}} = 2.76$ TeV for the 0-5% centrality class across five different p_T fitting intervals. The model calculations for pions begin to deviate significantly from experimental measurements for $p_T > 2.0$ GeV/ c , so only the $0.1 < p_T < 2.0$ GeV/ c range is shown in the figure to emphasize the low- p_T region. From left to right, the lower bound of the p_T^π range is progressively narrowed from 0.1 to 0.5 GeV/ c . The upper panel compares the model predictions against the experimental data, while the lower panel displays the data-to-model ratios. The lower panel also includes an uncertainty band that reflects the combined statistical and systematic uncertainties of the experimental data, summed in quadrature. Given that the pion excess in the low- p_T regime is similar across all collision systems, Pb–Pb collisions at $\sqrt{s_{\text{NN}}} = 2.76$ TeV serve as a representative example.

From the figure, it can be observed that the inclusion of low- p_T pion spectra in the Bayesian inference reduces the data-to-model ratio in the $p_T < 0.5$ GeV/ c range by approximately 15%. Despite this reduction, significant deviations up to 75% from unity remain, indicating that the model fails to accurately describe the data in the low- p_T interval.

Figure 4.6 presents the pion excess for the four collision systems as a function of centrality. The excess is calculated by subtracting the integral of the pion spectra computed within our framework from the integral of the experimentally measured pion spectra, both within the interval $p_T < 0.5$ GeV/ c . Notably, the excess is computed using different p_T intervals for the LHC and RHIC: at the LHC (left panel), pion spectra are

4 Quantification of the pion excess in the low transverse momentum regime in heavy-ion collisions

measured down to $p_T = 0.1$ GeV/ c , while at RHIC (right panel), measurements extend down to $p_T = 0.2$ GeV/ c .

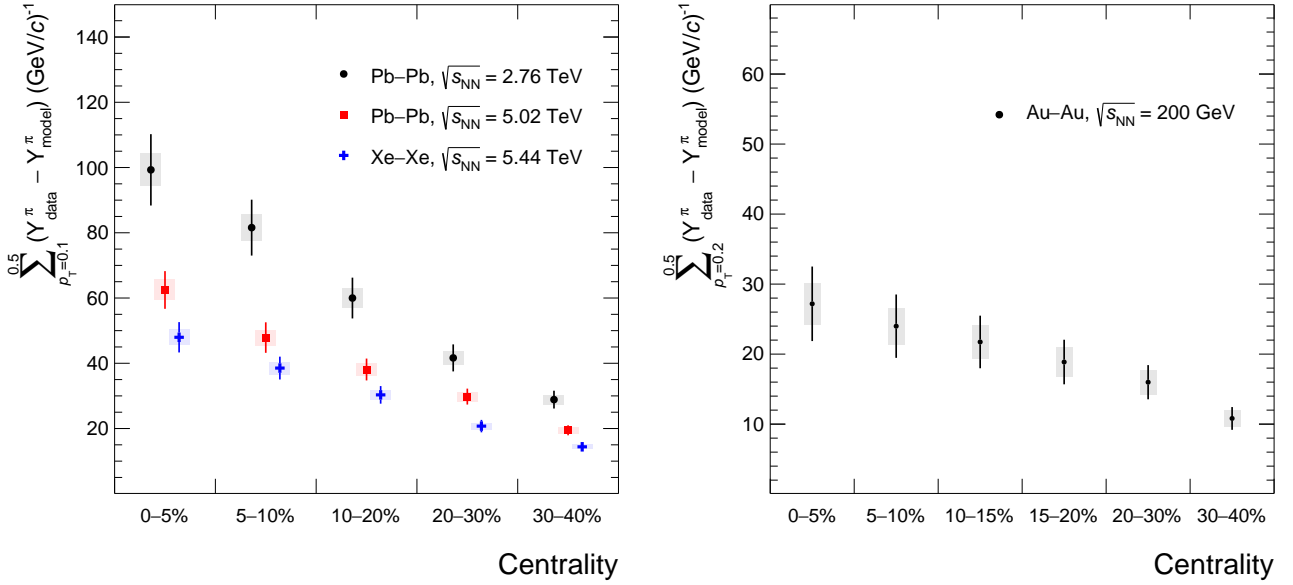


Figure 4.6: The integrated pion excess as a function of the centrality class in the three collision systems at the LHC (left panel) and at the RHIC (right panel). The bars represent the experimental uncertainties propagated as fully uncorrelated across p_T .

The error bars depict the total experimental uncertainties, which are summed in quadrature. Both systematic and statistical uncertainties are propagated as fully uncorrelated across the p_T intervals. The shaded bands represent the model uncertainties, reflecting the spread in the posterior samples. These bands account for different sources of model and experimental uncertainty, as well as any tension in the optimal fit parameters. Further details about model uncertainties will be discussed in [Chapter 5](#). In [Figure 4.4](#), it is demonstrated that the best set of model parameters describes the data with reasonable accuracy within the p_T fitting range. The ratios of the p_T spectra for pions, kaons, and protons to the model predictions remain close to unity, with deviations up to 20% across all centrality classes. Therefore, the model uncertainties should primarily originate from the neural network emulator. The uncertainty in the posterior distribution could be reduced by running the calibration with more design points and a narrower range of parameter values, increasing the density of training points to minimize interpolation uncertainty.

In our analysis, the significance of the excess (the ratio of the difference between the experimental data and the model prediction to the experimental uncertainty) is above 5, with values ranging from 9.3 to 11.1 across all centrality classes and collision systems. This measure provides a statistical indication of how many standard deviations the data deviates from the model, helping to assess the reliability and accuracy of the model predictions. Additionally, a decreasing trend in the excess from central to peripheral collisions is observed for all collision systems.

In [Figure 4.7](#), the relative excess of pions is shown as a function of centrality for different collision systems. The left panel represents the LHC data with the pion spectra integrated over the range $0.1 < p_T < 2.0$ GeV/ c , while the right panel corresponds to RHIC data, where the pion spectra are integrated over

$0.2 < p_T < 2.0 \text{ GeV}/c$. The relative excess is calculated by normalizing the excess pion yield in the range $0.1 < p_T < 0.5 \text{ GeV}/c$ for the LHC (and $0.2 < p_T < 0.5 \text{ GeV}/c$ for RHIC) to the total pion yield in the broader interval $0.1 < p_T < 2.0 \text{ GeV}/c$ (or $0.2 < p_T < 2.0 \text{ GeV}/c$ for RHIC).

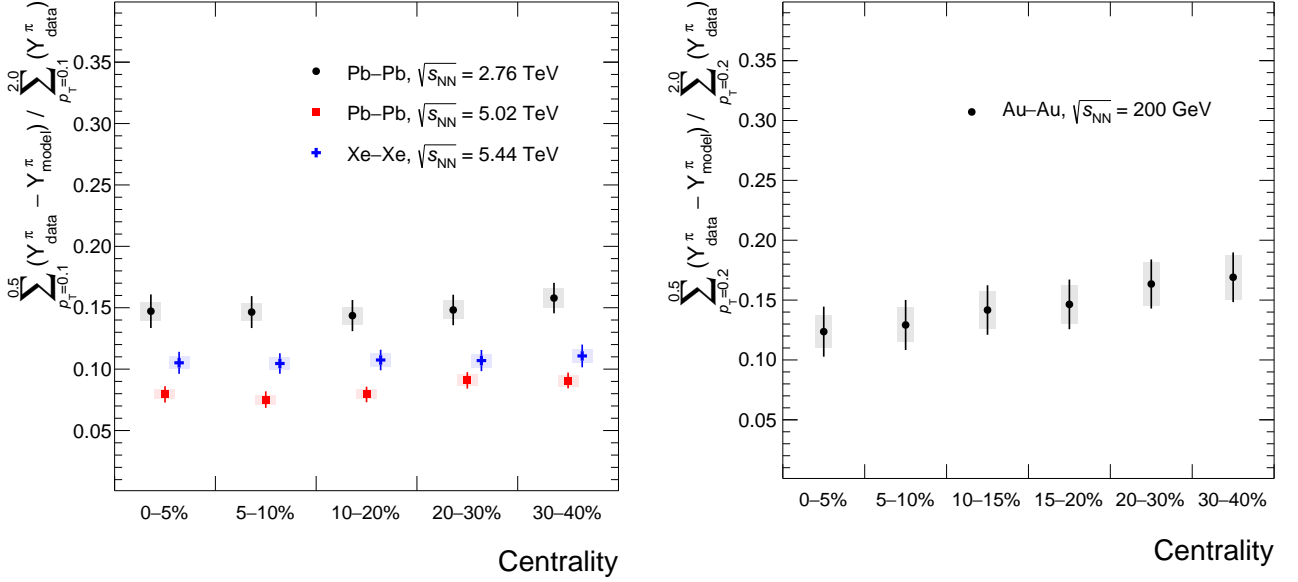


Figure 4.7: Relative excess of pions in the range $0.1 < p_T < 0.5 \text{ GeV}/c$, normalized to the integrated pion yields over $0.1 < p_T < 2.0 \text{ GeV}/c$ for various centrality classes at the LHC (left panel). A similar normalization against pion yields over $0.2 < p_T < 2.0 \text{ GeV}/c$ is presented as a function of centrality classes at the RHIC (right panel). The bars represent the experimental uncertainties propagated as fully uncorrelated across p_T .

While the initial analysis of the model calculations and experimental data assumes uncorrelated uncertainties, a different situation arises when calculating the relative excess. This relative excess is determined by taking the ratio of two related quantities: the excess yield and the integrated pion yield. Although the uncertainties were treated as uncorrelated in the primary analysis, the relationship between these two yields introduces a natural correlation when their ratio is considered. This correlation emerges because both the excess yield and the integrated yield are derived from the same experimental data and are influenced by similar systematic uncertainties. Consequently, when calculating their ratio, these shared uncertainties partially cancel out.

The relative excess exhibits a consistent trend across different centrality classes in all collision systems, with values ranging from 10% to 20%. This suggests that fluid dynamic calculations account for approximately 80% to 90% of the total pion production in heavy-ion collisions, implying that the remaining excess, particularly in the low- p_T region, may originate from additional physical mechanisms. Thus, accurately quantifying the low- p_T pion excess is essential for refining theoretical models of heavy-ion collisions and could offer deeper insights into the underlying processes that contribute to this discrepancy.

Comparing the same centrality class in Pb-Pb collisions at $\sqrt{s_{NN}} = 2.76 \text{ TeV}$ and $\sqrt{s_{NN}} = 5.02 \text{ TeV}$, there is an indication that the integrated excess is lower in Pb-Pb at $\sqrt{s_{NN}} = 5.02 \text{ TeV}$. Given that the excess is normalized, one would typically expect the normalized pion excess to be similar across different collision

energies, especially in comparable centrality classes. The substantial difference observed between the two energies, therefore, raises questions.

Upon closer examination, a significant discrepancy is evident in the low- p_T region of the pion spectra between the two energy scales. As shown in Figure 4.8, for $p_T < 0.3$ GeV/ c , the pion spectra at $\sqrt{s_{NN}} = 5.02$ TeV exhibit noticeable discrepancies compared to those at $\sqrt{s_{NN}} = 2.76$ TeV. This observation is particularly surprising because one would generally expect the higher energy collision at $\sqrt{s_{NN}} = 5.02$ TeV to produce more pions across the p_T spectrum due to the increased energy density and overall particle production. The fact that the pion yields are lower at $\sqrt{s_{NN}} = 5.02$ TeV is counterintuitive and suggests that there may be underlying issues with the experimental data in this low- p_T region. These unexpected discrepancies highlight the need for careful scrutiny of the data.

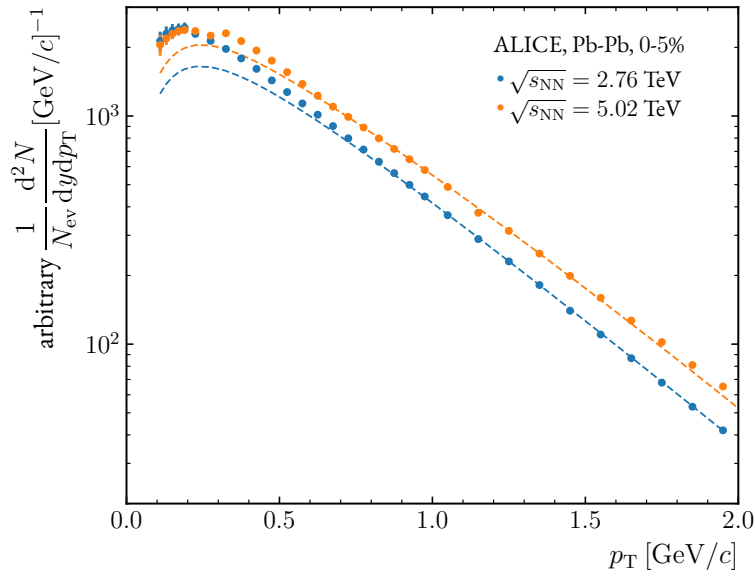


Figure 4.8: Comparison of the pion p_T spectra between Pb–Pb collisions at $\sqrt{s_{NN}} = 2.76$ TeV [113] (blue) and $\sqrt{s_{NN}} = 5.02$ TeV [114] (orange). The dashed lines represent model predictions for pion p_T spectra, while the data points correspond to the experimental measurements. The observed discrepancy in the low- p_T region ($p_T < 0.2$ GeV/ c) between the two energy scales, where the 5.02 TeV data show lower values than the 2.76 TeV data, is particularly notable and suggests potential issues in the experimental data or its interpretation.

This unusual trend in the low- p_T region could be due to several issues within the experimental data. There may be differences in systematic uncertainties between the two datasets, particularly in how low- p_T pions are reconstructed and corrected. Such discrepancies can lead to biases that affect the lowest p_T bins.

Finally, a thorough examination of the experimental procedures, with a focus on the estimation of systematic uncertainties and the application of corrections, is essential to fully understand and resolve these discrepancies.

5 MAPPING PROPERTIES OF THE QGP

The objective of this chapter is to investigate the model parameters related to the evolution of heavy-ion collisions, such as the initialization time and kinetic freeze-out temperature, along with key transport coefficients of the QGP, specifically the shear and bulk viscosity to entropy density ratios. To achieve this, we will conduct a Bayesian parameter estimation using p_T -differential spectra and p_T -differential flow harmonics ($v_n(p_T)$) of pions, kaons, and protons produced in Pb-Pb collisions at $\sqrt{s_{NN}} = 2.76$ TeV and 5.02 TeV, as well as Xe-Xe collisions at $\sqrt{s_{NN}} = 5.44$ TeV, across centrality classes of 0-5%, 5-10%, 10-20%, 20-30%, and 30-40%. In the predecessor of this work, Bayesian inference was employed to determine the key parameters of the QGP evolution and its properties [122]. However, even though the analysis was performed using three collision systems, it was limited to a single observable: p_T spectra. The results demonstrated that the scale value of temperature-dependent shear viscosity to entropy density ratio and correspondingly minimum value, $(\eta/s)_{\min}$, was not constrained by the p_T spectra alone. Therefore, these findings indicated that the inclusion of additional observables, such as flow coefficients, is necessary to possibly constrain the transport coefficients of the QGP. The current study aims to build on the previous work by including flow coefficients $v_2(p_T)$, $v_3(p_T)$, and $v_4(p_T)$, into the Bayesian analysis. Including these observables is expected to lead to a more robust estimation of the model parameters.

5.1 ANALYSIS OF INDIVIDUAL COLLISION SYSTEMS

In this section, separate Bayesian analyses of Pb-Pb collisions at $\sqrt{s_{NN}} = 2.76$ TeV and 5.02 TeV, as well as Xe-Xe collisions at $\sqrt{s_{NN}} = 5.44$ TeV, will be presented. Each system will be analyzed individually to examine the model parameters and transport coefficients of the QGP. The subsequent section will discuss the global fit, which integrates data from all three collision systems to provide a comprehensive analysis.

5.1.1 EXPERIMENTAL DATA

[Table 5.1](#) summarizes the experimental data sets used for Bayesian inference analyses in this chapter. This includes details of the collision systems, observables, particle species, and centrality classes. The p_T spectra are presented in the differential form of $\frac{1}{N_{ev}} \frac{1}{2\pi p_T} \frac{d^2N}{dp_T dy}$, where N_{ev} is the number of events in a centrality bin. Throughout this chapter, the term " p_T spectra" is used as a shorthand for " p_T -differential spectra" to improve readability. Experimental data for low p_T pions (with $p_T < 0.5$ GeV/ c) are excluded from the fits, based on findings from [Chapter 4](#), which indicated that current fluid dynamic models significantly underestimate the yields of low p_T pions. Additionally, the upper p_T limit for the experimental data used in this analysis is set to 2 GeV/ c for all observables.

Table 5.1: Details of experimental data sets used for Bayesian parameter estimation in this chapter, including collision systems, observables, particle species, and centrality classes.

Collision system	Observables	Particles	Centrality classes	Ref.
Pb–Pb, $\sqrt{s_{\text{NN}}} = 2.76$ TeV	p_{T} -differential spectra	π^+, K^+, p	0-5, 5-10, 10-20, 20-30, 30-40	[113]
	$v_2(p_{\text{T}})$	π^+, K^+, p	0-5, 5-10, 10-20, 20-30, 30-40	[141]
	$v_3(p_{\text{T}}), v_4(p_{\text{T}})$	π^+, K^+, p	0-5, 5-10, 10-20, 20-30, 30-40	[142]
Pb–Pb, $\sqrt{s_{\text{NN}}} = 5.02$ TeV	p_{T} -differential spectra	π^+, K^+, p	0-5, 5-10, 10-20, 20-30, 30-40	[114]
	$v_2(p_{\text{T}})$	π^+, K^+, p	0-5, 5-10, 10-20, 20-30, 30-40	[143]
Xe–Xe, $\sqrt{s_{\text{NN}}} = 5.44$ TeV	p_{T} -differential spectra	π^+, K^+, p	0-5, 5-10, 10-20, 20-30, 30-40	[115]
	$v_2(p_{\text{T}})$	π^+, K^+, p	0-5, 5-10, 10-20, 20-30, 30-40	[144]

5.1.2 PARAMETER INTERVALS, INITIAL CONDITIONS, AND PARTIAL CHEMICAL EQUILIBRIUM

As discussed earlier, our framework employs partial chemical equilibrium (PCE), which introduces two distinct freeze-out temperatures in the calculation of final hadron spectra. However, the application of PCE in the calculation of flow coefficients is currently not feasible due to the absence of specific system files, referred to as "kernels." Kernels are specific functions that encapsulate the precomputed integrations, specifically the azimuthal and rapidity integrations, over the freeze-out hypersurface. These functions are essential for calculating the final particle spectra, as they store dependencies on fluid fields and mean p_{T} . By precomputing these integrations, the kernels facilitate efficient and consistent evaluations of the spectra across different fluid evolutions and freeze-out conditions. This approach significantly reduces computational complexity, ensuring accurate results without the need to repeatedly perform full integrations for each scenario [58].

In the results presented throughout this thesis, as well as in the work of our group, the p_{T} spectra correspond to the background spectra without the inclusion of perturbation effects in Equation 2.56. Consequently, we have only required PCE kernels for the background spectra, and the absence of PCE-specific kernels for the perturbation spectra has not been an issue so far. However, the calculation of flow coefficients depends on the perturbation spectra, as shown in Equation 2.75. Since the necessary kernels are not available for the perturbation spectra, we are unable to apply PCE in the calculation of flow coefficients. In Equation 2.75, both background and perturbation spectra are involved, and they must be treated consistently, either with PCE or without PCE, to ensure accurate results.

Currently, the perturbation kernels are computed using only a single freeze-out temperature. Therefore, the analyses in this chapter are conducted using a single kinetic freeze-out temperature, $T_{\text{fo}} = T_{\text{ch}} = T_{\text{kin}}$. Consequently, the parameter intervals used in this study are designed to accommodate this constraint, as summarized in Table 5.2. The range for T_{kin} is chosen to include the ranges of both kinetic and chemical freeze-out temperatures. The other parameter ranges are determined as discussed in Chapter 4.

To demonstrate the influence of PCE, we compare the maximum a posteriori (MAP) estimates of the p_{T} spectra with and without PCE. Figure 5.1 illustrates the impact of PCE on the p_{T} spectra for pions, kaons, and protons in Pb–Pb collisions at $\sqrt{s_{\text{NN}}} = 2.76$ TeV across various centrality classes (0-5%, 5-10%, 10-

Table 5.2: Defined intervals for the five model parameters across the three collision systems. Norm and τ_0 are recognized as system-dependent parameters.

	$(\eta/s)_{\text{scale}}$	$(\zeta/s)_{\text{max}}$	T_{kin} (GeV)	Norm	τ_0 (fm/c)
Pb-Pb, $\sqrt{s_{\text{NN}}} = 2.76$ TeV	0.31–3.0	10^{-4} –0.3	0.110–0.155	5–80	0.01–3.0
Pb-Pb, $\sqrt{s_{\text{NN}}} = 5.02$ TeV				80–140	2.0–7.0
Xe-Xe, $\sqrt{s_{\text{NN}}} = 5.44$ TeV				70–150	2.0–7.0

20%, 20-30%, and 30-40%). The plot compares the model predictions with PCE (dashed lines) and without PCE (solid lines) against the experimental data. The data-to-model ratio panels include an uncertainty band that accounts for the statistical and systematic uncertainties of the experimental data, which are summed in quadrature and treated as uncorrelated, as detailed in Chapter 4. It is important to highlight that this figure differs from those presented in Chapter 4 by incorporating five centrality classes in the inference process rather than a single centrality class.

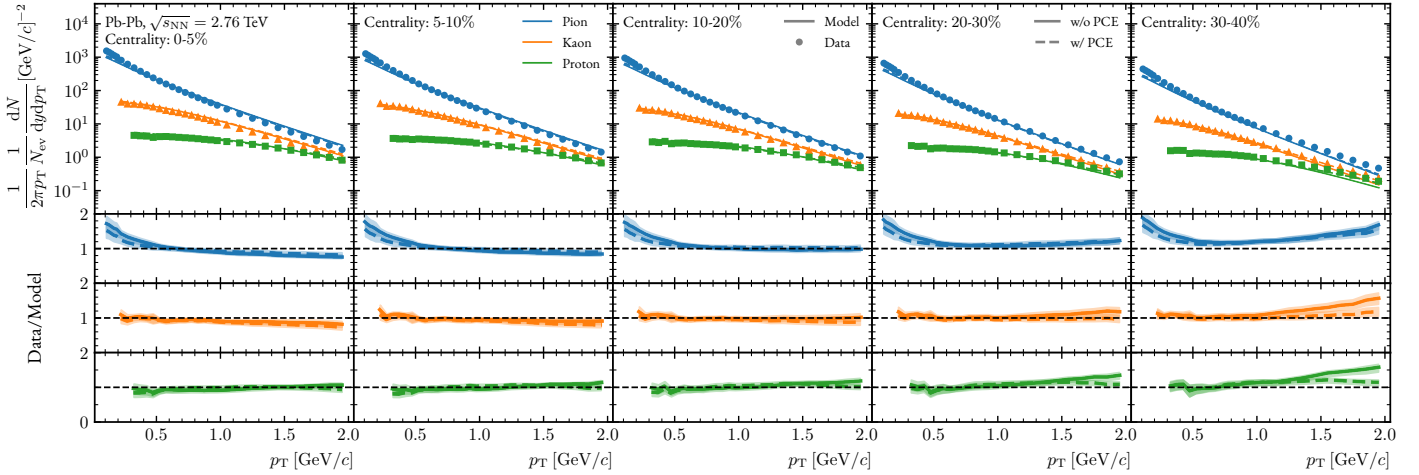


Figure 5.1: Comparison of p_T spectra from the model with partial chemical equilibrium (PCE) (dashed lines) and without PCE (solid lines) to the experimental data for pions, kaons, and protons in Pb-Pb collisions at $\sqrt{s_{\text{NN}}} = 2.76$ TeV across various centrality classes (0-5%, 5-10%, 10-20%, 20-30%, and 30-40%).

For pions, no significant differences are observed in the fitting interval; however, in the low- p_T regime ($p_T < 0.5$ GeV/c), the deviation from the experimental data is reduced when PCE is included. For the most peripheral centralities, PCE significantly enhances the model's ability to describe the high- p_T spectra for protons and kaons. These observations underscore the importance of PCE, which effectively accounts for the hadron rescattering contribution during the hadron gas phase. Although the chemical composition is fixed at chemical freeze-out, ongoing elastic scatterings under PCE continue to modify the kinetic distributions of the particles, which is crucial for accurately capturing the influence of radial flow, particularly on heavier particles such as protons. Consequently, it is important to note that the absence of PCE in our model is expected to affect our analysis, potentially leading to a less accurate description of the experimental data presented in this chapter.

Lastly, the initial condition parameters used in this chapter are the same as those listed in Section 4.1.

5.1.3 ALL RESULTS IN A TABULAR FORM

To provide a comprehensive overview of the results from our various fits, which will be discussed in the following sections, we present a summary of the posterior distributions for all collision systems and fit scenarios in [Table 5.3](#).

Table 5.3: Summary of posterior distributions. For each parameter, mean, median, MAP value, and credible interval uncertainties are given.

	Parameter	Mean	Median	MAP	68% Uncertainty	95% Uncertainty	99% Uncertainty
p_T spec. only	Norm	55.8753	55.9633	56.0081	+1.6131 / -1.7623	+3.3021 / -3.3966	+4.2357 / -4.4496
	$(\eta/s)_{\text{scale}}$	0.3286	0.3223	0.3224	+0.0218 / -0.0092	+0.0611 / -0.0119	+0.1009 / -0.0122
	$(\zeta/s)_{\text{max}}$	0.0012	0.0009	0.0008	+0.0013 / -0.0006	+0.0034 / -0.0008	+0.0049 / -0.0008
	τ_0 [fm/c]	0.2080	0.2067	0.2075	+0.0242 / -0.0227	+0.0565 / -0.0411	+0.0765 / -0.0513
	T_{kin} [GeV]	0.1455	0.1455	0.1455	+0.0003 / -0.0003	+0.0005 / -0.0006	+0.0007 / -0.0008
Pb-Pb, 2.76 TeV	Norm	66.9524	67.0120	67.0258	+0.6090 / -0.6191	+1.2025 / -1.2414	+1.5363 / -1.6991
	$(\eta/s)_{\text{scale}}$	0.8369	0.8370	0.8369	+0.0065 / -0.0065	+0.0129 / -0.0128	+0.0168 / -0.0175
	$(\zeta/s)_{\text{max}}$	0.0007	0.0005	0.0004	+0.0008 / -0.0003	+0.0019 / -0.0004	+0.0032 / -0.0005
	τ_0 [fm/c]	0.7052	0.7058	0.7063	+0.0256 / -0.0255	+0.0513 / -0.0496	+0.0673 / -0.0657
	T_{kin} [GeV]	0.1446	0.1446	0.1446	+0.0002 / -0.0002	+0.0005 / -0.0004	+0.0006 / -0.0006
p_T spec. + v_n	Norm	52.9870	52.9891	52.9717	+1.4373 / -1.5318	+2.7643 / -3.1460	+3.6904 / -4.3296
	$(\eta/s)_{\text{scale}}$	0.6953	0.6956	0.6957	+0.0046 / -0.0046	+0.0091 / -0.0091	+0.0124 / -0.0126
	$(\zeta/s)_{\text{max}}$	0.0647	0.0647	0.0647	+0.0031 / -0.0032	+0.0063 / -0.0063	+0.0084 / -0.0084
	τ_0 [fm/c]	0.2794	0.2799	0.2791	+0.0245 / -0.0244	+0.0480 / -0.0486	+0.0632 / -0.0658
	T_{kin} [GeV]	0.1413	0.1413	0.1412	+0.0002 / -0.0002	+0.0004 / -0.0004	+0.0006 / -0.0005
Pb-Pb, 5.02 TeV	Norm	189.8632	189.0113	189.0451	+0.5970 / -0.5860	+1.2990 / -1.1876	+93.3501 / -1.6349
	$(\eta/s)_{\text{scale}}$	0.6334	0.6256	0.6253	+0.0071 / -0.0070	+0.0148 / -0.0143	+0.4877 / -0.2175
	$(\zeta/s)_{\text{max}}$	0.0030	0.0004	0.0003	+0.0007 / -0.0003	+0.0022 / -0.0004	+0.1989 / -0.0004
	τ_0 [fm/c]	3.0731	3.1219	3.1245	+0.0507 / -0.0513	+0.1008 / -0.1187	+0.1336 / -3.1101
	T_{kin} [GeV]	0.1437	0.1435	0.1435	+0.0002 / -0.0002	+0.0004 / -0.0003	+0.0108 / -0.0004
Xe-Xe, 5.44 TeV	Norm	162.2513	162.3138	162.1903	+2.2735 / -2.2480	+4.3864 / -4.4391	+5.6870 / -6.0560
	$(\eta/s)_{\text{scale}}$	0.4969	0.4968	0.4966	+0.0084 / -0.0081	+0.0167 / -0.0162	+0.0221 / -0.0208
	$(\zeta/s)_{\text{max}}$	0.0438	0.0439	0.0443	+0.0072 / -0.0076	+0.0137 / -0.0147	+0.0182 / -0.0193
	τ_0 [fm/c]	1.1149	1.1127	1.1087	+0.0820 / -0.0750	+0.1613 / -0.1437	+0.2184 / -0.1915
	T_{kin} [GeV]	0.1470	0.1470	0.1470	+0.0003 / -0.0003	+0.0007 / -0.0007	+0.0009 / -0.0009
Three systems combined	Norm _{2.76}	65.5521	65.5684	65.5772	+0.6375 / -0.6628	+1.2110 / -1.3995	+1.6344 / -2.1327
	Norm _{5.02}	185.7215	185.3688	185.3665	+0.5929 / -0.6182	+1.1784 / -1.2734	+1.7323 / -1.7614
	Norm _{5.44}	176.2690	176.4074	176.3873	+1.1086 / -1.1934	+2.1447 / -2.4753	+2.7737 / -3.9032
	$(\eta/s)_{\text{scale}}$	0.6982	0.6988	0.6988	+0.0043 / -0.0044	+0.0084 / -0.0090	+0.0113 / -0.0131
	$(\zeta/s)_{\text{max}}$	0.0021	0.0010	0.0011	+0.0019 / -0.0008	+0.0054 / -0.0010	+0.0101 / -0.0010
	$\tau_{0,2.76}$ [fm/c]	0.5634	0.5610	0.5662	+0.0207 / -0.0203	+0.0406 / -0.0422	+0.0628 / -0.0586
	$\tau_{0,5.02}$ [fm/c]	2.8524	2.8643	2.8649	+0.0479 / -0.0511	+0.0945 / -0.1071	+0.1238 / -0.1751
	$\tau_{0,5.44}$ [fm/c]	2.0991	2.0998	2.0993	+0.0698 / -0.0724	+0.1358 / -0.1483	+0.1773 / -0.2010
T_{kin} [GeV]	0.1449	0.1449	0.1448	+0.0001 / -0.0001	+0.0003 / -0.0003	+0.0004 / -0.0003	

This table includes the mean, median, MAP value, and credible interval uncertainties for each model parameter. The tabular summary serves as a preview of the detailed analysis presented in the subsequent sections, highlighting the differences and similarities across different collision energies and fit combinations. In our analyses, the proximity of the MAP values to the medians of the posterior distributions indicates that our posterior distributions are relatively symmetric and unimodal, thereby enhancing the reliability of our parameter estimates.

5.1.4 RESULTS FOR Pb-Pb COLLISIONS AT $\sqrt{s_{\text{NN}}} = 2.76$ TeV

PRIORS

Figure 5.2 shows the priors for the 10-20% centrality class in Pb–Pb collisions at $\sqrt{s_{\text{NN}}} = 2.76$ TeV as an example. The rows, from top to bottom, display the p_{T} spectra, $v_2(p_{\text{T}})$, $v_3(p_{\text{T}})$, and $v_4(p_{\text{T}})$ flow coefficients. The columns, from left to right, correspond to pions, kaons, and protons. The solid markers in the plots indicate the experimental data points used in the MCMC procedure, while the open markers represent the full experimental dataset.

The 10-20% centrality class was chosen as an example because FLUIDUM performs better in lower centrality classes due to its mode expansion technique, which decomposes the hydrodynamic fields into a background part and perturbation modes [55]. In heavy-ion collisions, the random positions of the nuclei lead to overlap zones with random orientations. When events are averaged within a single centrality class, the resulting fluid profiles exhibit symmetry under azimuthal rotations, making the background component invariant under these transformations. The background represents the primary features of the system that are symmetric and regular, such as the average geometry of the overlap zone and the bulk collective flow patterns, which are more consistent and less affected by fluctuations in lower centralities. The perturbation modes, on the other hand, capture fluctuations and deviations from this symmetry, which are more challenging to describe accurately in higher centrality classes due to increased irregularities and complex geometries. As a result, while the 0-5% class benefits most from this decomposition due to its highly symmetric profiles, and the 30-40% class is hindered by excessive fluctuations, the 10-20% centrality class provides an optimal balance where both the background and perturbation modes can be objectively represented.

The priors, based on our initial parameter estimates, provide a good description of the p_{T} spectra. Specifically, the experimental data points fall within the model’s predicted range, spanning nearly an order of magnitude in the logarithmic plot, with the data consistently positioned in the middle of the distribution. This suggests that the model captures the underlying physics of particle production reasonably. Furthermore, the v_2 flow coefficients are accurately represented by the model, as the experimental data points, including their uncertainties, are covered by the model’s predictions.

However, the model does not capture the v_3 and v_4 flow coefficients as effectively. For v_3 and v_4 , the experimental data points for pions and kaons are located at the upper edge of the prior distributions. This discrepancy may arise from several factors:

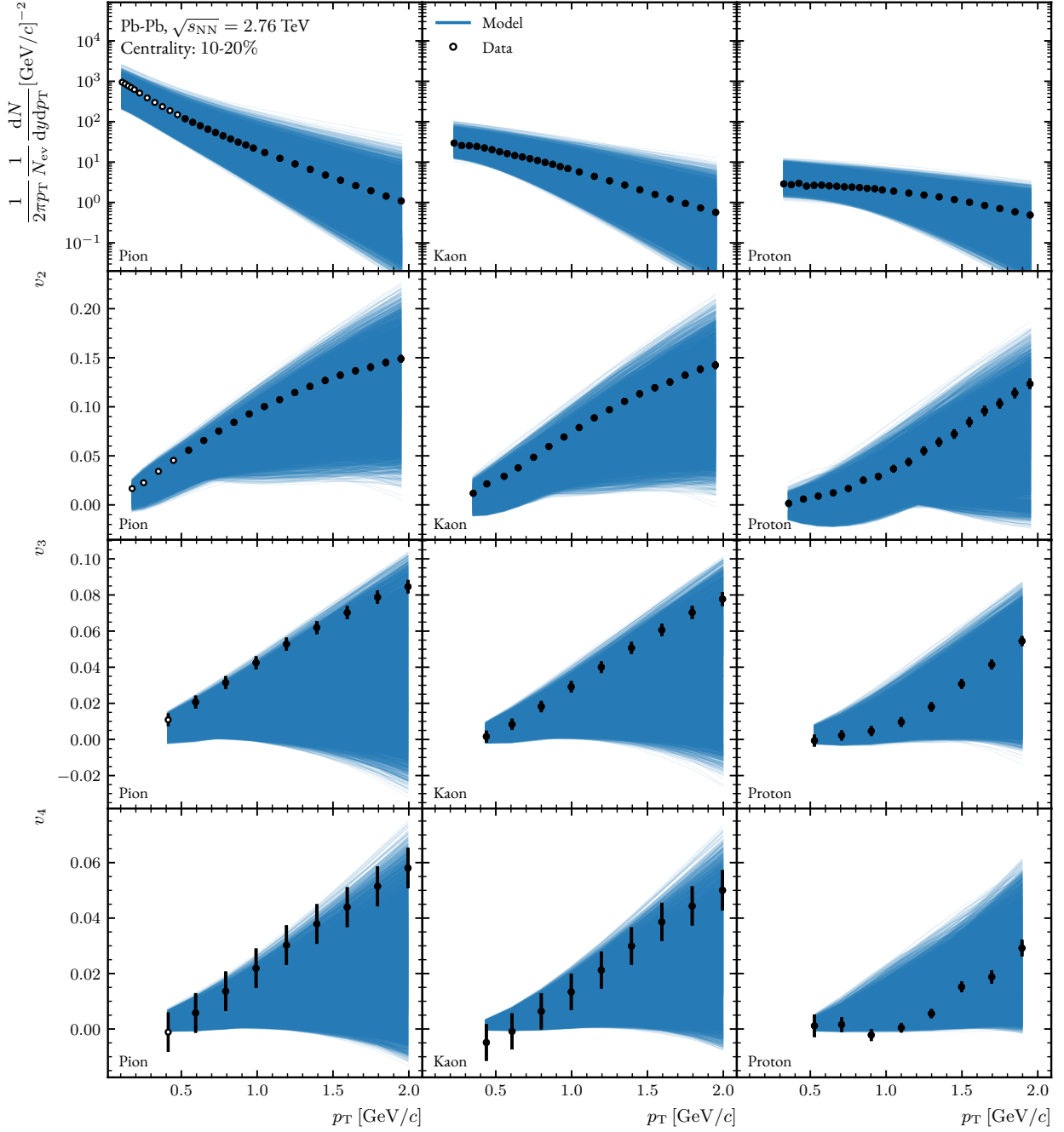


Figure 5.2: Priors, i.e., model outputs, for the 10-20% centrality class, obtained using initial conditions corresponding to Pb–Pb collisions at $\sqrt{s_{NN}} = 2.76$ TeV. These priors represent the initial parameter space used in the Bayesian inference process, serving as a reference for comparing model predictions with experimental data.

1. **Initial state fluctuations** [55, 145]: As discussed in Subsection 2.2.4, FLUIDUM does not fully account for the fluctuations in the initial geometry, affecting its ability to produce triangular and quadrangular flow coefficients. However, it is important to note that the TRENTo parameters were kept fixed during these calculations, which limits the robustness of any conclusions regarding the full capabilities of FLUIDUM in capturing initial state fluctuations.

2. **Missing non-linear interactions** [146, 147]: FLUIDUM treats the QGP evolution primarily as a linear response. However, higher-order flow coefficients (v_3 and v_4) are significantly influenced by mode-couplings between different flow harmonics. This can lead to discrepancies between predicted and observed flow patterns, especially for v_3 and v_4 .
3. **Higher sensitivity to model parameters** [148]: Higher-order flow coefficients exhibit greater sensitivity to specific model parameters, i.e. $(\eta/s)_{\text{scale}}$, compared to lower-order coefficients. Since higher-order flow coefficients are built upon lower-order ones, any approximations in the model's representation of v_2 will propagate and magnify when calculating v_3 , v_4 , and so on.

Additional model calculations were conducted using the same TRENTo parameters but with wider parameter ranges than those listed in Table 5.2. Despite these adjustments, the model still failed to accurately capture the experimental data for the v_3 and v_4 flow coefficients. This persistent discrepancy indicates that the current model parametrization and underlying assumptions may not fully account for the complexities of higher-order flow harmonics. Consequently, further investigations of TRENTo parameters and possible improvements to the FLUIDUM model are necessary to enhance our ability to describe the physics underlying v_3 and v_4 . Addressing these issues and refining the model to better encapsulate the complexities of higher-order flow harmonics will be an important focus for future work.

EMULATOR PERFORMANCE

With the priors established, we proceed to construct the emulator, which serves as a surrogate for the full model during MCMC sampling by efficiently predicting the model outputs for any parameter set within the trained range.

Figure 5.3 presents the emulator's performance in reproducing the model outputs for various observables and centrality classes in Pb–Pb collisions at $\sqrt{s_{\text{NN}}} = 2.76$ TeV. Each subfigure displays a scatter plot comparing the model calculations (y-axis) with the corresponding emulator predictions (x-axis) for different observables related to pions, kaons, and protons. In these plots, each point represents the value of a specific observable for a particle type at a given p_{T} bin. The diagonal line in each plot represents the ideal case where the emulator exactly matches the model, providing a direct visual assessment of the emulator's accuracy in approximating the full model outputs.

The first row of subfigures shows the comparison for the p_{T} spectra across different centrality classes. The emulator accurately reproduces the p_{T} spectra, as indicated by the data points closely following the diagonal line. The performance remains consistent across all centrality classes, from 0-5% to 30-40%.

The second row illustrates the emulator's performance for v_2 . Similar to the p_{T} spectra, the emulator effectively captures the v_2 values, with the data points lying close to the diagonal line. This demonstrates the emulator's capability to represent the elliptic flow dynamics accurately.

Likewise, the third and fourth rows present the emulator's performance for v_3 and v_4 , respectively. The emulator's accuracy is lower compared to the p_{T} spectra and v_2 , with data points deviating from the diagonal line, especially as centrality increases (i.e., moving from more central to more peripheral collisions). This

5 Mapping properties of the QGP

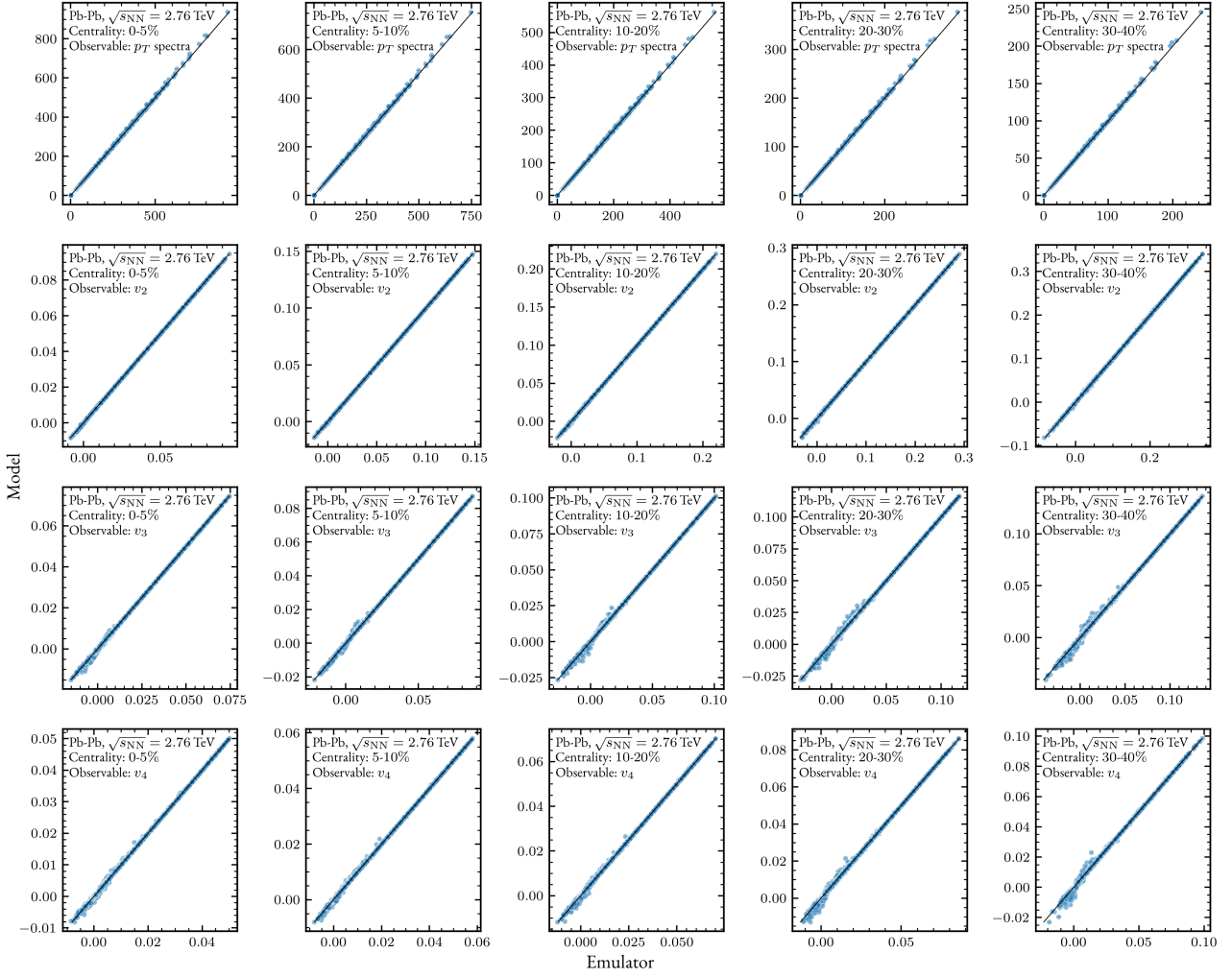


Figure 5.3: Comparison between the model and emulator for various observables and centrality classes in Pb–Pb collisions at $\sqrt{s_{NN}} = 2.76$ TeV. Each subfigure corresponds to a different observable (rows) and centrality class (columns). The diagonal line in each plot represents the ideal agreement between the model and the emulator, where all points would lie exactly on the line. Deviations from this line are expected due to the inherent limitations of the NN emulator, such as the number of training points and the size of the NN ensemble, both of which can affect the emulator’s accuracy and generalization.

deviation may be attributed to the inherent complexities of higher-order flow coefficients. Unlike v_2 , which are primarily influenced by the overall elliptic shape of the overlap region, higher-order coefficients capture finer details of the system’s anisotropies. Consequently, these coefficients are more challenging to model accurately, especially when the emulator is trained on a limited dataset (83% of 20,000 model calculations), potentially leading to less precise representations of these higher-order flow dynamics.

Overall, the emulator demonstrates performance that is close to the ideal case across the majority of observables and centrality classes. This high level of accuracy, particularly for the p_T spectra and v_2 , suggests that the emulator reliably captures the key dynamics of the model. Consequently, we can trust the emulator’s performance and proceed to use it in our MCMC procedure to estimate the posterior probability densities of the model parameters.

POSTERIOR

In this subsection, the posterior probability density functions (PDFs) of the model parameters are presented. Two sets of posteriors will be discussed: one estimated using p_T spectra and $v_2(p_T)$ observables, illustrated in [Figure 5.4](#), and the other using p_T spectra along with $v_2(p_T)$, $v_3(p_T)$, and $v_4(p_T)$ observables, illustrated in [Figure 5.5](#). The posterior plots throughout this thesis are generated using the CORNER package [149].

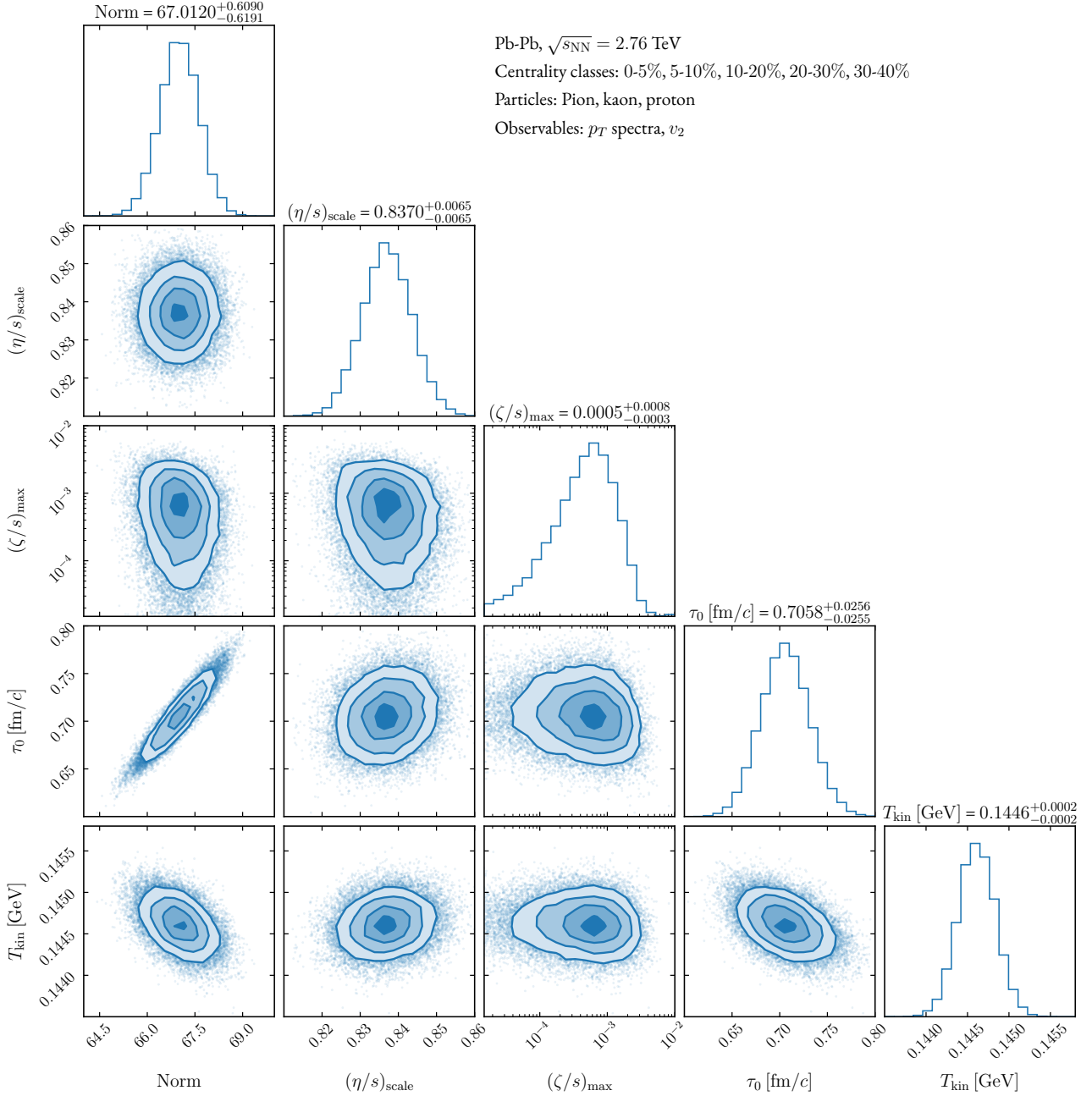


Figure 5.4: Marginal and joint posterior probability density functions (PDFs) for model parameters in Pb–Pb collisions at $\sqrt{s_{NN}} = 2.76$ TeV obtained using p_T spectra and $v_2(p_T)$ observables in the Bayesian estimation.

The corner plots in [Figure 5.4](#) and [Figure 5.5](#) provide comprehensive visualizations of the marginal and joint posterior distributions, highlighting the inferred parameter values, their uncertainties, and the correlations between them. Each diagonal panel represents the marginal distribution for a single model parameter,

5 Mapping properties of the QGP

obtained by integrating the posterior distribution over all other parameters. The values above each diagonal panel indicate both the median and the 68% highest posterior density interval (HPDI), also known as the credible interval. The HPDI, being the narrowest interval containing 68% of the posterior density,

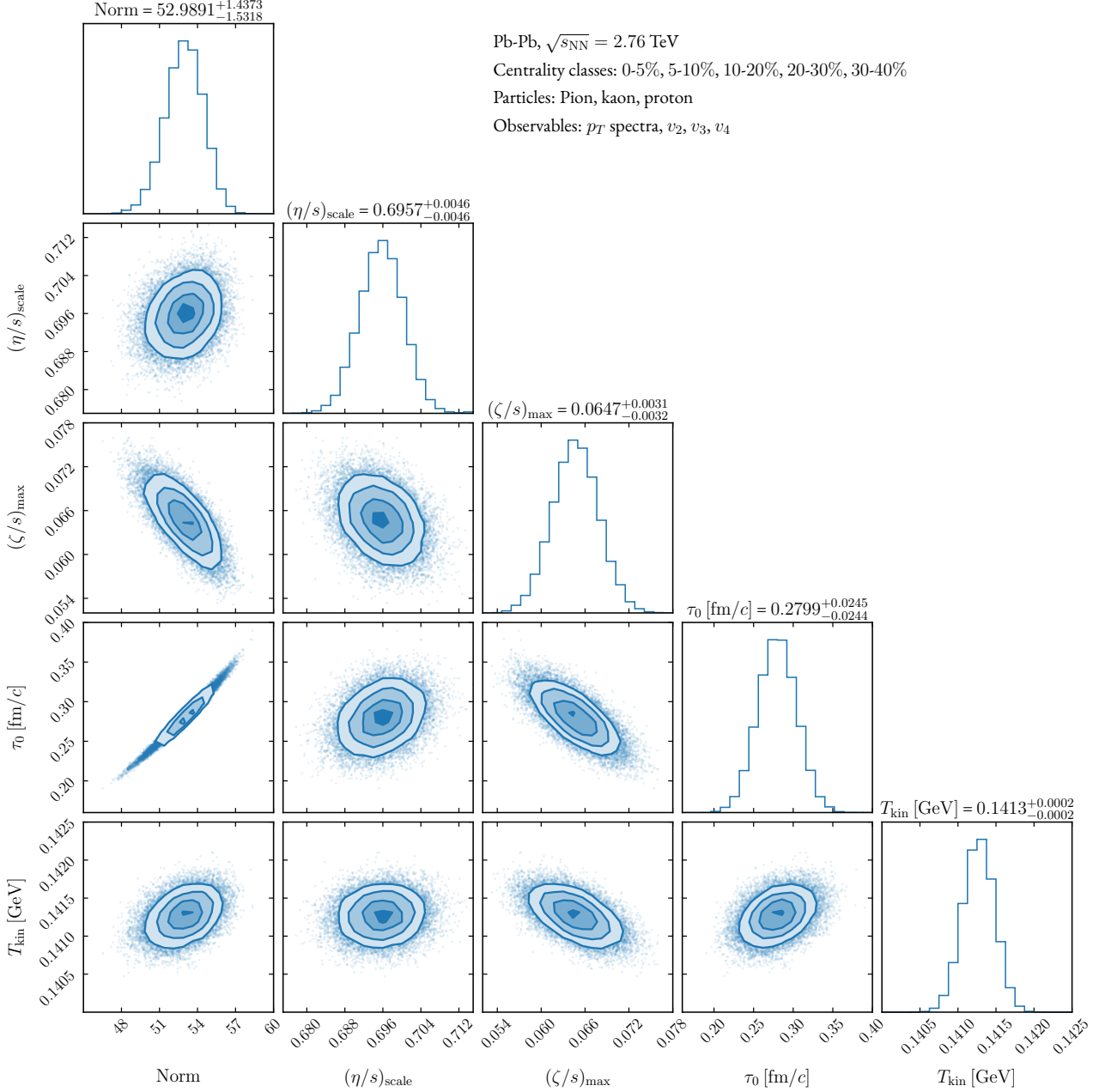


Figure 5.5: Marginal and joint posterior probability density functions (PDFs) for model parameters in Pb–Pb collisions at $\sqrt{s_{NN}} = 2.76$ TeV obtained using p_T spectra, $v_2(p_T)$, $v_3(p_T)$, and $v_4(p_T)$ observables in the Bayesian estimation.

implies that the true parameter value is expected to lie within this interval 68% of the time. Furthermore, the off-diagonal panels (2D histograms) illustrate the joint posterior distributions, highlighting correlations between pairs of parameters. The contours represent the (0.5, 1, 1.5, 2)-sigma equivalent regions, encompassing 11.8%, 39.3%, 67.5%, and 86.4% of the samples, respectively [149]. This notation reflects the integral

properties of a Gaussian distribution in two dimensions, where the sigma levels correspond to these specific percentages of the volume.

Firstly, we will discuss the results of $(\eta/s)_{\text{scale}}$. In the first analysis, using only the p_T spectra and v_2 observables, the inferred value is $(\eta/s)_{\text{scale}} = 0.8370_{-0.0065}^{+0.0065}$, indicating a relatively narrow credible interval and suggesting a high degree of confidence in this estimate. When the analysis is extended to include higher-order flow coefficients v_3 and v_4 along with the p_T spectra and v_2 , we observe a decrease in the inferred value to $(\eta/s)_{\text{scale}} = 0.6957_{-0.0046}^{+0.0046}$. The inclusion of these additional observables resulted in a lower estimate of the $(\eta/s)_{\text{scale}}$. This reduction can be attributed to the fact that larger values of η/s tend to suppress the flow coefficients v_n . Since our model tends to produce smaller v_3 and v_4 compared to the experimental data while capturing v_2 , the Bayesian inference process reduces the η/s value to obtain larger v_3 and v_4 with respect to the case in which only the v_2 coefficient is fitted. The corresponding minimum values of $(\eta/s)_{\text{min}}$ can be calculated using Equation 2.47 and they are reported as $(\eta/s)_{\text{min}} = 0.2180_{-0.0017}^{+0.0017}$ for p_T spectra+ v_2 fit, and $(\eta/s)_{\text{min}} = 0.1812_{-0.0012}^{+0.0012}$ for p_T spectra+ $v_2+v_3+v_4$ fit.

The inclusion of flow coefficients significantly enhances the ability to constrain the $(\eta/s)_{\text{scale}}$ parameter. In the case where only the p_T spectra were utilized, as shown in the posterior distributions in Figure A.1 and the detailed parameter values listed in Table 5.3, the $(\eta/s)_{\text{scale}}$ remained unconstrained. However, even the inclusion of the v_2 coefficient alone in the fit provides a notable improvement in constraining $(\eta/s)_{\text{scale}}$. This demonstrates the sensitivity of flow observables to transport coefficients. Through this approach, we achieve one of the primary objectives of this chapter: to employ additional observables beyond the p_T spectra to impose tighter constraints on the transport coefficients of the QGP.

Next, we turn to the bulk viscosity to entropy density ratio, $(\zeta/s)_{\text{max}}$. In the p_T spectra and v_2 analysis, the inferred value of $(\zeta/s)_{\text{max}}$ is $0.0005_{-0.0003}^{+0.0008}$, with uncertainties comparable to the median, suggesting that $(\zeta/s)_{\text{max}}$ is not constrained in this fit. This large uncertainty indicates a significant lack of precision, making it difficult to draw firm conclusions about the bulk viscosity from this dataset alone. However, when higher-order flow coefficients v_3 and v_4 are included, the value of $(\zeta/s)_{\text{max}}$ becomes $0.0647_{-0.0032}^{+0.0031}$, with much tighter constraints. This result is somewhat unexpected, as bulk viscosity is generally influenced by radial flow, quantified by the mean transverse momentum, $\langle p_T \rangle$, rather than higher-order anisotropic flow coefficients [35]. One possible explanation is that the inclusion of v_3 and v_4 indirectly constrains the overall hydrodynamic evolution, which, in turn, affects the correlations among model parameters that influence the estimation of bulk viscosity. This additional information could improve the precision of the $(\zeta/s)_{\text{max}}$ estimate, as changes in the inferred values of one parameter may affect others due to these correlations. Therefore, the broader range of observables likely alters the overall constraint on the model parameters, even if the direct sensitivity to $(\zeta/s)_{\text{max}}$ is not immediately apparent from higher-order flow harmonics alone. It has been observed in Ref. [130] that including bulk viscosity leads to a reduction in η/s . In our analysis, $(\eta/s)_{\text{scale}}$ is reduced due to the inclusion of v_3 and v_4 , which could potentially explain the increase in $(\zeta/s)_{\text{max}}$, as also seen in the correlations between these two parameters.

Thirdly, we examine the initialization time τ_0 . In the analysis using p_T spectra and v_2 observables, the inferred value of τ_0 is $0.7058_{-0.0255}^{+0.0256}$ fm/c. This estimate indicates a narrowly constrained initialization time based on the given data, and it is consistent with the findings from the predecessor of this work [122]. When

the analysis is extended to include v_3 and v_4 , the inferred τ_0 decreases to $0.2799_{-0.0244}^{+0.0245}$ fm/c. This reduction in τ_0 implies an earlier initialization time, which leads to a more extended hydrodynamic evolution and potentially stronger collective flow development.

In addition, it is insightful to consider the normalization constant Norm alongside τ_0 . The normalization factor accounts for variations in the fits from the TRENTo multiplicity scaling and is scaled by τ_0 to consider the longitudinal expansion effect. In the p_T spectra and v_2 analysis, $\text{Norm} = 67.0120_{-0.6191}^{+0.6090}$, whereas in the extended analysis including v_3 and v_4 , Norm decreases to $52.9891_{-1.5318}^{+1.4373}$. This change suggests a correlation between τ_0 and Norm, as both parameters are adjusted to maintain the consistency of the initial entropy density profile. The ratio Norm/τ_0 is a critical quantity as it directly affects the initial entropy density $s(r)$ in Equation 4.2. Comparing these ratios, we find that $\text{Norm}/\tau_0 = 94.97$ for the p_T spectra and v_2 analysis, and $\text{Norm}/\tau_0 = 189.25$ for the extended analysis. This increase in the Norm/τ_0 ratio in the analysis where v_3 and v_4 are included indicates a higher initial entropy density requirement intending to describe the higher-order flow coefficients complexity.

Lastly, for the marginal PDFs, we compare the kinetic freeze-out temperature, T_{kin} . In the analysis using p_T spectra and v_2 observables, the inferred value of T_{kin} is $0.1446_{-0.0002}^{+0.0002}$ GeV. When v_3 and v_4 are included, T_{kin} decreases to $0.1413_{-0.0002}^{+0.0002}$ GeV. This reduction could be attributed to the additional constraints imposed by v_3 and v_4 on the collective dynamics, which may require a longer evolution time and a more extended cooling period to accurately reproduce these observables. It is important to note that our analysis is conducted in the absence of a PCE phase. This simplification might influence the inferred freeze-out temperature as the model attempts to compensate for the missing complexity of the hadron gas phase interactions.

Furthermore, analyzing the correlations between model parameters provides deeper insights into the dynamics and constraints of the Bayesian estimations. Firstly, in both cases, there is a strong positive correlation between Norm and τ_0 . This is expected, as both parameters are involved in scaling the initial entropy density, indicating that changes in one parameter are compensated by adjustments in the other to maintain a consistent entropy profile. In the p_T spectra and v_2 fit, there are negative correlations between Norm and T_{kin} , as well as τ_0 and T_{kin} . This suggests that a higher normalization or earlier initialization times are associated with lower kinetic freeze-out temperatures. Conversely, in the extended fit, including v_3 and v_4 , these correlations become positive. This change indicates that with the additional constraints from higher-order flow harmonics, the model requires higher T_{kin} values to be consistent with larger Norm and earlier τ_0 .

In the p_T spectra and v_2 fit, other parameter pairs appear uncorrelated, implying that each parameter independently affects the model without significant interplay. However, in the extended fit, including v_3 and v_4 , $(\zeta/s)_{\text{max}}$ exhibits negative correlations with all other model parameters. This suggests that increasing bulk viscosity requires adjustments in other parameters to maintain consistency with the observed data, highlighting the sensitivity of $(\zeta/s)_{\text{max}}$ to the overall hydrodynamic evolution. Additionally, there is a small positive correlation between $(\eta/s)_{\text{scale}}$ and τ_0 in the extended fit, indicating that lower shear viscosity values are consistent with earlier initialization times, possibly due to the need for weaker shear effects to match the higher-order flow coefficients.

Figure 5.6 presents the model results for p_T spectra and $v_n(p_T)$ measured in various centrality classes (0-5%, 5-10%, 10-20%, 20-30%, and 30-40%) in Pb–Pb collisions at $\sqrt{s_{NN}} = 2.76$ TeV. These results are derived from 400 model calculations, where the input parameters are randomly sampled from the posterior distributions, considering parameter correlations, as shown in Figure 5.5. As in the priors plot, the solid markers indicate the experimental data points used in the MCMC procedure, while the open markers represent the experimental data not used in the fit. The sampling algorithm draws parameters from the MCMC

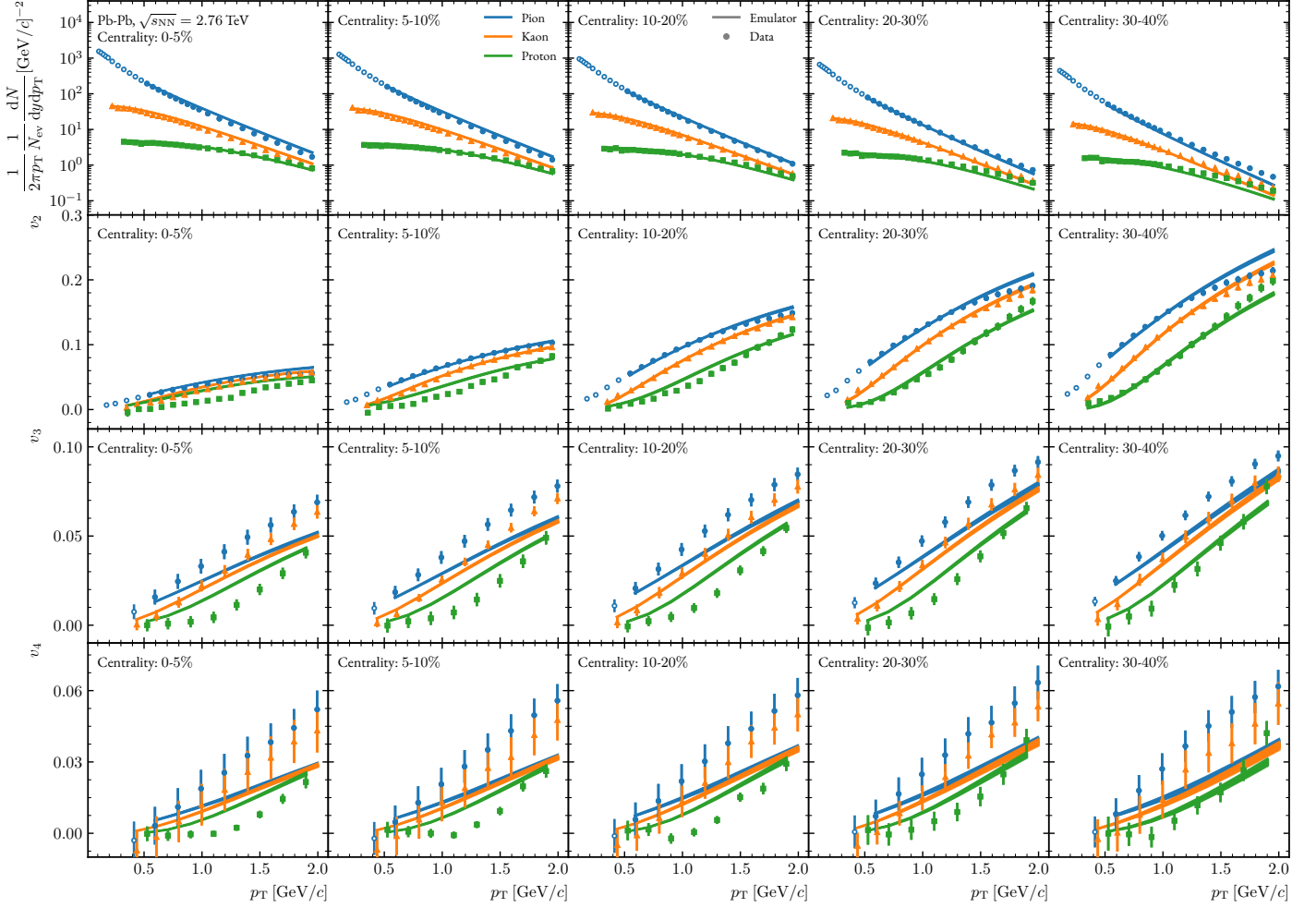


Figure 5.6: Model results for p_T spectra and $v_n(p_T)$ in Pb–Pb collisions at $\sqrt{s_{NN}} = 2.76$ TeV across various centrality classes (0-5%, 5-10%, 10-20%, 20-30%, and 30-40%). These results are derived from 400 model calculations, with input parameters randomly sampled from the posterior distributions. Solid markers indicate experimental data points used in the MCMC procedure, while open markers represent experimental data not used in the fit. The model uncertainty, represented by the band, primarily originates from the neural network emulator. Detailed quantitative comparisons of the model calculations and experimental data presented in this figure can be found in Appendix B.

chains after the burn-in period, ensuring that the sampled points reflect the posterior distributions accurately. The band of model results represents the model uncertainty, primarily originating from the neural network emulator, as discussed in Chapter 4. While it is observed that the model uncertainties (1 standard deviation) are approximately one order of magnitude smaller than the experimental uncertainties, as presented in Appendix B, the spread of the model calculations appears compatible with the experimental uncertainties

for certain p_T intervals in Figure 5.6. This is because the bands in the figure encompass the full spread of 400 model calculations, including those outside one standard deviation, resulting in a seemingly larger band.

The top row shows the p_T spectra for different centrality classes. A characteristic feature of the p_T spectra is their decrease as p_T increases. This trend is expected in hadronic collisions because higher transverse momenta require more energy, resulting in fewer particles being produced at these higher energies. Additionally, the hierarchy of particle yields—where pion spectra are higher than kaon spectra, and kaon spectra are higher than proton spectra—can be explained by their masses. In thermal models, the particle yield decreases exponentially with increasing particle mass, modulated by the temperature of the system at freeze-out [30, 150]. Moreover, the slopes of the p_T spectra for pions are steeper than those for kaons, which in turn are steeper than those for protons due to their mass differences and their sensitivity to radial flow.

Our model shows varying degrees of accuracy across different centrality classes. For the 10-20% centrality class, the model accurately reproduces the experimental data. However, for more central collisions (0-5% and 5-10%), the model tends to overestimate the experimental data, while it underestimates the data for more peripheral collisions (20-30% and 30-40%) at higher p_T values. This suggests that while the model captures the general trends, it encounters difficulties in achieving precise reproduction at the extremes of the centrality range. These discrepancies reflect the challenge of a simultaneous fit across all centralities, where a single set of model parameters must account for a wide spectrum of collision conditions. The simultaneous fitting approach inherently involves trade-offs, balancing accuracy across centralities, and may lead to a compromise in precision at specific centrality intervals. The quantification of these deviations will be provided using model calculations obtained from the MAP values.

In the second row, the $v_2(p_T)$ flow coefficients are displayed for the same set of particles and centralities. The mass hierarchy observed in the v_2 values, where $v_2^{\text{pion}} > v_2^{\text{kaon}} > v_2^{\text{proton}}$, can be attributed to the mass dependence of particle flow. In the collision scenario where the final particles are produced via freeze-out of the locally thermalized matter exhibiting collective flow, the interplay of radial expansion and anisotropic flow results in a characteristic mass dependence of the differential flow [151]. Furthermore, the v_2 values increase as we move to more peripheral centralities. This increase is due to the larger spatial anisotropy in the initial overlap region of the colliding nuclei in peripheral collisions [152]. The elliptic shape of the overlap region in peripheral collisions creates stronger pressure gradients, enhancing the anisotropic flow and resulting in higher v_2 values.

The model samples align well with the experimental data at lower p_T values but start to deviate at higher p_T values as centrality increases. This suggests that while the model describes the elliptic flow dynamics reasonably well, there are limitations in its accuracy at higher transverse momenta and more peripheral collisions, where the hydrodynamic description of the data is expected to be less accurate [125].

The third and fourth rows present the $v_3(p_T)$ and $v_4(p_T)$ flow coefficients, where the model samples show significant deviations from the experimental data. This discrepancy indicates that our model struggles to accurately describe the v_3 and v_4 observables. The observed hierarchy in v_3 and v_4 values ($v_{3,4}^{\text{pion}} > v_{3,4}^{\text{kaon}} > v_{3,4}^{\text{proton}}$) follows a trend similar to that of v_2 , driven by mass-dependent effects on the particles' response to the medium's radial flow. The increase in v_3 and v_4 with more peripheral centralities is less pronounced than that for v_2 , as v_3 and v_4 are more directly tied to fluctuations rather than the overlap geometry. Given the model's

limitations in describing the $v_3(p_T)$ and $v_4(p_T)$ flow coefficients, it is reasonable to question the reliability of the fit results from the p_T spectra + $v_2 + v_3 + v_4$ analysis. If our model cannot adequately capture the higher-order flow coefficients, the inferred parameter values from this fit may not be trustworthy. Therefore, it may be more prudent to rely on the p_T spectra + v_2 fit, where the model performs better. For this reason, we will include only the p_T spectra + v_2 fits for different collision energies in the global fit presented in [Section 5.2](#).

Additionally, our model consistently fails to accurately describe all flow coefficients (v_n) for protons across lower centrality classes (0-5%, 5-10%, and 10-20%) by overpredicting them at lower p_T . This discrepancy can be attributed to the model's lack of PCE, which is essential for accurately modeling the behavior of protons. Without incorporating PCE, the model fails to capture the full strength of the radial flow gained during the hadronic phase and cannot shift the flow coefficients to higher p_T values in central events.

To further investigate the impact of proton data on the model's accuracy, we performed Bayesian inference for p_T spectra and v_2 observables under two scenarios: one including proton data in v_2 and the other excluding it. The results indicated no substantial difference in the overall fit quality, suggesting that the proton v_n 's do not play a significant role in our model. Detailed results of these fits are presented in [Appendix A](#), specifically in [Figure A.2](#), [Figure A.3](#), and [Figure A.4](#). Future studies incorporating PCE are expected to provide further insights into this issue.

In addition to examining the impact of proton data on the model's accuracy, we also investigated the influence of centrality classes on the inferred model parameters for Pb–Pb collisions at $\sqrt{s_{NN}} = 2.76$ TeV. This analysis involved a Bayesian inference approach, initially utilizing data from all five centrality classes (0-5%, 5-10%, 10-20%, 20-30%, and 30-40%), and subsequently excluding the most peripheral centrality class stepwise, resulting in fits with four, three, and two centrality classes. Separate fits were also performed for each individual centrality class to assess the variation of the model parameters to different centralities. This investigation was conducted prior to our decision to prioritize the p_T spectra + v_2 fit over the p_T spectra + v_n fit. As such, the detailed results of this study are not presented in the main text but are provided in [Appendix C](#).

In order to demonstrate the influence of model uncertainties on the results, we compare the log posterior probability $-2 \log \mathcal{P}$ with the χ^2 value for the visited parameter configurations during the MCMC sampling procedure. The use of the log posterior probability is preferred due to its numerical stability, as the logarithm of the posterior probability is more manageable than the posterior itself, which can vary over many orders of magnitude. The log posterior probability can be calculated using [Equation 5.1](#), where \mathcal{L} represents the likelihood and π denotes the priors

$$\log \mathcal{P}(\theta|y) = \log \mathcal{L}(y|\theta) + \log \pi(\theta). \quad (5.1)$$

Here, the logarithms of the uniform prior ([Equation 3.13](#)) and likelihood ([Equation 3.18](#)) are taken as follows:

$$\log \pi(\theta) = \begin{cases} 0 & \text{if } \min(\theta_i) \leq \theta_i \leq \max(\theta_i) \text{ for all } i, \\ -\infty & \text{otherwise} \end{cases} \quad (5.2)$$

$$-\log \mathcal{L}(\mathcal{D}|\theta) = -\frac{1}{2} \log((2\pi)^n \det \Sigma) - \frac{1}{2} (\mathbf{y}_{model}(\theta) - \mathbf{y}_{exp})^T \Sigma^{-1} (\mathbf{y}_{model}(\theta) - \mathbf{y}_{exp}), \quad (5.3)$$

where i is the number of model parameters. When Equation 5.3 is multiplied by -2, the resulting log posterior probability is given as

$$-2 \log \mathcal{P} = \begin{cases} (\mathbf{y}_{model}(\theta) - \mathbf{y}_{exp})^T \Sigma^{-1} (\mathbf{y}_{model}(\theta) - \mathbf{y}_{exp}) & \text{if } \min(\theta_i) \leq \theta_i \leq \max(\theta_i) \text{ for all } i, \\ \infty & \text{otherwise.} \end{cases} \quad (5.4)$$

where $-2 \log \mathcal{P}$ differs from χ^2 only in the covariance matrix. The covariance matrix for $-2 \log \mathcal{P}$ contains both experimental uncertainties (diagonal terms, as no experimental data correlations are used in our framework) and model uncertainties (which include off-diagonal terms). In contrast, the χ^2 value contains only experimental uncertainties. Therefore, comparing $-2 \log \mathcal{P}$ and χ^2 provides insights into how model uncertainties influence the results.

Figure 5.7 presents the distributions of $-2 \log \mathcal{P}$ and χ^2 for the visited parameter configurations during the MCMC sampling after the burn-in period. It is evident that incorporating model uncertainties increases the posterior probability, impacting the overall distribution. The $-2 \log \mathcal{P}$ distribution is narrower and exhibits a 20% higher probability density compared to the χ^2 distribution, which is broader and displays a longer tail extending towards higher values.

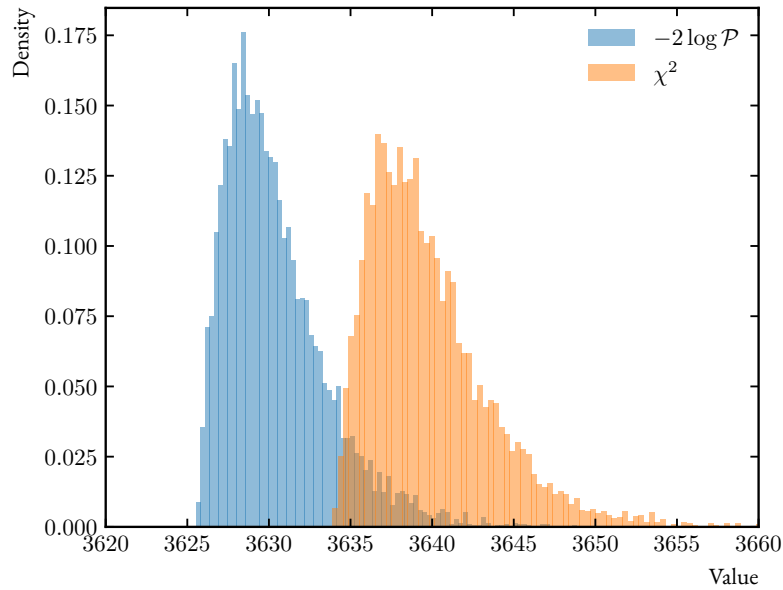


Figure 5.7: Distributions of log posterior probability ($-2 \log \mathcal{P}$) and χ^2 -values for the visited parameter configurations during the MCMC simulation. The observed differences arise from the inclusion of model uncertainties in the log \mathcal{P} calculation.

The MCMC simulations operate within a confined region of the probability space, characterized by variations in the log probability from 3625 to 3650 and χ^2 varying from 3633 to 3660. In contrast, the χ^2 values for the training samples range widely, from a minimum of 4203 to a maximum of 7201446. Notably, the training sample with the smallest χ^2 value of 4203 lies well outside the region to which the MCMC simulation converged, which has a χ^2 value around 3640. This indicates that the region of the highest posterior probability is achieved predominantly through the interpolation capabilities of the neural network ensemble. Incorporating additional training points from the region of the highest probability could be advantageous. This would likely reduce the ensemble error further and enhance the accuracy of the posterior parameter estimates. The reduced chi-squared values of the MAP estimates are reported in [Table 5.4](#).

MAXIMUM A POSTERIORI ESTIMATES

[Figure 5.8](#) displays the MAP estimates of p_T spectra for two distinct fit scenarios: one combining spectra with v_n fits (solid lines), and the other combining spectra with v_2 fits (dashed lines). The best agreement between experimental data and model predictions is observed in the 10-20% centrality class. For the 0-5% and 5-10% centrality classes, the ratios generally remain close to unity, though deviations up to 20% are present, especially for pions at high p_T in the 0-5% centrality class. On the other hand, the model's accuracy de-

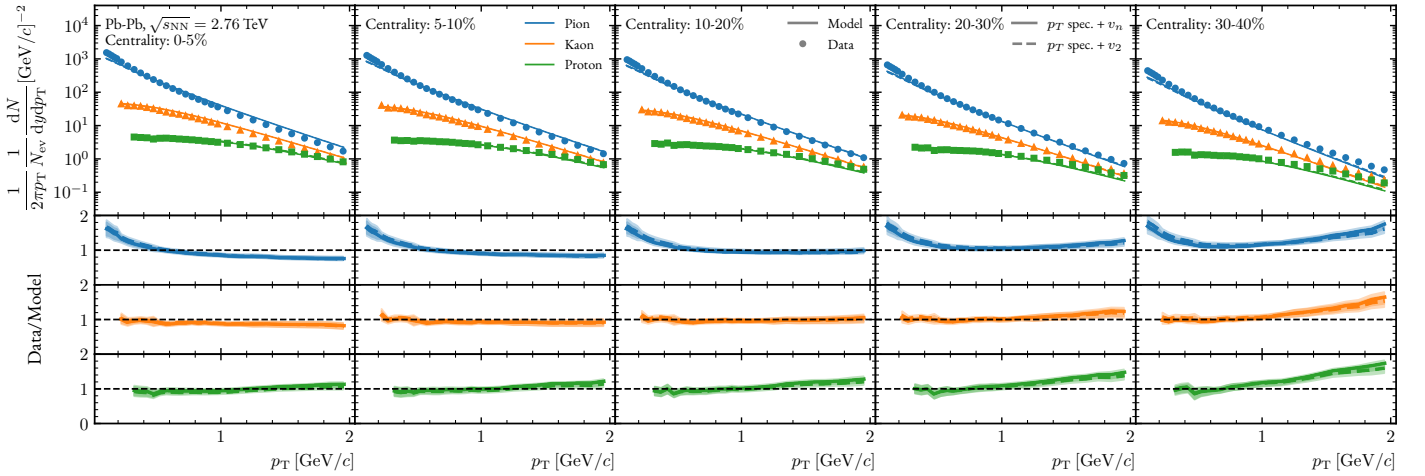


Figure 5.8: The MAP estimates of p_T spectra for pions, kaons, and protons across various centrality classes in Pb–Pb collisions at $\sqrt{s_{NN}} = 2.76$ TeV. The columns correspond to different centrality classes, and the data-to-model ratios are shown in the bottom panels with uncertainty bands representing experimental uncertainties. The solid lines represent model predictions from p_T spectra combined with v_n fits, while the dashed lines represent model predictions from p_T spectra combined with v_2 fits.

creases in more peripheral collisions, particularly in the 30-40% centrality class, where it significantly underestimates the experimental data in the high p_T regime. This deviation may be attributed to the limitations of FLUIDUM in accounting for the characteristics of peripheral collisions, as the background-fluctuation splitting ansatz of FLUIDUM works best for central collisions, where the profiles are the most symmetric [55]. Additionally, as centrality increases, the data-to-model ratio for protons becomes tilted, indicating a lack of radial flow in the model. This deviation is reduced in the presence of PCE, as shown in [Figure 5.1](#). It is also

noteworthy that this figure differs from those presented in [Chapter 4](#) by incorporating five centrality classes in the inference process rather than a single centrality class and by using a different number of observables.

The data-to-model ratio panels include an uncertainty band, which reflects the statistical and systematic uncertainties of the experimental data. It is crucial to note that these ratios do not account for model uncertainties shown in [Figure 5.6](#), which could partly explain the observed discrepancies. Furthermore, despite the different model parameters obtained from the spectra+ v_2 fit and the spectra+ $v_2+v_3+v_4$ fit, the resulting p_T spectra are nearly identical. This observation can be attributed to parameter correlations in the Bayesian analysis, where variations in certain parameters are compensated by adjustments in others, leading to similar model outputs. It suggests that the p_T spectra are mainly sensitive to the bulk properties of the QGP, effectively constrained by the p_T spectra and v_2 coefficient together. Lastly, as discussed in [Chapter 4](#), a notable excess of low p_T pions below 0.5 GeV/c is observed across all centrality classes, indicating that the model underestimates yields in this region.

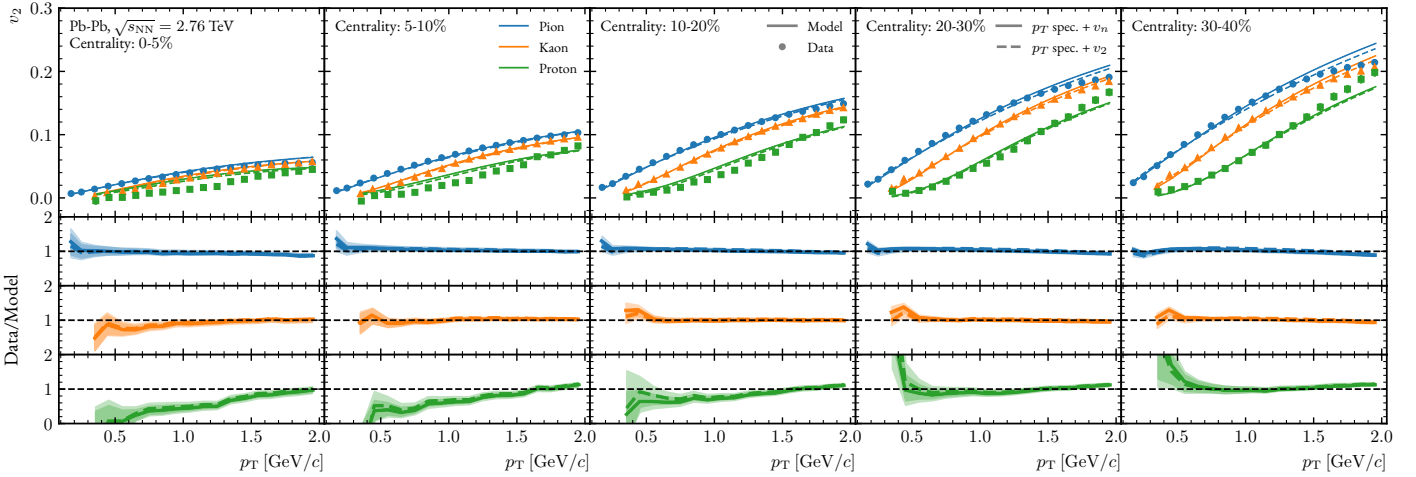


Figure 5.9: The MAP estimates of v_2 for pions, kaons, and protons across various centrality classes in Pb–Pb collisions at $\sqrt{s_{\text{NN}}} = 2.76$ TeV.

[Figure 5.9](#) presents the MAP estimates of the elliptic flow coefficient v_2 for pions, kaons, and protons across various centrality classes in Pb–Pb collisions at $\sqrt{s_{\text{NN}}} = 2.76$ TeV for two distinct fit scenarios. The comparison reveals that both fit scenarios yield similar results across all centrality classes. This similarity again may be attributed to the parameter correlations in the Bayesian analysis, where variations in specific parameters are compensated by adjustments in others, resulting in consistent v_2 values despite different parameter sets. The v_2 data-to-model ratios for pions and kaons remain very close to unity across all centrality classes, indicating that the model accurately captures the elliptic flow for these particles, providing a good fit to the experimental data. However, for protons, significant discrepancies are observed in the lower centrality classes (0-5% and 5-10%). In central collisions, protons gain additional radial flow during the hadronic phase [153]. In our model, the v_2 of protons is overpredicted at small p_T for the most central collisions, suggesting that the model does not adequately capture the strength of the radial flow, which pushes the elliptic flow to higher p_T in these central events. In more peripheral collisions (20-30% and 30-40%), the additional radial flow is

less pronounced, and the agreement with proton measurements improves. This indicates that the model's balance between radial and elliptic flow is an important aspect that needs to be properly considered.

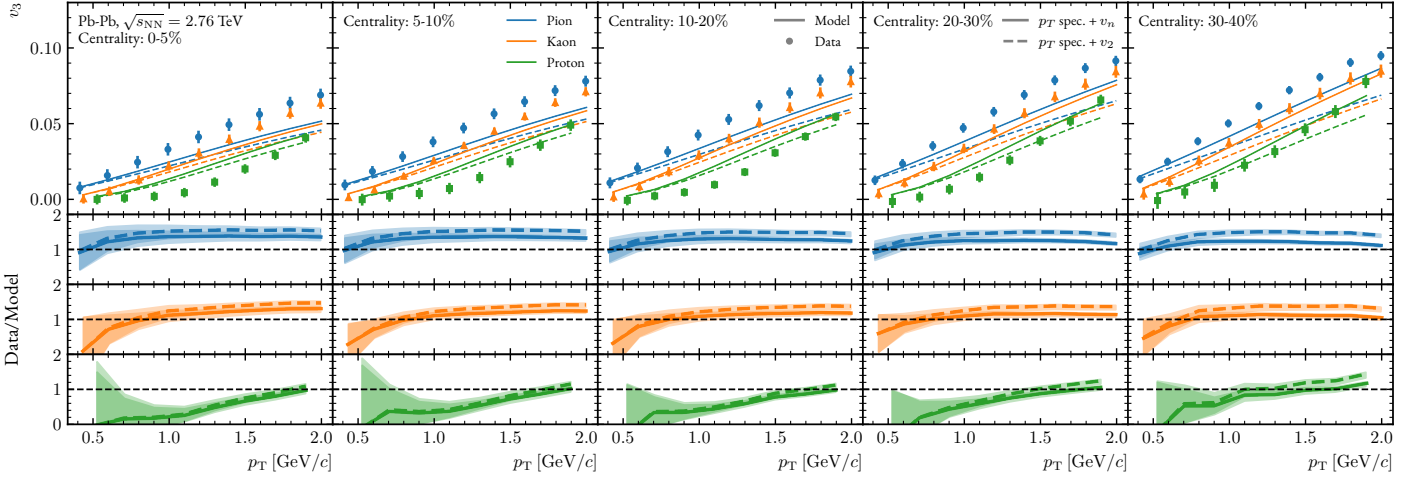


Figure 5.10: The MAP estimates of v_3 for pions, kaons, and protons across various centrality classes in Pb–Pb collisions at $\sqrt{s_{\text{NN}}} = 2.76$ TeV.

Figure 5.10 presents the MAP estimates of the triangular flow coefficient v_3 , comparing two fit scenarios. Although the spectra+ v_n MAP estimates describe v_3 better than the spectra+ v_2 estimation, the model still fails to reproduce the experimental data accurately. The v_3 coefficient arises primarily from initial state fluctuations rather than from the collision geometry. These fluctuations are included in our model only at the first order [55, 145], indicating that even with the inclusion of v_3 in the fit, the model does not fully capture its magnitude.

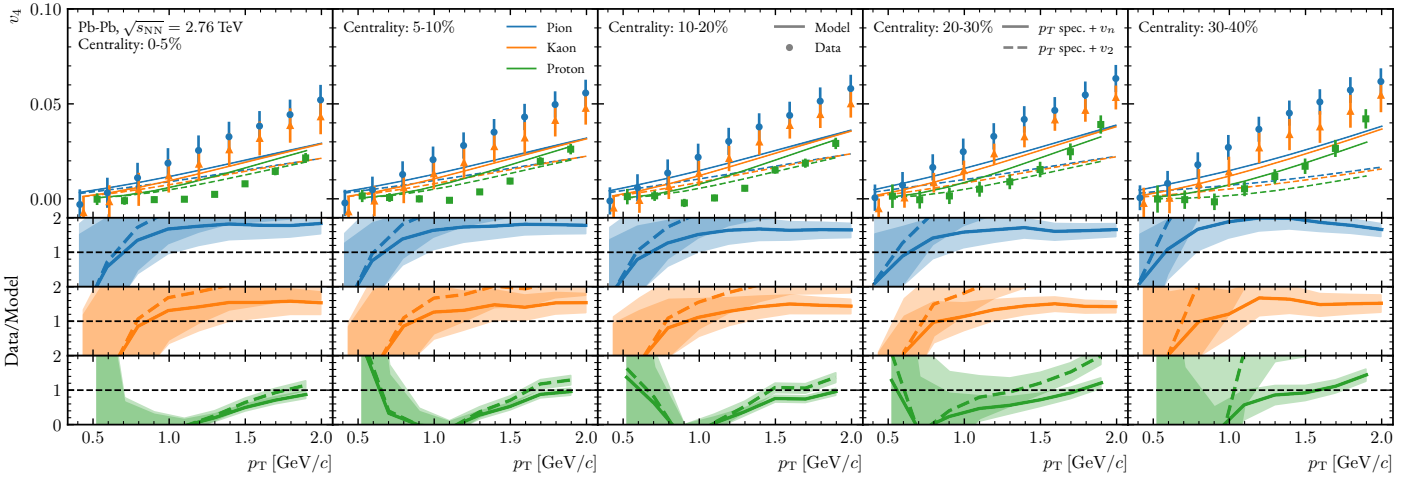


Figure 5.11: The MAP estimates of v_4 for pions, kaons, and protons across various centrality classes in Pb–Pb collisions at $\sqrt{s_{\text{NN}}} = 2.76$ TeV.

Figure 5.11 presents the MAP estimates of the quadrangular flow coefficient v_4 , comparing two fit scenarios. As in the case of v_3 , the spectra+ v_n MAP estimates describe v_4 better than the spectra+ v_2 estimation, yet the model results do not fully match the experimental data. Although the improvement between the

two fits is evident, it is less prominent than for v_3 . Despite the inclusion of v_3 and v_4 in the fits, the model struggles to accurately describe v_4 in both fit scenarios across all centralities. The discrepancies between the model and experimental data for v_4 are more pronounced than for v_2 and v_3 , indicating the absence of flow mode-couplings [146, 147] in the model, in addition to a first-order approximation in the initial state fluctuations.

Figure 5.12 shows the MAP estimates of the flow coefficients v_2 , v_3 , and v_4 for charged hadrons in Pb–Pb collisions at $\sqrt{s_{\text{NN}}} = 2.76$ TeV for two different fit scenarios. It is important to note that charged hadron v_n 's are not directly included in the Bayesian inference in this study. Instead, they are calculated using the most probable parameters. For charged hadrons, the model shows a good agreement with the experimental data across all centrality classes for v_2 and v_3 when using the spectra+ v_n fits. The inclusion of higher-order flow coefficients in the fits improves the description of the data more quantitatively. For instance, the data-to-model ratio for v_3 deviates from unity by approximately 40% when only p_T spectra and v_2 are used in the Bayesian analysis. After the inclusion of v_3 and v_4 , this deviation is reduced to below 20%. Similarly, for v_4 , the deviation from unity is reduced to around 40% for the centrality classes 0-5%, 5-10%, and 10-20%.

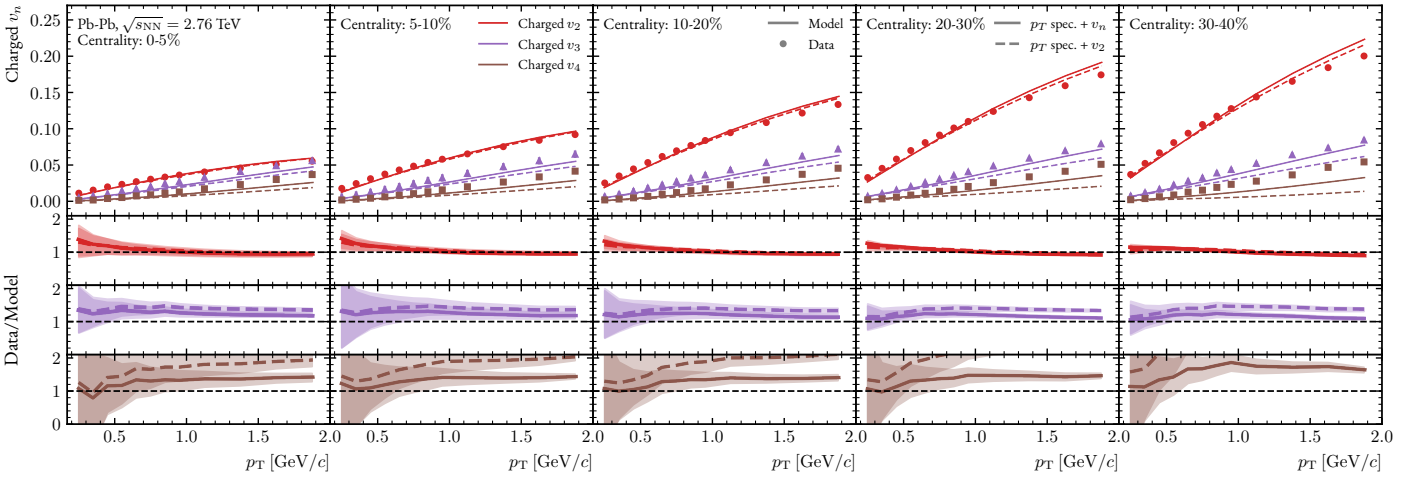


Figure 5.12: The MAP estimates of v_2 , v_3 , and v_4 for charged hadrons across various centrality classes in Pb–Pb collisions at $\sqrt{s_{\text{NN}}} = 2.76$ TeV.

5.1.5 RESULTS FOR Pb–Pb COLLISIONS AT $\sqrt{s_{\text{NN}}} = 5.02$ TeV

Having examined the results for Pb–Pb collisions at $\sqrt{s_{\text{NN}}} = 2.76$ TeV, we now turn our attention to the analysis of Pb–Pb collisions at the higher energy of $\sqrt{s_{\text{NN}}} = 5.02$ TeV. Similar to the lower energy case, our model encounters difficulties in accurately describing the higher-order flow coefficients, $v_3(p_T)$ and $v_4(p_T)$, at this energy as well. Given these limitations, the analysis in this subsection will focus on the posteriors obtained from the p_T spectra+ v_2 fit. Only the posterior results and sampled emulator examples are presented here, while details regarding the priors and emulator checks can be found in Figure A.5 and Figure A.6 in Appendix A. The MAP estimates are not included, as they are similar to those for the 2.76 TeV case; they will be provided in the context of the global fit, incorporating data from all collision systems, as discussed in Section 5.2.

POSTERIOR

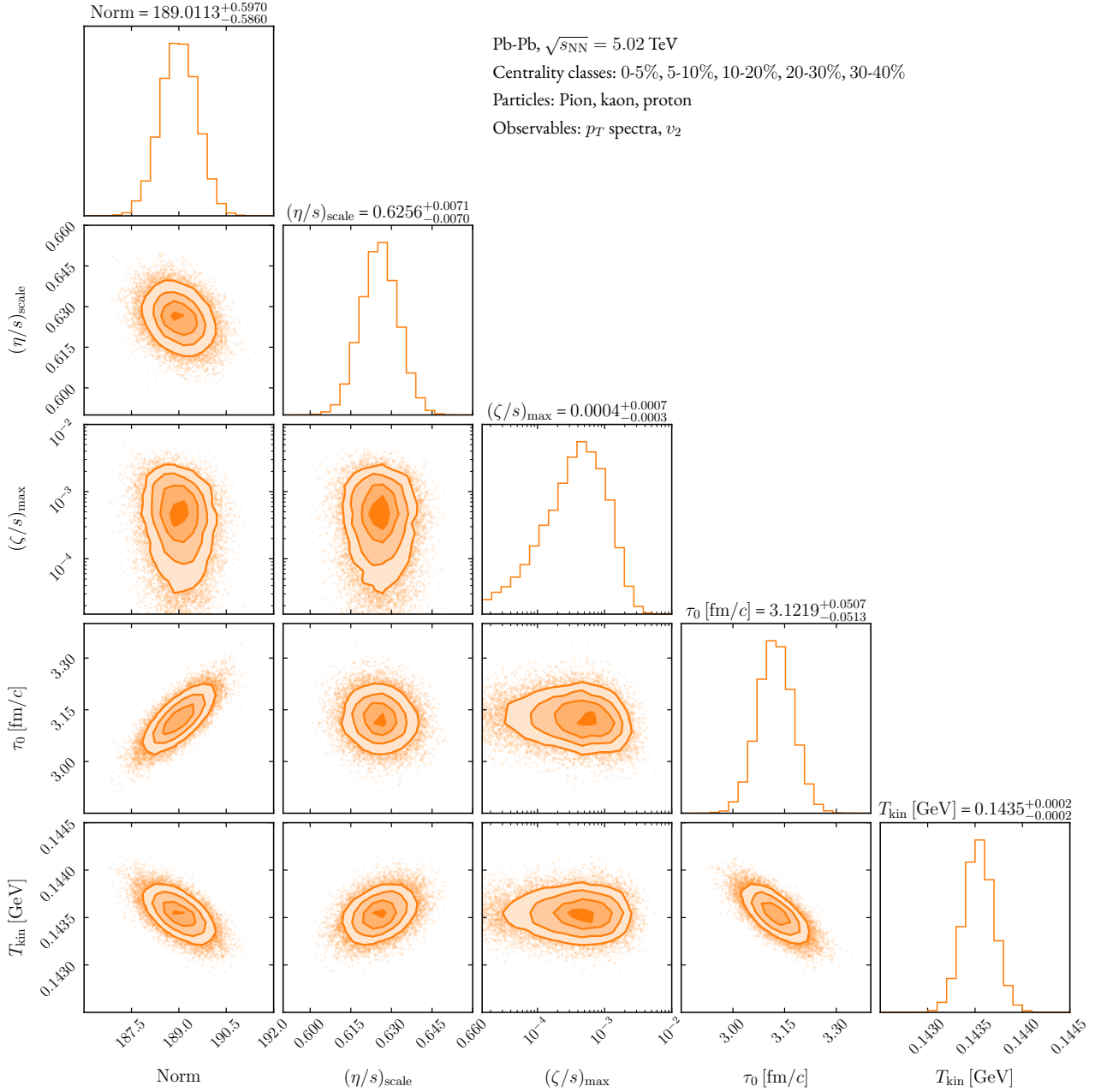


Figure 5.13: Marginal and joint posterior probability densities for model parameters in Pb–Pb collisions at $\sqrt{s_{\text{NN}}} = 5.02$ TeV obtained using p_T spectra and v_2 observables.

Figure 5.13 shows the marginal and joint posterior PDFs for the model parameters in Pb–Pb collisions at $\sqrt{s_{\text{NN}}} = 5.02$ TeV estimated using p_T spectra and $v_2(p_T)$ observables, considering centrality classes 0–5%, 5–10%, 10–20%, 20–30%, and 30–40%, and particles pions, kaons, protons. Key observations from the posterior distributions can be listed as follows by comparing the results for Pb–Pb collisions at $\sqrt{s_{\text{NN}}} = 5.02$ TeV with those at $\sqrt{s_{\text{NN}}} = 2.76$ TeV (Figure 5.4):

- In our model, only the Norm and τ_0 are system-dependent parameters, meaning we expect these parameters to change with different collision systems and energies. In contrast, $(\eta/s)_{\text{scale}}$, $(\zeta/s)_{\text{max}}$, and

T_{kin} should ideally remain consistent across different collision energies. However, the posterior distributions indicate deviations from this expectation. $(\zeta/s)_{\text{max}}$ remains small and unconstrained in both cases. Specifically, $(\zeta/s)_{\text{max}} = 0.0004_{-0.0003}^{+0.0007}$ at $\sqrt{s_{\text{NN}}} = 5.02$ TeV and $(\zeta/s)_{\text{max}} = 0.0005_{-0.0003}^{+0.0008}$ at $\sqrt{s_{\text{NN}}} = 2.76$ TeV. On the other hand, the $(\eta/s)_{\text{scale}}$ decreases from $0.8370_{-0.0065}^{+0.0065}$ at $\sqrt{s_{\text{NN}}} = 2.76$ TeV to $0.6256_{-0.0070}^{+0.0071}$ at $\sqrt{s_{\text{NN}}} = 5.02$ TeV. T_{kin} also decreases from $0.1446_{-0.0002}^{+0.0002}$ GeV to $0.1435_{-0.0002}^{+0.0002}$ GeV. These differences might not indicate intrinsic changes in the QGP properties but could reflect systematic uncertainties in our modeling and the different sensitivity of the experimental data used in the Bayesian inference. In the global fit involving multiple collision energies, $(\eta/s)_{\text{scale}}$ and T_{kin} are treated as system-independent, implying that the QGP exhibits consistent properties across different collision energies.

- For Pb–Pb collisions at $\sqrt{s_{\text{NN}}} = 2.76$ TeV, the normalization is $\text{Norm} = 67.0120_{-0.6191}^{+0.6090}$ and the initialization time is $\tau_0 = 0.7058_{-0.0255}^{+0.0256}$ fm/c. At $\sqrt{s_{\text{NN}}} = 5.02$ TeV, these values change significantly, with $\text{Norm} = 189.0113_{-0.5860}^{+0.5970}$ and $\tau_0 = 3.1219_{-0.0513}^{+0.0507}$ fm/c. The increase in Norm reflects the higher particle multiplicity and energy density at the higher collision energy.
- The correlations among the model parameters remained consistent across different collision energies. For instance, a strong positive correlation between Norm and τ_0 is observed in both cases, which is expected as these parameters jointly influence the initial entropy density profile. Similarly, the negative correlations between Norm and T_{kin} , as well as τ_0 and T_{kin} , are present in both analyses. This consistency suggests that the underlying physics governing these parameters is robust and not significantly affected by the change in collision energy. Additionally, the correlations involving $(\eta/s)_{\text{scale}}$ and $(\zeta/s)_{\text{max}}$ with other parameters also exhibit similar patterns, indicating stable relationships among these transport coefficients and other model parameters.

The 400 model calculations for Pb–Pb collisions at $\sqrt{s_{\text{NN}}} = 5.02$ TeV, where input parameters are randomly sampled from the walker steps in the MCMC process shown in [Figure 5.13](#), demonstrate a performance similar to that observed at $\sqrt{s_{\text{NN}}} = 2.76$ TeV. These calculations, shown in [Figure 5.14](#), present p_{T} spectra and $v_2(p_{\text{T}})$ for pions, kaons, and protons across various centrality classes (0-5%, 5-10%, 10-20%, 20-30%, and 30-40%).

For both collision energies, the p_{T} spectra exhibit similar characteristics, with no significant differences observed. The model accurately reproduces the experimental data for the 10-20% centrality class. However, it tends to overestimate the experimental data for more central collisions (0-5% and 5-10%) and underestimate it for more peripheral collisions (20-30% and 30-40%) at higher p_{T} values. Similarly, the v_2 results of pions and kaons for both collision systems align with experimental data at lower p_{T} values but start to deviate at higher p_{T} values as centrality increases. On the other hand, for protons, there are significant discrepancies in the lower centrality classes (0-5% and 5-10%), indicating that the model does not adequately capture the strength of the radial flow, which pushes the elliptic flow to higher p_{T} in these central events. In more peripheral collisions (20-30% and 30-40%), the radial flow is less pronounced, resulting in better agreement with proton measurements.

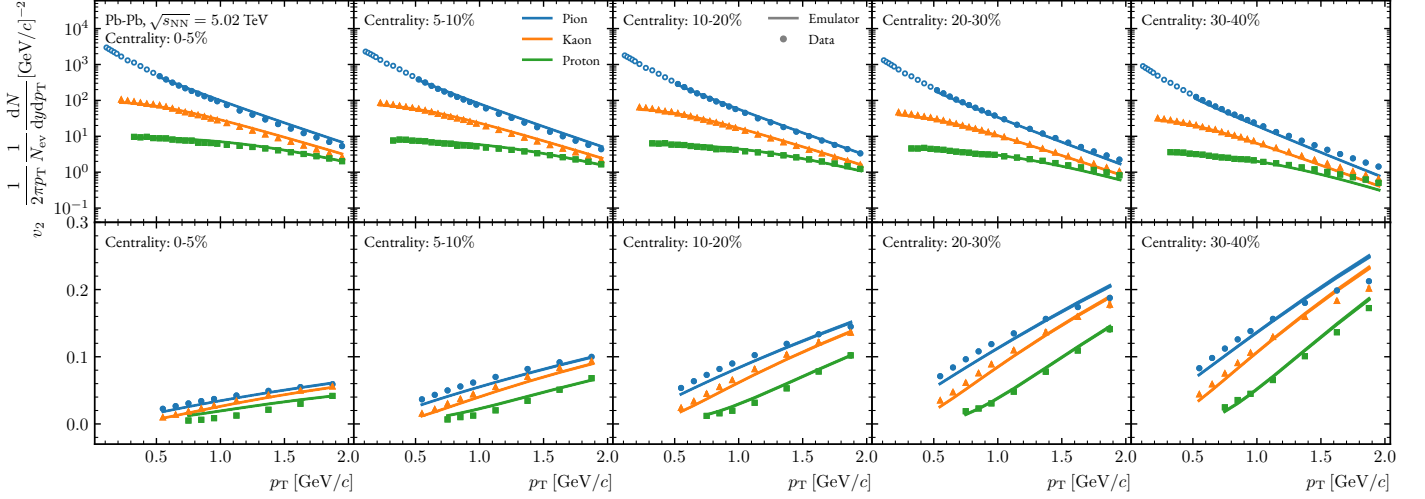


Figure 5.14: Model results for p_T spectra and $v_2(p_T)$ in Pb–Pb collisions at $\sqrt{s_{NN}} = 5.02$ TeV across various centrality classes (0-5%, 5-10%, 10-20%, 20-30%, and 30-40%). These results are derived from 400 model calculations, with input parameters randomly sampled from the posterior distributions. Solid markers indicate experimental data points used in the MCMC procedure, while open markers represent experimental data not used in the fit. The model uncertainty, represented by the band, primarily originates from the neural network emulator.

5.1.6 RESULTS FOR XE-XE COLLISIONS AT $\sqrt{s_{NN}} = 5.44$ TeV

Lastly, the results for Xe-Xe collisions at $\sqrt{s_{NN}} = 5.44$ TeV are presented, focusing on the posterior PDFs obtained using p_T spectra and $v_2(p_T)$ observables, and their corresponding model samples. As in the case of Pb–Pb collisions at $\sqrt{s_{NN}} = 5.02$ TeV, interested readers can refer to [Figure A.7](#) and [Figure A.8](#) in [Appendix A](#) for details on the priors and emulator checks.

POSTERIORS

Comparing [Figure 5.15](#) to [Figure 5.4](#) and [Figure 5.13](#), key observations are as follows:

- For Xe-Xe collisions at $\sqrt{s_{NN}} = 5.44$ TeV, $\text{Norm} = 162.3138_{-2.2480}^{+2.2735}$, which is between the values for Pb-Pb collisions at $\sqrt{s_{NN}} = 2.76$ TeV ($67.0120_{-0.6191}^{+0.6090}$) and $\sqrt{s_{NN}} = 5.02$ TeV ($189.0113_{-0.5860}^{+0.5970}$). The higher energy density at $\sqrt{s_{NN}} = 5.44$ TeV might be influenced by the smaller size of the Xe nucleus compared to Pb, resulting in a different normalization factor that reflects the combined effects of collision energy and system size.
- The $(\eta/s)_{\text{scale}}$ for Xe-Xe collisions is $0.4968_{-0.0081}^{+0.0084}$, which is lower than the values for Pb-Pb collisions at $\sqrt{s_{NN}} = 2.76$ TeV ($0.8370_{-0.0065}^{+0.0065}$) and $\sqrt{s_{NN}} = 5.02$ TeV ($0.6256_{-0.0070}^{+0.0071}$). Again, these differences could reflect systematic uncertainties in our modeling and the different sensitivity of the experimental data used in the Bayesian inference.
- T_{kin} for Xe-Xe collisions is $0.1470_{-0.0003}^{+0.0003}$ GeV, higher than for the Pb-Pb cases. It is important to note that the most central collisions in Xe–Xe correspond to the 10-20% centrality class in Pb-Pb at $\sqrt{s_{NN}} = 5.02$ TeV, while the 30-40% centrality class in Xe–Xe corresponds to the 40-50% centrality

5 Mapping properties of the QGP

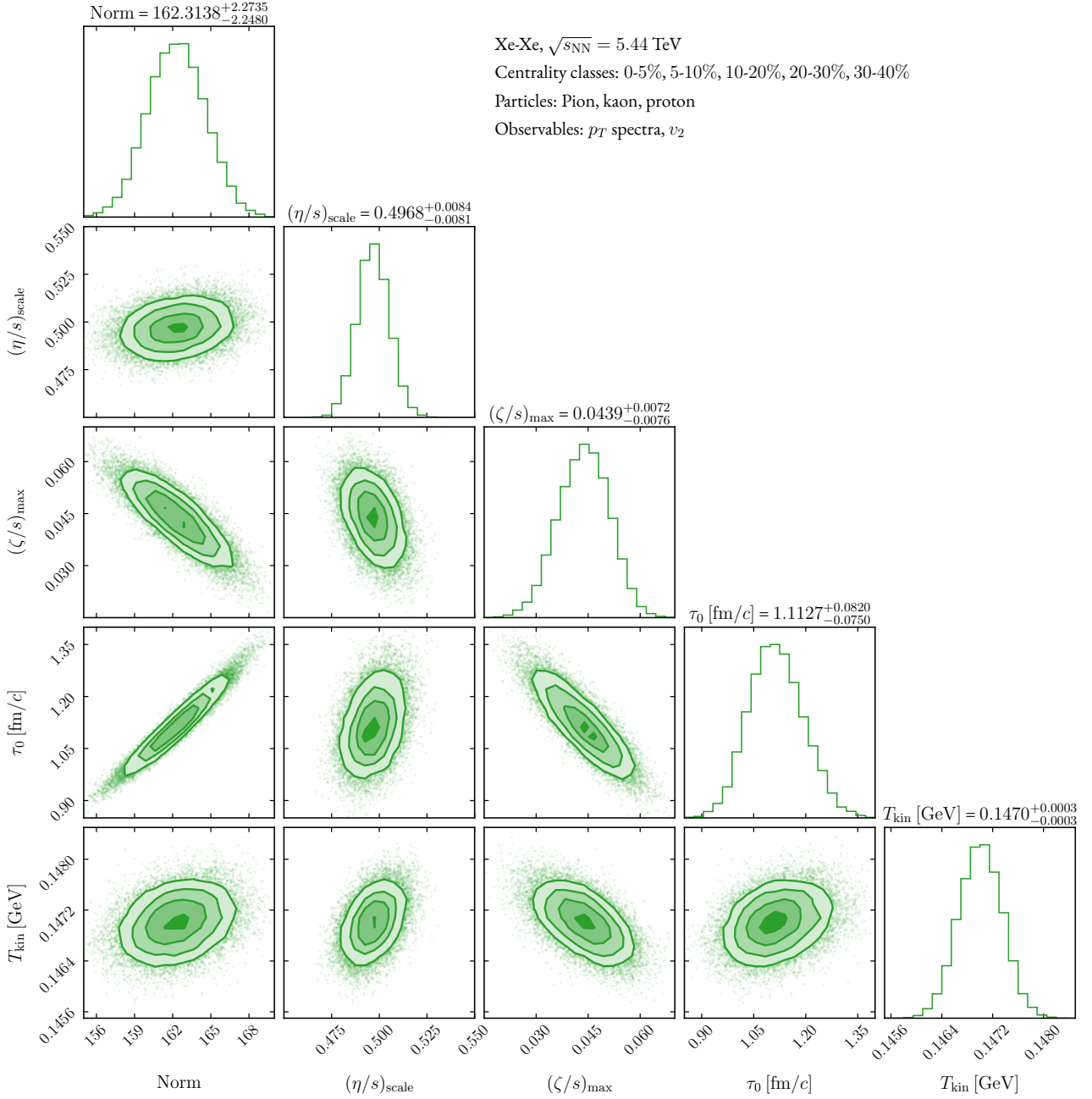


Figure 5.15: Marginal and joint posterior probability densities for model parameters in Xe–Xe collisions at $\sqrt{s_{\text{NN}}} = 5.44$ TeV.

class in Pb–Pb at $\sqrt{s_{\text{NN}}} = 5.02$ TeV, considering particle multiplicity [137]. Therefore, as discussed in Chapter 4, this phenomenon can be attributed to the systematic increase in T_{kin} as collisions become more peripheral.

- $(\zeta/s)_{\text{max}}$ for Xe–Xe collisions is $0.0439^{+0.0072}_{-0.0076}$, which is not only higher but also better constrained than in the Pb–Pb cases, where $(\zeta/s)_{\text{max}}$ remains unconstrained. Furthermore, $(\zeta/s)_{\text{max}}$ in the Xe–Xe case is negatively correlated with all other parameters, suggesting a unique bulk viscosity behavior in the smaller Xe–Xe system. This finding is unexpected and requires further investigation to better understand the underlying mechanisms.

Figure 5.16 illustrates the emulator samples for p_T spectra and v_2 observables in Xe-Xe collisions at $\sqrt{s_{NN}} = 5.44$ TeV, derived from parameters sampled from the posterior distributions shown in Figure 5.15. Comparing these results with those from Pb-Pb collisions at $\sqrt{s_{NN}} = 2.76$ TeV and $\sqrt{s_{NN}} = 5.02$ TeV, two key observations can be made:

- The deviations between the model samples and the experimental data are more significant in the 0-5% and 30-40% centrality classes for Xe-Xe collisions. Since the 30-40% centrality class in Xe-Xe collisions corresponds to the 40-50% centrality class in Pb-Pb collisions when considering multiplicity, the larger deviation at 30-40% centrality class in Xe-Xe collisions compared to Pb-Pb collisions may be attributed to the limitations of FLUIDUM in accounting for the characteristics of smaller system sizes since the background-fluctuation splitting ansatz of FLUIDUM is more effective for central collisions.
- The v_2 coefficient of protons in Xe-Xe collisions is poorly described across all centralities, similar to the observations in Pb-Pb collisions. This discrepancy could be attributed to the absence of PCE in the FLUIDUM.

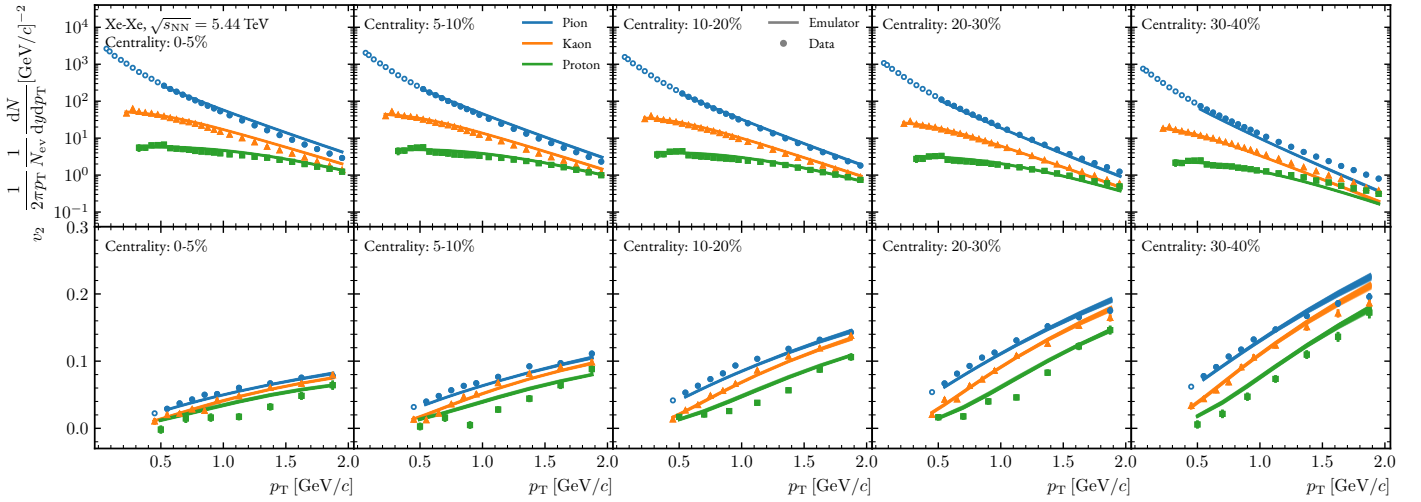


Figure 5.16: Model results for p_T spectra and $v_2(p_T)$ in Xe-Xe collisions at $\sqrt{s_{NN}} = 5.44$ TeV across various centrality classes (0-5%, 5-10%, 10-20%, 20-30%, and 30-40%). These results are derived from 400 model calculations, with input parameters randomly sampled from the posterior distributions. Solid markers indicate experimental data points used in the MCMC procedure, while open markers represent experimental data not used in the fit. The model uncertainty, represented by the band, primarily originates from the neural network emulator.

5.2 COMBINED ANALYSIS OF MULTIPLE COLLISION SYSTEMS

In this section, we extend the analysis to a global fit involving multiple collision systems to estimate the probability density functions of the model parameters more robustly. By leveraging data from Pb–Pb collisions at $\sqrt{s_{\text{NN}}} = 2.76$ TeV and $\sqrt{s_{\text{NN}}} = 5.02$ TeV, as well as Xe–Xe collisions at $\sqrt{s_{\text{NN}}} = 5.44$ TeV, we aim to obtain a comprehensive understanding of the QGP properties that may transcend the limitations of individual system analyses.

To achieve this, the likelihood function $\mathcal{L}(\mathcal{D}|\theta)$ is reformulated as a joint likelihood function across all considered systems. This is expressed as:

$$\mathcal{L}(\mathcal{D}|\theta) = \prod_i \mathcal{L}(\mathcal{D}_i|\theta_i), \quad (5.5)$$

where i indexes the different collision systems. This joint likelihood function allows for the simultaneous fitting of the model to multiple datasets, ensuring that the inferred parameters are consistent across different collision systems. The Markov Chain Monte Carlo procedure follows the methodology described in [Chapter 3](#), where the parameter space is sampled to generate posterior distributions that account for the combined data. This integrated approach not only enhances the statistical power of the parameter estimates but also helps to identify and mitigate system-specific biases, and hopefully would provide a more unified and accurate characterization of the QGP.

POSTERIORES

The combined analysis of Pb–Pb collisions at $\sqrt{s_{\text{NN}}} = 2.76$ TeV and $\sqrt{s_{\text{NN}}} = 5.02$ TeV, along with Xe–Xe collisions at $\sqrt{s_{\text{NN}}} = 5.44$ TeV using p_{T} spectra and $v_2(p_{\text{T}})$ observables, yields comprehensive posterior distributions for the normalization factors specific to each collision system, $(\eta/s)_{\text{scale}}$, $(\zeta/s)_{\text{max}}$, the initialization times τ_0 for each system, and T_{kin} , as shown in [Figure 5.17](#). Key observations and differences from a comparison of the combined posterior distributions with the individual system posteriors are highlighted below:

- In the individual system analyses, the normalization factors were found to be $67.0120_{-0.6191}^{+0.6090}$ for Pb–Pb collisions at $\sqrt{s_{\text{NN}}} = 2.76$ TeV, $189.0113_{-0.5860}^{+0.5970}$ for Pb–Pb collisions at $\sqrt{s_{\text{NN}}} = 5.02$ TeV, and $162.3138_{-2.2480}^{+2.2735}$ for Xe–Xe collisions at $\sqrt{s_{\text{NN}}} = 5.44$ TeV. In the combined analysis, these values are adjusted to $65.5684_{-0.6628}^{+0.6375}$ for $\sqrt{s_{\text{NN}}} = 2.76$ TeV, $185.3688_{-0.6182}^{+0.5929}$ for $\sqrt{s_{\text{NN}}} = 5.02$ TeV, and $176.4074_{-1.1934}^{+1.1086}$ for $\sqrt{s_{\text{NN}}} = 5.44$ TeV. The consistency observed in the Pb–Pb cases suggests that the combined fit maintains the overall particle multiplicity and energy density well for these systems. However, the increase in the normalization factor for the Xe–Xe system may reflect adjustments needed to balance variations in the other model parameters.
- The individual system analyses provided initialization times of $0.7058_{-0.0255}^{+0.0256}$ fm/c for Pb–Pb collisions at $\sqrt{s_{\text{NN}}} = 2.76$ TeV, $3.1219_{-0.0513}^{+0.0507}$ fm/c for Pb–Pb collisions at $\sqrt{s_{\text{NN}}} = 5.02$ TeV, and

5.2 Combined analysis of multiple collision systems

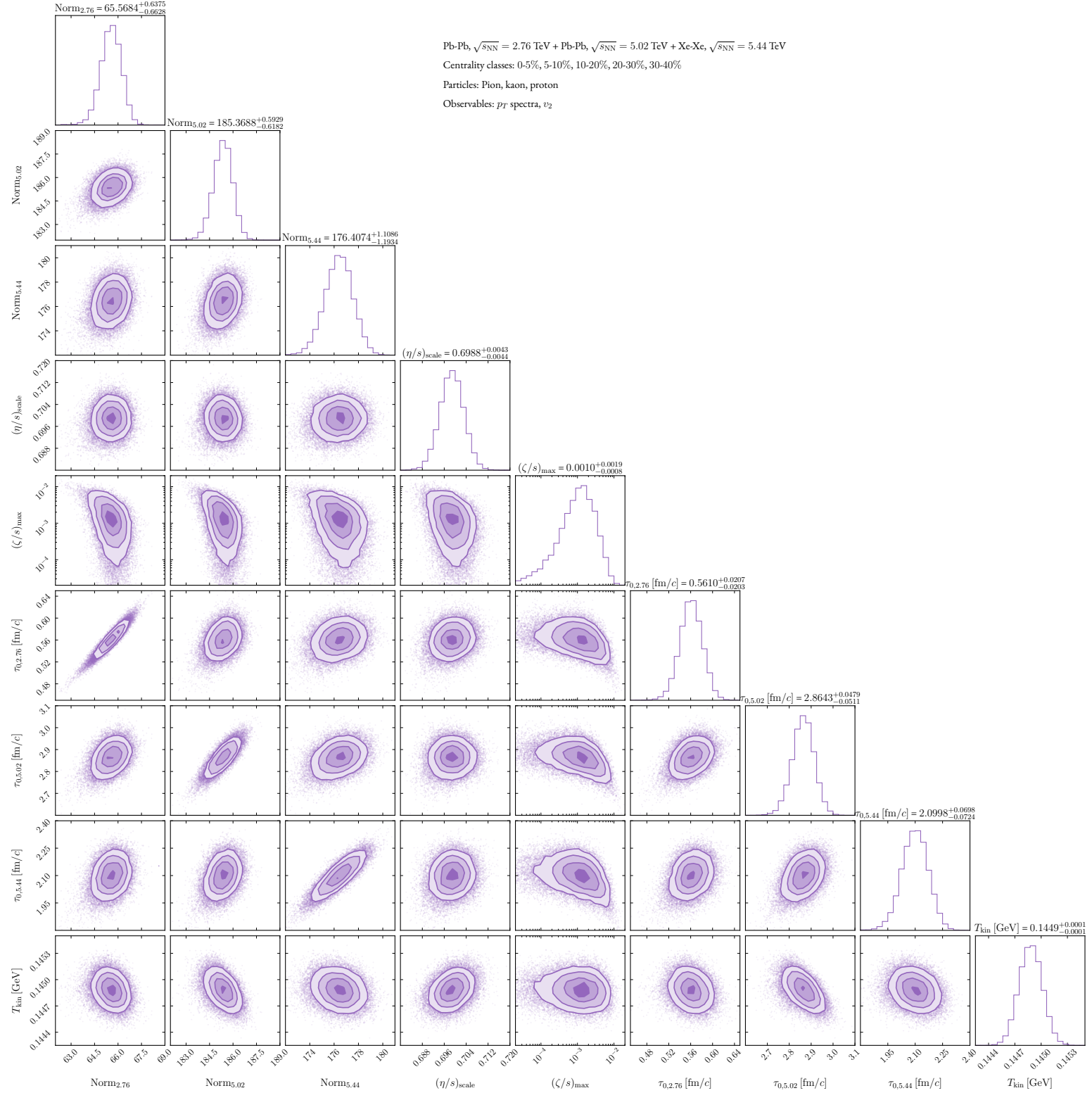


Figure 5.17: Marginal and joint posterior probability densities for model parameters in combined Pb-Pb collisions at $\sqrt{s_{\text{NN}}} = 2.76$ TeV, $\sqrt{s_{\text{NN}}} = 5.02$ TeV, and Xe-Xe collisions at $\sqrt{s_{\text{NN}}} = 5.44$ TeV. The combined analysis includes centrality classes 0-5%, 5-10%, 10-20%, 20-30%, and 30-40%, and considers pions, kaons, and protons with p_T spectra and $v_2(p_T)$ observables.

1.1127^{+0.0820}_{-0.0750} fm/c for Xe-Xe collisions at $\sqrt{s_{\text{NN}}} = 5.44$ TeV. In the combined analysis, these ini-

tialization times are adjusted to $0.5610^{+0.0207}_{-0.0203}$ fm/c for $\sqrt{s_{\text{NN}}} = 2.76$ TeV, $2.8643^{+0.0479}_{-0.0511}$ fm/c for $\sqrt{s_{\text{NN}}} = 5.02$ TeV, and $2.0998^{+0.0698}_{-0.0724}$ fm/c for $\sqrt{s_{\text{NN}}} = 5.44$ TeV. The change in τ_0 is most prominent in Xe-Xe collisions. One possible explanation could be that since τ_0 is negatively correlated with bulk viscosity, in the global fit bulk viscosity decreases significantly compared to the individual fit of Xe-Xe, resulting in an increase in τ_0 . However, the bulk viscosity in the global fit is similar to that in the individual Pb-Pb fits, and correspondingly, the τ_0 values are also similar to those in the individual Pb-Pb fits.

- The kinetic freeze-out temperatures were found to be $0.1446^{+0.0002}_{-0.0002}$ GeV for Pb–Pb collisions at $\sqrt{s_{\text{NN}}} = 2.76$ TeV, $0.1435^{+0.0002}_{-0.0002}$ GeV for Pb–Pb collisions at $\sqrt{s_{\text{NN}}} = 5.02$ TeV, and $0.1470^{+0.0003}_{-0.0003}$ GeV for Xe-Xe collisions at $\sqrt{s_{\text{NN}}} = 5.44$ TeV. In the combined analysis, the value is estimated as $0.1449^{+0.0001}_{-0.0001}$ GeV. This combined result lies within the range of the individual system values and is closer to the values obtained from the Pb–Pb analyses rather than the Xe–Xe analysis. This suggests that the Pb–Pb collision data have a stronger influence on the global fit, potentially dominating the estimation of the kinetic freeze-out temperature.
- In the individual system analyses, $(\zeta/s)_{\text{max}}$ was found to be unconstrained for Pb–Pb collisions, with values of $0.0005^{+0.0008}_{-0.0003}$ at $\sqrt{s_{\text{NN}}} = 2.76$ TeV and $0.0004^{+0.0007}_{-0.0003}$ at $\sqrt{s_{\text{NN}}} = 5.02$ TeV. Conversely, for Xe-Xe collisions at $\sqrt{s_{\text{NN}}} = 5.44$ TeV, $(\zeta/s)_{\text{max}}$ was more constrained, with a value of $0.0439^{+0.0072}_{-0.0076}$. In the combined analysis, the value of $(\zeta/s)_{\text{max}}$ is adjusted to $0.0010^{+0.0019}_{-0.0008}$, though it remains unconstrained overall.
- In the individual system analyses, the shear viscosity to entropy density ratio $(\eta/s)_{\text{scale}}$ was estimated to be $0.8370^{+0.0065}_{-0.0065}$ for Pb–Pb collisions at $\sqrt{s_{\text{NN}}} = 2.76$ TeV, $0.6256^{+0.0071}_{-0.0070}$ for Pb–Pb collisions at $\sqrt{s_{\text{NN}}} = 5.02$ TeV, and $0.4968^{+0.0084}_{-0.0081}$ for Xe-Xe collisions at $\sqrt{s_{\text{NN}}} = 5.44$ TeV. In the combined analysis, this value is adjusted to $0.6988^{+0.0043}_{-0.0044}$. This combined $(\eta/s)_{\text{scale}}$ value lies between the individual estimates and again is closer to the values obtained from the Pb–Pb analyses rather than the Xe–Xe analysis, suggesting the domination of Pb–Pb data in the global fit.

The temperature-dependent shear viscosity to entropy density ratio, $\eta/s(T)$, for each collision system is derived by substituting the estimated $(\eta/s)_{\text{scale}}$ values obtained from the fits into the parametrization given by Equation 2.47. The left panel of Figure 5.18 illustrates the $\eta/s(T)$, for Pb–Pb collisions at $\sqrt{s_{\text{NN}}} = 2.76$ TeV, Pb–Pb collisions at $\sqrt{s_{\text{NN}}} = 5.02$ TeV, and Xe–Xe collisions at $\sqrt{s_{\text{NN}}} = 5.44$ TeV, along with the combined analysis. The figure displays the posterior median and the 68% credible region for each system. These results highlight several important points. First, the expectation that shear viscosity is collision-system independent is not entirely met, as evidenced by the different minimum values of $\eta/s(T)$ for each collision system. The minimum value of η/s is $0.2180^{+0.0017}_{-0.0017}$ for Pb–Pb collisions at $\sqrt{s_{\text{NN}}} = 2.76$ TeV, $0.1630^{+0.0018}_{-0.0018}$ for Pb–Pb collisions at $\sqrt{s_{\text{NN}}} = 5.02$ TeV, and $0.1294^{+0.0022}_{-0.0022}$ for Xe–Xe collisions at $\sqrt{s_{\text{NN}}} = 5.44$ TeV, with the minimum located at 0.145 GeV for all values. The combined analysis yields a minimum shear viscosity of $0.1820^{+0.0011}_{-0.0011}$. This discrepancy can be regarded as a source of systematic uncertainty arising from different collision dynamics, specific experimental data used in the fit, and the approximations in

the model. The combined analysis provides a median value that lies between the individual system values, suggesting a balanced estimate of $\eta/s(T)$ across different collision environments. The observed minimum values are also compared to the KSS bound [154], which sets a theoretical lower limit for shear viscosity and remains larger than the KSS bound $\eta/s \geq 1/(4\pi)$.

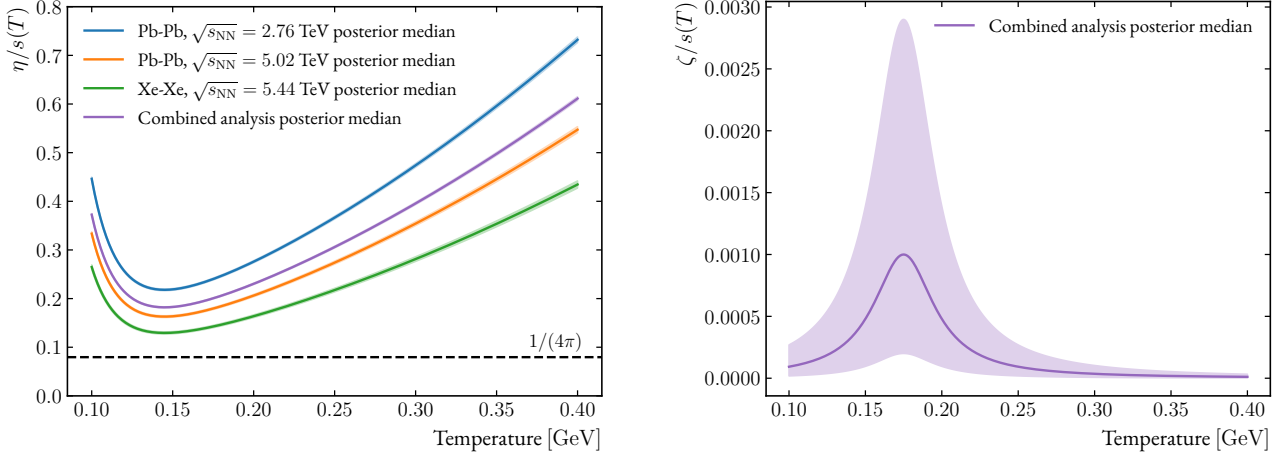


Figure 5.18: Temperature-dependent shear viscosity to entropy density ratio $\eta/s(T)$ (left panel) for Pb–Pb collisions at $\sqrt{s_{NN}} = 2.76$ TeV, Pb–Pb collisions at $\sqrt{s_{NN}} = 5.02$ TeV, Xe–Xe collisions at $\sqrt{s_{NN}} = 5.44$ TeV, and the combined analysis. The right panel shows the temperature-dependent bulk viscosity to entropy density ratio $\zeta/s(T)$ for the combined analysis only. The shaded bands represent the 68% credible intervals, indicating the uncertainty range for each estimate, with the posterior medians shown as solid lines.

Comparing our results with those obtained by other Bayesian analysis groups, it is important to note the differences in the parametrization of $\eta/s(T)$. Three groups, specifically Duke [82], Jyväskylä [83], and Trajectum [84], have parameterized the temperature-dependent shear viscosity of the QGP with a three-parameter modified linear ansatz. These groups report minimum η/s values of $0.085^{+0.0026}_{-0.0025}$, $0.1010^{+0.0046}_{-0.0046}$, and $0.065^{+0.038}_{-0.040}$, respectively. In contrast, our shear viscosity parametrization is given by Equation 2.47. This methodological difference can lead to variations in the resulting minimum values of $\eta/s(T)$. Our combined analysis yields a minimum shear viscosity of $0.1820^{+0.0011}_{-0.0011}$, which is higher than those reported by Duke, Jyväskylä, and Trajectum. Additionally, the JETSCAPE collaboration [85] and the Ohio State-Northwestern [86] use a different parametrization. These groups do not report a specific $(\eta/s)_{\min}$ value; however, our $(\eta/s)_{\min}$ value is compatible with their 90% credible intervals based on their posterior results.

The right panel of Figure 5.18 presents the temperature-dependent bulk viscosity to entropy density ratio, $\zeta/s(T)$. The temperature dependence follows the functional form described by Equation 2.48, with the parameters T_{peak} and T_{width} fixed to 175 MeV and 24 MeV, respectively, as referenced in [66]. The posterior median value for the maximum bulk viscosity is $(\zeta/s)_{\max} = 0.0010^{+0.0019}_{-0.0008}$. This value is very close to zero, and the credible interval indicates that $(\zeta/s)_{\max}$ is not constrained. Such small values of bulk viscosity are also estimated by other Bayesian analysis groups [83, 84]. The near-zero values suggest that bulk viscosity has a minimal impact on the QGP’s hydrodynamic evolution compared to shear viscosity. This underscores the challenges in precisely constraining $(\zeta/s)_{\max}$ and indicates that, within our current model and data constraints, the QGP’s bulk viscosity remains an elusive property.

It is worth noting, however, that other studies, such as the one presented in [155], have reported significantly larger bulk viscosity values. This discrepancy can be attributed to differences in the initial condition models employed. Specifically, the IP-Glasma model used in their analysis requires a larger ζ/s to accurately describe the experimental observables. This suggests that the initial condition parameters play a crucial role in determining the inferred bulk viscosity. Consequently, to achieve a more precise constraint on ζ/s , it would be beneficial to explore a wider range of initial condition parameters within our model. Although our current analysis does not vary these parameters, future studies could adopt this approach to gain deeper insights into the QGP's bulk viscosity.

MAXIMUM A POSTERIORI ESTIMATES

The MAP estimates of the p_T spectra and $v_2(p_T)$ for Pb–Pb collisions at $\sqrt{s_{NN}} = 2.76$ TeV, $\sqrt{s_{NN}} = 5.02$ TeV, and Xe–Xe collisions at $\sqrt{s_{NN}} = 5.44$ TeV, where the model parameters are estimated through a combined analysis of these systems, show similar characteristics across all three collision systems.

Figure 5.19, Figure 5.20, and Figure 5.21 present the p_T spectra for Pb–Pb collisions at $\sqrt{s_{NN}} = 2.76$ TeV, Pb–Pb collisions at $\sqrt{s_{NN}} = 5.02$ TeV, and Xe–Xe collisions at $\sqrt{s_{NN}} = 5.44$ TeV, respectively. For all systems, the data-to-model ratios remain close to unity, with deviations within 20% in the fitting p_T range for centrality classes 0-5%, 5-10%, and 10-20%. This indicates that the global fit accurately describes the spectra for these centrality classes across all collision systems. However, the data-to-model ratio begins to diverge for the 20-30% centrality class, where the model tends to underestimate the experimental data, particularly at high p_T . This deviation is more pronounced in the 30-40% centrality class, where the model significantly underestimates the data at high p_T , with the data-to-model ratio reaching values up to a factor of 2.

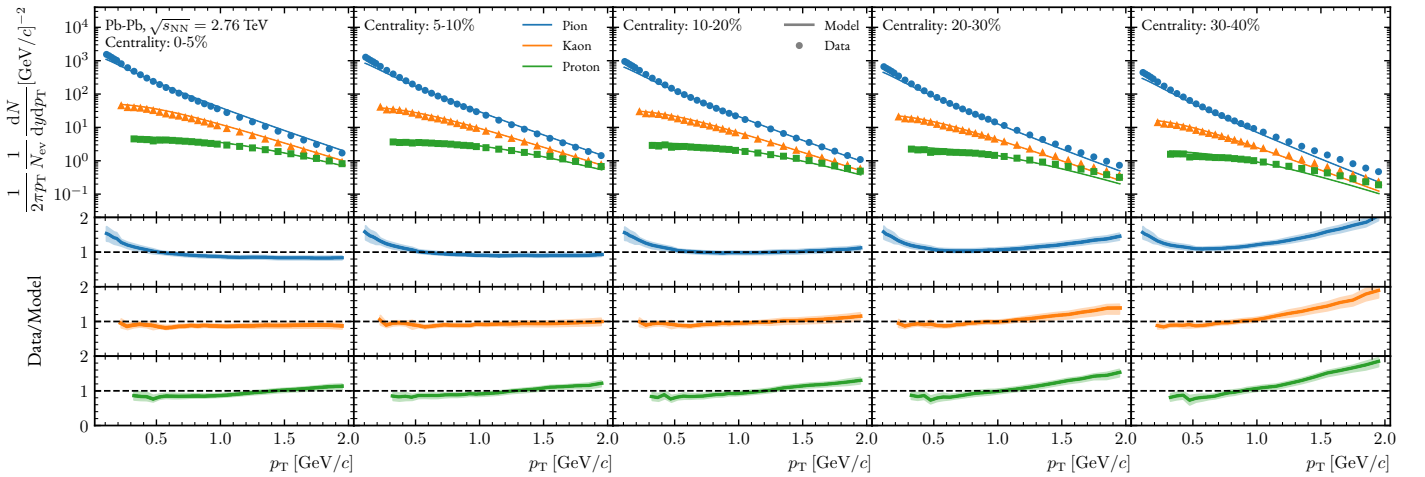


Figure 5.19: MAP estimates of p_T spectra for Pb–Pb collisions at $\sqrt{s_{NN}} = 2.76$ TeV, where the model parameters are estimated through a combined analysis of Pb–Pb and Xe–Xe collisions.

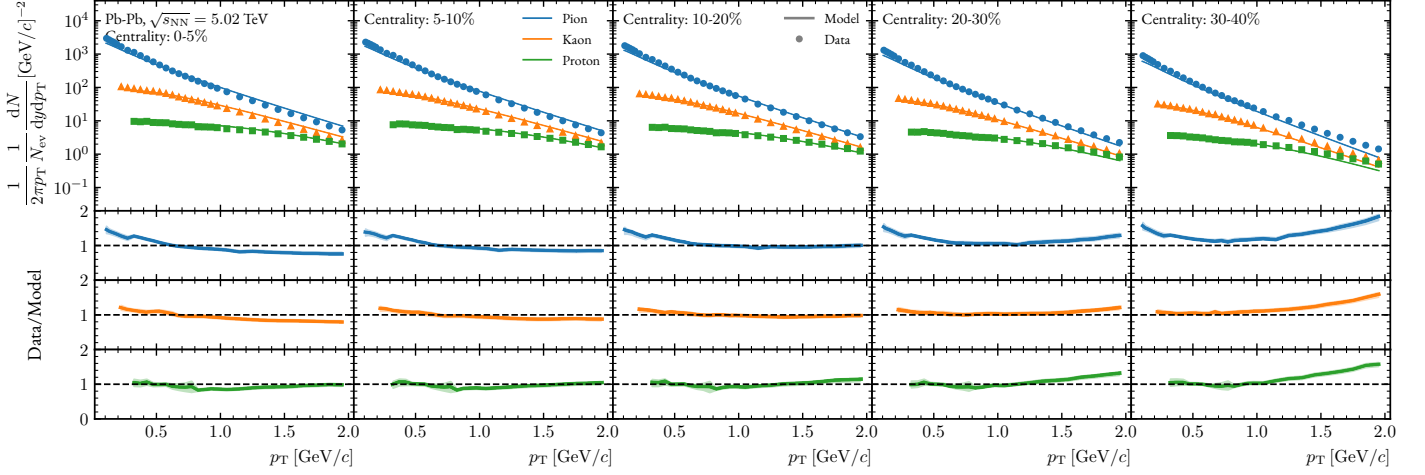


Figure 5.20: MAP estimates of p_T spectra for Pb–Pb collisions at $\sqrt{s_{\text{NN}}} = 5.02$ TeV, where the model parameters are estimated through a combined analysis of Pb–Pb and Xe–Xe collisions.

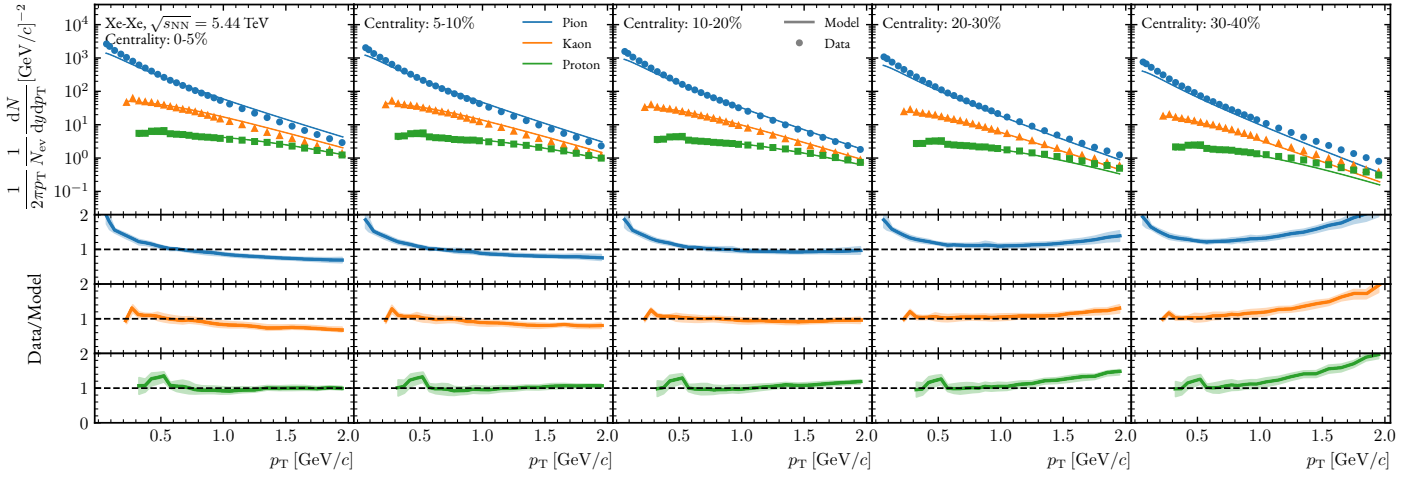


Figure 5.21: MAP estimates of p_T spectra for Xe–Xe collisions at $\sqrt{s_{\text{NN}}} = 5.44$ TeV, where the model parameters are estimated through a combined analysis of Pb–Pb and Xe–Xe collisions.

Figure 5.22, Figure 5.23, and Figure 5.24 present the $v_2(p_T)$ results for Pb–Pb collisions at $\sqrt{s_{\text{NN}}} = 2.76$ TeV, Pb–Pb collisions at $\sqrt{s_{\text{NN}}} = 5.02$ TeV, and Xe–Xe collisions at $\sqrt{s_{\text{NN}}} = 5.44$ TeV, respectively. Across all systems, the global fit shows a good agreement with the experimental data for pions and kaons across all centrality classes, with deviations from unity within 20% at low p_T , indicating the model’s robustness in describing the elliptic flow for these particles. However, the model encounters significant challenges in accurately describing the v_2 for protons, particularly in central collisions (0-5% and 5-10% centrality classes). This issue persists in both the individual and combined fits, highlighting a consistent difficulty in modeling the elliptic flow for protons. This difficulty might arise because the current model does not adequately capture the strength of the radial flow, which pushes the elliptic flow to higher p_T in these central events.

5 Mapping properties of the QGP

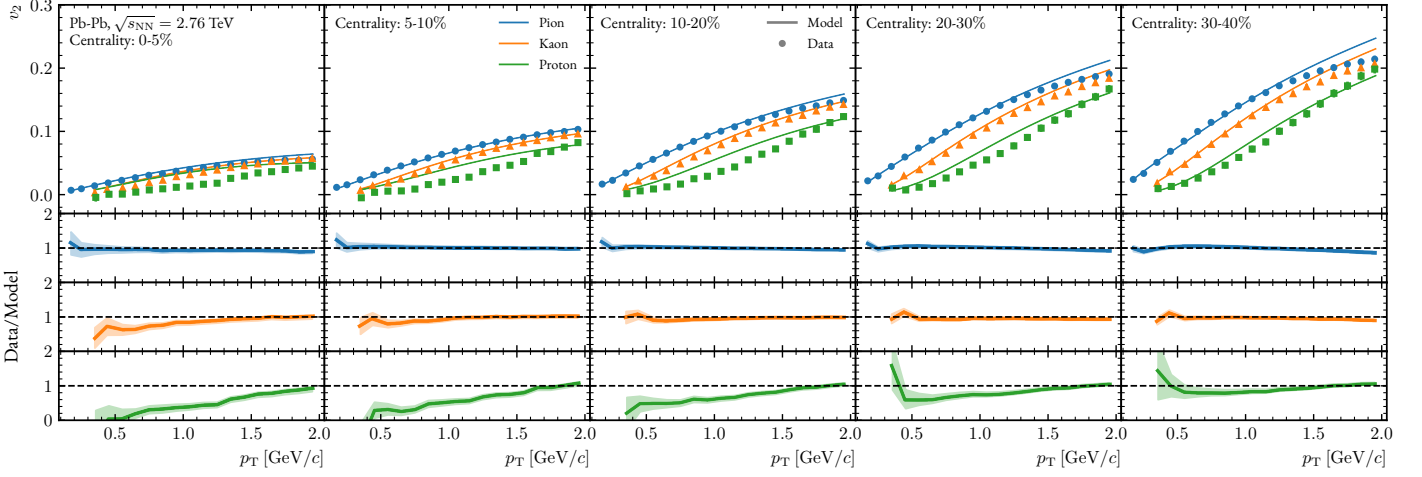


Figure 5.22: MAP estimates of v_2 for Pb–Pb collisions at $\sqrt{s_{\text{NN}}} = 2.76$ TeV, where the model parameters are estimated through a combined analysis of Pb–Pb and Xe–Xe collisions.

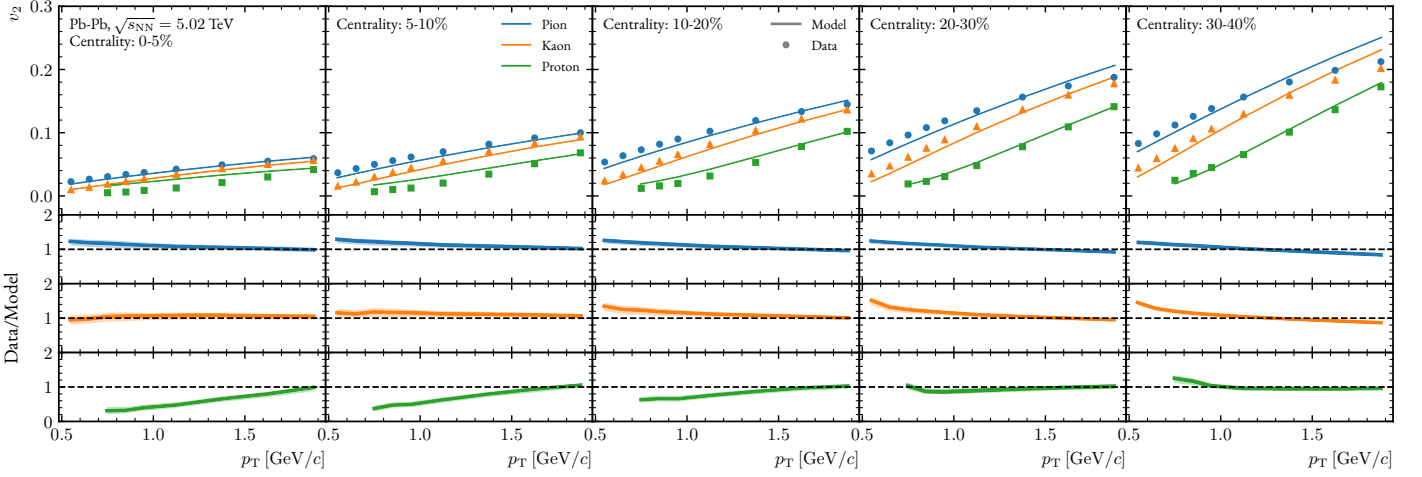


Figure 5.23: MAP estimates of v_2 for Pb–Pb collisions at $\sqrt{s_{\text{NN}}} = 5.02$ TeV, where the model parameters are estimated through a combined analysis of Pb–Pb and Xe–Xe collisions.

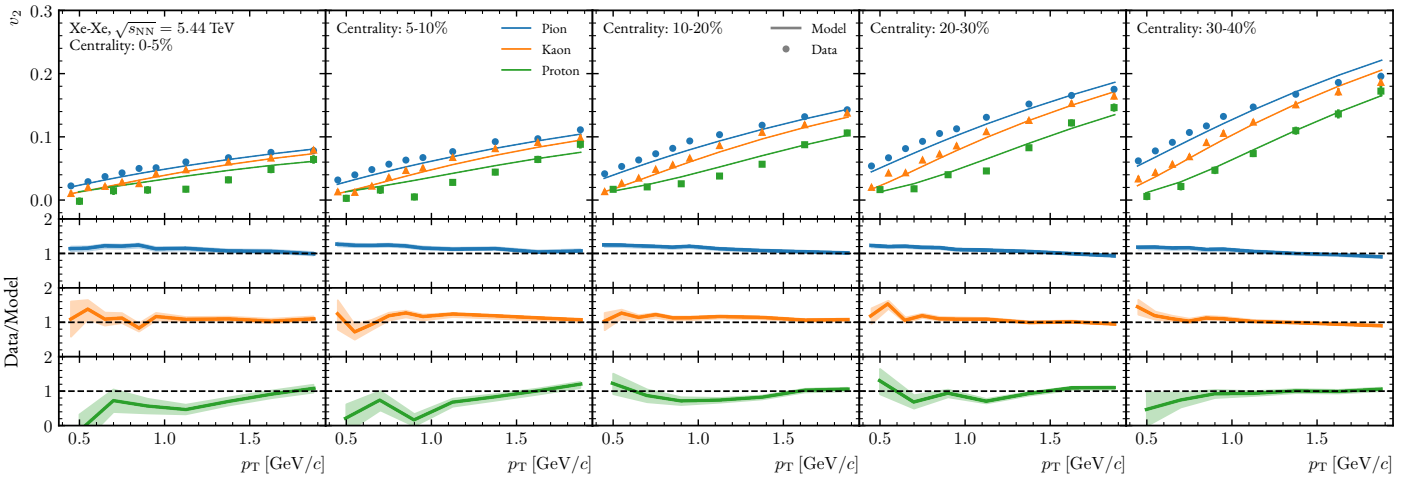


Figure 5.24: MAP estimates of v_2 for Xe–Xe collisions at $\sqrt{s_{\text{NN}}} = 5.44$ TeV, where the model parameters are estimated through a combined analysis of Pb–Pb and Xe–Xe collisions.

The χ^2/N_{dof} values for the MAP estimates throughout this thesis are calculated using Equation 5.6 and are reported in Table 5.4. In this equation, N_{points} denotes the number of p_{T} values used in the Bayesian inference for the respective collision system, while $n_{\text{parameters}}$ represents the number of model parameters. The term σ_i represents the statistical and systematic experimental data uncertainties, summed in quadrature. The subtraction of 1 in the denominator follows the approach outlined in [156], which accounts for the adjustment in degrees of freedom due to the estimation process.

$$\frac{\chi^2}{N_{\text{dof}}} = \frac{1}{N_{\text{points}} - n_{\text{parameters}} - 1} \sum_{i=1}^n \left(\frac{\mathbf{y}_{\text{model},i} - \mathbf{y}_{\text{exp},i}}{\sigma_i} \right)^2. \quad (5.6)$$

Table 5.4: χ^2/N_{dof} values for MAP estimates across different collision systems and observables.

Collision system	Observables	χ^2/N_{dof}
Pb–Pb, $\sqrt{s_{\text{NN}}} = 2.76$ TeV	p_{T} -differential spectra + $v_2(p_{\text{T}})$	3.004
Pb–Pb, $\sqrt{s_{\text{NN}}} = 2.76$ TeV	p_{T} -differential spectra + $v_n(p_{\text{T}})$	4.431
Pb–Pb, $\sqrt{s_{\text{NN}}} = 5.02$ TeV	p_{T} -differential spectra + $v_2(p_{\text{T}})$	11.806
Xe–Xe, $\sqrt{s_{\text{NN}}} = 5.44$ TeV	p_{T} -differential spectra + $v_2(p_{\text{T}})$	6.152
Combined analysis	p_{T} -differential spectra + $v_2(p_{\text{T}})$	7.640

The χ^2/N_{dof} values indicate the goodness of the fit for each collision system. Notably, the χ^2/N_{dof} for Pb–Pb collisions at $\sqrt{s_{\text{NN}}} = 5.02$ TeV is significantly higher than that for Pb–Pb collisions at $\sqrt{s_{\text{NN}}} = 2.76$ TeV. This can be attributed to the smaller experimental data uncertainties for the $\sqrt{s_{\text{NN}}} = 5.02$ TeV data, which makes the fit more sensitive to discrepancies.

In the combined analysis, the χ^2/N_{dof} value lies between the ranges observed for the individual collision systems, suggesting that the combined analysis effectively compensates for the higher and lower χ^2/N_{dof} values of the individual systems.

6 CONCLUSION AND OUTLOOK

In this thesis, the Bayesian inference framework has been extended and employed in two significant studies to investigate key aspects of heavy-ion collisions and the properties of QGP.

The first study centered on quantifying the pion excess observed in the very low- p_T regime in heavy-ion collisions. This analysis spanned various centrality classes, collision energies, and collision systems at the LHC and top RHIC energy. As a preliminary step, a p_T range scan was conducted to identify the optimal pion p_T range for Bayesian inference, leading to the determination that the ideal range is $0.5 < p_T^\pi < 2.0$ GeV/ c . Subsequently, a significant excess in pion yield was systematically observed across all centrality classes and collision systems at low p_T . The relative excess remained consistent at 10–20% across different centrality classes, indicating that fluid dynamic calculations account for 80–90% of the measured pion production in heavy-ion collisions. This suggests that the observed low- p_T component arises from physics mechanisms beyond thermal production.

In the second study, the Bayesian inference framework was applied to further investigate the model parameters associated with the evolution of heavy-ion collisions, with a particular focus on the initialization time, kinetic freeze-out temperature, and key transport coefficients of the quark-gluon plasma, namely the shear and bulk viscosity to entropy density ratios. By incorporating p_T -differential spectra and p_T -differential flow coefficients ($v_n(p_T)$) of pions, kaons, and protons from Pb-Pb and Xe-Xe collisions at varying energies and centrality classes, this study extended the analysis beyond the limitations of previous work [122]. The inclusion of flow coefficients, particularly $v_2(p_T)$, $v_3(p_T)$, and $v_4(p_T)$, allowed for a more precise estimation of the temperature-dependent shear viscosity to entropy density ratio.

While the extension of the Bayesian inference framework has provided a robust foundation, there remain several critical areas where further enhancements can increase the precision and scope of the analysis. These potential improvements and additional research directions are outlined below.

- In the current study, the TRENTo model parameters are not estimated through Bayesian analysis; instead, they are fixed based on previous work, as detailed in Ref. [131]. This approach restricts the exploration of the full parameter space for initial conditions. By varying these initial conditions and including the TRENTo parameters in the Bayesian analysis, we can potentially identify optimal parameters that lead to more accurate hydrodynamic evolution and a better match between model predictions and experimental data.
- Additional observables, such as the mean transverse momentum $\langle p_T \rangle$ and its fluctuations, can be incorporated to further constrain model parameters and transport coefficients. These observables are

particularly valuable if the TRENTo model parameters are included in the Bayesian framework, as $\langle p_T \rangle$ fluctuations serve as a sensitive probe of initial state fluctuations [157, 158].

- Additional model parameters, such as the peak temperature T_{peak} and the width T_{width} of the bulk viscosity parametrization (as defined in Equation 2.48), along with the shear relaxation time τ_{shear} (as given in Equation 2.50), can also be incorporated into the Bayesian analysis, as demonstrated in previous studies [122]. Although these parameters were found to have a negligible impact when only the p_T spectra were used as observables in Ref. [122], the inclusion of $\langle p_T \rangle$ could offer tighter constraints on them [35]. This approach has the potential to provide more precise estimations of viscosity and relaxation times, thereby enhancing our understanding of the transport properties of the QGP.
- A theoretically motivated parametrization for the temperature-dependent bulk viscosity to entropy density ratio could be employed, similar to the approach used for the shear viscosity. In the current study, we utilize a three-parameter (unnormalized) Cauchy distribution for bulk viscosity, as outlined in Ref. [66]. However, adopting a parametrization based on theoretical calculations, analogous to the Yang-Mills theory-inspired expression used for shear viscosity [64, 65], could provide a more accurate description of the bulk viscosity behavior in QCD.
- New perturbation kernels can be computed by incorporating both kinetic and chemical freeze-out temperatures, enabling the use of PCE in the calculation of flow coefficients. Without PCE, the model fails to capture the full strength of radial flow gained during the hadronic phase and cannot shift the flow coefficients to higher p_T values in central events, especially for particles with large mass like protons. Additionally, these new kernels would also allow for the inclusion of resonance decays, which have not been previously considered in flow coefficient calculations. Accounting for resonance decays could further improve the model's accuracy, as demonstrated in previous studies [159].
- Missing non-linear interactions can be incorporated into the model to address discrepancies observed between the model results and experimental data for $v_3(p_T)$ and $v_4(p_T)$. FLUIDUM currently treats the QGP evolution primarily as a linear response, which overlooks the significant influence of mode-couplings between different flow harmonics [146, 147]. By including these non-linear interactions, the model could provide a more accurate description of experimental data, particularly for higher-order flow coefficients.

A ADDITIONAL PRIORS AND POSTERIOR DISTRIBUTIONS

This appendix presents additional results related to the prior settings, posterior distributions, and model-to-data comparisons for the Bayesian parameter estimation in heavy-ion collisions. The figures include marginal

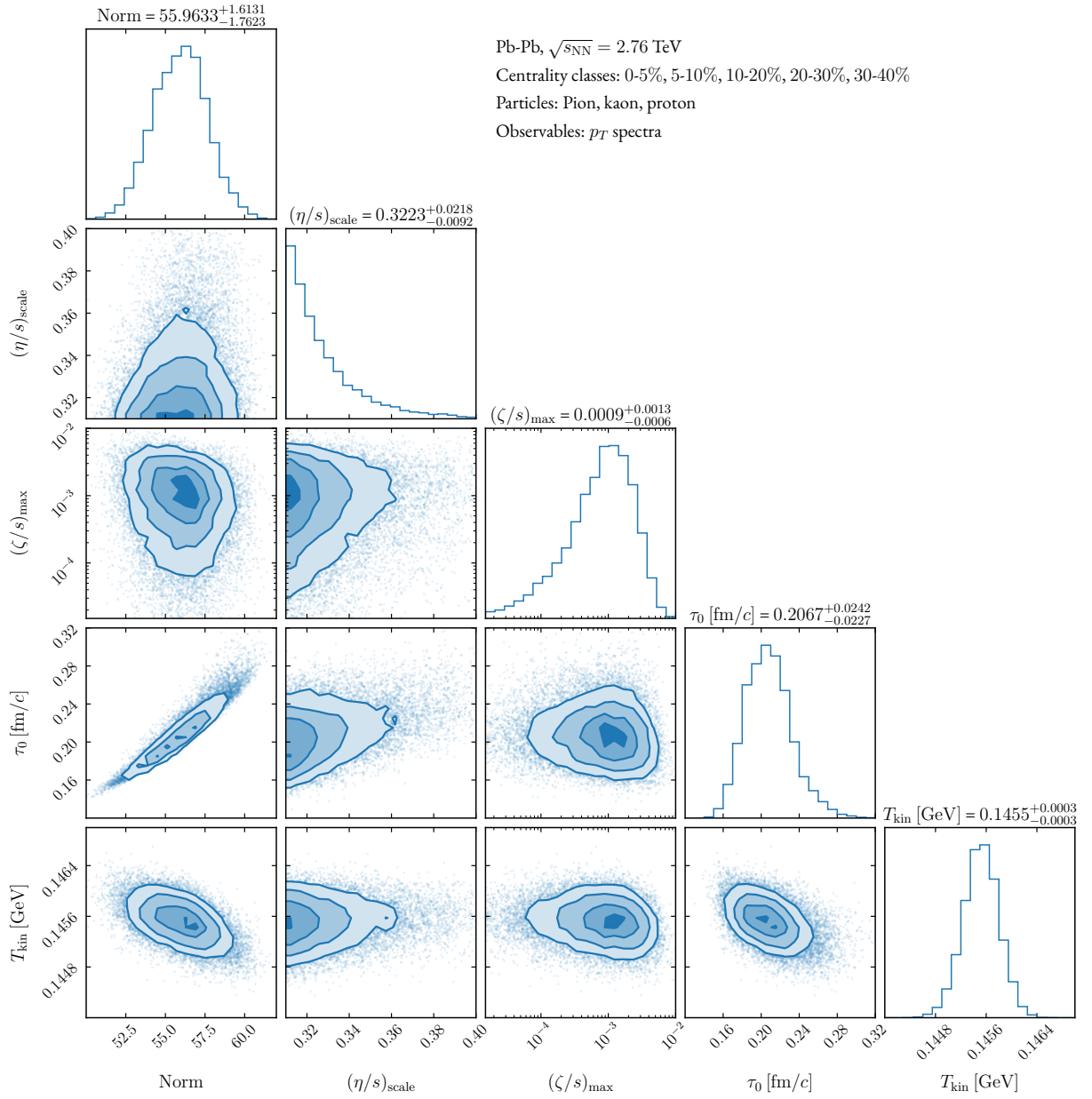


Figure A.1: Marginal and joint posterior probability density functions (PDFs) for model parameters in Pb–Pb collisions at $\sqrt{s_{NN}} = 2.76$ TeV obtained using only p_T spectra observable in the Bayesian parameter estimation.

A Additional priors and posteriors

and joint posterior probability density functions (PDFs) for model parameters obtained using different combinations of observables, such as transverse momentum spectra (p_T) and elliptic flow coefficients ($v_2(p_T)$), for Pb–Pb collisions at $\sqrt{s_{NN}} = 2.76$ TeV. Further comparisons are made between results obtained with and without the inclusion of proton data in the v_2 observable, highlighting the impact of different datasets on the parameter constraints. The appendix also covers prior distributions for specific centrality classes in Pb–Pb and Xe–Xe collisions at $\sqrt{s_{NN}} = 5.02$ and 5.44 TeV, respectively. Additionally, model predictions are compared to emulator outputs, demonstrating the accuracy and performance of the emulator in reproducing the model results.

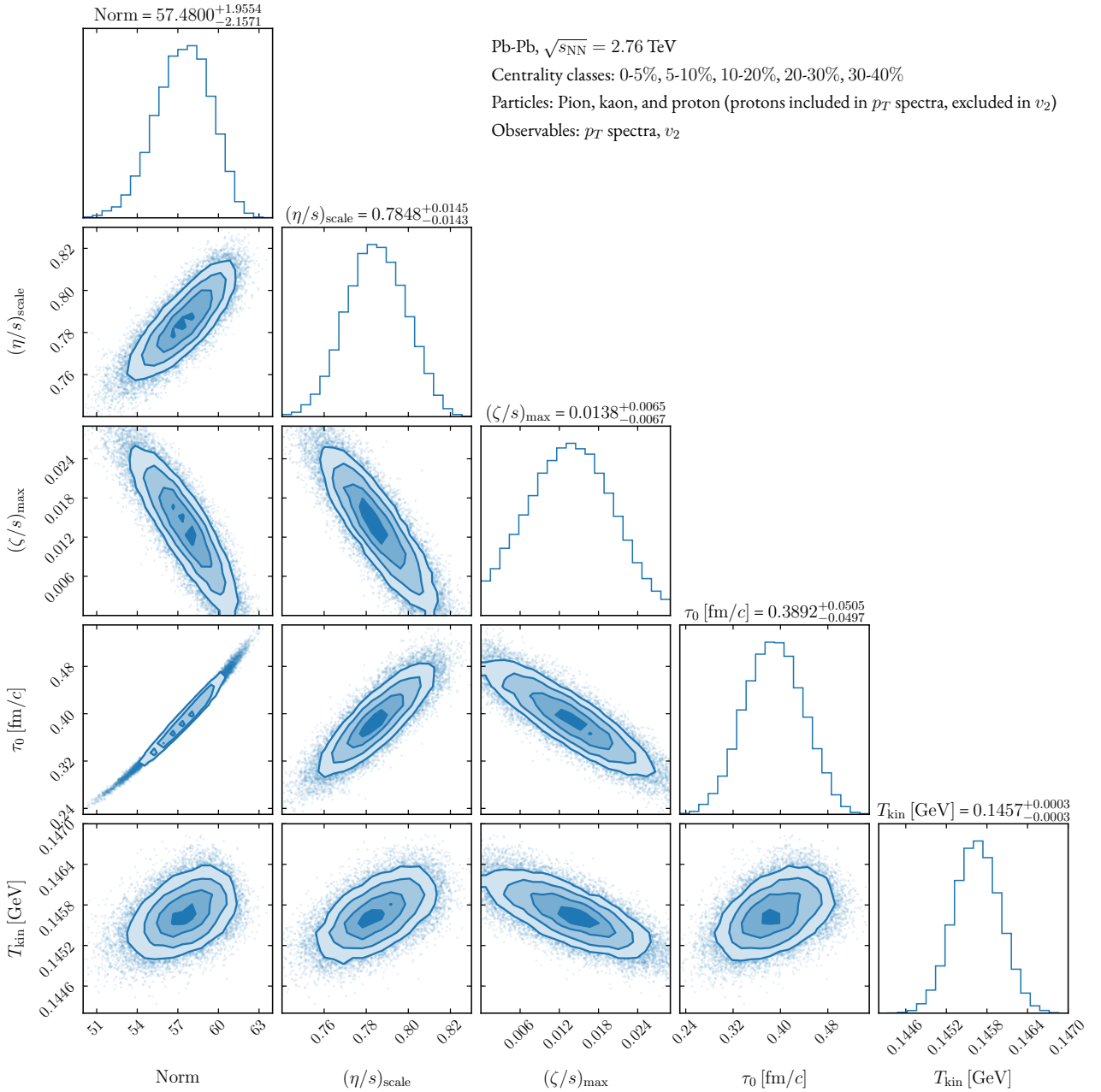


Figure A.2: Marginal and joint posterior probability density functions (PDFs) for model parameters in Pb–Pb collisions at $\sqrt{s_{NN}} = 2.76$ TeV obtained using p_T spectra and v_2 observables in the Bayesian parameter estimation when the proton data is excluded in v_2 .

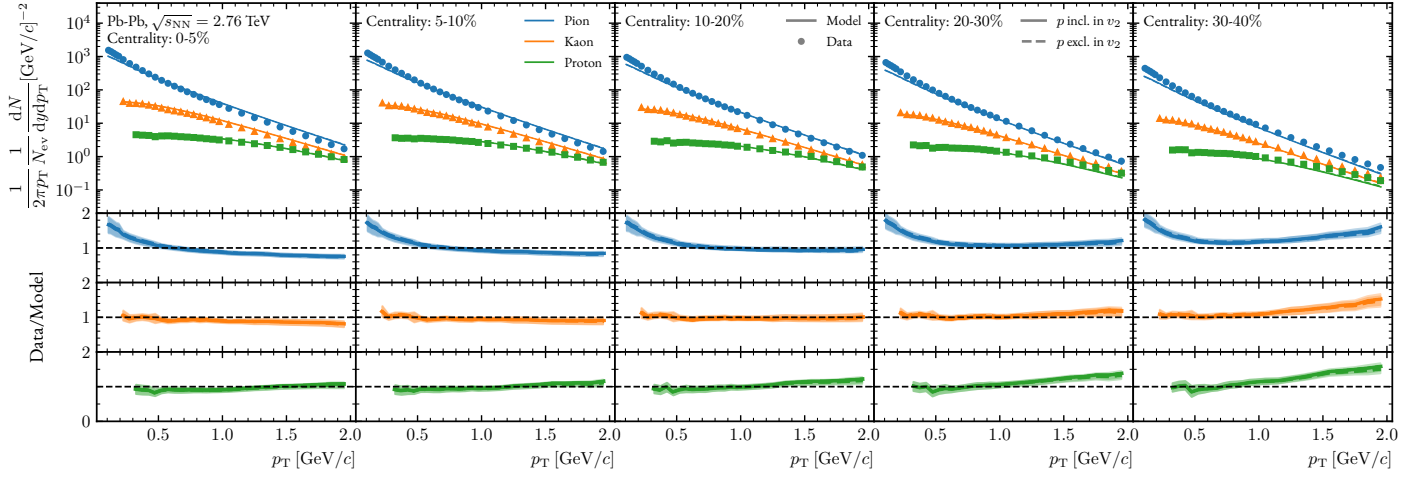


Figure A.3: Comparison of p_T spectra for Pb–Pb collisions at $\sqrt{s_{NN}} = 2.76$ TeV when the proton data is included (solid lines) and excluded (dashed lines) in the v_2 .

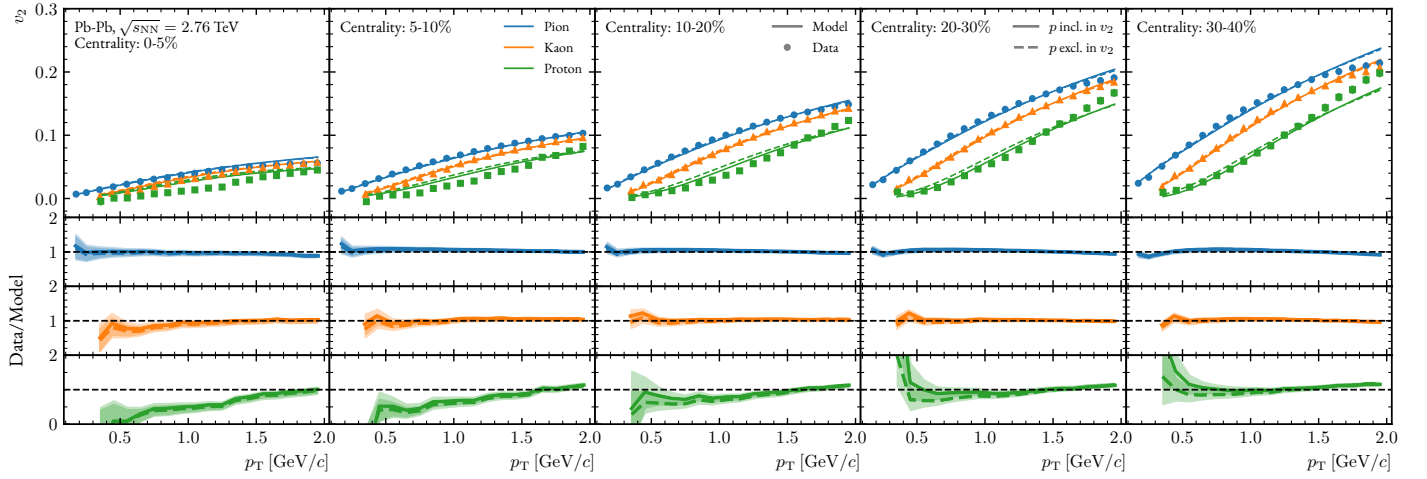


Figure A.4: Comparison of v_2 for Pb–Pb collisions at $\sqrt{s_{NN}} = 2.76$ TeV when the proton data is included (solid lines) and excluded (dashed lines) in the v_2 .

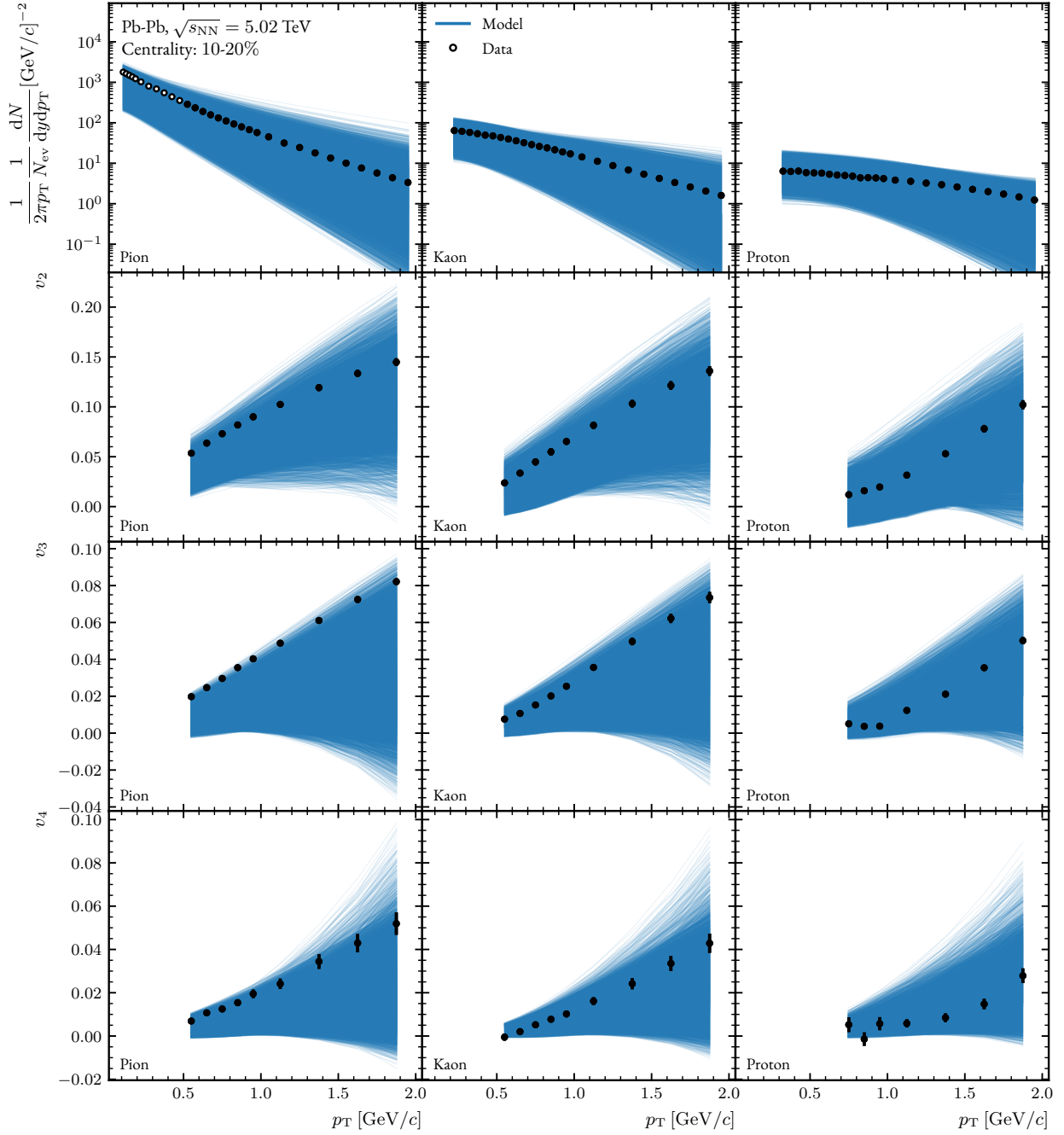


Figure A.5: Priors for the model parameters in the 10-20% centrality class for Pb–Pb collisions at $\sqrt{s_{NN}} = 5.02$ TeV.

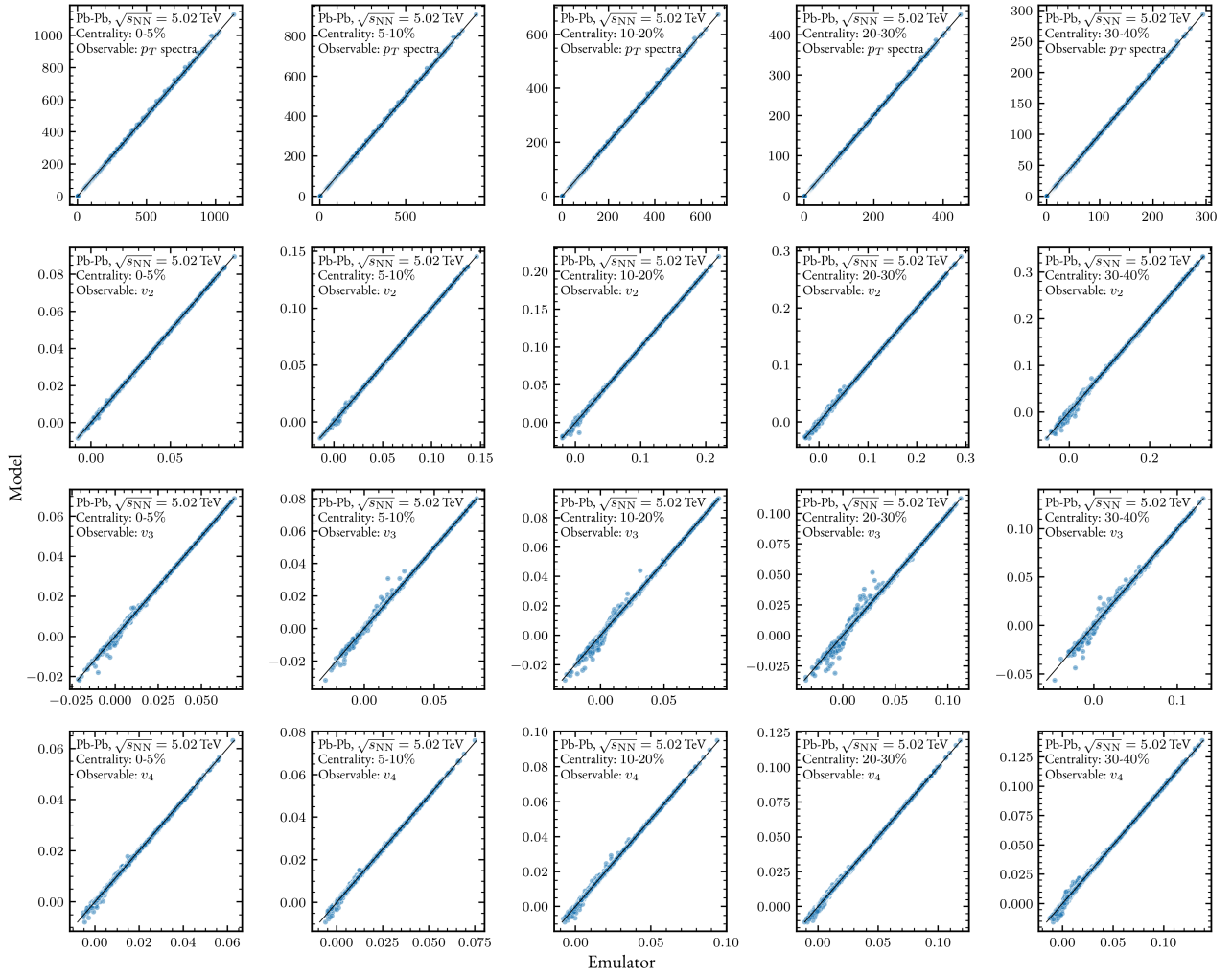


Figure A.6: Comparison between model predictions and emulator outputs for Pb-Pb collisions at $\sqrt{s_{NN}} = 5.02$ TeV, demonstrating the emulator's accuracy in reproducing the model results.

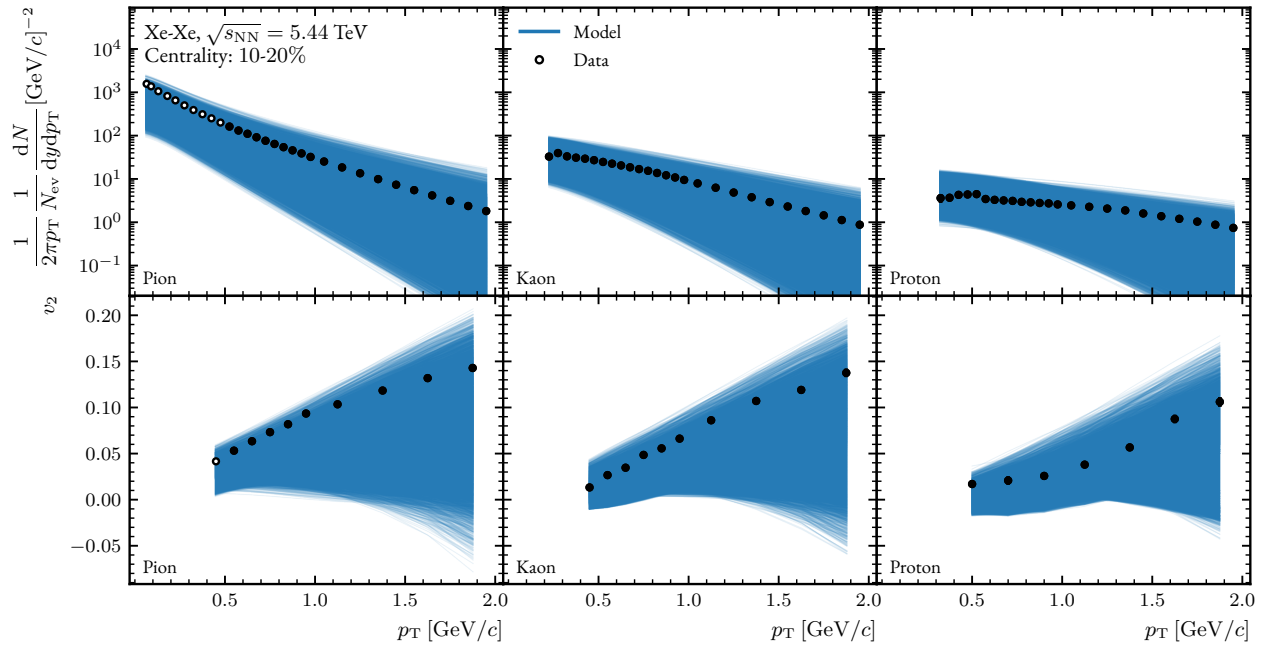


Figure A.7: Priors for the model parameters in the 10-20% centrality class for Xe–Xe collisions at $\sqrt{s_{NN}} = 5.44$ TeV.

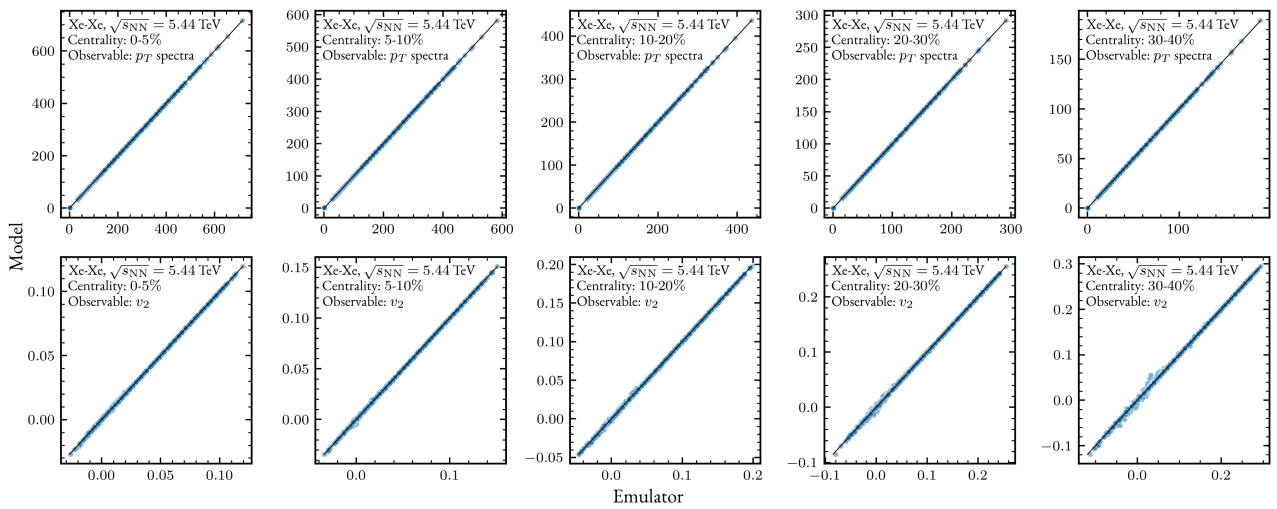


Figure A.8: Comparison between model predictions and emulator outputs for Xe–Xe collisions at $\sqrt{s_{NN}} = 5.44$ TeV, showing the emulator's performance in approximating the model results.

B QUANTITATIVE COMPARISONS OF MODEL CALCULATIONS TO EXPERIMENTAL DATA

The tables in this appendix provide quantitative comparisons derived from the 400 model results shown in [Figure 5.6](#). Each table presents a detailed comparison between model outputs and experimental measurements for p_T differential spectra, $v_2(p_T)$, $v_3(p_T)$, and $v_4(p_T)$. The first column indicates the centrality class, ranging from 0 – 5% to 30 – 40%, while the second column specifies the particle species (pion, kaon, or proton). The third column shows the transverse momentum (p_T) value used in the fit for the corresponding particle-centrality class-observable combination. The fourth and fifth columns list the mean and standard deviation (SD) of the 400 model results, respectively. The sixth column provides the experimental data corresponding to the p_T bin, with the seventh column presenting the associated experimental uncertainty, which includes statistical and systematic uncertainties summed in quadrature. The eighth column shows the total uncertainty, combining the experimental and model uncertainties. The final column represents the data-to-model ratio, calculated using the mean value of the model results, with its associated uncertainties.

Table B.1: Comparison of model results to experimental data for different centrality classes and particle species for the observable: p_T differential spectra. The columns represent the centrality class, particle species, p_T values in [GeV/c] (first and last), mean, standard deviation (SD) of 400 model results, corresponding experimental data, experimental data uncertainty (the statistical and systematic uncertainties summed in quadrature), total uncertainty (the statistical and systematic uncertainties of the experimental data and the model uncertainty summed in quadrature), and the data-to-model ratio (mean value used for the model). The total uncertainties are used in the data-to-model ratio uncertainties.

Centrality	Particle	p_T value	Mean	SD	Exp data	Exp unc.	Total unc.	Data-to-model ratio
0 – 5%	Pion	0.525	192.41995	0.74389	193.00000	9.91262	9.94049	1.00301 ± 0.05166
0 – 5%	Pion	1.950	2.24884	0.02235	1.71000	0.11673	0.11885	0.76039 ± 0.05285
0 – 5%	Kaon	0.225	44.50326	0.26687	44.61000	6.04587	6.05175	1.00240 ± 0.13598
0 – 5%	Kaon	1.950	1.10217	0.00973	0.89940	0.09363	0.09413	0.81602 ± 0.08541
0 – 5%	Proton	0.325	4.74655	0.04418	4.52600	0.66837	0.66982	0.95353 ± 0.14112
0 – 5%	Proton	1.950	0.73468	0.00582	0.81790	0.05814	0.05843	1.11328 ± 0.07953
5 – 10%	Pion	0.525	153.19576	0.60450	158.20000	7.91581	7.93886	1.03267 ± 0.05182
5 – 10%	Pion	1.950	1.68269	0.01718	1.42900	0.09749	0.09900	0.84923 ± 0.05883
5 – 10%	Kaon	0.225	36.41987	0.22971	40.28000	5.23692	5.24195	1.10599 ± 0.14393
5 – 10%	Kaon	1.950	0.83139	0.00757	0.76090	0.07930	0.07966	0.91521 ± 0.09582
5 – 10%	Proton	0.325	3.91752	0.03696	3.66400	0.52227	0.52358	0.93528 ± 0.13365
5 – 10%	Proton	1.950	0.56531	0.00460	0.67440	0.04804	0.04826	1.19298 ± 0.08537
10 – 20%	Pion	0.525	111.97466	0.45476	118.30000	5.80775	5.82553	1.05649 ± 0.05203
10 – 20%	Pion	1.950	1.09883	0.01185	1.09100	0.07481	0.07575	0.99288 ± 0.06893
10 – 20%	Kaon	0.225	28.04760	0.18882	29.52000	3.66415	3.66901	1.05250 ± 0.13081
10 – 20%	Kaon	1.950	0.55013	0.00527	0.56990	0.05899	0.05922	1.03594 ± 0.10765
10 – 20%	Proton	0.325	3.06912	0.02963	2.88700	0.39266	0.39377	0.94066 ± 0.12830
10 – 20%	Proton	1.950	0.38574	0.00329	0.48910	0.03449	0.03465	1.26796 ± 0.08982
20 – 30%	Pion	0.525	72.53655	0.31023	79.02000	3.78583	3.79852	1.08938 ± 0.05237
20 – 30%	Pion	1.950	0.58265	0.00688	0.73340	0.05016	0.05063	1.25873 ± 0.08689
20 – 30%	Kaon	0.225	19.93644	0.14618	20.54000	2.43977	2.44415	1.03027 ± 0.12260
20 – 30%	Kaon	1.950	0.29855	0.00311	0.36050	0.03747	0.03760	1.20751 ± 0.12593
20 – 30%	Proton	0.325	2.25356	0.02251	2.23800	0.29496	0.29582	0.99309 ± 0.13127
20 – 30%	Proton	1.950	0.21937	0.00203	0.31840	0.02253	0.02263	1.45141 ± 0.10314
30 – 40%	Pion	0.525	45.21994	0.20410	50.82000	2.36542	2.37421	1.12384 ± 0.05250
30 – 40%	Pion	1.950	0.27403	0.00359	0.47130	0.03232	0.03252	1.71989 ± 0.11868
30 – 40%	Kaon	0.225	14.06835	0.11046	13.88000	1.58534	1.58918	0.98661 ± 0.11296
30 – 40%	Kaon	1.950	0.14414	0.00172	0.23240	0.02426	0.02432	1.61231 ± 0.16873
30 – 40%	Proton	0.325	1.66052	0.01715	1.57000	0.20035	0.20108	0.94549 ± 0.12110
30 – 40%	Proton	1.950	0.11216	0.00118	0.19020	0.01354	0.01359	1.69586 ± 0.12115

Table B.2: The $v_2(p_T)$ coefficient comparison of model results to experimental data for different centrality classes and particle species. The columns represent the centrality class, particle species, p_T values in [GeV/c] (first and last), mean, standard deviation (SD) of 400 model results, corresponding experimental data, experimental data uncertainty (the statistical and systematic uncertainties summed in quadrature), total uncertainty (the statistical and systematic uncertainties of the experimental data and the model uncertainty summed in quadrature), and the data-to-model ratio (mean value used for the model). The total uncertainties are used in the data-to-model ratio uncertainties.

Centrality	Particle	p_T value	Mean	SD	Exp data	Exp unc.	Total unc.	Data-to-model ratio
0 – 5%	Pion	0.548114	0.02287	0.00007	0.02262	0.00208	0.00209	0.98907 ± 0.09120
0 – 5%	Pion	1.94846	0.06355	0.00019	0.05618	0.00276	0.00276	0.88394 ± 0.04349
0 – 5%	Kaon	0.35087	0.00571	0.00007	0.00288	0.00218	0.00218	0.50425 ± 0.38264
0 – 5%	Kaon	1.9479	0.05797	0.00015	0.05720	0.00330	0.00330	0.98675 ± 0.05700
0 – 5%	Proton	0.357532	0.00578	0.00007	-0.00437	0.00660	0.00660	-0.75656 ± 1.14170
0 – 5%	Proton	1.94861	0.04959	0.00012	0.04503	0.00376	0.00376	0.90798 ± 0.07584
5 – 10%	Pion	0.548114	0.03568	0.00011	0.03867	0.00220	0.00220	1.08386 ± 0.06170
5 – 10%	Pion	1.94846	0.10375	0.00030	0.10319	0.00329	0.00330	0.99461 ± 0.03181
5 – 10%	Kaon	0.35087	0.00702	0.00012	0.00670	0.00220	0.00221	0.95516 ± 0.31432
5 – 10%	Kaon	1.9479	0.09487	0.00026	0.09589	0.00355	0.00356	1.01084 ± 0.03749
5 – 10%	Proton	0.357532	0.00570	0.00009	-0.00499	0.00443	0.00443	-0.87534 ± 0.77702
5 – 10%	Proton	1.94861	0.07681	0.00018	0.08224	0.00439	0.00439	1.07076 ± 0.05714
10 – 20%	Pion	0.548114	0.05256	0.00017	0.05569	0.00238	0.00239	1.05960 ± 0.04540
10 – 20%	Pion	1.94846	0.15625	0.00047	0.14893	0.00402	0.00405	0.95313 ± 0.02590
10 – 20%	Kaon	0.35087	0.00923	0.00020	0.01182	0.00211	0.00212	1.28066 ± 0.22982
10 – 20%	Kaon	1.9479	0.14354	0.00043	0.14249	0.00408	0.00411	0.99269 ± 0.02860
10 – 20%	Proton	0.357532	0.00487	0.00013	0.00151	0.00361	0.00362	0.30996 ± 0.74264
10 – 20%	Proton	1.94861	0.11479	0.00031	0.12338	0.00523	0.00524	1.07487 ± 0.04565
20 – 30%	Pion	0.548114	0.06907	0.00022	0.07363	0.00262	0.00263	1.06602 ± 0.03811
20 – 30%	Pion	1.94846	0.20803	0.00066	0.19080	0.00491	0.00495	0.91719 ± 0.02381
20 – 30%	Kaon	0.35087	0.01227	0.00029	0.01496	0.00216	0.00217	1.21942 ± 0.17729
20 – 30%	Kaon	1.9479	0.19155	0.00063	0.18391	0.00496	0.00500	0.96011 ± 0.02612
20 – 30%	Proton	0.357532	0.00303	0.00018	0.01038	0.00457	0.00457	3.42973 ± 1.51106
20 – 30%	Proton	1.94861	0.15241	0.00052	0.16700	0.00625	0.00627	1.09574 ± 0.04114
30 – 40%	Pion	0.548114	0.08108	0.00027	0.08462	0.00279	0.00281	1.04365 ± 0.03462
30 – 40%	Pion	1.94846	0.24400	0.00083	0.21415	0.00539	0.00546	0.87766 ± 0.02237
30 – 40%	Kaon	0.35087	0.01694	0.00035	0.01806	0.00217	0.00220	1.06640 ± 0.12979
30 – 40%	Kaon	1.9479	0.22473	0.00083	0.20666	0.00545	0.00551	0.91956 ± 0.02452
30 – 40%	Proton	0.357532	0.00263	0.00026	0.00954	0.00556	0.00556	3.63036 ± 2.11639
30 – 40%	Proton	1.94861	0.17779	0.00079	0.19843	0.00683	0.00687	1.11609 ± 0.03865

Table B.3: The $v_3(p_T)$ coefficient comparison of model results to experimental data for different centrality classes and particle species. The columns represent the centrality class, particle species, p_T values in [GeV/c] (first and last), mean, standard deviation (SD) of 400 model results, corresponding experimental data, experimental data uncertainty (the statistical and systematic uncertainties summed in quadrature), total uncertainty (the statistical and systematic uncertainties of the experimental data and the model uncertainty summed in quadrature), and the data-to-model ratio (mean value used for the model). The total uncertainties are used in the data-to-model ratio uncertainties.

Centrality	Particle	p_T value	Mean	SD	Exp data	Exp unc.	Total unc.	Data-to-model ratio
0 – 5%	Pion	0.594128	0.01306	0.00004	0.01577	0.00414	0.00414	1.20761 ± 0.31722
0 – 5%	Pion	1.99433	0.05150	0.00020	0.06891	0.00421	0.00422	1.33802 ± 0.08189
0 – 5%	Kaon	0.437333	0.00327	0.00004	0.00035	0.00313	0.00313	0.10768 ± 0.95718
0 – 5%	Kaon	1.99495	0.04975	0.00019	0.06355	0.00373	0.00373	1.27737 ± 0.07508
0 – 5%	Proton	0.526573	0.00214	0.00004	-0.00002	0.00334	0.00334	-0.00781 ± 1.56459
0 – 5%	Proton	1.89632	0.04288	0.00017	0.04068	0.00318	0.00318	0.94870 ± 0.07427
5 – 10%	Pion	0.594128	0.01543	0.00005	0.01847	0.00354	0.00354	1.19748 ± 0.22939
5 – 10%	Pion	1.99433	0.05996	0.00025	0.07804	0.00363	0.00364	1.30149 ± 0.06064
5 – 10%	Kaon	0.437333	0.00391	0.00005	0.00114	0.00229	0.00229	0.29265 ± 0.58652
5 – 10%	Kaon	1.99495	0.05779	0.00024	0.07105	0.00306	0.00307	1.22945 ± 0.05318
5 – 10%	Proton	0.526573	0.00214	0.00004	-0.00018	0.00394	0.00394	-0.08520 ± 1.84053
5 – 10%	Proton	1.89632	0.04920	0.00020	0.04902	0.00378	0.00379	0.99644 ± 0.07704
10 – 20%	Pion	0.594128	0.01812	0.00005	0.02068	0.00361	0.00361	1.14144 ± 0.19923
10 – 20%	Pion	1.99433	0.06911	0.00032	0.08461	0.00373	0.00375	1.22422 ± 0.05422
10 – 20%	Kaon	0.437333	0.00485	0.00005	0.00161	0.00327	0.00327	0.33137 ± 0.67471
10 – 20%	Kaon	1.99495	0.06665	0.00031	0.07773	0.00387	0.00388	1.16622 ± 0.05819
10 – 20%	Proton	0.526573	0.00229	0.00006	-0.00064	0.00331	0.00331	-0.28010 ± 1.44186
10 – 20%	Proton	1.89632	0.05637	0.00026	0.05447	0.00278	0.00279	0.96628 ± 0.04955
20 – 30%	Pion	0.594128	0.02098	0.00006	0.02352	0.00315	0.00315	1.12120 ± 0.14997
20 – 30%	Pion	1.99433	0.07861	0.00041	0.09146	0.00336	0.00338	1.16340 ± 0.04301
20 – 30%	Kaon	0.437333	0.00617	0.00005	0.00369	0.00330	0.00330	0.59870 ± 0.53430
20 – 30%	Kaon	1.99495	0.07568	0.00040	0.08427	0.00392	0.00394	1.11343 ± 0.05211
20 – 30%	Proton	0.526573	0.00288	0.00007	-0.00141	0.00428	0.00428	-0.49186 ± 1.48771
20 – 30%	Proton	1.89632	0.06357	0.00035	0.06566	0.00345	0.00347	1.03292 ± 0.05454
30 – 40%	Pion	0.594128	0.02298	0.00008	0.02487	0.00265	0.00265	1.08221 ± 0.11544
30 – 40%	Pion	1.99433	0.08610	0.00048	0.09491	0.00301	0.00305	1.10234 ± 0.03545
30 – 40%	Kaon	0.437333	0.00747	0.00004	0.00349	0.00370	0.00370	0.46757 ± 0.49578
30 – 40%	Kaon	1.99495	0.08245	0.00048	0.08468	0.00434	0.00436	1.02712 ± 0.05293
30 – 40%	Proton	0.526573	0.00392	0.00007	-0.00078	0.00551	0.00551	-0.19779 ± 1.40487
30 – 40%	Proton	1.89632	0.06817	0.00044	0.07786	0.00442	0.00444	1.14219 ± 0.06513

Table B.4: The $v_4(p_T)$ coefficient comparison of model results to experimental data for different centrality classes and particle species. The columns represent the centrality class, particle species, p_T values in [GeV/c] (first and last), mean, standard deviation (SD) of 400 model results, corresponding experimental data, experimental data uncertainty (the statistical and systematic uncertainties summed in quadrature), total uncertainty (the statistical and systematic uncertainties of the experimental data and the model uncertainty summed in quadrature), and the data-to-model ratio (mean value used for the model). The total uncertainties are used in the data-to-model ratio uncertainties.

Centrality	Particle	p_T value	Mean	SD	Exp data	Exp unc.	Total unc.	Data-to-model ratio
0 – 5%	Pion	0.594128	0.00555	0.00003	0.00319	0.00792	0.00792	0.57431 ± 1.42762
0 – 5%	Pion	1.99433	0.02875	0.00023	0.05207	0.00794	0.00794	1.81132 ± 0.27626
0 – 5%	Kaon	0.437333	0.00125	0.00001	-0.00728	0.00876	0.00876	-5.82184 ± 7.00519
0 – 5%	Kaon	1.99495	0.02843	0.00023	0.04318	0.00918	0.00918	1.51908 ± 0.32300
0 – 5%	Proton	0.526573	0.00053	0.00001	-0.00020	0.00307	0.00307	-0.36719 ± 5.77060
0 – 5%	Proton	1.89632	0.02489	0.00018	0.02154	0.00261	0.00262	0.86553 ± 0.10513
5 – 10%	Pion	0.594128	0.00634	0.00004	0.00476	0.00692	0.00692	0.75057 ± 1.09196
5 – 10%	Pion	1.99433	0.03171	0.00028	0.05575	0.00697	0.00697	1.75812 ± 0.21994
5 – 10%	Kaon	0.437333	0.00151	0.00001	-0.00687	0.00813	0.00813	-4.55831 ± 5.39735
5 – 10%	Kaon	1.99495	0.03131	0.00027	0.04767	0.00859	0.00859	1.52243 ± 0.27449
5 – 10%	Proton	0.526573	0.00064	0.00001	0.00153	0.00325	0.00325	2.37884 ± 5.07161
5 – 10%	Proton	1.89632	0.02738	0.00022	0.02614	0.00272	0.00273	0.95486 ± 0.09974
10 – 20%	Pion	0.594128	0.00740	0.00006	0.00580	0.00715	0.00715	0.78439 ± 0.96673
10 – 20%	Pion	1.99433	0.03569	0.00036	0.05807	0.00726	0.00727	1.62718 ± 0.20378
10 – 20%	Kaon	0.437333	0.00188	0.00001	-0.00487	0.00661	0.00661	-2.59105 ± 3.51983
10 – 20%	Kaon	1.99495	0.03516	0.00035	0.05003	0.00726	0.00727	1.42279 ± 0.20679
10 – 20%	Proton	0.526573	0.00084	0.00001	0.00116	0.00408	0.00408	1.37816 ± 4.83255
10 – 20%	Proton	1.89632	0.03071	0.00029	0.02918	0.00299	0.00300	0.95013 ± 0.09774
20 – 30%	Pion	0.594128	0.00814	0.00008	0.00720	0.00693	0.00693	0.88442 ± 0.85194
20 – 30%	Pion	1.99433	0.03876	0.00047	0.06336	0.00715	0.00716	1.63460 ± 0.18479
20 – 30%	Kaon	0.437333	0.00218	0.00002	-0.00524	0.00540	0.00540	-2.40282 ± 2.47922
20 – 30%	Kaon	1.99495	0.03785	0.00046	0.05336	0.00630	0.00631	1.40966 ± 0.16677
20 – 30%	Proton	0.526573	0.00107	0.00002	0.00140	0.00620	0.00620	1.29927 ± 5.76815
20 – 30%	Proton	1.89632	0.03266	0.00040	0.03913	0.00481	0.00483	1.19821 ± 0.14793
30 – 40%	Pion	0.594128	0.00757	0.00011	0.00815	0.00654	0.00654	1.07717 ± 0.86354
30 – 40%	Pion	1.99433	0.03772	0.00057	0.06178	0.00695	0.00697	1.63787 ± 0.18480
30 – 40%	Kaon	0.437333	0.00202	0.00003	-0.00242	0.00826	0.00826	-1.19740 ± 4.08839
30 – 40%	Kaon	1.99495	0.03653	0.00056	0.05454	0.00894	0.00895	1.49299 ± 0.24510
30 – 40%	Proton	0.526573	0.00097	0.00003	-0.00012	0.00716	0.00716	-0.12000 ± 7.37119
30 – 40%	Proton	1.89632	0.02973	0.00051	0.04211	0.00510	0.00513	1.41662 ± 0.17246

C ANALYSIS OF MARGINAL POSTERIOR DISTRIBUTIONS FOR MODEL PARAMETERS ACROSS CENTRALITY CLASSES IN Pb–Pb COLLISIONS AT $\sqrt{s_{\text{NN}}} = 2.76 \text{ TeV}$

In [Chapter 5](#), we demonstrated that the inclusion of higher-order flow coefficients, such as $v_3(p_T)$ and $v_4(p_T)$, poses challenges for Bayesian inference results due to the model’s limited ability to accurately describe these observables. Before reaching this conclusion, however, an additional analysis was conducted to investigate the influence of centrality class inclusion and exclusion on the model parameters using all available observables. This appendix presents the results of that analysis for readers interested in an alternative perspective of the model’s behavior across different centrality classes.

[Figure C.1](#) illustrates the marginal posterior probability density functions (PDFs) for the model parameters in Pb–Pb collisions at $\sqrt{s_{\text{NN}}} = 2.76 \text{ TeV}$, obtained using p_T -differential spectra, $v_2(p_T)$, $v_3(p_T)$, and $v_4(p_T)$ observables within a Bayesian framework. Each row in the figure represents the marginal PDFs obtained from Bayesian fits performed for different centrality classes. The centrality classes, denoted as 0-5%, 5-10%, 10-20%, 20-30%, and 30-40%, are sequentially excluded to examine the robustness of the parameter estimates. The marginal PDFs are presented as the median values of the marginal distributions, with 68% confidence intervals represented by error bars. Each column corresponds to a distinct model parameter, providing a comprehensive overview of their posterior distributions across varying centrality exclusions. The parameters examined include $(\eta/s)_{\text{scale}}$, $(\zeta/s)_{\text{max}}$, T_{kin} , and Norm/τ_0 .

The $(\eta/s)_{\text{scale}}$ shows consistent posterior distributions across most cases, except for the 0-5% centrality class, which exhibits a notable deviation. This deviation could be attributed to the larger radial flow present in the most central collisions, which is not well reproduced due to the absence of PCE in the model. In such central collisions, larger values of η/s might modify the particle production at higher p_T , trying to compensate for the significant radial flow observed in the 0-5% centrality class.

The $(\zeta/s)_{\text{max}}$ exhibits relatively stable posterior distributions for most centrality classes, with some notable deviations. Specifically, the 30-40% centrality class has the narrowest credible intervals among the single centrality cases, followed by the 20-30%, 10-20%, 5-10%, and 0-5% classes. This progression suggests that the inclusion of the 30-40% class significantly affects the overall fit, resulting in narrower credible intervals when all centrality classes are included. As certain centrality classes are excluded, the credible intervals for $(\zeta/s)_{\text{max}}$

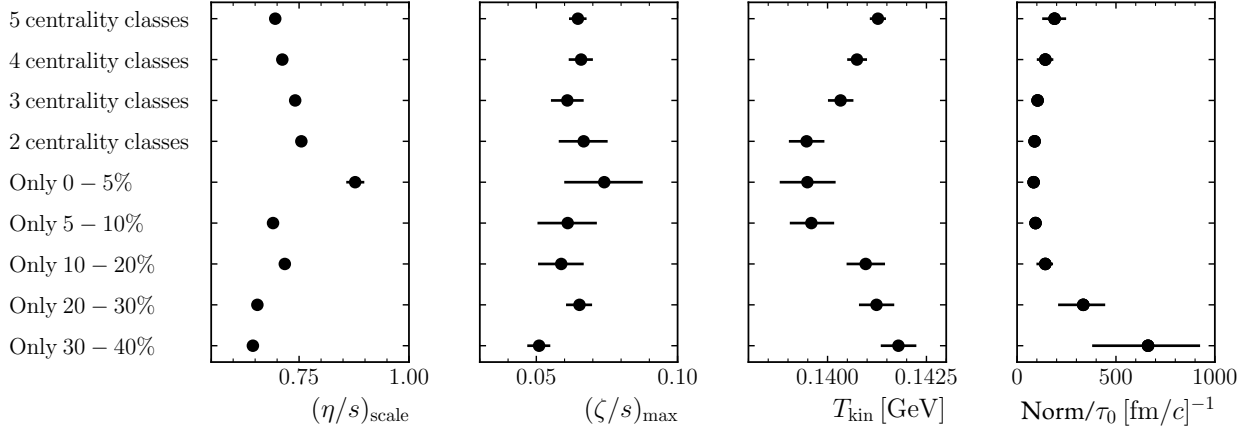


Figure C.1: Marginal posterior PDFs of parameters for different centrality cases in Pb–Pb collisions at $\sqrt{s_{\text{NN}}} = 2.76 \text{ TeV}$, obtained using p_{T} differential spectra, $v_2(p_{\text{T}})$, $v_3(p_{\text{T}})$, and $v_4(p_{\text{T}})$ observables. The parameters shown are $(\eta/s)_{\text{scale}}$, $(\zeta/s)_{\text{max}}$, T_{kin} , and Norm/τ_0 . Starting with all 5 centrality classes, the most peripheral centrality class is excluded stepwise, resulting in 4, 3, and 2 centrality classes, respectively. The marginal PDFs are represented as the median of the marginal distribution with 68% confidence interval uncertainties, depicted as error bars.

widen, indicating that the fit robustness is particularly enhanced by the constraints provided by the 30-40% centrality class data.

The T_{kin} shows a clear increasing trend as collisions become more peripheral. This increase in T_{kin} can be understood by examining the dynamics of the system at different centralities. In the most central collisions, the nuclei overlap significantly, creating a high-energy density and temperature in the initial state. The system formed in these collisions undergoes more explosive expansion due to large pressure gradients, resulting in significant radial flow [20]. As the system expands rapidly, it cools substantially before reaching kinetic freeze-out, leading to a lower T_{kin} . In more peripheral collisions, the overlap region between the colliding nuclei is smaller, resulting in lower initial energy density and temperature. The system experiences larger initial spatial anisotropy, leading to higher flow coefficients driven by geometric anisotropy. However, due to the smaller pressure gradients, the radial expansion is less pronounced, and the cooling is less efficient. As a result, the system reaches kinetic freeze-out at a relatively higher temperature, resulting in a higher T_{kin} . This trend is reflected in the fits that include multiple centrality classes. As higher centrality classes are included, the inferred estimates for T_{kin} tend to be higher, capturing the varying freeze-out conditions across different centralities. The model’s sensitivity to these differences in expansion and cooling dynamics underscores the importance of considering centrality-dependent behavior in the analysis of heavy-ion collision data. This systematic shift of T_{kin} is also observed in Chapter 4 where its median value was increasing from central to peripheral collisions. This observation aligns with previous findings obtained using a Blast-wave fit [113] and supports the idea of a more rapid expansion with increasing centrality [20]. In peripheral collisions, this behavior is consistent with the expectation of a shorter-lived fireball exhibiting stronger radial pressure gradients [160].

The normalization factor divided by the thermalization time, Norm/τ_0 , displays broader credible intervals compared to other parameters. This parameter is crucial as it scales the initial entropy density profile,

$\langle T_R(r) \rangle$, which is used to determine the initial conditions for the hydrodynamic evolution. In central collisions, the system's high energy density and temperature result in a well-defined initial entropy density profile. The high multiplicity and significant particle production provide a robust constraint to Norm/τ_0 . In more peripheral collisions, the lower multiplicity and increased fluctuations in the initial entropy density profile lead to greater uncertainty in the Norm/τ_0 estimates. The fits for two centrality classes (excluding the most peripheral ones) yield the most constrained estimates with the narrowest credible intervals. As additional peripheral centralities are included, the credible intervals widen, and the fit starts to shift, indicating increased uncertainty. This suggests that the inclusion of peripheral centralities, with their lower multiplicity and higher fluctuations, complicates the estimation of Norm/τ_0 and highlights the sensitivity of this parameter to the varying initial state conditions and its fluctuations.

BIBLIOGRAPHY

1. W. Marciano and H. Pagels. “Quantum chromodynamics”. *Physics Reports* 36:3, 1978, pp. 137–276. ISSN: 0370-1573. DOI: [https://doi.org/10.1016/0370-1573\(78\)90208-9](https://doi.org/10.1016/0370-1573(78)90208-9). URL: <https://www.sciencedirect.com/science/article/pii/0370157378902089>.
2. D. J. Gross and F. Wilczek. “Ultraviolet Behavior of Non-Abelian Gauge Theories”. *Phys. Rev. Lett.* 30, 26 1973, pp. 1343–1346. DOI: [10.1103/PhysRevLett.30.1343](https://doi.org/10.1103/PhysRevLett.30.1343). URL: <https://link.aps.org/doi/10.1103/PhysRevLett.30.1343>.
3. H. D. Politzer. “Reliable Perturbative Results for Strong Interactions?” *Phys. Rev. Lett.* 30, 26 1973, pp. 1346–1349. DOI: [10.1103/PhysRevLett.30.1346](https://doi.org/10.1103/PhysRevLett.30.1346). URL: <https://link.aps.org/doi/10.1103/PhysRevLett.30.1346>.
4. S. Bethke. “Determination of the QCD coupling α_s ”. *Journal of Physics G: Nuclear and Particle Physics* 26:7, 2000, R27–R66. ISSN: 1361-6471. DOI: [10.1088/0954-3899/26/7/201](https://doi.org/10.1088/0954-3899/26/7/201). URL: <http://dx.doi.org/10.1088/0954-3899/26/7/201>.
5. M. Czakon. “The four-loop QCD β -function and anomalous dimensions”. *Nuclear Physics B* 710:1–2, 2005, pp. 485–498. ISSN: 0550-3213. DOI: [10.1016/j.nuclphysb.2005.01.012](https://doi.org/10.1016/j.nuclphysb.2005.01.012). URL: <http://dx.doi.org/10.1016/j.nuclphysb.2005.01.012>.
6. R. L. Workman et al. “Review of Particle Physics”. *PTEP* 2022, 2022, p. 083C01. DOI: [10.1093/ptep/ptac097](https://doi.org/10.1093/ptep/ptac097).
7. K. G. Wilson. “Confinement of quarks”. *Phys. Rev. D* 10, 8 1974, pp. 2445–2459. DOI: [10.1103/PhysRevD.10.2445](https://doi.org/10.1103/PhysRevD.10.2445). URL: <https://link.aps.org/doi/10.1103/PhysRevD.10.2445>.
8. S. Dürr, Z. Fodor, J. Frison, C. Hoelbling, R. Hoffmann, S. D. Katz, S. Krieg, T. Kurth, L. Lellouch, T. Lippert, K. K. Szabo, and G. Vulvert. “Ab Initio Determination of Light Hadron Masses”. *Science* 322:5905, 2008, pp. 1224–1227. DOI: [10.1126/science.1163233](https://doi.org/10.1126/science.1163233). eprint: <https://www.science.org/doi/pdf/10.1126/science.1163233>. URL: <https://www.science.org/doi/abs/10.1126/science.1163233>.
9. E. Follana, C. T. H. Davies, G. P. Lepage, and J. Shigemitsu. “High-Precision Determination of the π , K , D , and D_s Decay Constants from Lattice QCD”. *Phys. Rev. Lett.* 100, 6 2008, p. 062002. DOI: [10.1103/PhysRevLett.100.062002](https://doi.org/10.1103/PhysRevLett.100.062002). URL: <https://link.aps.org/doi/10.1103/PhysRevLett.100.062002>.

10. J. C. Collins and M. J. Perry. “Superdense Matter: Neutrons or Asymptotically Free Quarks?” *Phys. Rev. Lett.* 34, 21 1975, pp. 1353–1356. DOI: [10.1103/PhysRevLett.34.1353](https://doi.org/10.1103/PhysRevLett.34.1353). URL: <https://link.aps.org/doi/10.1103/PhysRevLett.34.1353>.
11. E. V. Shuryak. “Quantum chromodynamics and the theory of superdense matter”. *Physics Reports* 61:2, 1980, pp. 71–158. ISSN: 0370-1573. DOI: [https://doi.org/10.1016/0370-1573\(80\)90105-2](https://doi.org/10.1016/0370-1573(80)90105-2). URL: <https://www.sciencedirect.com/science/article/pii/0370157380901052>.
12. “The Frontiers of Nuclear Science: A Long-Range Plan”, 2007. DOI: [10.2172/1375323](https://doi.org/10.2172/1375323). URL: <https://www.osti.gov/biblio/1375323>.
13. Y. Aoki, G. Endrodi, Z. Fodor, S. D. Katz, and K. K. Szabo. “The Order of the quantum chromodynamics transition predicted by the standard model of particle physics”. *Nature* 443, 2006, pp. 675–678. DOI: [10.1038/nature05120](https://doi.org/10.1038/nature05120). arXiv: [hep-lat/0611014](https://arxiv.org/abs/hep-lat/0611014).
14. A. Bazavov, T. Bhattacharya, M. Cheng, C. DeTar, H.-T. Ding, S. Gottlieb, R. Gupta, P. Hegde, U. M. Heller, F. Karsch, E. Laermann, L. Levkova, S. Mukherjee, P. Petreczky, C. Schmidt, R. A. Soltz, W. Soeldner, R. Sugar, D. Toussaint, W. Unger, and P. Vranas. “Chiral and deconfinement aspects of the QCD transition”. *Phys. Rev. D* 85, 5 2012, p. 054503. DOI: [10.1103/PhysRevD.85.054503](https://doi.org/10.1103/PhysRevD.85.054503). URL: <https://link.aps.org/doi/10.1103/PhysRevD.85.054503>.
15. D. Boyanovsky, H. de Vega, and D. Schwarz. “Phase Transitions in the Early and Present Universe”. *Annual Review of Nuclear and Particle Science* 56:Volume 56, 2006, 2006, pp. 441–500. ISSN: 1545-4134. DOI: <https://doi.org/10.1146/annurev.nucl.56.080805.140539>. URL: <https://www.annualreviews.org/content/journals/10.1146/annurev.nucl.56.080805.140539>.
16. E. Laermann and O. Philipsen. “LATTICE QCD AT FINITE TEMPERATURE”. *Annual Review of Nuclear and Particle Science* 53:Volume 53, 2003, 2003, pp. 163–198. ISSN: 1545-4134. DOI: <https://doi.org/10.1146/annurev.nucl.53.041002.110609>. URL: <https://www.annualreviews.org/content/journals/10.1146/annurev.nucl.53.041002.110609>.
17. I. Arsene, I. Bearden, D. Beavis, C. Besliu, B. Budick, H. Bøggild, C. Chasman, C. Christensen, P. Christiansen, J. Cibor, R. Debbe, E. Enger, J. Gaardhøje, M. Germinario, O. Hansen, A. Holm, A. Holme, K. Hagel, H. Ito, E. Jakobsen, A. Jipa, F. Jundt, J. Jørdre, C. Jørgensen, R. Karabowicz, E. Kim, T. Kozik, T. Larsen, J. Lee, Y. Lee, S. Lindahl, G. Løvholden, Z. Majka, A. Makeev, M. Mikelsen, M. Murray, J. Natowitz, B. Neumann, B. Nielsen, D. Ouerdane, R. Płaneta, F. Rami, C. Ristea, O. Ristea, D. Röhrich, B. Samset, D. Sandberg, S. Sanders, R. Scheetz, P. Staszczel, T. Tvetter, F. Videbæk, R. Wada, Z. Yin, and I. Zgura. “Quark–gluon plasma and color glass condensate at RHIC? The perspective from the BRAHMS experiment”. *Nuclear Physics A* 757:1, 2005. First Three Years of Operation of RHIC, pp. 1–27. ISSN: 0375-9474. DOI: <https://doi.org/10.1016/j.nuclphysa.2005.02.130>. URL: <https://www.sciencedirect.com/science/article/pii/S0375947405002770>.

18. K. Adcox et al. “Formation of dense partonic matter in relativistic nucleus–nucleus collisions at RHIC: Experimental evaluation by the PHENIX Collaboration”. *Nuclear Physics A* 757:1, 2005. First Three Years of Operation of RHIC, pp. 184–283. ISSN: 0375-9474. DOI: <https://doi.org/10.1016/j.nuclphysa.2005.03.086>. URL: <https://www.sciencedirect.com/science/article/pii/S0375947405005300>.
19. B. Back, M. Baker, M. Ballintijn, D. Barton, B. Becker, R. Betts, A. Bickley, R. Bindel, A. Budzanowski, W. Busza, A. Carroll, Z. Chai, M. Decowski, E. García, T. Gburek, N. George, K. Gulbrandsen, S. Gushue, C. Halliwell, J. Hamblen, A. Harrington, M. Hauer, G. Heintzelman, C. Henderson, D. Hofman, R. Hollis, R. Hołyński, B. Holzman, A. Iordanova, E. Johnson, J. Kane, J. Katzy, N. Khan, W. Kucewicz, P. Kulinich, C. Kuo, J. Lee, W. Lin, S. Manly, D. McLeod, A. Mignerey, R. Nouicer, A. Olszewski, R. Pak, I. Park, H. Pernegger, C. Reed, L. Remsberg, M. Reuter, C. Roland, G. Roland, L. Rosenberg, J. Sagerer, P. Sarin, P. Sawicki, H. Seals, I. Sedykh, W. Skulski, C. Smith, M. Stankiewicz, P. Steinberg, G. Stephans, A. Sukhanov, J.-L. Tang, M. Tonjes, A. Trzupek, C. Vale, G. van Nieuwenhuizen, S. Vaurynovich, R. Verrier, G. Veres, E. Wenger, F. Wolfs, B. Wosiek, K. Woźniak, A. Wuosmaa, B. Wysłouch, and J. Zhang. “The PHOBOS perspective on discoveries at RHIC”. *Nuclear Physics A* 757:1, 2005. First Three Years of Operation of RHIC, pp. 28–101. ISSN: 0375-9474. DOI: <https://doi.org/10.1016/j.nuclphysa.2005.03.084>. URL: <https://www.sciencedirect.com/science/article/pii/S0375947405005282>.
20. J. Adams et al. “Experimental and theoretical challenges in the search for the quark–gluon plasma: The STAR Collaboration’s critical assessment of the evidence from RHIC collisions”. *Nuclear Physics A* 757:1, 2005. First Three Years of Operation of RHIC, pp. 102–183. ISSN: 0375-9474. DOI: <https://doi.org/10.1016/j.nuclphysa.2005.03.085>. URL: <https://www.sciencedirect.com/science/article/pii/S0375947405005294>.
21. M. Aaboud et al. “Jet energy scale measurements and their systematic uncertainties in proton-proton collisions at $\sqrt{s} = 13$ TeV with the ATLAS detector”. *Phys. Rev. D* 96:7, 2017, p. 072002. DOI: [10.1103/PhysRevD.96.072002](https://doi.org/10.1103/PhysRevD.96.072002). arXiv: [1703.09665](https://arxiv.org/abs/1703.09665) [hep-ex].
22. S. Acharya et al. “Investigations of Anisotropic Flow Using Multiparticle Azimuthal Correlations in pp, p-Pb, Xe-Xe, and Pb-Pb Collisions at the LHC”. *Phys. Rev. Lett.* 123:14, 2019, p. 142301. DOI: [10.1103/PhysRevLett.123.142301](https://doi.org/10.1103/PhysRevLett.123.142301). arXiv: [1903.01790](https://arxiv.org/abs/1903.01790) [nucl-ex].
23. P. Braun-Munzinger and B. Dönigus. “Loosely-bound objects produced in nuclear collisions at the LHC”. *Nuclear Physics A* 987, 2019, pp. 144–201. ISSN: 0375-9474. DOI: <https://doi.org/10.1016/j.nuclphysa.2019.02.006>. URL: <https://www.sciencedirect.com/science/article/pii/S0375947419300405>.
24. J. D. Bjorken. “Highly relativistic nucleus-nucleus collisions: The central rapidity region”. *Phys. Rev. D* 27, 1 1983, pp. 140–151. DOI: [10.1103/PhysRevD.27.140](https://doi.org/10.1103/PhysRevD.27.140). URL: <https://link.aps.org/doi/10.1103/PhysRevD.27.140>.

25. J. E. Bernhard. *Bayesian parameter estimation for relativistic heavy-ion collisions*. 2018. arXiv: [1804.06469](https://arxiv.org/abs/1804.06469) [nucl-th].
26. L. McLerran and R. Venugopalan. “Gluon distribution functions for very large nuclei at small transverse momentum”. *Phys. Rev. D* 49, 7 1994, pp. 3352–3355. DOI: [10.1103/PhysRevD.49.3352](https://doi.org/10.1103/PhysRevD.49.3352). URL: <https://link.aps.org/doi/10.1103/PhysRevD.49.3352>.
27. W. Busza, K. Rajagopal, and W. van der Schee. “Heavy Ion Collisions: The Big Picture and the Big Questions”. *Annual Review of Nuclear and Particle Science* 68:Volume 68, 2018, 2018, pp. 339–376. ISSN: 1545-4134. DOI: <https://doi.org/10.1146/annurev-nucl-101917-020852>. URL: <https://www.annualreviews.org/content/journals/10.1146/annurev-nucl-101917-020852>.
28. A. Kurkela, A. Mazeliauskas, J.-F. ç. Paquet, S. Schlichting, and D. Teaney. “Effective kinetic description of event-by-event pre-equilibrium dynamics in high-energy heavy-ion collisions”. *Phys. Rev. C* 99, 3 2019, p. 034910. DOI: [10.1103/PhysRevC.99.034910](https://doi.org/10.1103/PhysRevC.99.034910). URL: <https://link.aps.org/doi/10.1103/PhysRevC.99.034910>.
29. A. Andronic, P. Braun-Munzinger, K. Redlich, and J. Stachel. “Decoding the phase structure of QCD via particle production at high energy”. *Nature* 561:7723, 2018, pp. 321–330. DOI: [10.1038/s41586-018-0491-6](https://doi.org/10.1038/s41586-018-0491-6). arXiv: [1710.09425](https://arxiv.org/abs/1710.09425) [nucl-th].
30. E. Schnedermann, J. Sollfrank, and U. Heinz. “Thermal phenomenology of hadrons from 200A GeV S+S collisions”. *Phys. Rev. C* 48, 5 1993, pp. 2462–2475. DOI: [10.1103/PhysRevC.48.2462](https://doi.org/10.1103/PhysRevC.48.2462). URL: <https://link.aps.org/doi/10.1103/PhysRevC.48.2462>.
31. R. J. Fries, B. Müller, C. Nonaka, and S. A. Bass. “Hadron production in heavy ion collisions: Fragmentation and recombination from a dense parton phase”. *Phys. Rev. C* 68, 4 2003, p. 044902. DOI: [10.1103/PhysRevC.68.044902](https://doi.org/10.1103/PhysRevC.68.044902). URL: <https://link.aps.org/doi/10.1103/PhysRevC.68.044902>.
32. J.-Y. Ollitrault. “Anisotropy as a signature of transverse collective flow”. *Phys. Rev. D* 46, 1 1992, pp. 229–245. DOI: [10.1103/PhysRevD.46.229](https://doi.org/10.1103/PhysRevD.46.229). URL: <https://link.aps.org/doi/10.1103/PhysRevD.46.229>.
33. M. A. Lisa, S. Pratt, R. Soltz, and U. Wiedemann. “FEMTOSCOPY IN RELATIVISTIC HEAVY ION COLLISIONS: Two Decades of Progress”. *Annual Review of Nuclear and Particle Science* 55:Volume 55, 2005, 2005, pp. 357–402. ISSN: 1545-4134. DOI: <https://doi.org/10.1146/annurev.nucl.55.090704.151533>. URL: <https://www.annualreviews.org/content/journals/10.1146/annurev.nucl.55.090704.151533>.
34. S. Sarkar, H. Satz, and B. Sinha, eds. *The Physics of the Quark-Gluon Plasma: Introductory Lectures*. en. Vol. 785. Lecture Notes in Physics. Springer, Berlin, Heidelberg, 2010. ISBN: 978-3-642-02286-9. DOI: [10.1007/978-3-642-02286-9](https://doi.org/10.1007/978-3-642-02286-9). URL: <https://link.springer.com/10.1007/978-3-642-02286-9>.

35. U. Heinz and R. Snellings. “Collective Flow and Viscosity in Relativistic Heavy-Ion Collisions”. *Annual Review of Nuclear and Particle Science* 63:Volume 63, 2013, 2013, pp. 123–151. ISSN: 1545-4134. DOI: <https://doi.org/10.1146/annurev-nucl-102212-170540>. URL: <https://www.annualreviews.org/content/journals/10.1146/annurev-nucl-102212-170540>.
36. K. H. Ackermann et al. “Elliptic flow in Au + Au collisions at $\sqrt{s_{NN}} = 130$ GeV”. *Phys. Rev. Lett.* 86, 2001, pp. 402–407. DOI: [10.1103/PhysRevLett.86.402](https://doi.org/10.1103/PhysRevLett.86.402). arXiv: [nucl-ex/0009011](https://arxiv.org/abs/nuclex/0009011).
37. E. Shuryak. “What RHIC experiments and theory tell us about properties of quark–gluon plasma?” *Nuclear Physics A* 750:1, 2005. Quark-Gluon Plasma. New Discoveries at RHIC: Case for the Strongly Interacting Quark-Gluon Plasma. Contributions from the RBRC Workshop held May 14-15, 2004, pp. 64–83. ISSN: 0375-9474. DOI: <https://doi.org/10.1016/j.nuclphysa.2004.10.022>. URL: <https://www.sciencedirect.com/science/article/pii/S0375947404011340>.
38. S. Voloshin and Y. Zhang. “Flow study in relativistic nuclear collisions by Fourier expansion of azimuthal particle distributions”. *Zeitschrift für Physik C Particles and Fields* 70:4, 1996, pp. 665–671. ISSN: 1431-5858. DOI: [10.1007/s002880050141](https://doi.org/10.1007/s002880050141). URL: <http://dx.doi.org/10.1007/s002880050141>.
39. A. M. Poskanzer and S. A. Voloshin. “Methods for analyzing anisotropic flow in relativistic nuclear collisions”. *Phys. Rev. C* 58, 3 1998, pp. 1671–1678. DOI: [10.1103/PhysRevC.58.1671](https://doi.org/10.1103/PhysRevC.58.1671). URL: <https://link.aps.org/doi/10.1103/PhysRevC.58.1671>.
40. C. Gale, S. Jeon, and B. Schenke. “Hydrodynamic Modeling of Heavy-Ion Collisions”. *Int. J. Mod. Phys. A* 28, 2013, p. 1340011. DOI: [10.1142/S0217751X13400113](https://doi.org/10.1142/S0217751X13400113). arXiv: [1301.5893](https://arxiv.org/abs/1301.5893) [nucl-th].
41. R. J. Glauber. “Cross-sections in deuterium at high-energies”. *Phys. Rev.* 100, 1955, pp. 242–248. DOI: [10.1103/PhysRev.100.242](https://doi.org/10.1103/PhysRev.100.242).
42. D. Soeder, W. Ke, J. .- Paquet, and S. A. Bass. *Bayesian parameter estimation with a new three-dimensional initial-conditions model for ultrarelativistic heavy-ion collisions*. 2023. arXiv: [2306.08665](https://arxiv.org/abs/2306.08665) [nucl-th]. URL: <https://arxiv.org/abs/2306.08665>.
43. J. S. Moreland. *Initial conditions of bulk matter in ultrarelativistic nuclear collisions*. 2019. arXiv: [1904.08290](https://arxiv.org/abs/1904.08290) [nucl-th]. URL: <https://arxiv.org/abs/1904.08290>.
44. J. S. Moreland, J. E. Bernhard, and S. A. Bass. “Alternative ansatz to wounded nucleon and binary collision scaling in high-energy nuclear collisions”. *Phys. Rev. C* 92, 1 2015, p. 011901. DOI: [10.1103/PhysRevC.92.011901](https://doi.org/10.1103/PhysRevC.92.011901). URL: <https://link.aps.org/doi/10.1103/PhysRevC.92.011901>.
45. M. L. Miller, K. Reygers, S. J. Sanders, and P. Steinberg. “Glauber Modeling in High-Energy Nuclear Collisions”. *Annual Review of Nuclear and Particle Science* 57:Volume 57, 2007, 2007, pp. 205–243. ISSN: 1545-4134. DOI: <https://doi.org/10.1146/annurev.nucl.57.090506.123020>. URL: <https://www.annualreviews.org/content/journals/10.1146/annurev.nucl.57.090506.123020>.
46. P. F. Kolb and U. Heinz. *Hydrodynamic description of ultrarelativistic heavy-ion collisions*. 2003. arXiv: [nucl-th/0305084](https://arxiv.org/abs/nucloth/0305084) [nucl-th]. URL: <https://arxiv.org/abs/nucloth/0305084>.

47. E. Shuryak. “Why does the quark–gluon plasma at RHIC behave as a nearly ideal fluid?” *Progress in Particle and Nuclear Physics* 53:1, 2004. Heavy Ion Reaction from Nuclear to Quark Matter, pp. 273–303. ISSN: 0146-6410. DOI: <https://doi.org/10.1016/j.ppnp.2004.02.025>. URL: <https://www.sciencedirect.com/science/article/pii/S0146641004000444>.
48. L. Euler. “Principes généraux du mouvement des fluides”. *Mém. Acad. Sci. Berlin*, 1757. URL: <https://scholarlycommons.pacific.edu/euler-works/226/>.
49. L. Landau and E. Lifshitz. *Fluid Mechanics: Volume 6*. Butterworth-Heinemann; 2nd edition, 1987. ISBN: 978-0750627672.
50. L. Navier. “Mémoire sur les lois du mouvement des fluides”. *Mémoires de l’Académie royale des Sciences* 6, 1827.
51. G. G. Stokes. “On the theories of the internal friction of fluids in motion, and of the equilibrium and motion of elastic solids”, 2007.
52. W. A. Hiscock and L. Lindblom. “Generic instabilities in first-order dissipative relativistic fluid theories”. *Phys. Rev. D* 31, 4 1985, pp. 725–733. DOI: [10.1103/PhysRevD.31.725](https://doi.org/10.1103/PhysRevD.31.725). URL: <https://link.aps.org/doi/10.1103/PhysRevD.31.725>.
53. W. Israel and J. Stewart. “Transient relativistic thermodynamics and kinetic theory”. *Annals of Physics* 118:2, 1979, pp. 341–372. ISSN: 0003-4916. DOI: [https://doi.org/10.1016/0003-4916\(79\)90130-1](https://doi.org/10.1016/0003-4916(79)90130-1). URL: <https://www.sciencedirect.com/science/article/pii/0003491679901301>.
54. I. Müller. “Zum Paradoxon der Wärmeleitungstheorie”. *Zeitschrift für Physik* 198:4, 1967, pp. 329–344. DOI: [10.1007/BF01326412](https://doi.org/10.1007/BF01326412).
55. S. Floerchinger, E. Grossi, and J. Lion. “Fluid dynamics of heavy ion collisions with mode expansion”. *Phys. Rev. C* 100, 1 2019, p. 014905. DOI: [10.1103/PhysRevC.100.014905](https://doi.org/10.1103/PhysRevC.100.014905). URL: <https://link.aps.org/doi/10.1103/PhysRevC.100.014905>.
56. G. S. Denicol, H. Niemi, E. Molnár, and D. H. Rischke. “Derivation of transient relativistic fluid dynamics from the Boltzmann equation”. *Phys. Rev. D* 85, 11 2012, p. 114047. DOI: [10.1103/PhysRevD.85.114047](https://doi.org/10.1103/PhysRevD.85.114047). URL: <https://link.aps.org/doi/10.1103/PhysRevD.85.114047>.
57. E. Molnár, H. Niemi, G. S. Denicol, and D. H. Rischke. “Relative importance of second-order terms in relativistic dissipative fluid dynamics”. *Phys. Rev. D* 89, 7 2014, p. 074010. DOI: [10.1103/PhysRevD.89.074010](https://doi.org/10.1103/PhysRevD.89.074010). URL: <https://link.aps.org/doi/10.1103/PhysRevD.89.074010>.
58. A. Kirchner. “Fluid-dynamic description of an entire heavy-ion collision”. PhD thesis. Heidelberg U., 2024. DOI: [10.11588/heidok.00035168](https://doi.org/10.11588/heidok.00035168).
59. D. Boness. “Construction of flow coefficients in heavy-ion collisions using fluid dynamics with mode expansion (FluiduM)”. Master’s thesis. Universität Heidelberg, 2020.
60. A. Kirchner. “Calculation of particle spectra in heavy-ion collisions from a mode expansion with relativistic fluid dynamics taking viscous corrections and resonance decays into account”. Master’s thesis. Universität Heidelberg, 2020.

61. R. Soltz, C. DeTar, F. Karsch, S. Mukherjee, and P. Vranas. “Lattice QCD Thermodynamics with Physical Quark Masses”. *Annual Review of Nuclear and Particle Science* 65:Volume 65, 2015, 2015, pp. 379–402. ISSN: 1545-4134. DOI: <https://doi.org/10.1146/annurev-nucl-102014-022157>. URL: <https://www.annualreviews.org/content/journals/10.1146/annurev-nucl-102014-022157>.
62. P. Huovinen and P. Petreczky. “QCD equation of state and hadron resonance gas”. *Nuclear Physics A* 837:1, 2010, pp. 26–53. ISSN: 0375-9474. DOI: <https://doi.org/10.1016/j.nuclphysa.2010.02.015>. URL: <https://www.sciencedirect.com/science/article/pii/S0375947410003696>.
63. A. Bazavov, T. Bhattacharya, C. DeTar, H.-T. Ding, S. Gottlieb, R. Gupta, P. Hegde, U. M. Heller, F. Karsch, E. Laermann, L. Levkova, S. Mukherjee, P. Petreczky, C. Schmidt, C. Schroeder, R. A. Soltz, W. Soeldner, R. Sugar, M. Wagner, and P. Vranas. “Equation of state in (2 + 1)-flavor QCD”. *Phys. Rev. D* 90, 9 2014, p. 094503. DOI: [10.1103/PhysRevD.90.094503](https://doi.org/10.1103/PhysRevD.90.094503). URL: <https://link.aps.org/doi/10.1103/PhysRevD.90.094503>.
64. N. Christiansen, M. Haas, J. M. Pawłowski, and N. Strodthoff. “Transport Coefficients in Yang-Mills Theory and QCD”. *Phys. Rev. Lett.* 115, 11 2015, p. 112002. DOI: [10.1103/PhysRevLett.115.112002](https://doi.org/10.1103/PhysRevLett.115.112002). URL: <https://link.aps.org/doi/10.1103/PhysRevLett.115.112002>.
65. J. M. Pawłowski. Private communication. 2022.
66. J. S. Moreland, J. E. Bernhard, and S. A. Bass. “Bayesian calibration of a hybrid nuclear collision model using p –Pb and Pb-Pb data at energies available at the CERN Large Hadron Collider”. *Phys. Rev. C* 101, 2 2020, p. 024911. DOI: [10.1103/PhysRevC.101.024911](https://doi.org/10.1103/PhysRevC.101.024911). URL: <https://link.aps.org/doi/10.1103/PhysRevC.101.024911>.
67. F. Cooper and G. Frye. “Single-particle distribution in the hydrodynamic and statistical thermodynamic models of multiparticle production”. *Phys. Rev. D* 10, 1 1974, pp. 186–189. DOI: [10.1103/PhysRevD.10.186](https://doi.org/10.1103/PhysRevD.10.186). URL: <https://link.aps.org/doi/10.1103/PhysRevD.10.186>.
68. D. Teaney. “Effect of shear viscosity on spectra, elliptic flow, and Hanbury Brown–Twiss radii”. *Phys. Rev. C* 68, 3 2003, p. 034913. DOI: [10.1103/PhysRevC.68.034913](https://doi.org/10.1103/PhysRevC.68.034913). URL: <https://link.aps.org/doi/10.1103/PhysRevC.68.034913>.
69. J.-F. ç. Paquet, C. Shen, G. S. Denicol, M. Luzum, B. Schenke, S. Jeon, and C. Gale. “Production of photons in relativistic heavy-ion collisions”. *Phys. Rev. C* 93, 4 2016, p. 044906. DOI: [10.1103/PhysRevC.93.044906](https://doi.org/10.1103/PhysRevC.93.044906). URL: <https://link.aps.org/doi/10.1103/PhysRevC.93.044906>.
70. H. Bebie, P. Gerber, J. Goity, and H. Leutwyler. “The role of the entropy in an expanding hadronic gas”. *Nuclear Physics B* 378:1, 1992, pp. 95–128. ISSN: 0550-3213. DOI: [https://doi.org/10.1016/0550-3213\(92\)90005-V](https://doi.org/10.1016/0550-3213(92)90005-V). URL: <https://www.sciencedirect.com/science/article/pii/S055032139290005V>.

71. M. Bleicher, E. Zabrodin, C. Spieles, S. A. Bass, C. Ernst, S. Soff, L. Bravina, M. Belkacem, H. Weber, H. Stöcker, and W. Greiner. “Relativistic hadron-hadron collisions in the ultra-relativistic quantum molecular dynamics model”. *Journal of Physics G: Nuclear and Particle Physics* 25:9, 1999, p. 1859. DOI: [10.1088/0954-3899/25/9/308](https://doi.org/10.1088/0954-3899/25/9/308). URL: <https://dx.doi.org/10.1088/0954-3899/25/9/308>.
72. G. Torrieri, S. Steinke, W. Broniowski, W. Florkowski, J. Letessier, and J. Rafelski. “SHARE: Statistical hadronization with resonances”. *Computer Physics Communications* 167:3, 2005, pp. 229–251. ISSN: 0010-4655. DOI: <https://doi.org/10.1016/j.cpc.2005.01.004>. URL: <https://www.sciencedirect.com/science/article/pii/S0010465505000755>.
73. A. Mazeliauskas, S. Floerchinger, E. Grossi, and D. Teaney. “Fast resonance decays in nuclear collisions”. *The European Physical Journal C* 79:3, 2019. ISSN: 1434-6052. DOI: [10.1140/epjc/s10052-019-6791-7](https://doi.org/10.1140/epjc/s10052-019-6791-7). URL: <http://dx.doi.org/10.1140/epjc/s10052-019-6791-7>.
74. N. Borghini, P. M. Dinh, and J.-Y. Ollitrault. “New method for measuring azimuthal distributions in nucleus-nucleus collisions”. *Phys. Rev. C* 63, 5 2001, p. 054906. DOI: [10.1103/PhysRevC.63.054906](https://doi.org/10.1103/PhysRevC.63.054906). URL: <https://link.aps.org/doi/10.1103/PhysRevC.63.054906>.
75. A. Bilandzic, R. Snellings, and S. Voloshin. “Flow analysis with cumulants: Direct calculations”. *Phys. Rev. C* 83, 4 2011, p. 044913. DOI: [10.1103/PhysRevC.83.044913](https://doi.org/10.1103/PhysRevC.83.044913). URL: <https://link.aps.org/doi/10.1103/PhysRevC.83.044913>.
76. S. Floerchinger, E. Grossi, and K. Vahid Yousefnia. “Model comparison for initial density fluctuations in high-energy heavy-ion collisions”. *Phys. Rev. C* 102, 5 2020, p. 054914. DOI: [10.1103/PhysRevC.102.054914](https://doi.org/10.1103/PhysRevC.102.054914). URL: <https://link.aps.org/doi/10.1103/PhysRevC.102.054914>.
77. D. C. Montgomery. *Design and Analysis of Experiments*. Wiley, 2019. ISBN: 978-1-119-63542-0. URL: <https://www.wiley.com/en-us/Design+and+Analysis+of+Experiments%2C+10th+Edition-p-9781119492443>.
78. M. D. McKay, R. J. Beckman, and W. J. Conover. “A Comparison of Three Methods for Selecting Values of Input Variables in the Analysis of Output from a Computer Code”. *Technometrics* 21:2, 1979, pp. 239–245. ISSN: 00401706. URL: <http://www.jstor.org/stable/1268522>.
79. pyDOE3. *Randomized Designs*. URL: <https://pydoe3.readthedocs.io/en/stable/randomized.html#latin-hypercube>.
80. Y. Seemann. “Multidimensional parameter optimization in fluid dynamic simulations of heavy-ion collisions”. Master’s thesis. Universität Heidelberg, 2022. URL: <https://www.physi.uni-heidelberg.de/Publications/MasterThesisYannisSeemann.pdf>.
81. C. E. Rasmussen and C. K. I. Williams. *Gaussian Processes for Machine Learning*. MIT Press, Cambridge, MA, 2006. URL: <http://gaussianprocess.org/gpml>.
82. J. E. Bernhard, J. S. Moreland, and S. A. Bass. “Bayesian estimation of the specific shear and bulk viscosity of quark–gluon plasma”. *Nature Phys.* 15:11, 2019, pp. 1113–1117. DOI: [10.1038/s41567-019-0611-8](https://doi.org/10.1038/s41567-019-0611-8).

83. J. E. Parkkila, A. Onnerstad, and D. J. Kim. “Bayesian estimation of the specific shear and bulk viscosity of the quark-gluon plasma with additional flow harmonic observables”. *Phys. Rev. C* 104, 5 2021, p. 054904. DOI: [10.1103/PhysRevC.104.054904](https://doi.org/10.1103/PhysRevC.104.054904). URL: <https://link.aps.org/doi/10.1103/PhysRevC.104.054904>.
84. G. Nijs, W. van der Schee, U. Gürsoy, and R. Snellings. “Transverse Momentum Differential Global Analysis of Heavy-Ion Collisions”. *Phys. Rev. Lett.* 126, 20 2021, p. 202301. DOI: [10.1103/PhysRevLett.126.202301](https://doi.org/10.1103/PhysRevLett.126.202301). URL: <https://link.aps.org/doi/10.1103/PhysRevLett.126.202301>.
85. D. Everett, W. Ke, J.-F. Paquet, G. Vujanovic, S. A. Bass, L. Du, C. Gale, M. Heffernan, U. Heinz, D. Liyanage, M. Luzum, A. Majumder, M. McNelis, C. Shen, Y. Xu, A. Angerami, S. Cao, Y. Chen, J. Coleman, L. Cunqueiro, T. Dai, R. Ehlers, H. Elfner, W. Fan, R. J. Fries, F. Garza, Y. He, B. V. Jacak, P. M. Jacobs, S. Jeon, B. Kim, M. Kordell, A. Kumar, S. Mak, J. Mulligan, C. Nattrass, D. Oliinychenko, C. Park, J. H. Putschke, G. Roland, B. Schenke, L. Schwiebert, A. Silva, C. Sirimanna, R. A. Soltz, Y. Tachibana, X.-N. Wang, and R. L. Wolpert. “Multisystem Bayesian constraints on the transport coefficients of QCD matter”. *Phys. Rev. C* 103, 5 2021, p. 054904. DOI: [10.1103/PhysRevC.103.054904](https://doi.org/10.1103/PhysRevC.103.054904). URL: <https://link.aps.org/doi/10.1103/PhysRevC.103.054904>.
86. D. Liyanage, Ö. Sürer, M. Plumlee, S. M. Wild, and U. Heinz. “Bayesian calibration of viscous anisotropic hydrodynamic simulations of heavy-ion collisions”. *Phys. Rev. C* 108, 5 2023, p. 054905. DOI: [10.1103/PhysRevC.108.054905](https://doi.org/10.1103/PhysRevC.108.054905). URL: <https://link.aps.org/doi/10.1103/PhysRevC.108.054905>.
87. D. R. Phillips, R. J. Furnstahl, U. Heinz, T. Maiti, W. Nazarewicz, F. M. Nunes, M. Plumlee, M. T. Pratola, S. Pratt, F. G. Viens, and S. M. Wild. “Get on the BAND Wagon: a Bayesian framework for quantifying model uncertainties in nuclear dynamics”. *Journal of Physics G: Nuclear and Particle Physics* 48:7, 2021, p. 072001. ISSN: 1361-6471. DOI: [10.1088/1361-6471/abf1df](https://doi.org/10.1088/1361-6471/abf1df). URL: <http://dx.doi.org/10.1088/1361-6471/abf1df>.
88. R. M. Neal. “Priors for Infinite Networks”. In: *Bayesian Learning for Neural Networks*. Springer New York, New York, NY, 1996, pp. 29–53. ISBN: 978-1-4612-0745-0. DOI: [10.1007/978-1-4612-0745-0_2](https://doi.org/10.1007/978-1-4612-0745-0_2). URL: https://doi.org/10.1007/978-1-4612-0745-0_2.
89. D. Liyanage, Y. Ji, D. Everett, M. Heffernan, U. Heinz, S. Mak, and J.-F. Paquet. “Efficient emulation of relativistic heavy ion collisions with transfer learning”. *Phys. Rev. C* 105, 3 2022, p. 034910. DOI: [10.1103/PhysRevC.105.034910](https://doi.org/10.1103/PhysRevC.105.034910). URL: <https://link.aps.org/doi/10.1103/PhysRevC.105.034910>.
90. J.-F. Paquet. *Applications of emulation and Bayesian methods in heavy-ion physics*. 2023. arXiv: [2310.17618](https://arxiv.org/abs/2310.17618) [nucl-th].
91. I. Neutelings. *Neural Networks*. 2022. URL: https://tikz.net/neural_networks/.
92. D. E. Rumelhart, G. E. Hinton, and R. J. Williams. “Learning representations by back-propagating errors”. *Nature* 323:6088, 1, 1986, pp. 533–536. ISSN: 1476-4687. DOI: [10.1038/323533a0](https://doi.org/10.1038/323533a0). URL: <https://doi.org/10.1038/323533a0>.

93. X. Glorot and Y. Bengio. “Understanding the difficulty of training deep feedforward neural networks”. In: *Proceedings of the Thirteenth International Conference on Artificial Intelligence and Statistics*. Ed. by Y. W. Teh and M. Titterton. Vol. 9. Proceedings of Machine Learning Research. PMLR, Chia Laguna Resort, Sardinia, Italy, 2010, pp. 249–256. URL: <https://proceedings.mlr.press/v9/glorot10a.html>.
94. K. He, X. Zhang, S. Ren, and J. Sun. *Delving Deep into Rectifiers: Surpassing Human-Level Performance on ImageNet Classification*. 2015. arXiv: [1502.01852](https://arxiv.org/abs/1502.01852) [cs.CV].
95. D. P. Kingma and J. Ba. *Adam: A Method for Stochastic Optimization*. 2017. arXiv: [1412.6980](https://arxiv.org/abs/1412.6980) [cs.LG].
96. J. Duchi, E. Hazan, and Y. Singer. “Adaptive Subgradient Methods for Online Learning and Stochastic Optimization”. *Journal of Machine Learning Research* 12:61, 2011, pp. 2121–2159. URL: <http://jmlr.org/papers/v12/duchi11a.html>.
97. A. Paszke, S. Gross, F. Massa, A. Lerer, J. Bradbury, G. Chanan, T. Killeen, Z. Lin, N. Gimelshein, L. Antiga, A. Desmaison, A. Köpf, E. Yang, Z. DeVito, M. Raison, A. Tejani, S. Chilamkurthy, B. Steiner, L. Fang, J. Bai, and S. Chintala. *PyTorch: An Imperative Style, High-Performance Deep Learning Library*. 2019. arXiv: [1912.01703](https://arxiv.org/abs/1912.01703) [cs.LG].
98. Ray. *Ray Tune: Hyperparameter Tuning*. URL: <https://docs.ray.io/en/latest/tune/index.html>.
99. B. Lakshminarayanan, A. Pritzel, and C. Blundell. *Simple and Scalable Predictive Uncertainty Estimation using Deep Ensembles*. 2017. arXiv: [1612.01474](https://arxiv.org/abs/1612.01474) [stat.ML].
100. J. Gawlikowski, C. R. N. Tassi, M. Ali, J. Lee, M. Humt, J. Feng, A. Kruspe, R. Triebel, P. Jung, R. Roscher, M. Shahzad, W. Yang, R. Bamler, and X. X. Zhu. *A Survey of Uncertainty in Deep Neural Networks*. 2022. arXiv: [2107.03342](https://arxiv.org/abs/2107.03342) [cs.LG].
101. O. Sagi and L. Rokach. “Ensemble learning: A survey”. *WIREs Data Mining and Knowledge Discovery* 8:4, 2018, e1249. DOI: <https://doi.org/10.1002/widm.1249>. eprint: <https://wires.onlinelibrary.wiley.com/doi/pdf/10.1002/widm.1249>. URL: <https://wires.onlinelibrary.wiley.com/doi/abs/10.1002/widm.1249>.
102. S. Geman and D. Geman. “Stochastic Relaxation, Gibbs Distributions, and the Bayesian Restoration of Images”. *IEEE Transactions on Pattern Analysis and Machine Intelligence* PAMI-6:6, 1984, pp. 721–741. DOI: [10.1109/TPAMI.1984.4767596](https://doi.org/10.1109/TPAMI.1984.4767596).
103. N. Metropolis, A. W. Rosenbluth, M. N. Rosenbluth, A. H. Teller, and E. Teller. “Equation of State Calculations by Fast Computing Machines”. *The Journal of Chemical Physics* 21:6, 1953, pp. 1087–1092. ISSN: 0021-9606. DOI: [10.1063/1.1699114](https://doi.org/10.1063/1.1699114). eprint: https://pubs.aip.org/aip/jcp/article-pdf/21/6/1087/18802390/1087_1_online.pdf. URL: <https://doi.org/10.1063/1.1699114>.
104. W. K. Hastings. “Monte Carlo sampling methods using Markov chains and their applications”. *Biometrika* 57:1, 1970, pp. 97–109. ISSN: 0006-3444. DOI: [10.1093/biomet/57.1.97](https://doi.org/10.1093/biomet/57.1.97). eprint: <https://academic.oup.com/biomet/article-pdf/57/1/97/23940249/57-1-97.pdf>. URL: <https://doi.org/10.1093/biomet/57.1.97>.

105. R. M. Neal. “Slice sampling”. *The Annals of Statistics* 31:3, 2003, pp. 705–767. DOI: [10.1214/aos/1056562461](https://doi.org/10.1214/aos/1056562461). URL: <https://doi.org/10.1214/aos/1056562461>.
106. D. Foreman-Mackey, D. W. Hogg, D. Lang, and J. Goodman. “emcee: The MCMC Hammer”. *Publications of the Astronomical Society of the Pacific* 125:925, 2013, p. 306. DOI: [10.1086/670067](https://dx.doi.org/10.1086/670067). URL: <https://dx.doi.org/10.1086/670067>.
107. J. Goodman and J. Weare. “Ensemble samplers with affine invariance”. English (US). *Communications in Applied Mathematics and Computational Science* 5:1, 2010. Publisher Copyright: © 2010 by Mathematical Sciences Publishers., pp. 65–80. ISSN: 1559-3940. DOI: [10.2140/camcos.2010.5.65](https://doi.org/10.2140/camcos.2010.5.65).
108. C. Shen and L. Yan. “Recent development of hydrodynamic modeling in heavy-ion collisions”. *Nucl. Sci. Tech.* 31:12, 2020, p. 122. DOI: [10.1007/s41365-020-00829-z](https://doi.org/10.1007/s41365-020-00829-z). arXiv: [2010.12377](https://arxiv.org/abs/2010.12377) [nucl-th].
109. B. Schenke, C. Shen, and P. Tribedy. “Running the gamut of high energy nuclear collisions”. *Phys. Rev. C* 102:4, 2020, p. 044905. DOI: [10.1103/PhysRevC.102.044905](https://doi.org/10.1103/PhysRevC.102.044905). arXiv: [2005.14682](https://arxiv.org/abs/2005.14682) [nucl-th].
110. V. Begun and W. Florkowski. “Bose-Einstein condensation of pions in heavy-ion collisions at the CERN Large Hadron Collider (LHC) energies”. *Phys. Rev. C* 91, 2015, p. 054909. DOI: [10.1103/PhysRevC.91.054909](https://doi.org/10.1103/PhysRevC.91.054909). arXiv: [1503.04040](https://arxiv.org/abs/1503.04040) [nucl-th].
111. V. Begun. “Fluctuations as a test of chemical non-equilibrium at the LHC”. *Phys. Rev. C* 94:5, 2016, p. 054904. DOI: [10.1103/PhysRevC.94.054904](https://doi.org/10.1103/PhysRevC.94.054904). arXiv: [1603.02254](https://arxiv.org/abs/1603.02254) [nucl-th].
112. P. Huovinen, P. M. Lo, M. Marczenko, K. Morita, K. Redlich, and C. Sasaki. “Effects of ρ -meson width on pion distributions in heavy-ion collisions”. *Phys. Lett. B* 769, 2017, pp. 509–512. DOI: [10.1016/j.physletb.2017.03.060](https://doi.org/10.1016/j.physletb.2017.03.060). arXiv: [1608.06817](https://arxiv.org/abs/1608.06817) [hep-ph].
113. B. Abelev et al. “Centrality dependence of π , K , and p production in Pb-Pb collisions at $\sqrt{s_{NN}} = 2.76$ TeV”. *Phys. Rev. C* 88, 4 2013, p. 044910. DOI: [10.1103/PhysRevC.88.044910](https://doi.org/10.1103/PhysRevC.88.044910). URL: <https://link.aps.org/doi/10.1103/PhysRevC.88.044910>.
114. S. Acharya et al. “Production of charged pions, kaons, and (anti-)protons in Pb-Pb and inelastic pp collisions at $\sqrt{s_{NN}} = 5.02$ TeV”. *Phys. Rev. C* 101, 4 2020, p. 044907. DOI: [10.1103/PhysRevC.101.044907](https://doi.org/10.1103/PhysRevC.101.044907). URL: <https://link.aps.org/doi/10.1103/PhysRevC.101.044907>.
115. S. Acharya et al. “Production of pions, kaons, (anti-)protons and ϕ mesons in Xe–Xe collisions at $\sqrt{s_{NN}} = 5.44$ TeV”. *Eur. Phys. J. C* 81:7, 2021, p. 584. DOI: [10.1140/epjc/s10052-021-09304-4](https://doi.org/10.1140/epjc/s10052-021-09304-4). arXiv: [2101.03100](https://arxiv.org/abs/2101.03100) [nucl-ex].
116. J. Adam et al. “Multiplicity dependence of charged pion, kaon, and (anti)proton production at large transverse momentum in p-Pb collisions at $\sqrt{s_{NN}} = 5.02$ TeV”. *Phys. Lett. B* 760, 2016, pp. 720–735. DOI: [10.1016/j.physletb.2016.07.050](https://doi.org/10.1016/j.physletb.2016.07.050). arXiv: [1601.03658](https://arxiv.org/abs/1601.03658) [nucl-ex].
117. S. S. Adler et al. “Identified charged particle spectra and yields in Au + Au collisions at $\sqrt{s_{NN}} = 200$ GeV”. *Phys. Rev. C* 69, 3 2004, p. 034909. DOI: [10.1103/PhysRevC.69.034909](https://doi.org/10.1103/PhysRevC.69.034909). URL: <https://link.aps.org/doi/10.1103/PhysRevC.69.034909>.

118. K. Adcox et al. “Centrality Dependence of $\pi^{+/-}$, $K^{+/-}$, p , and \bar{p} Production from $\sqrt{s_{\text{NN}}} = 130$ GeV Au+Au Collisions at RHIC”. *Phys. Rev. Lett.* 88, 2002, p. 242301. DOI: [10.1103/PhysRevLett.88.242301](https://doi.org/10.1103/PhysRevLett.88.242301). arXiv: [nucl-ex/0112006](https://arxiv.org/abs/nuclex/0112006).
119. J. Adams et al. “Identified particle distributions in pp and Au+Au collisions at $\sqrt{s_{\text{NN}}} = 200$ GeV”. *Phys. Rev. Lett.* 92, 2004, p. 112301. DOI: [10.1103/PhysRevLett.92.112301](https://doi.org/10.1103/PhysRevLett.92.112301). arXiv: [nucl-ex/0310004](https://arxiv.org/abs/nuclex/0310004).
120. B. I. Abelev et al. “Systematic Measurements of Identified Particle Spectra in pp , d^+ Au and Au+Au Collisions from STAR”. *Phys. Rev. C* 79, 2009, p. 034909. DOI: [10.1103/PhysRevC.79.034909](https://doi.org/10.1103/PhysRevC.79.034909). arXiv: [0808.2041 \[nucl-ex\]](https://arxiv.org/abs/0808.2041).
121. P. F. Kolb and U. W. Heinz. “Hydrodynamic description of ultrarelativistic heavy ion collisions”, 2003. Ed. by R. C. Hwa and X.-N. Wang, pp. 634–714. arXiv: [nucl-th/0305084](https://arxiv.org/abs/nucloth/0305084).
122. L. Vermunt, Y. Seemann, A. Dubla, S. Floerchinger, E. Grossi, A. Kirchner, S. Masciocchi, and I. Selyuzhenkov. “Mapping properties of the quark gluon plasma in Pb-Pb and Xe-Xe collisions at energies available at the CERN Large Hadron Collider”. *Phys. Rev. C* 108, 6 2023, p. 064908. DOI: [10.1103/PhysRevC.108.064908](https://doi.org/10.1103/PhysRevC.108.064908). URL: <https://link.aps.org/doi/10.1103/PhysRevC.108.064908>.
123. D. Devetak, A. Dubla, S. Floerchinger, E. Grossi, S. Masciocchi, A. Mazeliauskas, and I. Selyuzhenkov. “Global fluid fits to identified particle transverse momentum spectra from heavy-ion collisions at the Large Hadron Collider”. *J. High Energ. Phys* 06, 2020, p. 044. DOI: [10.1007/JHEP06\(2020\)044](https://doi.org/10.1007/JHEP06(2020)044). arXiv: [1909.10485 \[hep-ph\]](https://arxiv.org/abs/1909.10485).
124. G. Nijs, W. van der Schee, U. Gürsoy, and R. Snellings. “Bayesian analysis of heavy ion collisions with the heavy ion computational framework Trajectum”. *Phys. Rev. C* 103, 5 2021, p. 054909. DOI: [10.1103/PhysRevC.103.054909](https://doi.org/10.1103/PhysRevC.103.054909).
125. A. Dubla, S. Masciocchi, J. M. Pawłowski, B. Schenke, C. Shen, and J. Stachel. “Towards QCD-assisted hydrodynamics for heavy-ion collision phenomenology”. *Nucl. Phys. A* 979, 2018, pp. 251–264. DOI: [10.1016/j.nuclphysa.2018.09.046](https://doi.org/10.1016/j.nuclphysa.2018.09.046). arXiv: [1805.02985 \[nucl-th\]](https://arxiv.org/abs/1805.02985).
126. C. Gale, S. Jeon, B. Schenke, P. Tribedy, and R. Venugopalan. “Event-by-event anisotropic flow in heavy-ion collisions from combined Yang-Mills and viscous fluid dynamics”. *Phys. Rev. Lett.* 110:1, 2013, p. 012302. DOI: [10.1103/PhysRevLett.110.012302](https://doi.org/10.1103/PhysRevLett.110.012302). arXiv: [1209.6330 \[nucl-th\]](https://arxiv.org/abs/1209.6330).
127. S. McDonald, C. Shen, F. Fillion-Gourdeau, S. Jeon, and C. Gale. “Hydrodynamic predictions for Pb+Pb collisions at 5.02 TeV”. *Phys. Rev. C* 95:6, 2017, p. 064913. DOI: [10.1103/PhysRevC.95.064913](https://doi.org/10.1103/PhysRevC.95.064913). arXiv: [1609.02958 \[hep-ph\]](https://arxiv.org/abs/1609.02958).
128. A. Mazeliauskas and V. Viskovic. “Temperature and fluid velocity on the freeze-out surface from π , K , p spectra in pp, p-Pb and Pb-Pb collisions”. *Phys. Rev. C* 101:1, 2020, p. 014910. DOI: [10.1103/PhysRevC.101.014910](https://doi.org/10.1103/PhysRevC.101.014910). arXiv: [1907.11059 \[hep-ph\]](https://arxiv.org/abs/1907.11059).

129. J. E. Bernhard, J. S. Moreland, S. A. Bass, J. Liu, and U. Heinz. “Applying Bayesian parameter estimation to relativistic heavy-ion collisions: Simultaneous characterization of the initial state and quark-gluon plasma medium”. *Phys. Rev. C* 94, 2 2016, p. 024907. DOI: [10.1103/PhysRevC.94.024907](https://doi.org/10.1103/PhysRevC.94.024907). URL: <https://link.aps.org/doi/10.1103/PhysRevC.94.024907>.
130. S. Ryu, J.-F. ç. Paquet, C. Shen, G. Denicol, B. Schenke, S. Jeon, and C. Gale. “Effects of bulk viscosity and hadronic rescattering in heavy ion collisions at energies available at the BNL Relativistic Heavy Ion Collider and at the CERN Large Hadron Collider”. *Phys. Rev. C* 97, 3 2018, p. 034910. DOI: [10.1103/PhysRevC.97.034910](https://doi.org/10.1103/PhysRevC.97.034910). URL: <https://link.aps.org/doi/10.1103/PhysRevC.97.034910>.
131. J. S. Moreland, J. E. Bernhard, and S. A. Bass. “Estimating initial state and quark-gluon plasma medium properties using a hybrid model with nucleon substructure calibrated to p -Pb and Pb-Pb collisions at $\sqrt{s_{NN}} = 5.02$ TeV”. 101:2, 21, 2020, p. 024911. ISSN: 2469-9985, 2469-9993. arXiv: [1808.02106](https://arxiv.org/abs/1808.02106)[nucl-ex, physics:nucl-th]. URL: <http://arxiv.org/abs/1808.02106>.
132. G. Giacalone. *There and Sharp Again: The Circle Journey of Nucleons and Energy Deposition*. 2022. arXiv: [2208.06839](https://arxiv.org/abs/2208.06839) [nucl-th]. URL: <https://arxiv.org/abs/2208.06839>.
133. A. Collaboration. “Centrality determination in heavy ion collisions”, 2018. URL: <https://cds.cern.ch/record/2636623>.
134. A. Adare et al. “Transverse energy production and charged-particle multiplicity at midrapidity in various systems from $\sqrt{s_{NN}} = 7.7$ to 200 GeV”. *Phys. Rev. C* 93, 2 2016, p. 024901. DOI: [10.1103/PhysRevC.93.024901](https://doi.org/10.1103/PhysRevC.93.024901). URL: <https://link.aps.org/doi/10.1103/PhysRevC.93.024901>.
135. B. Bally, M. Bender, G. Giacalone, and V. Somà. “Evidence of the Triaxial Structure of ^{129}Xe at the Large Hadron Collider”. *Phys. Rev. Lett.* 128, 8 2022, p. 082301. DOI: [10.1103/PhysRevLett.128.082301](https://doi.org/10.1103/PhysRevLett.128.082301). URL: <https://link.aps.org/doi/10.1103/PhysRevLett.128.082301>.
136. G. Giacalone. *A matter of shape: seeing the deformation of atomic nuclei at high-energy colliders*. 2021. arXiv: [2101.00168](https://arxiv.org/abs/2101.00168) [nucl-th].
137. S. Acharya et al. “Transverse momentum spectra and nuclear modification factors of charged particles in Xe-Xe collisions at $\sqrt{s_{NN}} = 5.44$ TeV”. *Phys. Lett. B* 788, 2019, pp. 166–179. DOI: [10.1016/j.physletb.2018.10.052](https://doi.org/10.1016/j.physletb.2018.10.052). arXiv: [1805.04399](https://arxiv.org/abs/1805.04399) [nucl-ex].
138. W. Busza and A. S. Goldhaber. “Nuclear stopping power”. *Physics Letters B* 139:4, 1984, pp. 235–238. ISSN: 0370-2693. DOI: [https://doi.org/10.1016/0370-2693\(84\)91070-0](https://doi.org/10.1016/0370-2693(84)91070-0). URL: <https://www.sciencedirect.com/science/article/pii/0370269384910700>.
139. S. Acharya et al. “The ALICE experiment: a journey through QCD”. *The European Physical Journal C* 84:8, 2024, p. 813. ISSN: 1434-6052. DOI: [10.1140/epjc/s10052-024-12935-y](https://doi.org/10.1140/epjc/s10052-024-12935-y). URL: <https://doi.org/10.1140/epjc/s10052-024-12935-y>.

140. P. Virtanen, R. Gommers, T. E. Oliphant, M. Haberland, T. Reddy, D. Cournapeau, E. Burovski, P. Peterson, W. Weckesser, J. Bright, S. J. van der Walt, M. Brett, J. Wilson, K. J. Millman, N. Mayorov, A. R. J. Nelson, E. Jones, R. Kern, E. Larson, C. J. Carey, Í. Polat, Y. Feng, E. W. Moore, J. VanderPlas, D. Laxalde, J. Perktold, R. Cimrman, I. Henriksen, E. A. Quintero, C. R. Harris, A. M. Archibald, A. H. Ribeiro, F. Pedregosa, P. van Mulbregt, and SciPy 1.0 Contributors. “SciPy 1.0: Fundamental Algorithms for Scientific Computing in Python”. *Nature Methods* 17, 2020, pp. 261–272. DOI: [10.1038/s41592-019-0686-2](https://doi.org/10.1038/s41592-019-0686-2).
141. A. Collaboration. “Elliptic flow of identified hadrons in Pb-Pb collisions at $\sqrt{s_{NN}} = 2.76$ TeV”. *Journal of High Energy Physics* 2015:6, 2015, p. 190. ISSN: 1029-8479. DOI: [10.1007/JHEP06\(2015\)190](https://doi.org/10.1007/JHEP06(2015)190). arXiv: [1405.4632\[nucl-ex\]](https://arxiv.org/abs/1405.4632). URL: <http://arxiv.org/abs/1405.4632>.
142. J. Adam et al. “Higher harmonic flow coefficients of identified hadrons in Pb-Pb collisions at $\sqrt{s_{NN}} = 2.76$ TeV”. *Journal of High Energy Physics* 2016:9, 28, 2016, p. 164. ISSN: 1029-8479. DOI: [10.1007/JHEP09\(2016\)164](https://doi.org/10.1007/JHEP09(2016)164). URL: [https://doi.org/10.1007/JHEP09\(2016\)164](https://doi.org/10.1007/JHEP09(2016)164).
143. S. Acharya et al. “Anisotropic flow of identified particles in Pb-Pb collisions at $\sqrt{s_{NN}} = 5.02$ TeV”. *Journal of High Energy Physics* 2018:9, 3, 2018, p. 6. ISSN: 1029-8479. DOI: [10.1007/JHEP09\(2018\)006](https://doi.org/10.1007/JHEP09(2018)006). URL: [https://doi.org/10.1007/JHEP09\(2018\)006](https://doi.org/10.1007/JHEP09(2018)006).
144. S. Acharya et al. “Anisotropic flow of identified hadrons in Xe-Xe collisions at $\sqrt{s_{NN}} = 5.44$ TeV”. *JHEP* 10, 2021, p. 152. DOI: [10.1007/JHEP10\(2021\)152](https://doi.org/10.1007/JHEP10(2021)152). arXiv: [2107.10592 \[nucl-ex\]](https://arxiv.org/abs/2107.10592).
145. S. Floerchinger and U. A. Wiedemann. “Kinetic freeze-out, particle spectra, and harmonic-flow coefficients from mode-by-mode hydrodynamics”. *Phys. Rev. C* 89, 3 2014, p. 034914. DOI: [10.1103/PhysRevC.89.034914](https://doi.org/10.1103/PhysRevC.89.034914). URL: <https://link.aps.org/doi/10.1103/PhysRevC.89.034914>.
146. S. Acharya et al. “Linear and non-linear flow mode in Pb–Pb collisions at $\sqrt{s_{NN}} = 2.76$ TeV”. *Physics Letters B* 773, 2017, pp. 68–80. ISSN: 0370-2693. DOI: [10.1016/j.physletb.2017.07.060](https://doi.org/10.1016/j.physletb.2017.07.060). URL: <http://dx.doi.org/10.1016/j.physletb.2017.07.060>.
147. S. Acharya et al. “Higher harmonic non-linear flow modes of charged hadrons in Pb-Pb collisions at $\sqrt{s_{NN}} = 5.02$ TeV”. *Journal of High Energy Physics* 2020:5, 2020. ISSN: 1029-8479. DOI: [10.1007/jhep05\(2020\)085](https://doi.org/10.1007/jhep05(2020)085). URL: [http://dx.doi.org/10.1007/JHEP05\(2020\)085](http://dx.doi.org/10.1007/JHEP05(2020)085).
148. B. Schenke, S. Jeon, and C. Gale. “Higher flow harmonics from (3 + 1)D event-by-event viscous hydrodynamics”. *Phys. Rev. C* 85, 2 2012, p. 024901. DOI: [10.1103/PhysRevC.85.024901](https://doi.org/10.1103/PhysRevC.85.024901). URL: <https://link.aps.org/doi/10.1103/PhysRevC.85.024901>.
149. D. Foreman-Mackey. “corner.py: Scatterplot matrices in Python”. *The Journal of Open Source Software* 1:2, 2016, p. 24. DOI: [10.21105/joss.00024](https://doi.org/10.21105/joss.00024). URL: <https://doi.org/10.21105/joss.00024>.
150. K. Adcox et al. “Single identified hadron spectra from $\sqrt{s_{NN}} = 130$ GeV Au + Au collisions”. *Phys. Rev. C* 69, 2 2004, p. 024904. DOI: [10.1103/PhysRevC.69.024904](https://doi.org/10.1103/PhysRevC.69.024904). URL: <https://link.aps.org/doi/10.1103/PhysRevC.69.024904>.

151. P. Huovinen, P. Kolb, U. Heinz, P. Ruuskanen, and S. Voloshin. “Radial and elliptic flow at RHIC: further predictions”. *Physics Letters B* 503:1, 2001, pp. 58–64. ISSN: 0370-2693. DOI: [https://doi.org/10.1016/S0370-2693\(01\)00219-2](https://doi.org/10.1016/S0370-2693(01)00219-2). URL: <https://www.sciencedirect.com/science/article/pii/S0370269301002192>.
152. S. Voloshin and A. Poskanzer. “The physics of the centrality dependence of elliptic flow”. *Physics Letters B* 474:1, 2000, pp. 27–32. ISSN: 0370-2693. DOI: [https://doi.org/10.1016/S0370-2693\(00\)00017-4](https://doi.org/10.1016/S0370-2693(00)00017-4). URL: <https://www.sciencedirect.com/science/article/pii/S0370269300000174>.
153. Snellings, Raimond. “How much does the hadronic phase contribute to the observed anisotropic flow at the LHC?” *EPJ Web of Conferences* 97, 2015, p. 00025. DOI: [10.1051/epjconf/20159700025](https://doi.org/10.1051/epjconf/20159700025). URL: <https://doi.org/10.1051/epjconf/20159700025>.
154. P. K. Kovtun, D. T. Son, and A. O. Starinets. “Viscosity in Strongly Interacting Quantum Field Theories from Black Hole Physics”. *Phys. Rev. Lett.* 94, 11 2005, p. 111601. DOI: [10.1103/PhysRevLett.94.111601](https://doi.org/10.1103/PhysRevLett.94.111601). URL: <https://link.aps.org/doi/10.1103/PhysRevLett.94.111601>.
155. B. Schenke, C. Shen, and P. Tribedy. “Running the gamut of high energy nuclear collisions”. *Phys. Rev. C* 102, 4 2020, p. 044905. DOI: [10.1103/PhysRevC.102.044905](https://doi.org/10.1103/PhysRevC.102.044905). URL: <https://link.aps.org/doi/10.1103/PhysRevC.102.044905>.
156. H. CRAMÉR. *Mathematical Methods of Statistics (PMS-9)*. Princeton University Press, 1999. ISBN: 9780691005478. URL: <http://www.jstor.org/stable/j.ctt1bpm9r4>.
157. B. Abelev et al. “Event-by-event mean p_T fluctuations in pp and Pb-Pb collisions at the LHC”. *The European Physical Journal C* 74:10, 2014, p. 3077. ISSN: 1434-6052. DOI: [10.1140/epjc/s10052-014-3077-y](https://doi.org/10.1140/epjc/s10052-014-3077-y). URL: <https://doi.org/10.1140/epjc/s10052-014-3077-y>.
158. G. Giacalone, F. G. Gardim, J. Noronha-Hostler, and J.-Y. Ollitrault. “Skewness of mean transverse momentum fluctuations in heavy-ion collisions”. *Phys. Rev. C* 103, 2 2021, p. 024910. DOI: [10.1103/PhysRevC.103.024910](https://doi.org/10.1103/PhysRevC.103.024910). URL: <https://link.aps.org/doi/10.1103/PhysRevC.103.024910>.
159. Z. Qiu, C. Shen, and U. Heinz. “Resonance decay contributions to higher-order anisotropic flow coefficients”. *Phys. Rev. C* 86, 6 2012, p. 064906. DOI: [10.1103/PhysRevC.86.064906](https://doi.org/10.1103/PhysRevC.86.064906). URL: <https://link.aps.org/doi/10.1103/PhysRevC.86.064906>.
160. U. W. Heinz. *Concepts of Heavy-Ion Physics*. 2004. arXiv: [hep-ph/0407360](https://arxiv.org/abs/hep-ph/0407360).

DECLARATION OF AUTHORSHIP

Ich versichere, dass ich diese Arbeit selbstständig verfasst und keine anderen als die angegebenen Quellen und Hilfsmittel benutzt habe.

Heidelberg, den 1. September 2024,

A handwritten signature in black ink, appearing to be 'Kraus', with a long horizontal line extending to the right.